ABSTRACT

Title of dissertation: STUDY AND MITIGATION OF TRANSVERSE RESONANCES WITH SPACE CHARGE EFFECTS AT THE UNIVERSITY OF MARYLAND ELECTRON RING

Levon Dovlatyan, Doctor of Philosophy, 2020

Dissertation directed by: Professor Thomas Antonsen
Department of Electrical and Computer Engineering

Associate Research Professor Brian Beaudoin
Institute for Research in Electronics and
Applied Physics

Research at the intensity frontier of particle physics has led to the consideration of accelerators that push the limits on achievable beam intensities. At high beam intensities Coulomb interactions between charged particles generate a space charge force that complicates beam dynamics. The space charge force can lead to a range of nonlinear, intensity-limiting phenomena that result in degraded beam quality and current loss. This is the central issue faced by the next generation of high-intensity particle accelerators. An improved understanding of the interaction of the space charge forces and transverse particle motion will help researchers better design around these limiting issues. Furthermore, any scheme able to mitigate the impacts of such destructive interactions for space charge dominated beams would help alleviate a significant limitation in reaching higher beam intensities. Experi-

mental work addressing these issues is presented using the University of Maryland Electron Ring (UMER).

This dissertation presents experimental studies of space charge dominated beams, and in particular the resonant interaction between the transverse motion of the beam and the periodic perturbations that occur due to the focusing elements in a circular ring. These interactions are characterized in terms of the tune shifts, Q_x and Q_y, that are the number of transverse oscillations (in and out of the plane of the ring) per trip around the ring. Resonances occur for both integer and half-integer values of tune shift. Particle tune measurement tools and resonance detection techniques are developed for use in the experiment. Results show no shift for either the integer ($Q_x = 7.0, Q_y = 7.0$) or half-integer ($Q_x = 6.5, Q_y = 6.5$) resonance bands as a function of space charge. Accepted theory predicts only a shift in the half-integer resonance case.

A second experiment testing the potential mitigation of transverse resonances through nonlinear detuning of particle orbits from resonance driving terms is also presented. The study included the design, simulation, and experimental test of a quasi- integrable accelerator lattice based on a single nonlinear octupole channel insert. Experiments measured a nonlinear amplitude dependent tune shift within the beam on the order of $\Delta Q_x \approx 0.02$ and $\Delta Q_y \approx 0.03$. The limited tolerances on accelerator steering prevented measuring any larger tune shifts.

STUDY AND MITIGATION OF TRANSVERSE RESONANCES WITH SPACE CHARGE EFFECTS AT THE UNIVERSITY OF MARYLAND ELECTRON RING

by

Levon Dovlatyan

Dissertation submitted to the Faculty of the Graduate School of the
University of Maryland, College Park in partial fulfillment
of the requirements for the degree of
Doctor of Philosophy
2020

Advisory Committee:
Professor Thomas Antonsen, Co-Chair/Advisor
Dr. Brian Beaudoin, Co-Chair/Advisor
Dr. Irving Haber
Professor Timothy Koeth
Professor Daniel Lathrop

Dedication

To my loving grandparents.

Acknowledgments

I would like to thank my advisors Professor Brian Beaudoin and Professor Thomas Antonsen for their continued support throughout this dissertation project. Thank you Brian for always being around to assist with any problems I had in the lab. All the hands on skills I have learned working with accelerators has been because of you. I am grateful that you were always around and willing to support me in any way possible. You have been a great mentor and advisor. I want to also thank Irving Haber, Professor Tim Koeth, and Professor Daniel Lathrop for taking the time to serve on my dissertation committee.

Many thanks to everyone within the UMER group for their invaluable support throughout my time at the University of Maryland. Thank you to Santiago Bernal, Irving Haber, David Sutter, Eric Montgomery, Antonio Ting, and Rami Kishek. I have learned a tremendous amount of accelerator physics knowledge from the UMER group. I want to especially thank Dr. Irving Haber for always being there to mentor me throughout my time at Maryland. Your willingness to help me better understand the theoretical and simulation work needed for my project helped push me towards the finsh line. Thank you for also painstakingly helping me shift through and edit my dissertation.

I want to thank my fellow graduate students and office mates for their support in assisting me through my dissertation work. Thank you to Kiersten Ruisard, Heidi Komkov, Moiz Siddiqi, David Matthew, Amith Narayan, Glenn Wyche, and Matthew Teperman. Special thanks to Kiersten, who was the senior graduate stu-

dent who helped mentor me during my first few years at UMER. Working with you and being able to bounce ideas back and forth was very helpful for me.

Lastly, I want to thank the many people and entities who worked behind the scenes to support my dissertation work. Thank you Dorothea Brosius for assisting me with implementing this new latex style. Thanks to the USPAS organization for allowing me to attend, as well as teach, various accelerator physics courses. I want to thank DOE-HEP (DE-SC0010301) and the NSF (PHY1414681) for funding the research presented in this dissertation.

Table of Contents

List of Tables

List of Figures

List of Abbreviations

AT	Accelerator Toolbox
BPM	Beam Position Monitor
DA	Dynamic Aperture
DFT	Discrete Fourier Transform
EL	Effective Length
FFT	Fast Fourier Transform
FMA	Frequency Map Analysis
FMAP	Frequency Map
FODO	Focusing and Defocusing alternating gradient lattice
GD	Gradient descent
HCM	Horizontal Corrector Magnet
IC#	Injection Chamber
IOTA	Integrable Optics Test Accelerator
IPAC	International Particle Accelerator Conference
LOCO	Linear Optics From Closed Orbits
NAFF	Numerical Algorithms of Fundamental Frequencies
ND	Nelder-Mead
NIO	Nonlinear Integrable Optics
PCBM	Printed Circuit Board Magnet
PIC	Particle in cell
PS	Peak Strength
PV	Process Variable
QD	Horizontally Defocusing Quadrupole
QF	Horizontally Focusing Quadrupole
RC#	Ring Chamber
RECT	Rectangular window filter function
RF	Radio Frequency
UMER	University of Maryland Electron Ring
VCM	Vertical Corrector Magnet
WCM	Wall Current Monitor

Chapter 1: Introduction

1.1 Motivation

In the early 1900s Rutherford was able to accelerate and scatter a beam of alpha particles off a gold foil, eventually discovering the atomic nucleus. Since then various machines have been developed to accelerate charge particle beams for experimental physics applications. The goals of these accelerators remain the same today: to achieve ever higher energies and intensities. At the energy frontier new technologies like plasma accelerated high gradient accelerators are aiming to disrupt the field by providing high energy beams at a table top scale [1]. More traditional accelerators such as the Large Hadron Collider (LHC) have achieved energies as high as 13 TeV and have proposed building a future super collider able to reach energies of 100 TeV [2].

At the intensity frontier accelerators are pushing the limits on achievable particle beam intensities. Intensity is a measure of the particle density in a beam and scales with beam current. Neutrino generation, medical treatments, and colliders are just a few applications that rely on the advancement of high-intensity accelerators. For example, within a collider a higher beam density leads to more collisions per an interaction enablings rare events to happen at a reasonable time scale and in the

medical field high-intensity beams help produce a larger quantity of radioisotopes for diagnostic purposes and treatments.

The next generation of high-intensity accelerators will need to push beam currents to higher levels. At high currents coulomb interactions between charged particles generate a nonlinear space charge forces that complicate particle dynamics. A central design issue in future high-intensity machines is better understanding the impact of space charge on the dynamics of particle resonances and instabilities. This applies not only to basic energy research accelerators, but also for medical and industrial accelerators which make up 99% of the current 30000 accelerators worldwide [3]. The work in this thesis focuses on studying the physics of space charge interactions with particle beam resonances and experimentally testing potential resonance mitigation techniques for future high-intensity accelerators.

1.2 Historical View

1.2.1 Space charge and instabilities

In the 1960s the potential future demand for high-intensity accelerators convinced researchers that the space charge phenomina in particle beams needed to be better understood and controlled. This led to the development of the rms envelope equations with space charge by Frank Sacherer [4]. Sacherer analyzed the general case for any order resonance in one dimension. The work continued with Gluckerstern's analysis of oscillation modes and resonances in two dimensions [5]. Later Hoftmann provided the first self-consistent Vlasov analysis of space charge induced

transverse instabilities in 2D beams within a periodic focusing system [6].

More recently, increasing intensity in circular accelerators has required a better understand of space charge interactions with particle beam instabilities and resonances. Work by Baartman in 1998 discussed the fact that forces, like space charge, arising from the beam itself can not be treated the same way as external magnet forces [7]. The collective efforts of Sacherer, Hoftmann, Baartman, and others led to the currently accepted theory on coherent and incoherent space charge resonance behaviors. Active theoretical research in the field continues in the present day with researchers continuing to extend existing theories as well as proposing new ones [8, 9, 10].

Space charge within particle accelerators has historically been studied from a theoretical angle, with the use of particle-in-cell (PIC) simulations to verify analytical models. Although a limited number of dedicated experiments have been carried out [11, 12], there still exists a large gap between the amount of theoretical work vs experimental tests within the field [13]. Experimental work is crucial in enhancing existing machines and better designing the next generation of high-intensity accelerators.

1.2.2 Nonlinear integrable optics

All modern day accelerators are based off the theory of alternate-gradient focusing developed by Courant and Snyder in the early 1950s [14]. Accelerators are built using a set of 'linear' focusing optics. Dipole magnets are used to bend

particles around a reference trajectory and alternating gradient quadrupole magnets keep the particles stable and focused on that reference trajectory. Such systems are referred to as 'linear' because they have a restoring force that varies linearly with distance from the reference trajectory center. The Hamiltonian in an alternating-gradient system is conserved and contains two invariants of motion, often called the Courant-Snyder invariants, which guarantee the motion to be fully integrable. In this sytem the particle orbits are bounded and stable over long periods of time on the order of weeks.

Linear magnet systems are susceptible to resonance driving perturbations caused by magnet imperfections and misalignments. The magnet perturbations can cause disruptive beam losses which force accelerator scientists to have strict limits on the size of any magnet field errors and precision of any machine component alignments. As an example, the comissioning work for the new ALS-U light source is designing tools to compensate for 50 μm magnet misalignments [15].

Recently a new accelerator design has been proposed for dealing with resonance based beam losses called the theory of nonlinear integrable optics [16]. The approach employs nonlinear optical elements to induce large frequency spreads within the particle beam causing a reduced response to resonance driving perturbations. Such an approach is not new as existing accelerators already employ sextupoles and octupoles for this purpose. The novelty in nonlinear integrable optics comes in keeping the accelerator system integrable and stable while also including the nonlinear magnets to damp out resonances. A dedicated experiment at Fermilab is underway to test the theory using a newly built machine called the Integrable Optics Test Accelera-

tor (IOTA) [17]. If the experiments are successful, nonlinear integrable optics has the potential to change the field of accelerator physics the same way Courant and Snyder did with the alternate-gradient focusing system in the 1950s.

1.3 Experimental Investigations

1.3.1 Space charge influence on transverse resonance structures

Currently accepted theory on space charge interactions with particle dynamics predicts certain coherent and incoherent tune shifts along with the shifting of resonance band structures in tune space. The particle tune is defined as the total number of transverse oscillations that occur in one revolution around a circular accelerator; it is the 'frequency' of oscillations of the beam as it travels around in a circle. The University of Maryland Electron Ring (UMER) is an ideal accelerator for experimentally testing space charge theories as it can access a wide space charge regime using its different apertured beams. UMER is a 10 keV beam energy, 11.52 meter circumference, alternating-gradient accelerator.

This dissertation experimentally measures particle beam tunes with varying degrees of space charge. It applys existing and novel measurement approaches at detecting resonance bands within tune space. Scans are conducted using a range of space charge dominated beams to observe any potential resonance band shifting at the integer and half-integer levels. A potential mitigation of resonance bands due to space charge induced tune shifts is also measured. A plethora of numerical tools, simulations models, and experimental measurement techniques are developed and

discussed in connection to the dissertation measurement goals.

1.3.2 Testing nonlinear quasi-integrable optics

The Integrable Optics Test Accelerator at Fermilab is currently online and running [18]. Their goal is to test the theory of nonlinear integrable optics using a specialized nonlinear magnet insert. IOTA plans to test the theory on high-intensity proton beams in 2022 and beyond; they employ a novel electron lense scheme to deal with the space charge within the beam [19]. UMER's ability to access large space charge regimes makes it an attractive test bed to demonstrate initial results of nonlinear optics with space charge dominated beams.

At UMER a long octupole channel has been built for nonlinear integrable optics tests. The magnet allows an experimental verification of a quasi-integrable solution where only one invariant of motion exists. In terms of particle dynamics, the single invariant guarantees a stable, but chaotic orbit. In this dissertation an accelerator lattice for testing quasi-integrable optics is designed, simulated, and employed within UMER. Experimental measurement of nonlinear tune shifts and resonance mitigation are performed.

1.4 Organization of the Dissertation

Figure 1.1 shows a flow schematic of the different chapters in this dissertation. The dissertation is organized into five main components. First an introduction is given. Next a discussion on the relevant background theory and experimental appa-

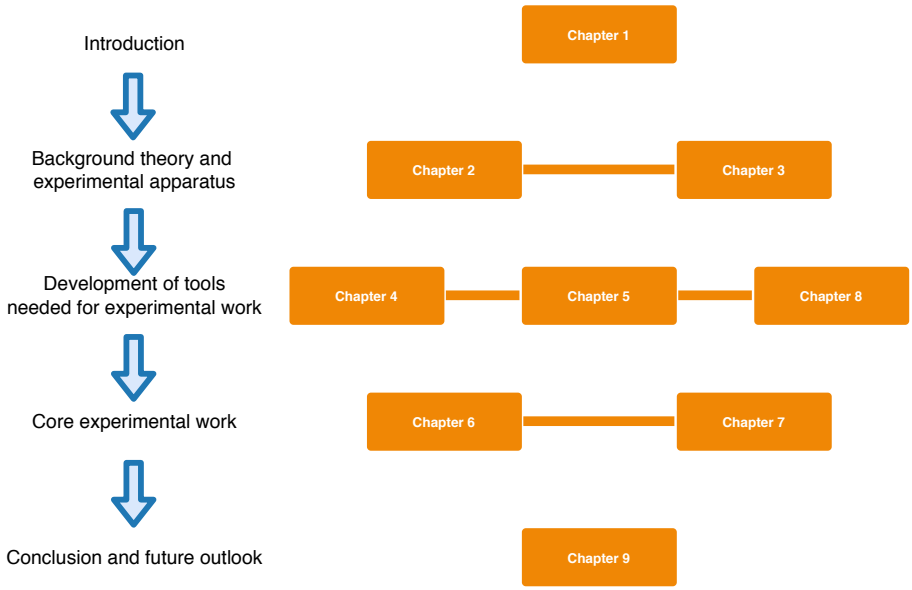

Figure 1.1: A schematic overview of the chapters within this dissertation.

ratus. At its core, the dissertation discusses the development of various numerical tools, simulation models, and experimental techniques needed to carry out the experimental work. The main experimental results and measurements are presented at the end. Lastly, a conclusion and future outlook is given.

Chapter 2 derives the relevant accelerator physics theory needed to understand the work within the dissertation. The theory and equations are derived using a Hamiltonian mechanics formalism. Chapter 3 describes UMER, the accelerator used for all the experimental work, and the various instruments and diagnostics devices that were needed for measurements.

Chapter 4 covers the development and use of various numerical tools and tech-

niques needed to carry out the experimental work within the dissertation. Chapter 5 discusses building accurate models and simulation codes for UMER. Before any experimental work can be done, initial simulations needed to be performed to test the viabililty of the proposed work. Chapter 8 deals with all the experimental tuning that needed to be done on UMER before any experimental measurements could take place.

Chapter 6 starts by discussing the experimental tune measurement and resonance detection work. The second half of the chapter goes through the core experimental measurements performed to detect space charge induced resonance shifting and mitigation. Chapter 7 discusses all nonlinear integrable optics work. The chapter is broken down into three sections. A theory section that derives the relevant equations needed to understand the work. A simulation section that discusses the initial UMER simulations performed when designing the experiment. A final experimental section that covers all the measurement results in testing the theory of nonlinear integrable optics in UMER.

Chapter 1: Bibliography

[1] C. Joshi and Thomas C. Katsouleas. Plasma accelerators at the energy frontier and on tabletops. *Phys. Today*, 56N6:47–53, 2003.

[2] A. Abada et al. FCC Physics Opportunities: Future Circular Collider Conceptual Design Report Volume 1. *Eur. Phys. J. C*, 79(6):474, 2019.

[3] Barney L. Doyle, Floyd Del McDaniel, and Robert W. Hamm. The future of industrial accelerators and applications. *Reviews of Accelerator Science and Technology*, 10(01):93–116, 2019.

[4] F.J. Sacherer. Rms envelope equations with space charge. *IEEE Trans. Nucl. Sci.*, 18:1105–1107, 1971.

[5] R.L. Gluckstern. Oscillation Modes in Two Dimensional Beams. pages H–5, 1971.

[6] I. Hofmann, L.J. Laslett, L. Smith, and I. Haber. Stability of the Kapchinskij-Vladimirskij (K-V) distribution in long periodic transport systems. *Part. Accel.*, 13:145–178, 1983.

[7] R. Baartman. Betatron resonances with space charge. *AIP Conf. Proc.*, 448(1):56–72, 1998.

[8] K. Kojima, H. Okamoto, and Y. Tokashiki. Empirical condition of betatron resonances with space charge. *Phys. Rev. Accel. Beams*, 22:074201, Jul 2019.

[9] Chao Li and R. A. Jameson. Structure resonances due to space charge in periodic focusing channels. *Phys. Rev. Accel. Beams*, 21:024204, Feb 2018.

[10] Ingo Hofmann and Oliver Boine-Frankenheim. Space-charge structural instabilities and resonances in high-intensity beams. *Phys. Rev. Lett.*, 115:204802, Nov 2015.

[11] G. Franchetti, O. Chorniy, I. Hofmann, W. Bayer, F. Becker, P. Forck, T. Giacomini, M. Kirk, T. Mohite, C. Omet, A. Parfenova, and P. Schütt. Experiment on space charge driven nonlinear resonance crossing in an ion synchrotron. *Phys. Rev. ST Accel. Beams*, 13:114203, Nov 2010.

[12] Giuliano Franchetti, Simone Gilardoni, Alexander Huschauer, Frank Schmidt, and Raymond Wasef. Space charge effects on the third order coupled resonance. *Phys. Rev. Accel. Beams*, 20:081006, Aug 2017.

[13] Ingo Hofmann. *Space Charge Physics for Particle Accelerators*. Springer International Publishing, 2017.

[14] Ernest D. Courant, M. Stanley Livingston, and Hartland S. Snyder. The strong-focusing synchroton—a new high energy accelerator. *Phys. Rev.*, 88:1190–1196, Dec 1952.

[15] Thorsten Hellert, Philipp Amstutz, Christoph Steier, and Marco Venturini. Toolkit for simulated commissioning of storage-ring light sources and application to the advanced light source upgrade accumulator. *Phys. Rev. Accel. Beams*, 22:100702, Oct 2019.

[16] V. Danilov and S. Nagaitsev. Nonlinear accelerator lattices with one and two analytic invariants. *Phys. Rev. ST Accel. Beams*, 13:084002, Aug 2010.

[17] S. Antipov, D. Broemmelsiek, D. Bruhwiler, D. Edstrom, E. Harms, V. Lebedev, J. Leibfritz, S. Nagaitsev, C.S. Park, H. Piekarz, P. Piot, E. Prebys, A. Romanov, J. Ruan, T. Sen, G. Stancari, C. Thangaraj, R. Thurman-Keup, A. Valishev, and V. Shiltsev. IOTA (integrable optics test accelerator): facility and experimental beam physics program. 12(03), mar 2017.

[18] Ben Freemire and Jeffrey Eldred. The integrable optics test accelerator, 2019.

[19] Alexander Valishev. Research at fast/iota: Strategy and priorities.

Chapter 2: Theory of Transverse Particle Motion in Accelerators

This chapter provides an introduction to transverse particle dynamics in circular accelerators; it covers all the relevant theory needed to understand the work in this thesis. Section 2.1 goes through the detailed derivation of the Hamiltonian for transverse linear single particle motion in an accelerator. The equations of motion from the Hamiltonian are derived and solved in Section 2.2. An introduction to key accelerator parameters such as the tune and betatron functions are in this section as well. Section 2.3 discusses single particle resonances as driving terms to the equations of motion. A transverse resonance equation is derived and studied in detail. Finally, Section 2.4 talks about space charge forces and collective motion. The envelope equations, envelope instabilities, and space charge tune shifts are all derived and discussed. Appendix A contains detailed step by step derivations for the majority of calculations and equations in this chapter.

2.1 Single Particle Hamiltonian

A series of nontrivial canonical transformations are needed in order to derive the standard equations of motion used to model particle beams in circular accelerators. The section starts with the standard Hamiltonian for a particle in

an electromagnetic field. Using a series of six transformations, the Hamiltonian is transformed to a new set of 6D phase space variables as well as a new independent variable. Vector potentials describing the different magnetic fields in an accelerator are discussed and their respective Hamiltonians derived. Lastly, the Hamiltonian is reduced to a set of equations resembling that of a harmonic oscillator system showing that transverse particle beam motion can be approximately modeled as a set of uncoupled 2D oscillators.

2.1.1 Relativistic Hamiltonian in an electromagnetic field

For a relativistic particle in an electromagnetic field, the Hamiltonian of the system can be written as:

$$H = q\phi + c\sqrt{m^2c^2 + (\vec{P} - q\vec{A})^2} \tag{2.1}$$

Where the ϕ is the electostatic potential and $\vec{A}$ is the magnetic vector potential. The conjugate momentum, $\vec{P}$, is defined as the sum of the mechanical and field momenta, $\vec{P} = \vec{p} + q\vec{A}$. For the case of an accelerator, we assume there are no electrostatic fields, $\phi = 0$, and that our magnetic fields are static and in the transverse planes, i.e. no longitudinal fields. The Hamiltonian in Eq. 2.1 is defined in a cartesian coordinate system with the standard unit vectors $(\hat{x}, \hat{y}, \hat{z})$. The first step in modeling particle motion is to transform the equation into a new coordinate system.

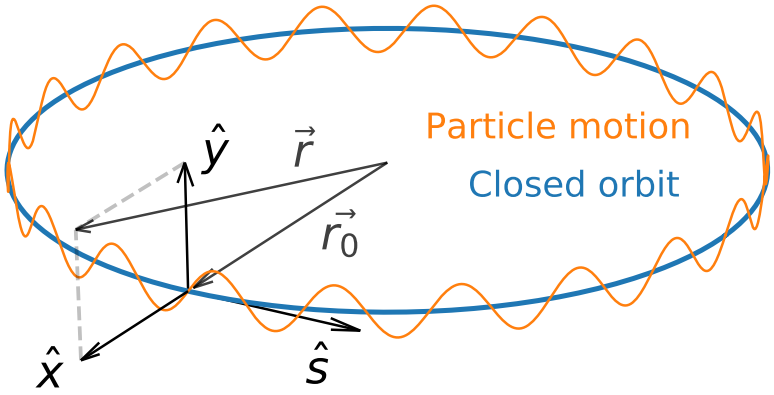

Figure 2.1: Coordinate system for particle motion in circular accelerators. A particle's position in the lab frame is expressed as $\vec{r} = \vec{r_0} + x\hat{x} + y\hat{y}$. In the closed orbit beam frame the position can be expressed as $x\hat{x} + y\hat{y}$.

2.1.2 Frenet-Serret coordinate system

Transverse particle motion in a circular accelerator is defined as small oscillations about a reference orbit called the closed orbit. The closed orbit is defined as a trajectory that closes back onto itself after one revolution in an accelerator. The coordinate system that describes particle motion around the closed orbit is called the Frenet-Serret coordinate system, shown in Figure 2.1. $\hat{s}$ is the direction of motion and the tangential vector to the closed orbit. $\hat{x}$ is perpendicular to $\hat{s}$ and $\hat{y} = \hat{x} \times \hat{s}$. These new orthonormal basis vector directions are summarized with the following equations:

$$\hat{s} = \frac{d\vec{r_0}}{ds}\,, \qquad \hat{x} = -R\frac{d\hat{s}}{ds}\,, \qquad \hat{y} = \hat{x} \times \hat{s}\,, \tag{2.2}$$

where R is defined as the radius of curvature. Equations in Eq. 2.2 are sometimes referred to as the Frenet-Serret formulas. Within accelerator physics, the Frenet-Serret coordinate system is the standard system to work in, and as such, will be the standard coordinate system used throughout this dissertation.

2.1.3 Canonical transformations

To convert the Hamiltonian in Eq. 2.1 into an appropriate format requires a series of transformations. Five main steps are needed:

1. Transform to Fenet-Serret system by using the generating function:

   $F_3(\vec{P}; x, y, s) = -\vec{P} \cdot (\vec{r_0}(s) + x\hat{x} + y\hat{y})$

2. Transform the independent variable from t to s giving new canonical variables:

   $(x(t), p_x(t), y(t), p_y(t), s(t), p_s(t)) \;\rightarrow\; (x(s), p_x(s), y(s), p_y(s), t(s), -H(s))$.

3. Pick a gauge where $\phi = 0\,, A_x = 0\,, A_y = 0$.

4. Scale variables by the nominal design momentum, i.e. $p_{x,y} \;\rightarrow\; \tilde{p}_{x,y} = \frac{p_{x,y}}{P_0}$

5. Final canonical transform using the generating function:

   $F_2(t, \delta, s) = \frac{c}{\beta_0}\,(1 + \beta_0^2\delta)\,(\frac{s}{\beta_0 c} - t)$

The full detailed derivation of each step can be found in Appendix A.1. Going through these steps leads to the final form of the Hamiltonian that will be used:

$$H = -(1 + \frac{x}{R})a_s - (1 + \frac{x}{R})\sqrt{(1+\delta)^2 - (p_x)^2 - (p_y)^2} + (1 + \delta) \qquad (2.3)$$

with phase space coordinates $(x, p_x, y, p_y, \Delta z = (s - v_0 t), \delta = \frac{\Delta p}{p})$

2.1.4 Magnetic fields

Circular accelerators require magnet fields to function. First order magnets, dipoles, are used to bend the beam around a circular orbit. Second order magnets,

quadrupoles, are used to focus the beam and keep it contained within the beam pipe. Third order magnets, sextupoles, are used to correct energy perturbations, also called chromaticity correction. Fourth order magnets, octupoles, are used for higher order corrections. The vector potentials for each of these upright fields are:

$$\begin{aligned}
\text{dipole: } A_s &= -B(s)\,x \\
\text{quadrupole: } A_s &= \frac{G(s)}{2}\,(y^2 - x^2) \\
\text{sextupole: } A_s &= S(s)\,(\frac{1}{2}xy^2 - \frac{1}{6}x^3) \\
\text{octupole: } A_s &= O(s)(\frac{1}{4}x^2y^2 - \frac{1}{24}x^4 - \frac{1}{24}y^4)
\end{aligned} \tag{2.4}$$

Using Maxwell's equations, a general potential can be written from the solution to Laplace's equation in cartesian coordinates:

$$A_s = B_0\ \mathrm{Re}\Big[\sum_{n=0}^{\infty} \frac{b_n + ia_n}{(n+1)!}(x+iy)^{n+1}\Big] \tag{2.5}$$

where Re represents the real part of the function, b_n and a_n are the upright and skew components of the potential, and $\frac{1}{R} = \frac{e}{p}B_0$. From this potential the general

multipole fields can also be written as:

$$B_y + iB_x = B_0 \sum_{n=0}^{\infty} (b_n + ia_n)(x + iy)^n$$

$$b_n = \frac{1}{B_0 n!} \frac{\partial B_y}{\partial^n x^n}\bigg|_{x=y=0}, \; a_n = \frac{1}{B_0 n!} \frac{\partial B_x}{\partial^n x^n}\bigg|_{x=y=0} \tag{2.6}$$

Circular accelerators usually utilize up to sextupole ($n = 2$) magnets. Very few machines use octupoles or higher order fields. UMER has dipoles and quadrupoles, and as such, these are the fields that will be considered in this dissertation.

Expanding the Hamiltonian in Eq. 2.3 in all coordinates and keeping only low order terms, the Hamiltonian for dipole and quadrupole potentials can be written:

$$\begin{aligned}
\text{drift } (A_s = 0)\text{: } H &= \frac{p_x^2 + p_y^2}{2(1+\delta)} - \frac{x}{R} - \frac{x\delta}{R} \\
\text{dipole: } H &= \frac{p_x^2 + p_y^2}{2(1+\delta)} + \frac{x^2}{2R^2} - \frac{x\delta}{R} \\
\text{quadrupole: } H &= \frac{eG}{2P_0}(x^2 - y^2) + \frac{p_x^2 + p_y^2}{2(1+\delta)} - \frac{x}{R} - \frac{x\delta}{R}
\end{aligned} \tag{2.7}$$

where the cyclotron condition, $\frac{eB(s)}{P_0} = \frac{1}{R}$, was used to substitute out $B(s)$. The full expansion is derived in Appendix A.2. Combining the two potentials and assuming

no energy perturbation ($\delta = 0$) gives a separable Hamiltonian:

$$
\begin{aligned}
H &= H_x + H_y \\
H_x &= (\frac{1}{R^2} + K)\frac{1}{2}x^2 + \frac{1}{2}p_x^2 \\
H_y &= -\frac{1}{2}Ky^2 + \frac{1}{2}p_y^2
\end{aligned}
\tag{2.8}
$$

where the quadrupole focusing term is $K = \frac{eG}{P_0}$. Note that $K(s)$ and $\frac{1}{R} = \frac{eB(s)}{P_0}$ are functions of s. This means they are only non-zero when traveling through a dipole or quadrupole field. If not traveling through a quadrupole field, $K = 0$ and not traveling through a dipole field, $\frac{1}{R} = 0$.

Eq. 2.8 fully describes the motion of a particle traveling through an accelerator populated with dipole and quadrupole magnetic fields. It is no coincidence that the Hamiltonian resembles that of a harmonic oscillator. Particle motion in an accelerator can be thought of as a 2-D uncoupled harmonic oscillator system.

2.2 Hill's Equation

Using the Hamiltonian from Eq. 2.8, the linear equation of motion can be derived; this is called Hill's equation. In this section Hill's equation is derived and solved. As part of the solution, a set of important equations and parameters are introduced: the tune Q, the betatron amplitude and phase β, Ψ, and the amplitude

equation in Eq. 2.12.

In solving Hill's equation, the difficulty comes in dealing with the periodic term. To resolve this issue Floquet transformations are used. The transformation replaces the periodic term with a constant. In applying this technique, Hill's equation is reduced to a simple harmonic oscillator system which greatly simplifies the rest of the derivations in this chapter.

2.2.1 Equations of motion

Hamilton's equations can be written from Eq. 2.8. Only the horizontal motion is considered as the vertical is very similar and can be derived the same way. The equations of motion give:

$$\dot{x} = p_x$$

$$\dot{p}_x = -x\,(\frac{1}{R^2} + K) \tag{2.9}$$

and substituting $(\frac{1}{R^2} + K) = k$ leads to a form of Hill's equation:

$$\ddot{x} + k(s)x = 0 \tag{2.10}$$

The difficulty in solving this equation comes from the fact that $k(s)$ is a piecewise function that is periodic with respect to the accelerator circumference, i.e. $k(s+L) =$

$k(s)$. $k(s)$ also has a value of zero outside of focusing magnets. Using a Floquet transformation leads to a solution in the form of:

$$x(s) = \sqrt{\epsilon\beta(s)}e^{\pm i\Psi(s)} \tag{2.11}$$

where ϵ is a constant called the single particle emittance, $\beta(s)$ is an amplitude function often called the beta function, and $\Psi(s)$ is a phase function. Plugging the solution back into Eq. 2.10 leads to two important equations:

$$\begin{aligned} \frac{1}{2}\beta\ddot{\beta} - \frac{1}{4}\dot{\beta}^2 + k(s)\beta^2 &= 1 \\ \dot{\Psi}(s) &= \frac{1}{\beta} \end{aligned} \tag{2.12}$$

The top equation is an amplitude equation that will be used to substitute out the piecewise $k(s)$ function. The bottom equation gives a definition for the phase function. The derivatives are with respect to the longitudinal s coordinate. The derivation of both equations can be found in A.3.

2.2.2 Betatron amplitude, phase advance, and tune

It is important now to take a detour to explain a set of key terms that are used throughout this dissertation. The beta function, or betatron amplitude is purely defined by the focusing force, $k(s)$; it determines how large particle oscillations

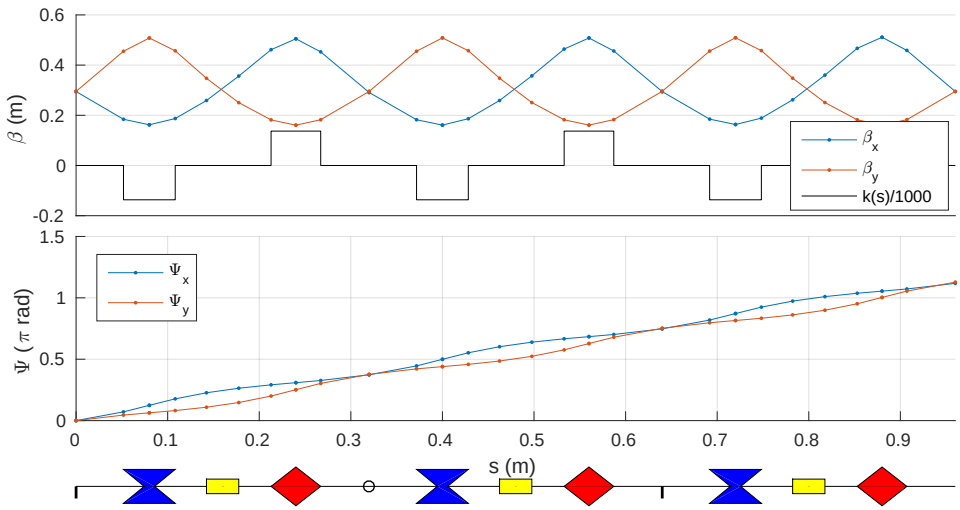

Figure 2.2: An example of the beta function and phase plotted for a simple accelerator lattice. The lattice is a 3 cell FODO design with dipoles inbetween, similar to UMER's lattice. Blue shapes represents defocusing (horizontally) quadrupoles, red are focusing (horizontally) quadrupoles, and yellow are dipoles (horizontally).

become in an accelerator. Fig. 2.2 shows an example of how the beta function behaves in a simple FODO[1] lattice design. Note the change in betatron amplitude as the particle moves along the s direction through the accelerator.

Using the bottom of Eq. 2.12 the phase advance can be defined as the integral of the inverse beta function:

$$\Delta\Psi_{s_1 \to s_2} \equiv \int_{s_1}^{s_2} \frac{1}{\beta(s)} ds \tag{2.13}$$

The phase advance is a key parameter in an accelerator that quantifies the focusing strength, $k(s)$. It can easily be measured experimentally and used to bench mark simulations of the accelerator. An even more important parameter, the betatron tune, is defined as the total number of oscillations per a revolution; there is a vertical,

[1]FODO is a type of accelerator lattice consisting of a focusing quad - drift section - defocusing quad - drift section

horizontal, and longitudinal tune in an accelerator. The mathematical definition is:

$$Q \equiv \frac{\Delta\Psi_{0\to L}}{2\pi} \equiv \frac{1}{2\pi}\int_0^L \frac{1}{\beta(s)}ds \tag{2.14}$$

where L is one full revolution around. The tune is a global parameter of an accelerator and can be measured experimentally. In terms of a harmonic oscillator, the tune is the oscillation frequency of the beam around the accelerator. The next section will show this mathematically.

2.2.3 Floquet transformation

By applying two variable transformations, the piecewise focusing term, $k(s)$ can be removed from Eq. 2.10. Using the equations:

$$\eta \equiv \frac{x(s)}{\beta^{1/2}}, \quad \phi \equiv \frac{\Psi(s)}{Q}, \quad \dot{\phi} \equiv \frac{\dot{\Psi}(s)}{Q} \equiv \frac{1}{Q\beta(s)} \tag{2.15}$$

as well as Eq. 2.12, Hill's equation from Eq. 2.10 is transformed to the form:

$$\eta'' + Q^2\eta = 0 \tag{2.16}$$

where prime denotes the partial derivative with respect to ϕ. The full derivation can be found in A.4.

There is no longer a focusing or piecewise term in Eq. 2.16. Instead, all information is contained in the tune Q, a global parameter of an accelerator lattice.

Eq. 2.16 also looks exactly like a harmonic oscillator making it more intuitive and simpler to work with in this form of Hill's equation. Note the independent parameter, ϕ, changes in values of 2π where each 2π represents one complete betatron oscillation and $2\pi Q$ represents one machine revolution.

2.3 Resonances

In a real accelerator several resonances appear due to magnetic field errors, fringe fields, alignment errors, and many more types of imperfections. If these resonant perturbations are driven towards the beam's resonant frequency, the tune Q, instabilities and amplitude growth will occur within the beam. In circular accelerators the amplitude growth will grow periodically and eventually lead to beam loss as particles are lost to the vacuum pipe walls. As a result, one aspect of designing and operating an accelerator is keeping the machine tune far away from any dangerous resonances.

In this section we add imperfections as driving forces to Hill's equation and derive the resonance conditions. This is first done for the one dimensional case and then for the more complicated two dimensional case. A general single particle resonance equation is derived and studied in detail.

2.3.1 One dimensional resonances

Considering only the horizontal plane, in the presence of magnet field errors Hill's equation can be written as:

$$\ddot{x} + k(s)x = \frac{\Delta B}{B\rho} \tag{2.17}$$

where ΔB is a magnetic field perturbation that can be written using the multipole expansion from Eq. 2.6 and ignoring skew terms ($a_n = 0$):

$$\Delta B = b_0 + b_1 x + b_3 x^2 + ... + b_n x^n$$

$$b_n = \frac{1}{n!}\frac{\partial^n \Delta B}{\partial x^n} \tag{2.18}$$

By applying the Floquet transformation from Eq. 2.15 and Eq. 2.16 the perturbed equation can be written as:

$$\eta'' + Q^2\eta = \frac{Q^2}{B\rho}\beta^{3/2}(b_0 + b_1\beta^{1/2}\eta + b_2\beta^{3/2}\eta^2 + ...)$$

$$\eta'' + Q^2\eta = \frac{Q^2}{B\rho}\beta^{(3+n)/2}b_n\eta^n$$

$$\eta'' + Q^2\eta = f_n(\phi)\eta^n \tag{2.19}$$

The benefit of the Floquet transformation is the fact that the beta function $\beta(\phi)$ and perturbation $\Delta B(\phi)$ are now both periodic functions of 2π; they change

by exactly 2π each revolution around the accelerator. This allows the ability to expand these terms into a fourier series:

$$\eta'' + Q^2\eta = \sum_{p=-\infty}^{\infty} c_n(p)e^{ip\phi}\eta^n$$

$$c_n(p) = \frac{1}{2\pi}\int_0^{2\pi} f_n(\phi)e^{-ip\phi}d\phi = \frac{1}{2\pi}\int_0^{2\pi} \beta^{3+n}b_n e^{-ip\phi}d\phi \tag{2.20}$$

An unperturbed solution to the equation can be written as:

$$\eta_0 = Ae^{iQ\phi} + Be^{-iQ\phi} \tag{2.21}$$

where A and B are constants of integration. Assuming the perturbations are small, the homogeneous solution above can be used as an approximate solution to the inhomogeneous equation in Eq. 2.20. The equation is then written as:

$$\eta'' + Q^2\eta = \sum_{p=-\infty}^{\infty} c_n(p)e^{ip\phi}(Ae^{iQ\phi} + Be^{-iQ\phi})^n \tag{2.22}$$

The term on the far right side can be rewritten using a binomial expansion:

$$\begin{aligned}(Ae^{iQ\phi} + Be^{-iQ\phi})^n &= \sum_{k=0}^{n}\binom{n}{k}A^{n-k}B^k e^{iQ\phi(n-k)}e^{-iQ\phi k} \\ &= \sum_{k=-n}^{n} c_n(k)e^{iQ\phi k}\end{aligned} \tag{2.23}$$

where $c_n(k) = \binom{n}{\frac{n-k}{2}}(AB)^{n/2}(A/B)^{k/2}$. Note the change in the index term $k \to \frac{n-k}{2}$.

Rewriting Eq. 2.22 with the binomial expansion term gives the final form of the equation as:

$$\eta'' + Q^2\eta = \sum_{p=-\infty}^{\infty} \sum_{k=-n}^{n} c_n(p)c_n(k)e^{i(p+Qk)\phi} \tag{2.24}$$

In general, a resonance will occur when the perturbation frequency on the right hand side of the equation matches that of the unperturbed oscillation. In Eq. 2.24 the unperturbed frequency is the tune Q. Consider a single fourier component as an example:

$$\eta'' + Q^2\eta = c_n(p)c_n(k)e^{i(p+Qk)\phi} \tag{2.25}$$

A particular solution to this equation can be written as:

$$\eta_p = ae^{i(p+Qk)\phi} \tag{2.26}$$

Plugging back in and solving for the constant a gives the solution:

$$\eta_p = \frac{c_n(p)c_n(k)}{[(Q-(p+Qk))(Q+(p+Qk))]}e^{i(p+Qk)\phi} \tag{2.27}$$

When the denominator is equal to zero the particle amplitude will increase unbounded, motion will become unstable, and resonance will occur. For this to happen the tune must satisfy the following condition:

$$Q_{\text{resonance}} = \frac{p}{1-k} \tag{2.28}$$

Note that p and k can have either sign. $|k|+1$ is called the order of the resonance

and p is the order of the perturbation harmonic.

Eq. 2.25 is the resonance equation for the one dimensional case. In order to have a fully accurate representation of transverse resonances, the two dimensional case must be considered. A detailed derivation and example is shown for the one dimensional case as a basis for understanding the more complicated two dimensional derivation.

2.3.2 Two dimensional resonances

Considering both the horizontal and vertical planes, a magnetic perturbation can be written as:

$$\ddot{x} + k_x(s)x = \frac{\Delta B_y}{B\rho} \ , \ \ddot{y} + k_y(s)y = -\frac{\Delta B_x}{B\rho} \tag{2.29}$$

and Floquet transformed to:

$$\eta'' + Q_x^2\eta = \frac{Q_x^2\beta_x^{3/2}}{B\rho}\Delta B_y \ , \ \xi'' + Q_y^2\xi = -\frac{Q_y^2\beta_y^{3/2}}{B\rho}\Delta B_x \tag{2.30}$$

where the perturbation has the form of the multipole expansion from Eq. 2.6:

$$\Delta B_y + i\Delta B_x = B_0 \sum_{n=0}^{\infty}(b_n + ia_n)(x+iy)^n$$

$$b_n = \frac{1}{B_0 n!}\frac{\partial \Delta B_y}{\partial^n x^n}\bigg|_{x=y=0} \ , \ a_n = \frac{1}{B_0 n!}\frac{\partial \Delta B_x}{\partial^n x^n}\bigg|_{x=y=0} \tag{2.31}$$

Terms up to third order ($n = 2$) are summarized in Table. 2.1. The perturbed equations can then be written as

$$\eta'' + Q_x^2\eta = f_{nrx}(\phi)\eta^n\xi^r \ , \ \xi'' + Q_y^2\xi = f_{nry}(\phi)\eta^n\xi^r \tag{2.32}$$

The remainder of the derivation follows the same rules as the one dimensional case. Since the horizontal and vertical equations give similar results, only the horizontal direction is considered below.

n	r	$f_{nrx}(\phi)$	$f_{nry}(\phi)$
0	0	$\frac{Q_x^2}{B\rho}b_0\beta_x^{3/2}$	$-\frac{Q_y^2}{B\rho}a_0\beta_y^{3/2}$
0	1	$-\frac{Q_x^2}{B\rho}a_1\beta_x^{3/2}\beta_y^{1/2}$	$-\frac{Q_y^2}{B\rho}b_1\beta_y^2$
0	2	$-\frac{Q_x^2}{B\rho}b_2\beta_x^{3/2}\beta_y$	$\frac{Q_y^2}{B\rho}a_2\beta_y^{5/2}$
1	0	$\frac{Q_x^2}{B\rho}b_1\beta_x^2$	$-\frac{Q_y^2}{B\rho}a_1\beta_y^{3/2}\beta_x^{1/2}$
1	1	$-\frac{Q_x^2}{B\rho}2a_2\beta_x^2\beta_y^{1/2}$	$-\frac{Q_y^2}{B\rho}2b_2\beta_y^2\beta_x^{1/2}$
2	0	$\frac{Q_x^2}{B\rho}b_2\beta_x^{5/2}$	$-\frac{Q_y^2}{B\rho}a_2\beta_y^{3/2}\beta_x$

Table 2.1: Multipole expansion up to third order.

The right hand side of Eq. 2.32 can be written as a fourier series expansion.

$$\eta'' + Q_x^2\eta = \sum_{p=-\infty}^{\infty} c_{nrx}(p)\eta^n\xi^r \ , \ c_{nrx}(p) = \frac{1}{2\pi}\int_0^{2\pi} f_{nrx}(\phi)e^{-ip\phi}d\phi \tag{2.33}$$

Assuming small perturbations, the unperturbed solution can be used in the perturbed equation:

$$\eta'' + Q_x^2\eta = \sum_{p=-\infty}^{\infty} c_{nrx}(p)(a_x e^{iQ_x\phi} + b_x e^{-iQ_x\phi})^n(a_y e^{iQ_y\phi} + b_y e^{-iQ_y\phi})^r \tag{2.34}$$

A binomial expansion is used for the terms on the right hand side of the equation to give the final form of the two dimensional perturbation equation:

$$\eta'' + Q_x^2\eta = \sum_{p=-\infty}^{\infty}\sum_{k=-n}^{n}\sum_{l=-r}^{r} c_{nrx}(p)c_{nrx}(k)c_{nrx}(l)e^{i(p+Q_xk+Q_yl)\phi} \tag{2.35}$$

where $c_{nrx}(k)$, $c_{nrx}(l)$ are the constants from the binomial expansion.

As an example, the particular solution for a single fourier component of Eq. 2.35 can be written as:

$$\eta_p = ae^{i(p+Q_xk+Q_yl)\phi} \tag{2.36}$$

Solving for the integration constant, a, leads to the following equation:

$$\eta_p = \frac{c_{nrx}(p)c_{nrx}(k)c_{nrx}(l)}{[(Q_x-(p+Q_xk+Q_yl))(Q_x+(p+Q_xk+Q_yl))]}e^{i(p+Q_xk+Q_yl)\phi} \tag{2.37}$$

which reveals the two dimensional resonance condition as:

$$(1+k)Q_x + lQ_y = p \tag{2.38}$$

where the integers k, l, p can be both positive or negative. This equation characterizes all transverse single particle resonance conditions that can occur in an accelerator. The next section will further analyze Eq. 2.38.

2.3.3 Resonance equation

Using the derived resonance condition from Eq. 2.38, a general transverse resonance equation can be written as:

$$mQ_x + nQ_y = p \tag{2.39}$$

where m, n, p are all integers and the sum $|m|+|n|$ is called the order of the resonance. Eq. 2.39 encompasses all single particle tranverse resonances that can occur in an accelerator. Resonances up to third order are summarized in Table 2.2. From Eq.

Driving Field	Order	m, n	Equation
Dipole	$o = 1$	$0, 1$	$Q_y = p$
		$1, 0$	$Q_x = p$
Quadrupole	$o = 2$	$0, 2$	$Q_y = p/2$
		$1, 1$	$Q_x + Q_y = p$
		$2, 0$	$Q_x = p/2$
Sextupole	$o = 3$	$0, 3$	$Q_y = p/3$
		$1, 2$	$Q_x + 2Q_y = p$
		$2, 1$	$2Q_x + Q_y = p$
		$3, 0$	$Q_x = p/3$

Table 2.2: Transverse resonances up to third order. Driving field terms are listed along with the resonance equations. Note only positive values of m, n are in the table; these terms can also be negative.

2.37, it can be observed that the growth in amplitude, and thus the strength of the resonance, decreases with increasing order number. Electron storage ring facilities that employ third order sextupole magnets must consider resonances up to third

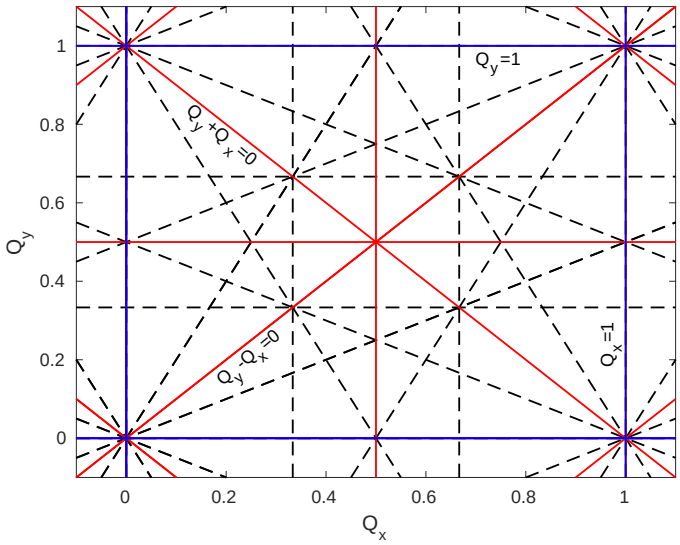

Figure 2.3: Tune diagram up to 3rd order resonances. Integer, sum, and difference resonances are labeled with their corresponding resonance equation. First order resonances are blue, second order are red, and third order are dashed black.

order. Similarly, collider facilities also use sextupole magnets, but have to deal with resonances much higher than third order, typically above 10th order. Separate from electron storage rings, colliders must consider beam-beam interactions and exotic optics as extra sources of resonances [1]. Very low loss rate requirements for collisions in physics detectors require avoidance of high order resonances.

Resonances are observed by plotting the resonance equation in tune space with Q_y, Q_x as the dependent and independent variables. See Figure 2.3 for a typical tune diagram for resonances up to third order. The diagram is plotted in the range of $p = 0$ to $p = 1$; this is referred to as the fractional part. The diagram repeats as you increase p. One of the requirements in designing and running any circular accelerator is to pick a tune operating point somewhere in the tune diagram that is away from destructive resonances. Most machines pick regions near the difference resonance $Q_y - Q_x = 0$, which tends to be a stable resonance. The difference resonance also

offers small pockets that are resonance free. Figure 2.4 shows resonances up to 12th order. Notice the small pockets of white space along the red colored difference resonance; these are the regions circular accelerators prefer to operate within.

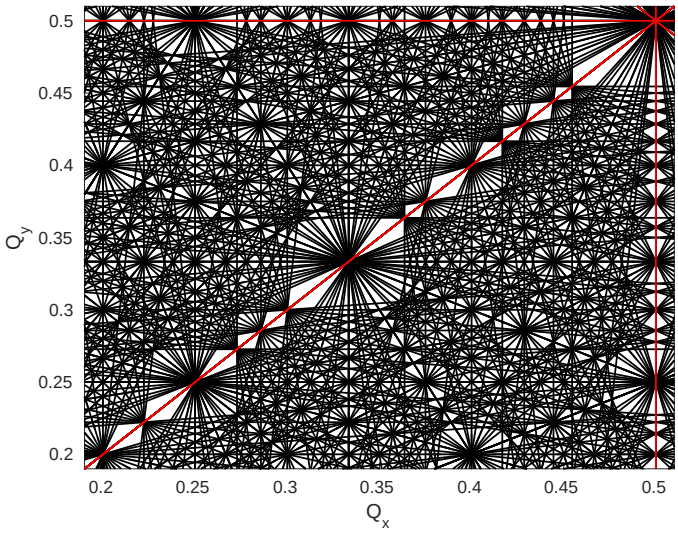

Figure 2.4: Tune diagram up to 12th order resonances. The red lines are second order resonances and black lines are all resonances that are third order or higher.

The tune diagrams in Figure 2.3 and 2.4 are in actuality somewhat deceiving. Resonance lines are depicted as having zero width when in reality resonances have finite widths, called resonance stopbands. The fourier amplitudes $c_n(p)$ and $c_{nrx}(p)$ from Eq. 2.20 and 2.33 are called the stopband integrals and determine the widths of resonances. More information on stopbands can be found here [2]. Resonances can also shift from their locations due to space charge forces; this is discussed in the next section and in section 6.3.1. Tunes are also thought of as having zero size when in reality there are tune spreads in any beam. The tune, number of transverse oscillations per a machine revolution, is defined for a single particle. Small variations in single particle energy and space charge can cause a variation in particle tunes. A large spread in tunes can cause particle loss to occur as the tune can touch nearby

resonances. Figure 2.5 shows a visual example of what a large tune spread might look like.

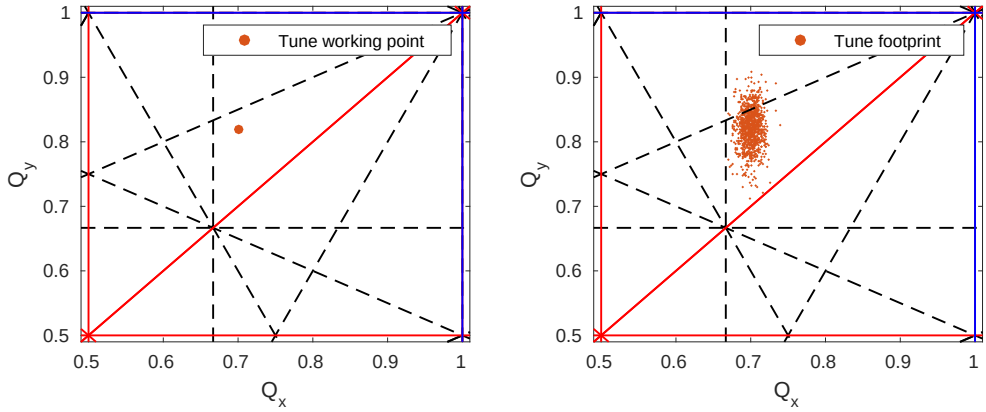

Figure 2.5: (left) Depicting the tune as a single point in tune space. (right) A realistic representation of what the tune might look like with large tune spread.

2.4 Space Charge and Collective Motion

Electric charges in particle beams can generate forces felt by individual particles within the beam; this is called the space charge force. In this section space charge forces are added to the equations of motion and the envelope equations are derived. These equations model the motion of the beam radii instead of the single particle motion. It is shown that small perturbations of the beam radii can lead to the development of envelope instabilities which cause two beating modes of the beam.

The space charge force is also responsible for an overall defocusing force on the beam, causing its tune to decrease in both planes. This phenomena is explored at the end of the chapter with derivations of the space charge dependent tune shifts.

2.4.1 Envelope equations

Eq. 2.11 defines the single particle envelope of the beam as $R = \sqrt{\epsilon\beta}$ where ϵ is the single particle emittance and β is the betatron amplitude function. Using the amplitude equation from Eq. 2.12, a single particle envelope equation can be derived as:

$$\ddot{R}_x + k(s)R_x - \frac{\epsilon_x}{R_x} = 0 \tag{2.40}$$

for an emittance dominated beam.

For high intensity beams the electric charge of the beam can itself create a strong force felt by individual particles within the beam; this is called the space charge force. Space charge forces are considered a collective self-force due to the Coulomb mean-field. In general, the Coulomb mean-field from an arbitrary beam distribution is nonlinear [2]. However, the Kapchinskij and Vladimirskij (KV) distribution is a special case where an ellipsoid beam distribution leads to a perfectly linear space-charge force within the beam radius [3]. The KV beam distribution can be written as:

$$\rho(x, p_x, y, p_y) = \frac{Ne}{\pi^2 a^2 b^2}\delta\Big(\frac{1}{a^2}(x^2 + p_x^2) + \frac{1}{b^2}(y^2 + p_y^2) - 1\Big) \tag{2.41}$$

where N is the number density, e is the charge, δ is a delta function, a and b are the envelope radii of the beam, and (x, p_x, y, p_y) are the transverse phase space coordinates.

The envelope radii are equal to $a = \sqrt{\epsilon_x\beta_x}, b = \sqrt{\epsilon_y\beta_y}$ where the emittances

are the single particle emittances. There is a another type of emittance called the rms emittance, ϵ_{rms}, that is used when working with a KV beam and space charge. The rms emittance is related to the single particle emittance as:

$$\epsilon_{x,\text{rms}} = \frac{< x^2 >}{\beta_x} = \frac{\epsilon_x}{4} \tag{2.42}$$

As a result, the rms envelope radii are equal to half of the beam radii in a KV beam distribution.

Given the KV distribution, an average space-charge force can be calculated. Assuming no longitudinal variations, the beam is modeled as an infinitely long wire with a given line-charge density and an electric field calculated as:

$$\vec{E}(x,y) = \frac{2Ne}{2\pi\epsilon_0}\left(\frac{x}{a(a+b)}\hat{x} + \frac{y}{b(a+b)}\hat{y}\right) \tag{2.43}$$

After calculating the corresponding force, a modified version of Hill's equations can be written for KV beams:

$$\begin{aligned} \ddot{x} + \left(k_x(s) - \frac{2K_{sc}}{a(a+b)}\right)x = 0 \\ \ddot{y} + \left(k_y(s) - \frac{2K_{sc}}{b(a+b)}\right)y = 0 \end{aligned} \tag{2.44}$$

where

$$K_{sc} = \frac{I}{I_0}\frac{2}{\beta^3\gamma^3} \tag{2.45}$$

is called the beam perveance, a dimensionless space charge parameter. Here β, γ are relativistic terms, I is the beam current. The characteristic current, I_0, has a value of $\approx$ 17kA for electrons. The beam current and particle energy solely determine the strength of the space charge force. Using the amplitude equation from Eq. 2.12, a set of KV envelope equations can be written with space charge forces included:

$$\ddot{a} + k_x a - \frac{2K_{sc}}{(a+b)} - \frac{\epsilon_x^2}{a^3} = 0 \tag{2.46a}$$

$$\ddot{b} + k_y b - \frac{2K_{sc}}{(a+b)} - \frac{\epsilon_y^2}{b^3} = 0 \tag{2.46b}$$

The KV equations from Eq. 2.46a and 2.46b are used to model the evolution of the RMS beam size. Note that the space charge force defocuses the beam in both planes. Solving these equations would be equivalent of solving Hill's equation in the presence of space charge. Numerical tools are used to solve the KV equations. See Figure 2.6 for an example trajectory of a particle with and without space charge.

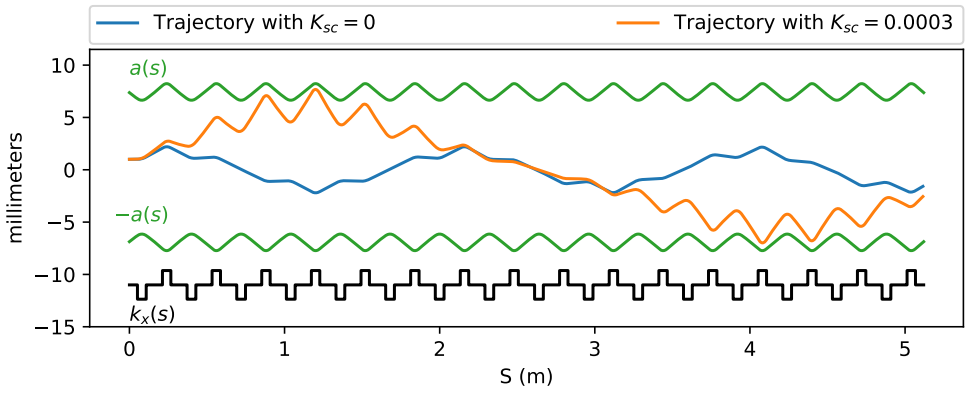

Figure 2.6: Trajectory of a single particle in the beam with and without space charge (K_{sc}) over several FODO lattice periods. The beam envelope and focusing strengths are plotted in green and black. An emittance of $\epsilon = 25.5$ mm-mr and focusing/defocusing strengths of $k_{x,y} = 137.0, 136.7$ 1/m^2 were used.

2.4.2 Envelope instabilities

If a beam's envelopes are not matched perfectly, a set of envelope modes can develop causing instabilities. No known solution exists for the envelope modes in an alternating-gradient (FODO) lattice, but approximations can be used to create a simplified model. Assuming an average focusing force where $k(s) = k_0^2$, a smooth approximation model can be used to solve for the envelope modes.

Assuming a small mismatch in the envelopes, the beam will not deviate much from the average radius $\bar{R}$. This can be written as:

$$\bar{a} = \bar{R} + \delta_a \tag{2.47a}$$

$$\bar{b} = \bar{R} + \delta_b \tag{2.47b}$$

where δ_a,$\delta_b \ll \bar{R}$. Plugging Eq. 2.47a and 2.47b into the envelope equations and keeping only first order terms in δ_a,δ_b gives:

$$\ddot{\delta_a} + \left(k_0^2 + \frac{K_{sc}}{2\bar{R}^2} + \frac{3\epsilon^2}{\bar{R}^4}\right)\delta_a + \frac{K_{sc}}{2\bar{R}^2}\delta_b + \left(k_0^2\bar{R} - \frac{K_{sc}}{\bar{R}} - \frac{\epsilon^2}{\bar{R}^3}\right) = 0 \tag{2.48a}$$

$$\ddot{\delta_b} + \left(k_0^2 + \frac{K_{sc}}{2\bar{R}^2} + \frac{3\epsilon^2}{\bar{R}^4}\right)\delta_b + \frac{K_{sc}}{2\bar{R}^2}\delta_a + \left(k_0^2\bar{R} - \frac{K_{sc}}{\bar{R}} - \frac{\epsilon^2}{\bar{R}^3}\right) = 0 \tag{2.48b}$$

where k_0^2 is the average focusing force and the emittance is equal in both planes $\epsilon = \epsilon_x = \epsilon_y$. In the case of a matched beam, where $a = b = \bar{R}$, the term on the right side in each equation is equal to zero. Using the substitutions of $k^2 = k_0^2 - \frac{K_{sc}}{\bar{R}^2}$ and

$\bar{R}^2 = \frac{\epsilon}{k}$, the equations can be simplified to:

$$\ddot{\delta_a} + A_1\delta_a + A_2\delta_b = 0 \tag{2.49a}$$

$$\ddot{\delta_b} + A_1\delta_b + A_2\delta_a = 0 \tag{2.49b}$$

where:

$$A_1 = \frac{1}{2}(3k_0^2 + 5k^2) \ , \ A_2 = \frac{1}{2}(k_0^2 - k^2) \tag{2.50}$$

Eq. 2.49a and 2.49b represent a set of coupled harmonic oscillators. The oscillators have two fundamental modes of oscillation defined by:

$$\eta_1(s) = \delta_a(s) + \delta_b(s) \ , \ \eta_2(s) = \delta_a(s) - \delta_b(s) \tag{2.51}$$

and frequencies of:

$$\omega_1 = (2k_0^2 + 2k^2)^{1/2} \ , \ \omega_2 = (k_0^2 + 3k^2)^{1/2} \tag{2.52}$$

The parallel mode represents envelope oscillations in phase while the antiparallel mode represents oscillations 180 degrees out of phase. In the limit of no space charge, $K_{sc} \to 0$, the frequencies become $\omega_1, \omega_2 = 2k_0$.

A more general approach can be taken where no average focusing force is assumed, $k(s)$. The envelope equations can be reduced to a system of four first-order differential equations and be written in matrix form. The resulting eigenvalues and eigenvectors can determine whether the solution is bounded or not. See [4] for the

full derivation and more details on envelope modes.

2.4.3 Space charge tune shift

Strong space charge forces can modify individual particle motion in the beam. Particles experience a defocusing force in both transverse planes causing their tunes to shift. The tune shifts however are not the same for all particles due to the beam's nonlinear charge distribution. Particles closer to the beam core suffer from a larger tune shift while particles with large amplitudes feel less of an effect. As a result, particles will have a large spread in tunes from a direct space charge force. This spread in tunes is referred to as the incoherent space charge tune shift.

While the beam travels around in a circular path, the electromagnetic fields created from the space charge forces will end up inducing image forces on the metallic vacuum chamber. These image forces will apply a separate space charge force on the beam as a whole. Both electric and magnetic image forces will effect the beam. The beam's coherent motion, behaving like a rigid body, will change and cause a tune shift due to the image charges. This is called the coherent tune shift.

A few things to note. The space charge force from the incoherent motion is centered on the beam and not the vacuum chamber or closed orbit; this force is independent of any transverse displacement by the beam. The coherent tune shift changes the frequency of the beam centroid while the incoherent tune shift changes the frequency of individual particles in the beam. The incoherent tune shift is very difficult to measure directly. Standard diagnostics tools in accelerators (Beam

Position Monitors) are only sensitive to coherent beam motion; they measure the average motion of the beam's center of charge. Unless mentioned specifically, when ever tune measurements are discussed in this dissertation it will be referring to the coherent tune measurements, also called the bare tune measurements. The rest of this section will derive the relevant equations to model these tune shifts.

Space charge tune shifts can be derived in various ways. The method used here assumes the space charge force as a distributed defocusing error around the ring and uses Courant-Snyder matrix treatment of circular lattices [5]. First a set of electric and magnetic fields are calculated due to the space charge forces, $E_{x,y}, B_{x,y}$. Then the Lorentz force is used to find the resulting focusing strength, $k_{x,y}$:

$$k_{x,y}(s) \propto \frac{dF_{x,y}}{d(x,y)} \quad , \quad F = e(E_{x,y} + \nu \times B_{x,y}) \tag{2.53}$$

The focusing strength is treated as a gradient perturbation and the corresponding tune shift can be calculated as:

$$dQ_{x,y} = \int k_{x,y}\beta_{x,y} ds \tag{2.54}$$

Eq. 2.54 is derived from Courant-Snyder theory [5]. More detailed information can be found in [6, 7].

As an example and approximation, consider the cross section of a round dc beam with uniform charge density ρ. Using Maxwell's equations, the electric and

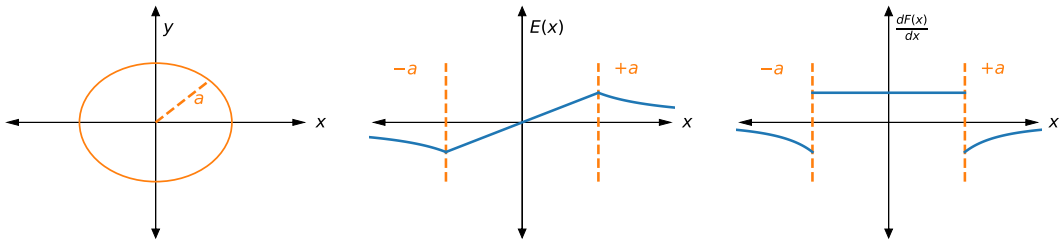

Figure 2.7: The electric fields for a cross section of a round uniformally charged dc beam. The gradient of the field is also plotted.

magnetic fields inside the beam are calculated as:

$$E_r = \frac{\rho}{2\epsilon_0} r \quad , \quad r < a \tag{2.55a}$$

$$B_\phi = \frac{\rho\nu}{2\epsilon_0 c^2} r \quad , \quad r < a \tag{2.55b}$$

See Appendix A.5 for a detailed derivation. Figure 2.7 shows a description of the electric field and its forces. The Lorentz force is found to be:

$$F_r = e(E + \nu \times B) = \frac{e\rho}{2\epsilon_0}(1 - \beta^2) r \tag{2.56}$$

where $\beta = v/c$ is the relativistic parameter. Using the defocusing strength,

$$k = \frac{1}{m\gamma\beta^2 c^2} \frac{dF_r}{dr} \tag{2.57}$$

the tune shift can be calculated as:

$$dQ = \frac{1}{4\pi} \int k(s)\beta(s) ds = \frac{N r_e}{\pi \gamma^3 \beta^2 a^2} \frac{R}{Q} \tag{2.58}$$

where N is the total number of particles in the beam, r_e is the classical electron radius, R is the ring radius, and β is the relativistic beta. The space charge tune shift is inversely proportional to the energy cubed, beam sized squared, and tune; it is proportional to the ring radius and total number of particles in the beam.

In reality beams do not have uniform transverse charge distributions; they tend to have a Gaussian distribution given by:

$$\rho(x,y) = \frac{\lambda}{2\pi\beta_x\beta_y} e^{-\frac{1}{2}\frac{x^2}{\beta_x^2} - \frac{1}{2}\frac{y^2}{\beta_y^2}} \tag{2.59}$$

where λ represents the line charge for a continuous beam of particles. Beam's are also not round, but elliptical in shape. Given a set of approximations, the electric and magnetic fields and their respective image fields can be calculated for a Gaussian beam; this is done in detail here [7]. To summarize the results, the tune shifts are given by:

$$\Delta Q_{u,\mathrm{sc,incoh}} \approx -\frac{r_e N \bar{R}}{2\pi Q_{0u} B \beta^2\gamma^3}\left[\frac{1}{\bar{\beta}_u(\bar{\beta}_x+\bar{\beta}_y)} + 2(1+\beta^2\gamma^2 B)\frac{\epsilon_1}{\bar{b}^2} + 2\beta^2\gamma^2 B\frac{\epsilon_2}{\bar{g}^2}\eta_b\right] \tag{2.60}$$

$$\Delta Q_{u,\mathrm{sc,coh}} \approx -\frac{r_e N \bar{R}}{2\pi Q_{0u} B \beta^2\gamma^3}\left[\frac{1}{\bar{\beta}_u(\bar{\beta}_x+\bar{\beta}_y)} + 2(1+\beta^2\gamma^2 B)\frac{\xi_1}{\bar{b}^2} + 2\beta^2\gamma^2 B\frac{\xi_2}{\bar{g}^2}\eta_b\right] \tag{2.61}$$

where $B = (n_b l_b)/(2\pi R)$ is the Laslett bunching factor with n_b being the number of bunches and l_b being the effective bunch length, $\epsilon_1, \epsilon_2, \xi_1, \xi_2$ are the Laslett form factors (constants), $2b$ is the pipe diameter, $2g$ is the distance between magnet poles, β, γ are relativistic terms, β_x, β_y are betatron amplitudes, and η_b is the magnetic

fill factor. Terms with bars above them are values averaged over the circumference of the ring. The u subscript can be equal to x or y, e.g. the horizontal tune shift would be written as $\Delta Q_{u=x}$. More information can be found on the Laslett factors here [8].

2.5 Chapter Summary

This chapter starts with the Hamiltonian of a particle in an electromagnetic field and derives the full transverse equations of motion for a particle in a circular accelerator. The equations of motion resembles that of a harmonic oscillator. The natural resonant frequency of this oscillator is called the tune, Q; it is the number of transverse oscillations per a revolution around the accelerator. Magnetic imperfections in the real world create driving terms that cause instabilities and beam loss if they match the beam's tune. At the same time space charge forces exist within the beam and cause its tune to spread and shift. The maximum tune shift that can occur is one where the beam is eventually moved onto a destructive driving resonance. This restriction puts a limit on how high the space charge force can be within a beam. Since space charge is proportional to beam current, it is also what limits accelerators from going to ever higher beam intensities.

Chapter 2: Bibliography

[1] Philip J. Bryant and Kjell Johnsen. *The Principles of Circular Accelerators and Storage Rings*. Cambridge University Press, 1993.

[2] S. Y. Lee. *Accelerator Physics*. World Scientific, 2012.

[3] I.M. Kapchinskij and V.V. Vladimirskij. Limitations of proton beam current in a strong focusing linear accelerator associated with the beam space charge. In *Proc. of the International Conference on High Energy Accelerators*, page 274, CERN, Geneva, 1959.

[4] Steven M. Lund and Boris Bukh. Stability properties of the transverse envelope equations describing intense ion beam transport. *Phys. Rev. ST Accel. Beams*, 7:024801, Feb 2004.

[5] Ernest D. Courant, M. Stanley Livingston, and Hartland S. Snyder. The strong-focusing synchroton—a new high energy accelerator. *Phys. Rev.*, 88:1190–1196, Dec 1952.

[6] W. T. Weng. Space charge effectstune shifts and resonances. *AIP Conference Proceedings*, 153(1):348–389, 1987.

[7] Helmut Wiedemann. *Particle accelerator physics; 4rd ed.* Springer, 2015.

[8] L. J. Laslett. On Intensity Limitations Imposed by Transverse Space-Charge Effects in Circular Particle Accelerators. *eConf*, C630610:324, 1963.

Chapter 3: UMER and its Diagnostics

The **U**niversity of **M**aryland **E**lectron **R**ing (UMER) is an operational particle accelerator facility. This chapter discusses the major components that make up UMER as well as the relevant diagnostics systems used to generate the majority of data for this dissertation. Section 3.1 discusses magnets and injection specifically and section 3.2 discusses the diagnostics on the accelerator. Appendix B contains information on the developement of a control system for operations within UMER.

3.1 UMER

UMER is made up of an electron gun, injection line, transfer section, and ring. This section starts by discussing the electron source and the different beams generated within UMER. There is a discussion on the magnet system layout throughout the machine. Import details that affect beam dynamics from injection to recirculation are discussed. Complex hardware including the RF system and a control system are briefly explained.

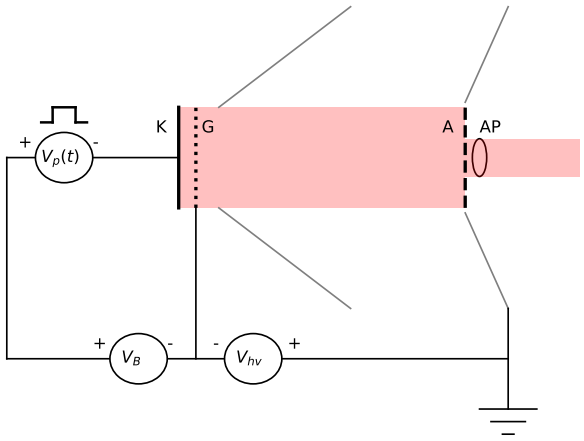

Figure 3.1: Schematic describing the UMER injector. Emission from the cathode (K) is controlled by the grid (G) potential. The 60 Hz pulsed voltage $V_p(t)$ and the bias voltage V_B maintain the potential between the cathode and grid. The high voltage supply V_{hv} is used to hold the cathode and grid at negative potentials. After accelerating towards the anode (A), the electron beam is apertured using an aperture plate (AP).

3.1.1 Electron source

The electron gun in UMER consists of a gridded, pierce-focusing triode hot dispenser cathode [1]. Emission is controlled by a bias (V_B) and pulsed voltage ($V_p(t)$) signal across the cathode (K) and grid (G). The high voltage (V_{hv}), $\approx$ 10keV, signal is used to hold the cathode and grid at negative potentials. The anode (A) is held at ground. The bias voltage is typically set to $V_B \approx 30V$ with the pulsed voltage, $V_p(t)$, running at 60 Hz and a 100 ns pulse width. Both are adjustable and can be varied based on the type of run or experiment being done. Figure 3.1 shows a detailed schematic of the electron gun setup.

The bias voltage setpoint is determined by experimentally measuring the IV (Miram) curves for UMER's dispenser cathode. A voltage is applied to thermionically heat the cathode and the emitted electron current is measured downstream in

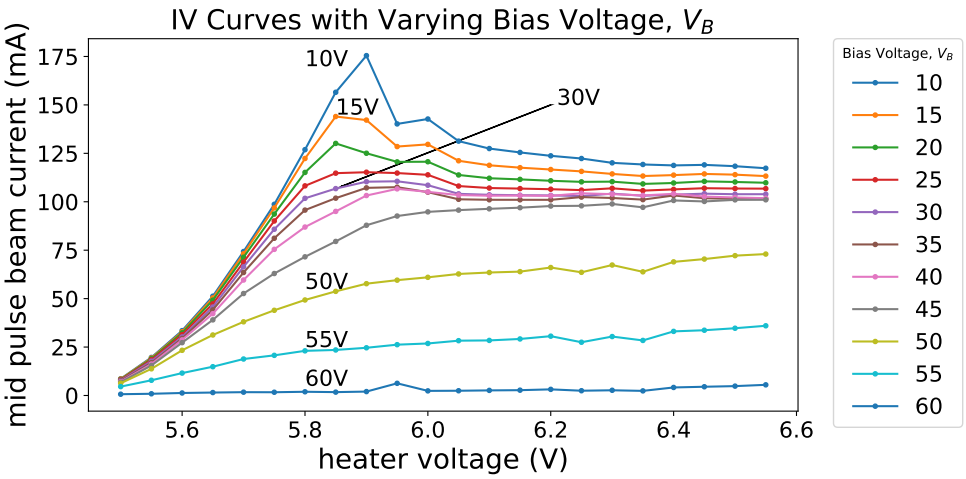

Figure 3.2: IV curves with the UMER electron gun while varying the bias voltage, V_B. The high voltage was set to 10 kV. A wait time of 10 minutes was used in between each measurement point.

the injection line; this is done for different bias voltage settings. Figure 3.2 shows the results. Note the abnormal hump that occurs around 5.9 volts and appears to depend on the bias voltage. It is hypothesized that this is due to circuit loading which causes the beam current to drop as a result of a drop in cathode/grid voltage when the heating voltage increases past 5.9 volts [2]. After 5.9 volts, the beam current saturates to a stable point of about 100 mA for a bias voltage of 30 volts. It takes a few hours for the beam current emission to reach a stable ($\pm$0.05 mA) enough equilibrium to run precision experiments. This is most likely due to the thermal expansion that occurs within the gun while heating the cathode.

The pulsed voltage waveform determines the longitudinal shape and repetition rate of each bunch. Nominally running at 60 Hz, the repetition rate of the machine has in special cases been reduced to as low as 1 Hz when using the RF system in UMER. The pulse shape, and hence bunch length, can range from 12 to 100+ ns in length. For reference, the circumference of the ring is roughly 197 ns long (11.52 m)

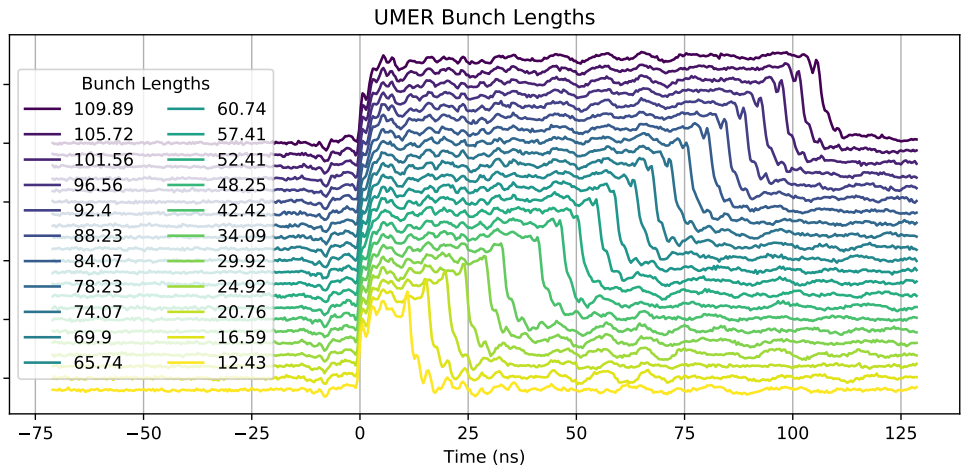

Figure 3.3: UMER electron bunch lengths measured by varying the pulse voltage, $V_p(t)$. A 6mA beam current was used and measurements were done using a Bergoz coil in the injection line.

so that the bunch fills half the ring when using a 100 ns bunch length. UMER only operates with a single bunch in the ring. Figure 3.3 shows the range of longitudinal bunches that can be generated in UMER.

An aperture wheel after the anode is used to aperture the nominally 100 mA beam. The different apertures reduce the current as well as the beam emittance. Eq. 2.45 shows that the space charge in a beam is dependent on the current. By reducing the current, the aperture also changes the amount of space charge in a beam, thus introducing a mechanism to produce beams of varying amounts of space charge. Table 3.1 summarizes the different beams that can be generated in UMER [3].

3.1.2 Injection line

After the 'beam' leaves the electron gun, it travels through a roughly 125 cm injection line leading to UMER's main ring. The injection line consists of quadrupoles

Current (mA)	ϵ (mm-mr)	Avg. Radius (mm)	Q/Q_0	$\Delta Q_{u,\mathrm{sc,incoh}}$
0.6	7.6	1.6	0.85	0.94
6	25.5	3.4	0.62	2.4
21	30.0	5.2	0.31	4.5
70	86.6	9.6	0.17	5.5
100	97.3	11.1	0.14	5.7

Table 3.1: UMER beam parameters based off measured beam current from different apertures.

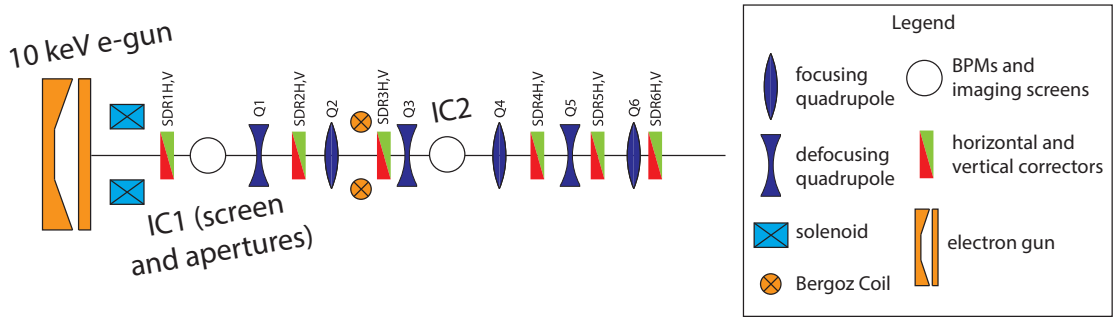

Figure 3.4: UMER injection line schematic.

(3 focusing and 3 defocusing), which are used to match the beam into the ring. Along with each quadrupole are six transverse plane corrector magnets (6 in x and 6 in y) used to steer the beam through the injection line. A iron core solenoid magnet is used at the start of injection to focus the beam coming out of the gun. Figure 3.4 shows a detailed diagram of the injection line.

The injection line has two access ports that holds diagnostic hardware. The first chamber, labeled IC1 in Figure 3.4, contains a second aperture plate, a mirror, and phosphor imaging screen. The aperture plate allows the creation of very small current beams (< 0.6 mA) with minimal amounts of space charge. The mirror is used to illuminate the cathode by using an external laser for photo-injection experiments. The phosphor screen is used to observe the transverse beam distributions directly

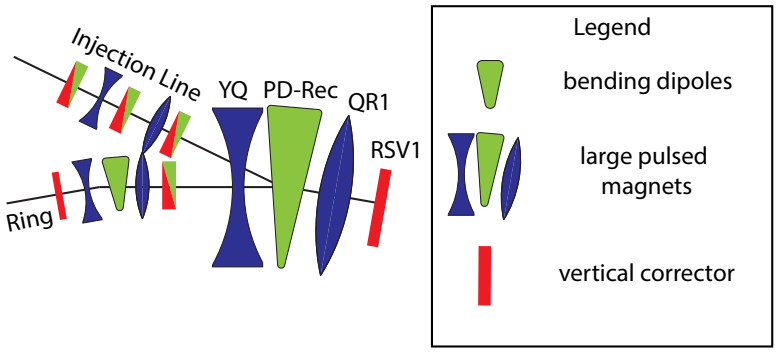

Figure 3.5: UMER transfer line schematic.

out of the electron gun.

3.1.3 Transfer section

The transfer section in UMER consists of three wide bore pulsed magnets over a Y-shaped beam pipe. Figure 3.5 shows a schematic of the section. The pulsed magnets are multipurpose in that they are used for injection and recirculation of the beam. After injecting the beam into the ring, the pulsed dipole's (PD-Rec) polarity switches within one half turn to allow for recirculation. Left side of Figure 3.6 shows the magnet pulses for all three magnets.

The magnet pulses last much longer than beam circulation time, starting and ending about 100 μs inbetween injections. The reason for this is to minimize the impact of eddy current effects on the beam. Also impacting the beam is the polarity switching time in the pulsed dipole magnet. Right side of Figure 3.6 shows the dipole pulse. Timing is adjusted such that beam is injected right before the rising edge of the polarity switch and recirculation occurs right at the tail end of the rising pulse. The pulse rise time is on the scale of one revolution and causes the edge of the beam to get clipped with the switching dipole field. Either the tail end on injection, or

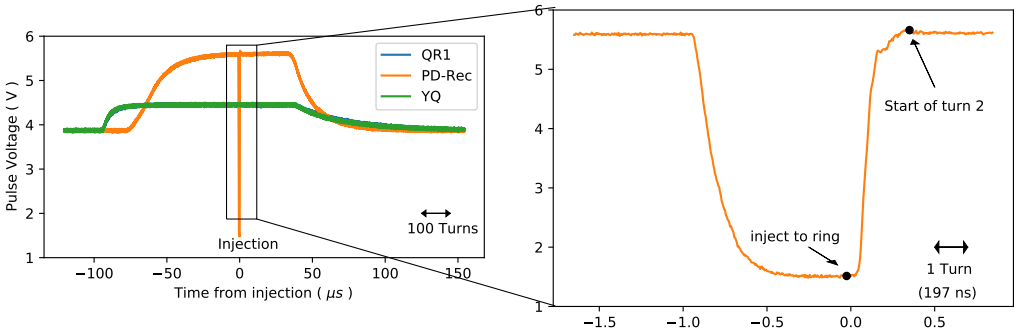

Figure 3.6: (Left) Pulses for transfer section magnets. (Right) zoomed in view of the pulsed dipole magnet. The first black dot is the time when beam is injected into the ring. The second dot is the start of the second turn. From dot to dot is the circulation time of the beam.

the head of the bunch on the second turn of recirculation, will feel the switching dipole field.

3.1.4 Ring

UMER's 11.52 m circumference ring consists of a FODO lattice with a total of 36 FODO cells, each being 32 cm long. An example was shown in Figure 2.2 of a particle tracking calculation through three cells. Unlike conventional accelerator magnets, UMER uses printed circuit board magnets (PCBM) [4]. PCBMs provide a cost effective and easy to maintain alternative to traditional magnets. In UMER's case, PCBMs operate at 0 - 3[1] amps of current and generate dipole fields on the order of 10-20 Gauss. The low strength fields are strong enough to contain UMER's 10 keV beam.

Beam Position Monitors (BPMs) are placed at the end of every other cell with four exceptions where a glassgap is used instead as well as the injection section

[1]Using water cooling, the PCBMs were able to operate at currents as high as 6-10 amps.

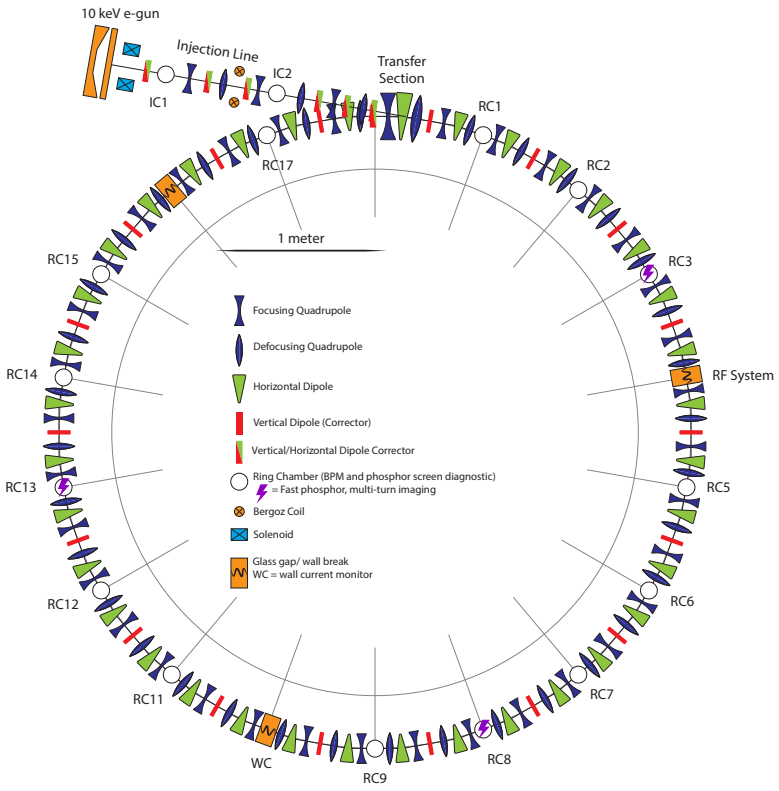

Figure 3.7: A full UMER schematic including injection line, transfer line, and ring.

taking up a BPM spot; this gives UMER a total of 14 BPMs. Cells without BPMs have vertical corrector magnets in their place. There are no horizontal correctors in UMER's ring. Instead, all 36 dipoles are used as horizontal correctors. Not pictured in Figure 3.7, is a set of 18 helmholtz coils that cover the entire ring and are used to minimize the effects of the earth's field on vertical steering. In certain locations around the ring the earth's field can account for 20-30% of the bending fields the beam interacts with. Additional diagnostics will be discussed later in this chapter.

3.1.5 RF system

Recently UMER has been testing a longitudinal beam confinement (RF) system. The setup works by creating a sinusoidal signal using an arbitrary waveform

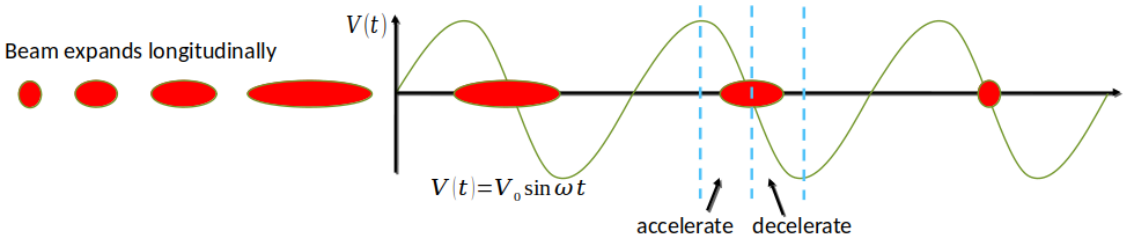

Figure 3.8: Basic operation principal of the RF system in UMER.

generator. The waveform then runs through two amplifiers before being applied across a glass gap section on UMER. The voltage amplification is on the order of 16x. For confinement of the 0.6 mA beam within UMER a 200 mV signal is generated and an amplified 4.75 V signal is applied to the beam. Right now only the 0.6 mA beam can be confined. Higher current beams expand too quickly causing the longitudinal distribution to change too much over one turn to be contained within the RF bucket. The once per a turn confinement is simply not enough to keep the beam contained. There is work ongoing to add two replica RF systems at opposite ends within UMER. With this setup the beam can be confined between 2-3 times per a turn making it possible to bunch the higher current beams. Figure 3.8 shows the basic principle of the RF confinement in UMER. See references for more information [5].

3.1.6 Control system

While UMER is small in scale and cost compared to other accelerator research laboratories, it still requires and maintains a control system similar in complexity to those used at the larger accelerator facilities. UMER has around 200 devices

connected on its control system along with roughly 500 process variables (PV[2]). For comparison, large accelerator facilities at the national laboratories have systems built to handle more than 20000 PVs [6]. In UMER's case, the majority of the devices are accelerator magnet power supplies that need to be controlled for operation and experiments. In order to understand how the tolerances of the equipment effect the experiment, a brief description of the control system is presented here to better understand its capabilities and limitations. A more detailed discussion of the control system can be found in Appendix B.

All magnets on UMER are individually powered and run approximately 0-3 amps of current. Many experiments on UMER take several hours to run, requiring power supplies to constantly be operating. As a test of power supply stability, currents were measured for all quadrupole magnets over a typical experiment length time period. Figure 3.9 shows the results with a measured standard deviation of 0.012 Amps. A standard deviation that large is enough to cause detectable shifts in beam parameters. For reference, a change of 0.001 A in all quadrupoles causes a change on the order of 0.005 in transverse tunes. Such variations can also be treated as field errors and will affect resonances in the accelerator. Apart from magnets there are a host of diagnostic tools used throughout the control system. These tools include devices like beam position monitors, wall current monitors, RF systems, etc. The set of errors and limitations of each device will be discussed in the next section inclusively.

[2]Process Variables are named data with a given value(s). An example being the set current for a particular magnet on the machine.

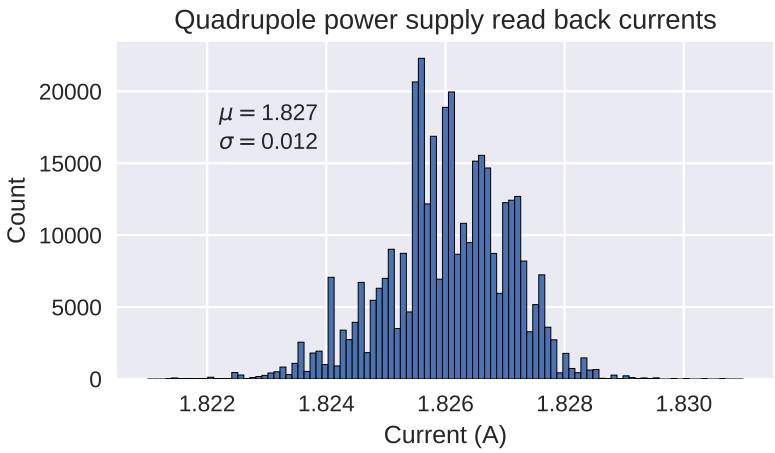

Figure 3.9: A histogram of the read back currents from all quadrupole power supplies. Several thousand automated measurements were done over a roughly 12 hour period. The setpoint for all quadrupoles is 1.826 Amps. μ and σ are the mean and standard deviation of the data.

A majority of magnets have polarity switches that will switch the direction of the fields. For example, this is how UMER sets up a lattice using focusing and defocusing quadrupoles. The switches are used to program specific combinations of focusing and defocusing quadrupoles for experiments with different FODO based lattices. Beam based measurements are typically used to determine and double check that polarities have the correct orientation for magnets. For quadrupoles, having one at the wrong polarity would be immediately obvious, but for corrector magnets this is less so. Figure 3.10 shows a scan of the vertical position vs magnet strengths for all the vertical corrector magnets (VCMs) in UMER. This type of polarity test is something to do during commissioning, after engineers have installed new magnets. From this measurement it was clear that several correctors were at the wrong polarity. Separately, the polarity switch in RSV1 was not working and RSV11 was offline completely. Such beam based measurements allow a quick way to detect and fix issues in the controls that would otherwise be difficult to find.

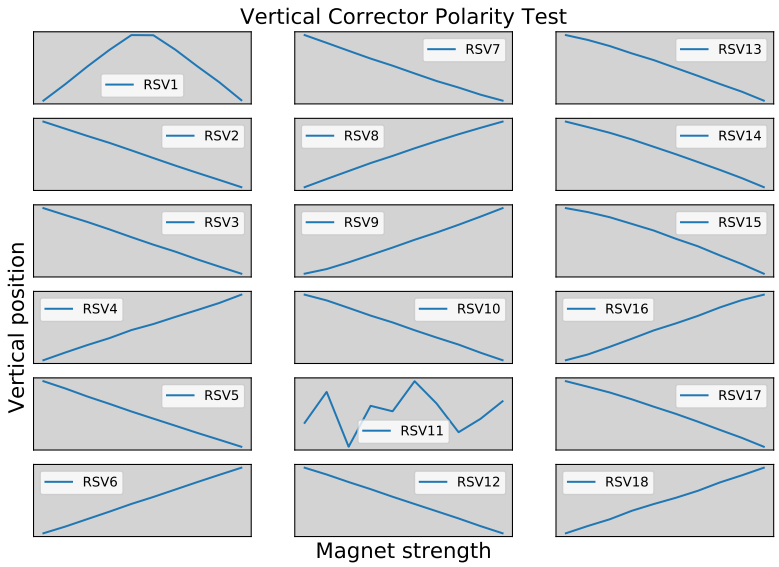

Figure 3.10: Each VCM is perturbed and a downstream beam position monitor is used to measure the response in the vertical orbit.

Access to all devices and magnets is through a central backend server. The server uses standard HTTP protocols and is built in python using Flask [7]. Different magnets and device run on different power supplies and hardware. In UMER's case there are about a dozen different types of hardware, each having its own custom API, communication protocols, and drivers. The server handles communication with all the devices in UMER. Each device is assigned a unique id used to access its data from the server. A user just needs a magnet id to set and read back its currents and other relevant properties. Considerable time was spent designing, building, and maintaining this control server, and as a result, has significantly reduced the amount of time needed in setting up experiments on the accelerator. With the current server and post processing tools, most experiments only require a few minutes of software setup time. Appendix B goes more into the technical details of building such a system.

3.2 Diagnostics

UMER has a comprehensive set of diagnostics that are routinely used for data collection. This section reviews the relevant diagnostics used for this dissertation. The physics behind Beam Position Monitors, Wall Current Monitors, and Phosphor screens are discussed. A detailed error analysis is presented using the Beam Position Monitors. This section covers the diagnostics themselves. Chapter 4 goes further into the details of processing the data generated from these diagnostics.

3.2.1 Beam Position Monitors

Beam Position Monitors (BPMs) are frequently used diagnostics in accelerators. This non-destructive diagnostic measures the transverse centroid position of the beam on a turn-by-turn basis. The majority of experimental data from this dissertation was collected via BPMs. It is thus important to understand how these diagnostics work and the possible errors associated with them.

BPMs use electromagnetic pick-ups to non-destructively measure the current of a bunched beam. In UMER's case, the BPMs have capacitive pick-ups, since a time-varying ac beam will induce image charges on the BPM pickup plates. The plates then form capacitors with respect to the grounded BPM housing. The induced charge on the plates will generate a voltage across the capacitor. The voltage is then measured for all four pick-ups. Figure 3.11 shows a cross sectional diagram of a BPM.

Assuming a bunched beam can be treated as a thin wire with current I_b, an

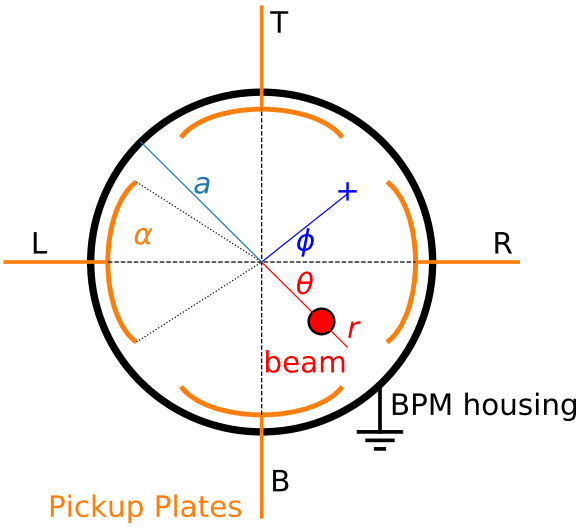

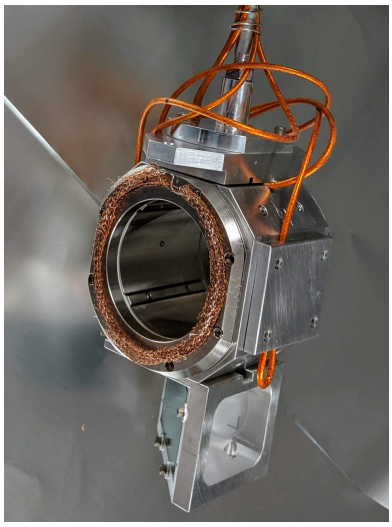

Figure 3.11: (left) Diagram of a BPM. The four plates are labeled (L)eft, (R)right, (T)op, and (B)ottom. (right) Image of a BPM from UMER (RC6). Note there is also a phosphor screen attached to the bottom of the BPM.

electrostatic model can be derived to describe how a BPM works [8]. The current density at the walls of the BPM can be described as:

$$J_{\text{im}}(\phi) = \frac{I_b}{2\pi a}\left(\frac{a^2 - r^2}{a^2 + r^2 - 2ar\cos(\phi - \theta)}\right) \tag{3.1}$$

where a is the BPM housing radius, and (r, θ) are the polar coordinates to describe the beam's position. If the BPM plates cover an angle α, then the image current on the plate is given by:

$$I_{\text{im}} = \int_{-\alpha/2}^{\alpha/2} a J_{\text{im}}(\phi) d\phi \tag{3.2}$$

The image current generates an image voltage across the pick-up plate and grounded BPM housing. The difference in voltage across the plates can be used to calculate the location of the center of charge with respect to the center of the beam pipe using

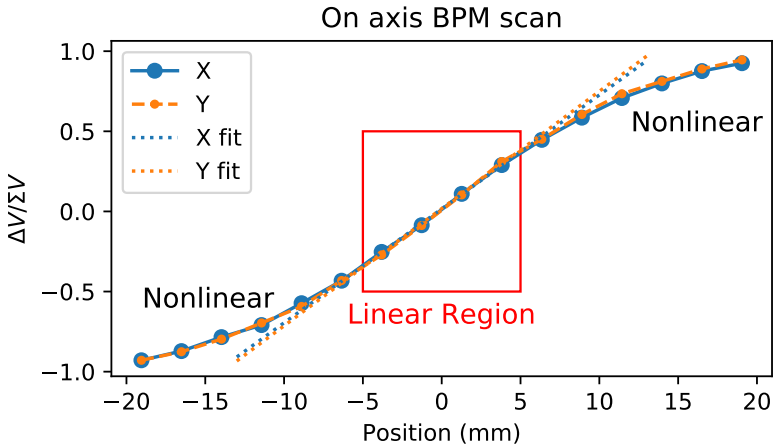

Figure 3.12: Experimentally, A thin wire representing the beam is moved from left plate to right plate while measuring the voltages on the plates. This is then redone in the vertical direction by moving up and down.

the following equations:

$$X = \frac{1}{S_x}\frac{V_R - V_L}{V_R + V_L} + \delta_x = \frac{1}{S_x}\frac{\Delta V_{rl}}{\Sigma V_{rl}} + \delta_x \tag{3.3a}$$

$$Y = \frac{1}{S_y}\frac{V_T - V_B}{V_T + V_B} + \delta_y = \frac{1}{S_y}\frac{\Delta V_{tb}}{\Sigma V_{tb}} + \delta_y \tag{3.3b}$$

where V is the voltage of the right,left,top, and bottom plates, $S_{x,y}$ is the position sensitivity in units of $[\%/mm]$, and $\delta_{x,y}$ is the offset.

In order to measure the position sensitivity an experimental linear scan is done across the BPM plates where a thin wire is moved in steps from one plate to the other. Results are shown in Figure 3.12. The region near the center of the BPM follows the linear trend shown in Eq. 3.3a,3.3b while the nonlinear effects from Eq. 3.1 start to occur closer to the BPM plates. A linear fit is done within the linear region. The slope of this fit is equal to the inverse position sensitivity

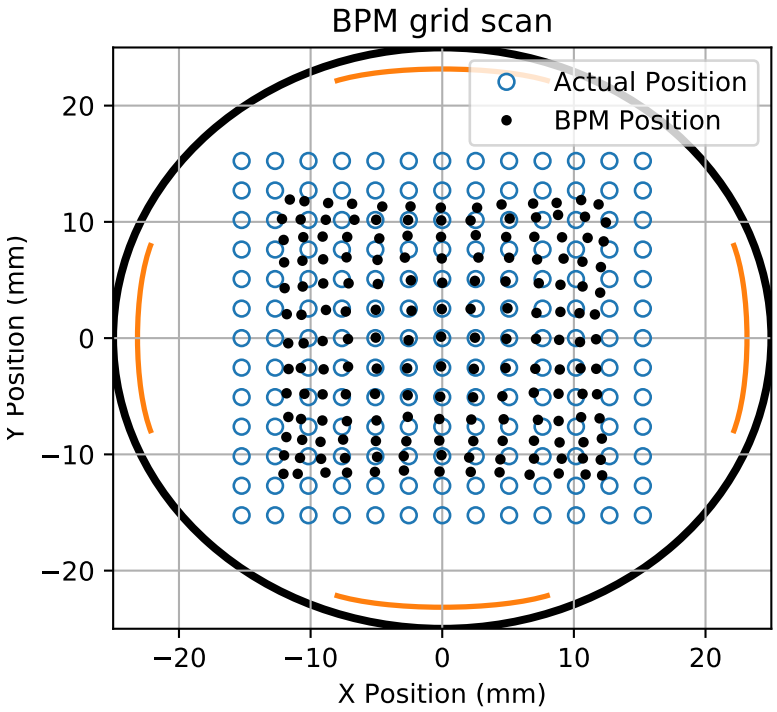

Figure 3.13: BPM measurements are done using a thin wire across a 2D transverse grid. Plotted are the actual true positions of the wire as well as the BPM measured positions.

constant, $1/S_{x,y}$. A 2D grid scan shown in Figure 3.13 is done to show the measure of nonlinearity when the beam is off axis. This is an experimental measurement using a thin wire to scan across the BPM. True 'actual' positions of the wire are measured along with the predicted position of the wire from reading the voltage signals off the BPM plates. Results show BPM readings to be accurate up to the 9-10 mm positions away from the center of the BPM. More information on designing and building UMER's BPMs can be found here [9].

BPM measurements in UMER are averaged over multiple shots[3] to improve precision by reducing noise. The number of shots averaged determines the uncertainty in position measurements. For a low current beam (0.6 mA) more shots are

[3]Shots refers to the repetition rate of the accelerator. e.g. 10 shots means 10 injections of beam into the accelerator at some injection rate. UMER's injection rate is 60 Hz.

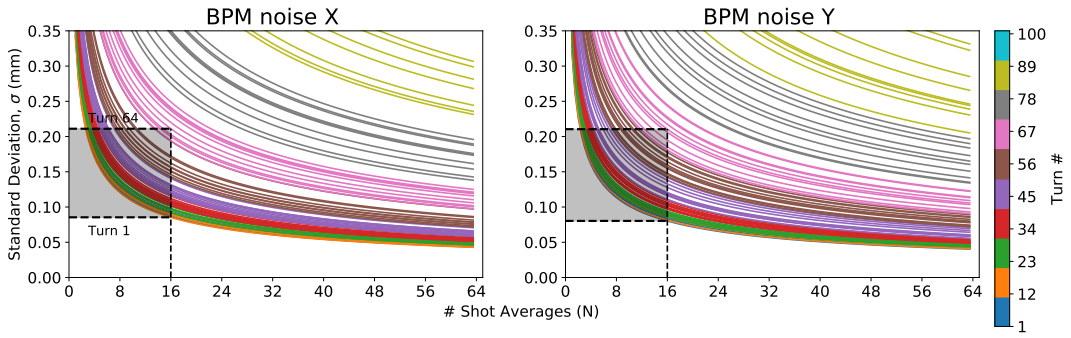

Figure 3.14: Using BPM RC3, 50 samples of 100 turn data were taken using different shot averages. A standard deviation was calculated for each turn and each shot average. The gray highlighted box shows the standard deviation range for turns 1 to 64 using a 16 shot average; this is the default setting used in UMER. Beam current here was 0.6 mA.

averaged to account for the higher noise to signal ratio while a higher current beam (6+ mA) can use fewer averages to achieve the same level of uncertainty. To quantify the level of uncertainty, many repeat position measurements were done over a range of shot averages at different turns using the 0.6 mA beam. A standard deviation was calculated over each set of samples. Results are shown in Figure 3.14.

The errors tend to follow a $c/\sqrt{N}$ trend where c varies between turns 1 to 100 and N represents the number of shot averages. For reference, $c \approx 1/3$ for turn 1 and generally increases with turn number. In UMER's case about 64 turns of data can be collected for the 0.6 mA beam before longitudinal effects make measurements unusable. In this 64 turn range, and assuming 16 shot averages, the uncertainty starts at ≈ 0.08 mm and increases to ≈ 0.21 by turn 64. 16 shot averages is used as that is the default setting for normal operation data collection. For this default average, Figure 3.15 shows the standard deviation as a function of turns. Results show a standard deviation that is constant up to about 25 turns in, and then starts to steadily rise. This can be seen as the variation in beam dynamics from shot

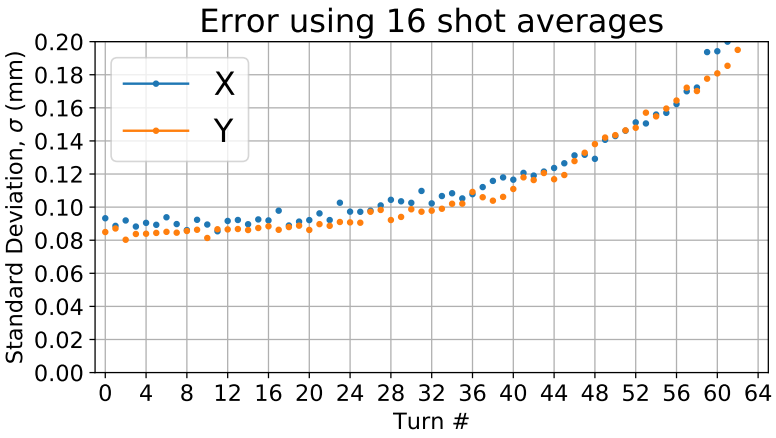

Figure 3.15: Standard deviation in position measurement as a function of turn number for the case of 16 shot averages. This data is extracted from Figure 3.14. A 0.6 mA beam is used.

to shot does not change significantly for the first 25 turns, after that point more complex dynamical behaviors cause larger variations from shot to shot.

Trying to model all points of error and uncertainty in BPM measurements is a nearly impossible task. The closest thing attainable is Figure 3.15. The data points in this figure are a representation of the error bars for the majority of position measurements. These errors include hardware uncertainty as well as nonlinear dynamical variations from beam shot to shot. The measurements were done with a single BPM (RC3), but an assumption is made that UMER's BPMs are similar enough that the same errors would hold across all BPMs.

3.2.2 Wall Current Monitor

A Wall Current Monitor (WCM) is a type of current monitor diagnostic that allows the non-destructive measurement of the beam current over successive turns. UMER has a WCM located at RC10 (see Figure 3.7). A schematic diagram is

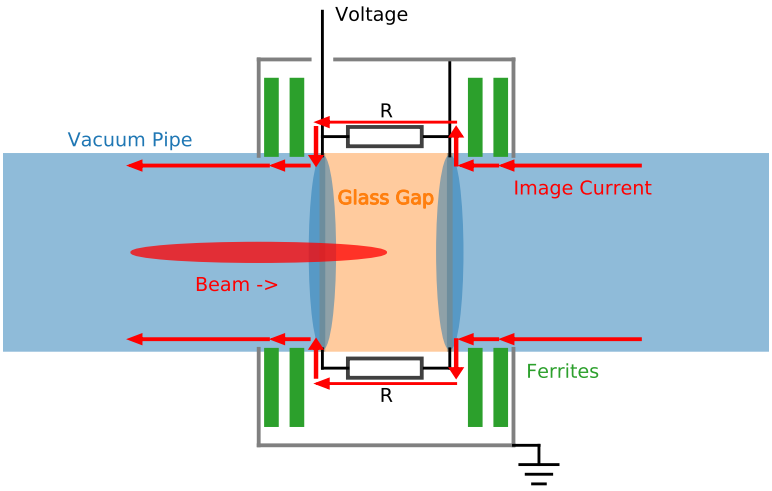

Figure 3.16: Schematic representation of a wall current monitor diagnostics system.

shown in Figure 3.16. The basic operating principles of a WCM rely on the image current generated by the moving beam on the vacuum pipe walls. A ceramic gap is introduced along with resistors across the gap to force the image current to travel across the resistors. The generated current over the resistance creates a voltage across the gap that can be measured. Using Ohm's law, $V = IR$, the voltage is used to calculated the image current and thus, the beam current.

Implementation of a WCM on an accelerator is more complex. To force the current to flow through the resistors instead of escaping, the wall current monitor is covered with ferrites. Resistors are also distributed evenly surrounding the gap, as opposed to a single resistor, to avoid any dipole kicks from the fields. The WCM in UMER can be represented by an equivalent LRC diagram with $L = 8\mu H$, $R = 4.545\Omega$, $C = 10pF$. Recently, a 10x amplifier was designed and built into the WCM to boost the output voltage signals. The 10x gain has allowed beam current measurements for the smallest current beams at UMER (≈ 0.1 mA).

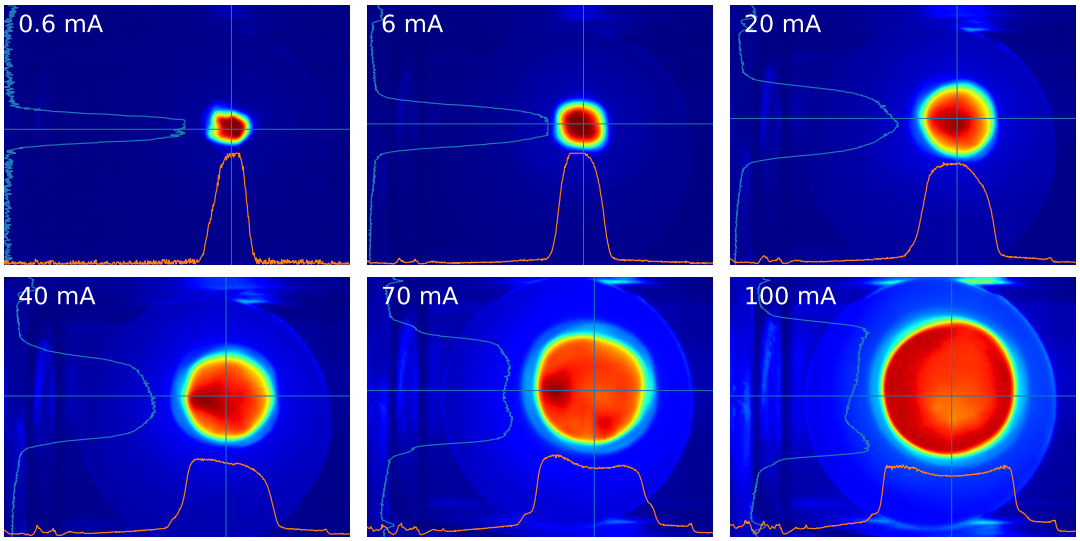

Figure 3.17: Using a phosphor screen at IC1, images were taken for all the different beam currents on the available aperture wheel. The solenoid was turned on and set to its default setpoint for the measurements (5.7 A).

3.2.3 Transverse Imaging

Transverse imaging screens distributed throughout UMER are used to image and measure the transverse beam profile. The screens are installed beneath the BPMs in the ring chambers. The right side of Figure 3.11 shows a BPM with an imaging screen underneath it. The screens are made with P43 phosphor (Gd_2O_2S:Tb, decay time of 1 ms) and measure 31.75 mm in diameter. [3]. The phosphor screens emit photons proportional to the electrons hitting it. The photons then reflect off a 90 degree mirror and exit the ring chamber into an imaging camera. The cameras have a 12 bit ADC, run at 120 frames per a second, and take images at 648x488 resolution. Example images taken of different beam currents are shown in Figure 3.17.

The phosphor screens are destructive diagnostics and can only image the beam

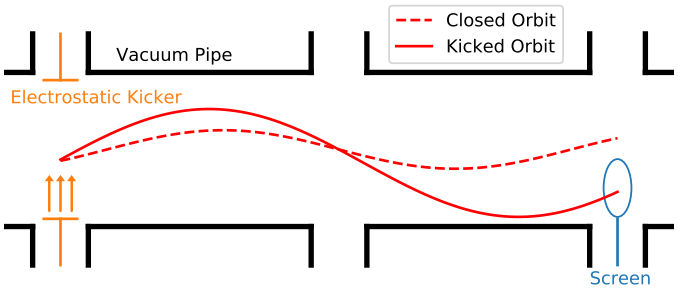

Figure 3.18: Schematic diagram of the knockout imaging technique employed at UMER. The electrostatic kicker is placed about one betatron wavelength before the knockout screen. The kick causes the downstream orbit to change and hit the partially inserted fast screen in the ring chamber.

on the first turn. Three locations around the ring (RC3, RC8, and RC13) have fast phosphor screens (ZnO:Ga, decay time < 3 ns) that are exceptions to this rule. The fast screens can be partially inserted into the ring chamber such that they avoid the beam until an electrostatic kicker is used to deflect the beam onto the screen at a specific turn. Figure 3.18 shows a diagram of the specific setup. With a faster camera, the three fast screens can also be used to image longitudinal slices of the bunch.

3.3 Chapter Summary

This chapter discusses the hardware that makes up UMER. From the electron source, through the injection line, and into the ring, the accelerator layout is described and discussed. The second half of the chapter reviews the different diagnostics installed on the accelerator. There is a discussion on BPMs and the errors associated with measurements, a description of the WCM system, and novel experimental configurations used with the phosphor imaging screens to image the beam past the first turn.

Chapter 3: Bibliography

[1] J. R. Harris and P. G. O'Shea. Gridded electron guns and modulation of intense beams. *IEEE Transactions on Electron Devices*, 53(11):2824–2829, Nov 2006.

[2] T. Godlove M. Virgo Hui Li S. Bernal, D. Kehne. Technical note: Electron gun tests. unpublished, 2000.

[3] Kiersten Ruisard. *Design of a nonlinear quasi-integrable lattice for resonance suppression at the University of Maryland Electron Ring*. PhD thesis, University of Maryland College Park, 2018.

[4] W. W. Zhang, S. Bernal, H. Li, T. Godlove, R. A. Kishek, P. G. O'Shea, M. Reiser, V. Yun, and M. Venturini. Design and field measurements of printed-circuit quadrupoles and dipoles. *Phys. Rev. ST Accel. Beams*, 3:122401, 2000.

[5] K. Hamilton, L. Dovlatvan, D. Matthew, D. Sutter, S. Bernal, T. Antonsen, and B. Beaudoin. Implementing traditional longitudinal beam focusing in umer. In *2018 IEEE Advanced Accelerator Concepts Workshop (AAC)*, pages 1–4, 2018.

[6] Kieran Evans. The epics process variable gateway – version 2. In *10th ICALEPCS Int. Conf. on Accelerator & Large Expt. Physics Control Systems.*, CERN, Geneva, 2005.

[7] Armin Ronacher. Flask, 2019.

[8] Peter Forck, P. Kowina, and Dmitry Liakin. Beam position monitors. *CAS - CERN Accelerator School: Course on Beam Diagnostics, Dourdan, France*, 06 2008.

[9] Bryan et al. Quinn. Design and testing of a fast beam position monitor. volume 4, pages 2571 – 2573 vol.4, 06 2003.

Chapter 4: Numerical Algorithms and Data Analysis

Throughout this dissertation many numerical algorithms and techniques are applied to accelerator related problems and tasks. In this chapter these algorithms are briefly introduced and explained. Section 4.1 discusses which tune measurement techniques result in the highest measurement accuracy. Section 4.2 is about the different optimization routines used in modeling, simulation, and experiment. Lastly, section 4.3 discusses the raw data processing techniques implemented to deal with the plethora of data generated by experimental diagnostic tools, e.g. BPM data.

4.1 Tune Measurements

The transverse betatron tunes are important global properties of any circular accelerator. The tunes determine the accuracy of the magnetic lattice and reveal how close the fields are aligned to the ideal design values. The tune can also be used to determine the beam's position in tune space relative to nearby resonances. If there is any beam deterioration, the measurement of tune is used as a diagnostic tool to move the beam away from any destructive resonances. Thus, it is important to be able to experimentally measure the transverse betatron tunes in an accelerator to a high degree of accuracy. This section discusses the different techniques and methods

employed for tune measurements at UMER and other circular accelerators.

4.1.1 Fourier Transform

The continous Fourier transform is defined as:

$$f(k) = \mathcal{F}_1[f(t)](k) = \int_{-\infty}^{\infty} f(t)e^{-2\pi ikt}dt \tag{4.1}$$

and allows the transformation of a function from time to frequency space. Given a discrete function with equally-spaced time steps, a generalization can be made to define a discrete Fourier transform (DFT) with equally spaced points in frequency space:

$$F_n = \sum_{k=1}^{N} f_k e^{-2\pi ink/N} \quad , \quad f_k = \sum_{n=1}^{N} F_n e^{-2\pi ikn/N} \tag{4.2}$$

where the discrete steps are defined as $n, k = 1, 2, 3, ..., N$.

The most common tune measurement technique involves inducing large transverse betatron oscillations and using a BPM to measure the beam response over successive turns. A DFT can then be used on the BPM data to extract the measured tune. This can be shown analytically by using the solution to Hill's equation, Eq. 2.11, and the definition of tune, Eq. 2.14, to write down the betatron motion of the beam as:

$$x(s) = \sqrt{\epsilon\beta(s)}e^{2\pi iQs} \tag{4.3}$$

where s is the equivalent of a continous time variable. With a single BPM in an accelerator, it can sample Eq. 4.3 once per a turn in discrete, evenly spaced, steps.

Each revolution is a discrete step that can be written as $n = 1, 2, 3, ..., N$ leading to the following discrete equations sampled by the BPM:

$$x(n) = \sum_{j=1}^{N} \hat{x}(Q_j)\, e^{2\pi i Q_j n/N} \quad , \quad \hat{x}(Q_j) = \sum_{n=1}^{N} x(n)\, e^{-2\pi i Q_j n/N} \tag{4.4}$$

After collecting the sampled signal from a BPM, the Fast Fourier transform algorithm is used to calculate the frequencies of the signal [1]. The frequency with the largest amplitude from $\hat{x}(Q)$ is taken to be the value of the tune.

The tune can be broken down into its integer and fractional parts:

$$Q = q_{int} + q_{frac} \tag{4.5}$$

where for example a tune of 6.62 would be written as $6 + 0.62$. Due to the fundamental nature of trigonometric functions, only the fractional part of the tune can be measured with Fourier transforms. Even with the fractional tune, there will be ambiguity between measuring q_{frac} and $1 - q_{frac}$. Appendix C.1 shows a more detailed explanation of this effect. Qualitatively, the BPM is only able to measure the phase change from one revolution to the next; it can not tell how many complete oscillations occur across that one revolution, but simply the change in phase. This phenomenon is sometimes called the stroboscopic effect.

Figure 4.1 shows the full start to finish process of measuring tunes. First the beam is excited to produce large, detectable, betatron oscillations. Using a BPM, the oscillations are sampled over many turns, 32 in this case. A FFT algorithm

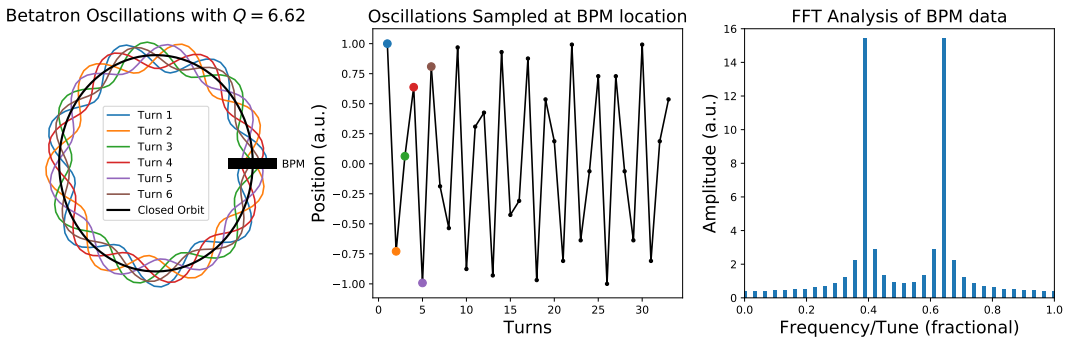

Figure 4.1: (left) Visual example of betatron oscillations around a ring. Six turns are plotted. (middle) Using the BPM on the left, the oscillations are sampled over 32 turns. The first 6 turns are visually shown oscillating around the ring on the left. (right) A FFT analysis done on the BPM signal in the middle.

is used on this BPM data to measure the frequencies in the signal. The fractional tune can then be determined from this spectrum. Again, note the ambiguity in the fractional tune being either $1 - q_{frac}$ or q_{frac}.

The uncertainty in the frequency measurement can be determined by the sampling frequency, F_s, and the total number of samples, N. The result of an N-point DFT gives an N-point complex vector representing frequency space. The frequency space ranges from 0 to F_s with N-point bins. Due to the symmetric nature of a Fourier transform, half the points are redundant complex conjugate images and can be ignored. This leaves the frequency range from 0 to $F_s/2$ with $N/2$ points. Dividing these two terms gives the frequency uncertainty for a DFT as F_s/N. As an example, if a signal is sampled for 100 points at a sampling frequency of 1200 Hz, the uncertainty in the bin to bin spacing in frequency space would be 12 Hz. Figure 4.2 shows a visual example of the bin spacing both in position space and frequency space.

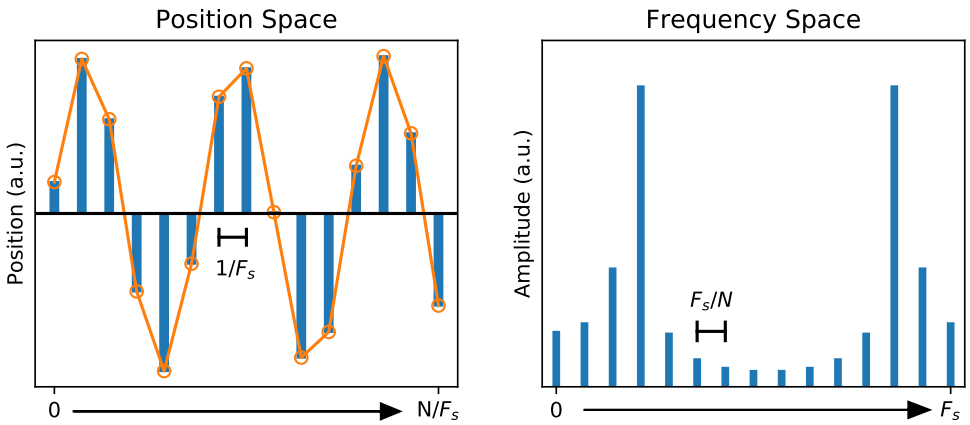

Figure 4.2: A signal is sampled N times at a sampling frequency of F_s. The signal is then decomposed in frequency space by applying a DFT.

$$\Delta Q = \frac{F_s}{N} = \frac{1}{N} \tag{4.6}$$

As an example, a resolution of 0.001 in tune measurements would require 1000 samples to be collected with a BPM. In practice there are many sources of errors that reduce the theoretical accuracy. Signal noise in the BPMs, tune spreads, space charge, etc can all cause the accuracy of tune measurements to go down.

4.1.2 Window Filters

Window filter functions can be used to improve the accuracy of standard DFT methods. Mathematically, functions are weighted with a window filter $w(n)$:

$$\hat{x}(Q_j) = \frac{1}{N} \sum_{n=1}^{N} x(n) w(n) e^{-2\pi i Q_j n} \tag{4.7}$$

where the $1/N$ in the exponential has been absorbed in Q_j. One type of filter is the zero-centered rectangular window defined by:

$$w_R(n) = \begin{cases} 1 & -\frac{M-1}{2} \leq n \leq \frac{M-1}{2} \\ 0 & \text{elsewhere} \end{cases} \tag{4.8}$$

Applying a DFT to $w_R(n)$ returns a sinc function:

$$\hat{w}_R(Q_j) = \frac{1}{M} \sum_{n=-\frac{M-1}{2}}^{\frac{M-1}{2}} e^{-2\pi i Q_j n} = \frac{\sin \pi M Q_j}{M \sin \pi Q_j} \tag{4.9}$$

Full derivation of Eq. 4.9 is shown in Appendix C.2.

Eq. 4.3 shows that the beam motion is governed by pure sinusoidal betatron oscillations. As a result, the underlining shape of the spectrum in frequency space is well known and can be exploited to improve measurements. Looking at Figure 4.3, the true tune exists somewhere inbetween the two largest discrete frequency peaks. By applying a rectangular window filter, an interpolation of the two peaks can improve measurement accuracy. Adding the weighted window filter function, the discrete BPM sampling equation becomes:

$$|\hat{x}(Q_j)| = |\frac{\sin \pi N(Q_{int} - Q_j)}{N \sin \pi (Q_{int} - Q_j)}| \tag{4.10}$$

where Q_{int} is the true frequency inbetween the largest frequency peaks. Dividing

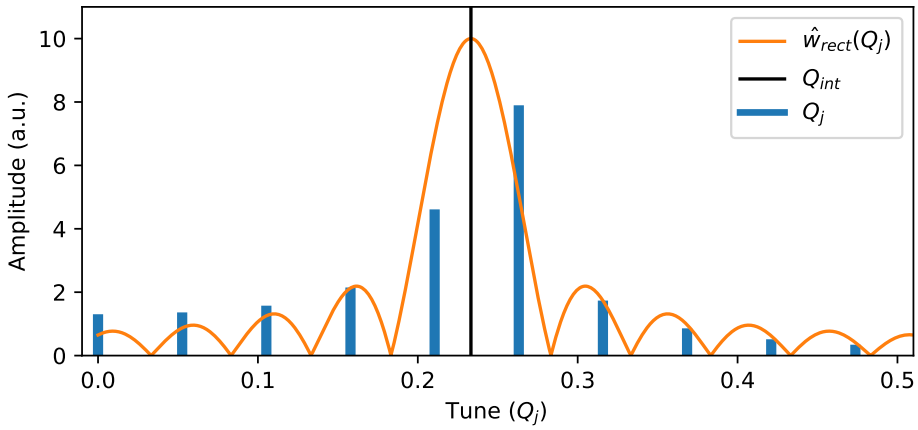

Figure 4.3: A discrete fourier transform of a signal is plotted along with the rectangular window filter. Q_{int} is the interpolated frequency of the window filter.

two points $|\hat{x}(Q_j)|/|\hat{x}(Q_{j+1})|$ allows Eq. 4.10 to be solved for Q_{int}:

$$Q_{int} = \frac{j}{N} + \frac{1}{\pi} \arctan\left(\frac{|\hat{x}(Q_{j+1})| \sin \pi/N}{|\hat{x}(Q_j)| + |\hat{x}(Q_{j+1})| \cos \pi/N}\right) \tag{4.11}$$

where $\hat{x}(Q_j)$ is the peak amplitude in the frequency spectrum and $\hat{x}(Q_{j+1})$ is the largest neighbor peak in the same spectrum. As a result of the filter, an improvement in accuracy is gained of the scale:

$$\Delta_{rect} Q = \frac{a}{N^2} \tag{4.12}$$

with a being some numeric constant. A rectangular window filter thus improves measurement accuracy quadratically with the sampled number of turns, a large improvement from a general DFT with no filters.

4.1.3 Numerical Analysis of Fundamental Frequencies

Numerical Analysis of Fundamental Frequencies (NAFF) is a frequency finding algorithm written by Jacques Laskar in order to study chaotic motion in planetary orbits [2]. The technique has since been successfully applied to accelerators and is the main method used to calculate betatron tunes in this dissertation. NAFF uses an FFT as the initial guess to seed the algorithm. It then applies a DFT with a Hanning window filter around the initial guess to calculate the tune.

Analytically, NAFF tries to find the maximum amplitude of the following function:

$$\Psi(\omega) = \frac{1}{2T}\int_{-T}^{T} w(t/T)\, f(t)\, e^{-i\omega t} dt \tag{4.13}$$

where $f(t)$ is a quasi-periodic function over some time span $[-T, T]$ and $w(t)$ is the added Hanning weight function: $w(t) = \sin^2(\pi t/N)$. The improvement in accuracy with this weight function increases to:

$$\Delta_{NAFF} Q = \frac{1}{N^4} \tag{4.14}$$

Figure 4.4 shows a visual example of a Hanning window filter. Note the lobe like shapes in frequency space; this is a result of the filter. In position space the signal is modulated by the $\sin^2$ term in the filter.

As a final way to summarize the various effects of filters, Figure 4.5 shows the errors in measurement accuracy as a function of the number of samples, N, and the type of window filter used. The predicted accuracies from Eq. 4.6, 4.12, 4.14 hold

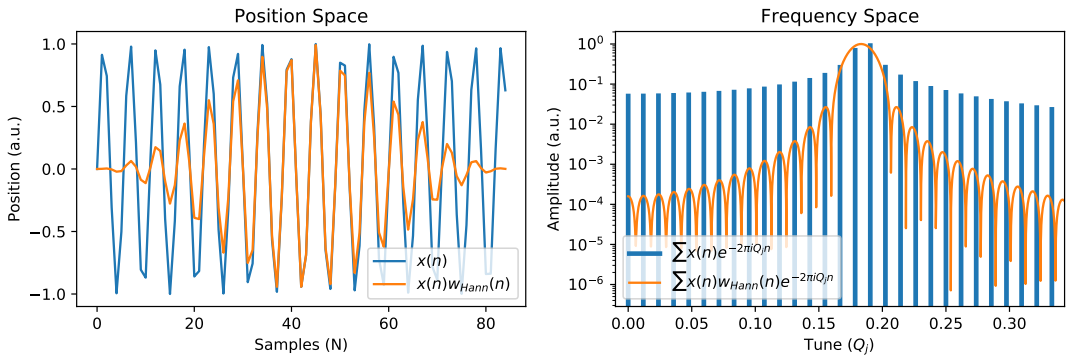

Figure 4.4: A discrete fourier transform of a signal is plotted along with the Hanning window filter. In frequency space a log scale is used to show the general space of a hanning window.

true in numerical simulations. With experimental data noise will become an issue and reduce measurement accuracies to well below the predicted theoretical values. However, in either case, using NAFF will give the most accurate measurements over other types of filters. As such, the majority of tune measurements presented in this thesis were measured using NAFF.

4.1.4 Four Turn Formula

While NAFF and DFT techniques can provide very accurate tune measurements, the algorithms require many BPM turns of data. For beams with large current densities, i.e. large space charge, containment of the beam might only last for a few turns, making standard DFT techniques impractical. As an alternative, Courant-Snyder theory can be used to derive a set of equations that can measure the fractional tune with only four turns of BPM data [3].

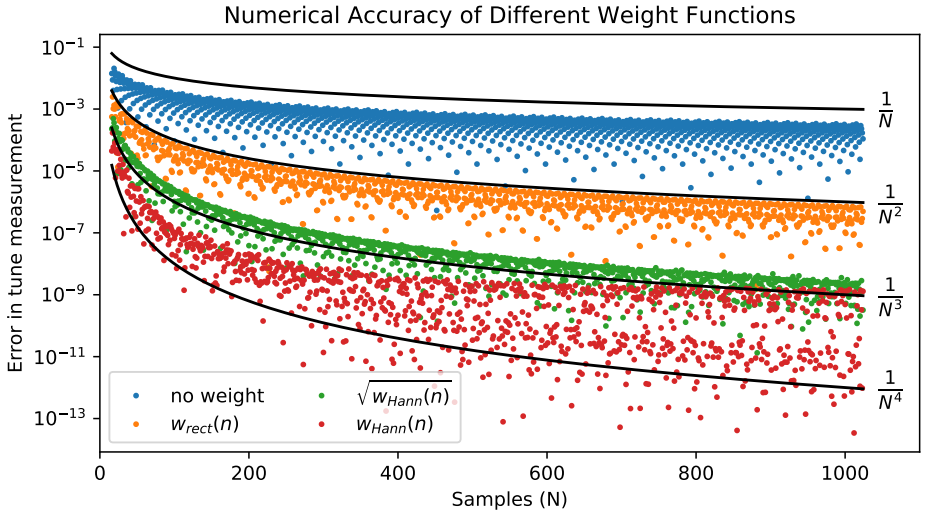

Figure 4.5: A DFT was used with various weight functions to calculate the measurement accuracy. The error is the absolute value difference between the measured frequency from the DFT and the true frequency of the signal.

The equation for the horizontal fractional tune is:

$$\cos\left(2\pi q_{frac}\right) = \frac{x_n - x_{n+1} + x_{n+2} - x_{n+3}}{2(x_{n+1} - x_{n+2})} \tag{4.15}$$

where x_n is the horizontal position data from turn n. The equation for the vertical fractional tune is the same, but with vertical position data. The full derivation of Eq. 4.15 can be found here [4]. Eq. 4.15 works well with large signal to noise ratios. If the noise becomes too large, there is a chance the denominator will be close to zero, causing the function to return obviously false results.

4.1.5 Curve Fitting

Curve fitting is another technique that can be used to measure the betatron tunes. Using BPMs installed on an accelerator, the betatron motion of the beam

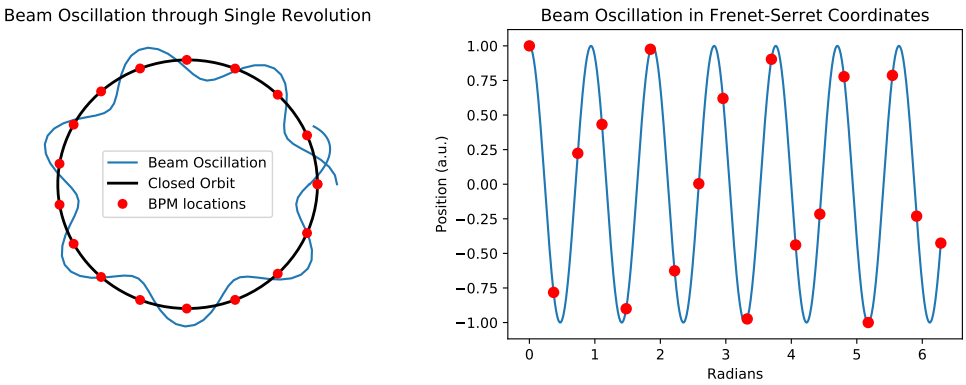

Figure 4.6: Using a set of BPMs (red), the betatron motion of the beam can be sampled. A sine/cosine curve can then be fit to the data to measure the oscillation frequency.

is sampled at a high enough rate to resolve the underlying sine signal and have an accurate fit to the BPM data. As a result, this technique can be used to get an accurate measurement of the full tune, integer plus fractional parts. Figure 4.6 shows a visual example of this process.

An important factor to consider when sampling any signal is the Nyquist limit/frequency. In order to reconstruct an underlying signal, it must be sampled at a minimum of twice the signal frequency; this is called the Nyquist frequency. Any less and the signal cannot be reconstructed. Based on this fact, it is common practice to have about 4x the number of BPMs compared to the machine tune. e.g. if an accelerator had a tune of (4.18), it would need around 17 BPMs. UMER has transverse tunes of $(6.70, 6.82)$ and only 14 BPMs, making it just above the minimum threshold for the Nyquist frequency.

4.2 Function Optimizations

From lattice design and modeling, to machine tuning, optimization routines are typically employed throughout the field of accelerator physics. Individual magnets, BPMs, etc are considered dimensions in some multidimentional function $F(\vec{x})$ that is being optimized. The objective/cost functions are commonly custom made for the task at hand. Optimization routines are used to solve various problems within this dissertation. This section presents and describes the basics of each routine.

4.2.1 Gradient Descent

Gradient descent (GD), sometimes called steepest descent, is an iterative optimization algorithm used to find a set of parameters, $\vec{x}_n$, of a function, $F(\vec{x}_n)$, that minimizes an objective function, $\nabla F(\vec{x}_n)$. The algorithm requires taking derivatives of the function being optimized. Starting from some point $\vec{x}_n$, $F(\vec{x}_n)$ decreases fastest by going in the direction of the negative gradient $-\nabla F(\vec{x}_n)$ from point $\vec{x}_n$. This then leads to the iterative algorithm:

$$\vec{x}_{n+1} = \vec{x}_n - \gamma \nabla F(\vec{x}_n) \tag{4.16}$$

An appropriate value for γ is used such that $F(\vec{x}_n) \geq F(\vec{x}_{n+1})$. Thus, starting at an initial guess $\vec{x}_0$, and taking n iterative steps will lead to a sequence of evaluations: $F(\vec{x}_0) \geq F(\vec{x}_1) \geq ... \geq F(\vec{x}_n)$ where the function is minimized.

Figure 4.7 shows an example of GD in one dimension. Different values of γ are

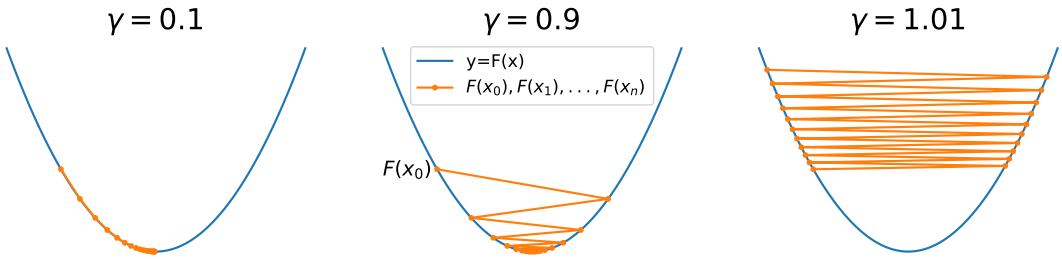

Figure 4.7: GD algorithm applied to the one dimensional function $F(x) = x^2$. 20 iterations are done with different values for γ.

selected and used to optimize a quadratic function. Note that a bad value of γ will cause the optimization to move in the wrong direction and lead to an unbounded solution. Figure 4.7 uses fixed values for γ, but γ is also allowed to vary after each iteration. Many different techniques exist to properly optimize γ. One such technique is the Barzilai-Borwein method which uses Eq. 4.17 as the optimal value for γ after each iteration [5].

$$\gamma_n = \frac{|(\vec{x}_n - \vec{x}_{n-1})^T(\nabla F(\vec{x}_n) - \nabla F(\vec{x}_{n-1}))|}{||\nabla F(\vec{x}_n) - \nabla F(\vec{x}_{n+1})||^2} \tag{4.17}$$

4.2.2 Nelder-Mead

Nelder-Mead (ND) is a simplex based search algorithm first published by Nelder and Mead in 1965 [6]. The method is a multidimentional unconstrained optimization of a given function, $F(\vec{x})$, without the use of any derivatives. The technique is especially useful for problems that involve non-smooth functions. In this dissertation ND is used often for simulation based optimizations. Designing lattices, tuning models, accounting for nonlinear elements, are all optimizations done in simulation using ND. As a result, a short description of the algorithm is presented

here.

ND begins with the initialization of a simplex S in $\mathbb{R}^n$. A simplex is defined as a convex hull of $n+1$ vertices $\vec{x}_0, \vec{x}_1, ..., \vec{x}_n \in \mathbb{R}^n$ e.g. in 1D the simplex would be a line, in 2D it would be a triangle, in 3D a tetrahedron. The direct search method begins with a given set of vertices, $\vec{x}_0, ..., \vec{x}_n$, of some simplex S and the set of function values at the given vertices, $F_i(\vec{x}_i)$ with $i = 0, ..., n$. Over each iteration a sequence of transformations are performed on the simplex to reduce the overall function values at the vertices. Each iteration looks at transforming the vertice with the worst function evaluation, $F_h(x_h)$, through means of reflection, expansion, contraction, or shrinking. More details about the actual algorithm implementation can be found here [7].

Although the technique of ND is quite simple, it can be achieved in many different ways. Certain steps in the transformations are done differently depending on the task at hand. Initialization of the simplex and termination/convergence of the algorithm are similarly implemented differently based on the specific task. For the case of this dissertation, any relevant changes will be discussed in the sections that use ND for optimizations. As a final comparison, Figure 4.8 shows both GD and ND algorithms applied to a 2D quadratic function. Generally, GD will converge significantly faster on smooth functions. When derivatives of a function are not necessarily smooth, ND will do better.

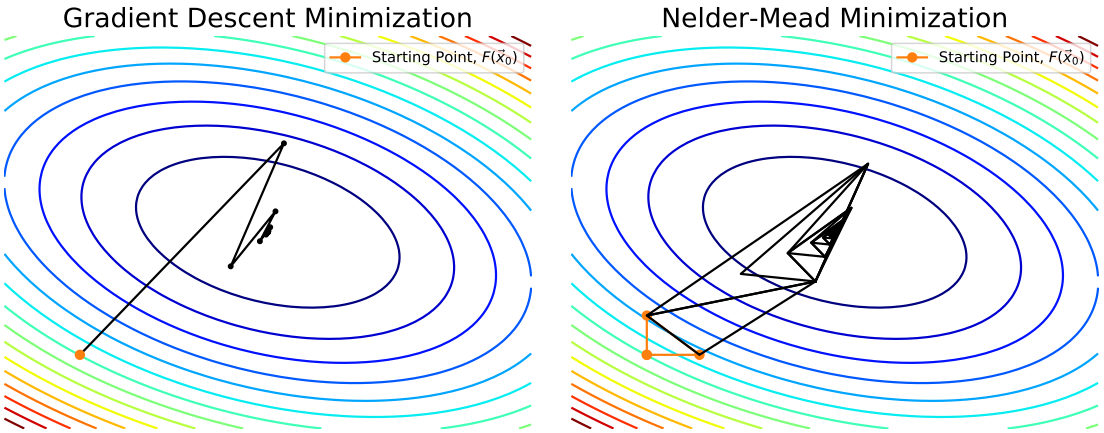

Figure 4.8: GD and ND minimization techniques are applied to the function $F(x, y) = ax^2 + by^2 + cxy$. Both algorithms start from the same initial conditions and run through 20 iterations.

4.2.3 Robust Conjugate Directional Search

Robust Conjugate Directional Search (RCDS) is a general optimization algorithm originally developed by Xiaobiao Huang for use on online accelerator systems [8]. The main difference from other algorithms, such as GD and NM, is the robust line optimizer used in RCDS. The optimizer is able to account for noise in its function evaluations, making it able to deal with the noisy systems of an experimental accelerator system. Introducing noise within traditional algorithms will tend to give false results as noise fluctuations across each iteration can cause the algorithms to move in wrong directions and give bad readings. As a result, RCDS is used for all online optimizations done on UMER. Experimental work with the algorithm is discussed in section 8.2. This section provides an introduction to the algorithm and briefly explains how it works.

The goal of RCDS, like other optimizers, is to minimize a function $F(\vec{x})$ where $\vec{x}$ is an N dimentional vector. The input range of $\vec{x}$ is normalized to be between

$[0, 1]$ giving an N dimensional cube as the parameter space being searched for a minimum. The search also requires the use of a choosen line minimizer.

Starting at a point $\vec{x}_0$, a vector $\vec{n}$ is choosen in the direction to be minimized. The line minimizer can then be used to minimize $F(\vec{x}_0)$ in the vector direction $\vec{n}$. The basic line minimizer algorithm is as follows. Given as input vectors $\vec{x}_0$ and $\vec{n}$, and a function F, find the scalar λ that minimizes $F(\vec{x}_0 + \lambda\vec{n})$. Then replace $\vec{x}_0$ by $\vec{x}_1 = \vec{x}_0 + \lambda\vec{n}$ and $\vec{n}$ by $\lambda\vec{n}$. The complexity comes when choosing the direction $\vec{n}$ to minimize along. One example would be to take the unit vectors $\vec{e}_1, \vec{e}_2, ..., \vec{e}_N$ as the set of directions to search. Iterate through all the directions and repeat until a minimum is found. The specific line minimizer that RCDS uses is called Powell's method [9].

Powell's method uses an iterative search algorithm along the conjugate directions in parameter space. Conjugate directions are ideal in minimization of a function as picking new directions to search along do not spoil the results of previous directions. The way to find conjugate directions is to first take a taylor expansion around some point $\vec{p}$:

$$F(\vec{x}) = F(\vec{p}) + \sum_i \frac{\partial F}{\partial x_i} x_i + \frac{1}{2} \sum_{i,j} \frac{\partial^2 F}{\partial x_i \partial x_j} x_i x_j + ... \tag{4.18a}$$

$$F(\vec{x}) \approx c - \vec{b}^T \vec{x} + \frac{1}{2} \vec{x}^T A \vec{x} \tag{4.18b}$$

where A is defined as the Hessian matrix. Taking the gradient of $F(\vec{x})$ gives:

$$\nabla F(\vec{x}) = A\vec{x} + \vec{b}^T \tag{4.19}$$

If a minimization has just been done along the direction $\vec{u}$, then the component of the gradient of F along $\vec{u}$ must be zero:

$$\nabla F \cdot \vec{u} = 0 \tag{4.20}$$

Picking a new direction $\vec{v}$ to search along, the gradient of F will change. In order not to interfere with the minimization of $\vec{u}$, the gradient must remain perpendicular to $\vec{u}$ requiring that:

$$\vec{u}^T A\vec{v} = 0 \tag{4.21}$$

The two vectors $\vec{u}$ and $\vec{v}$ are now considered conjugates. Minimizing along a set of N conjugate vectors will efficiently approach the minimum of a function F.

RCDS modifies the line optimizer in Powell's method to account for noise fluctuations. After each iteration, the new minimum of the function F is updated only if it is more than $3\sigma_f$ below the value of the previous iteration's minimum where σ_f is the noise level of the system. The minimum is found by bracketing the high/lows along a search direction, $[\vec{x}_l, \vec{x}_h]$. Within the bracket, RCDS uniformly samples the function and fits the data to a parabolic curve. The sampling gives a statistical advantage in improving the accuracy of the measurement. The use of conjugate directions, not requiring any derivatives, and accounting for noise in

the system make RCDS the superior choose in fast online optimization of complex accelerator systems.

4.3 Diagnostics Data Processing

Experimental measurements are only achievable through the use of diagnostics tools such as BPMs, WCMs, and imaging screens. These tools are used to better understand the underlying physics of the accelerator system. Thus it is important that the data resulting from these diagnostics is as accurate as possible. Certain numerical techniques have been developed to process the diagnostics data in a consistant and accurate way such as to best improve experimental meaurements. In this section these numerical techhniques are discussed in detail.

4.3.1 Raw Signal Analysis

All BPM and WCM diagnostics in UMER are connected to a high frequency sampling oscilloscope. The scope is able measure raw turn by turn signal data from the beam. This data is then digitally processed through software to calculate usable BPM and WCM measurements.

The data processing techniques are quite unique in UMER's case. Figure 4.9 shows an example of UMER BPM signal data. The signal is floating, meaning it is not connected to a natural ground, and as a result, simply measuring the peak beam current is not enough. The zero current signal must also be measured as that will be the ground reference for the peak current. Note from Figure 4.9 that

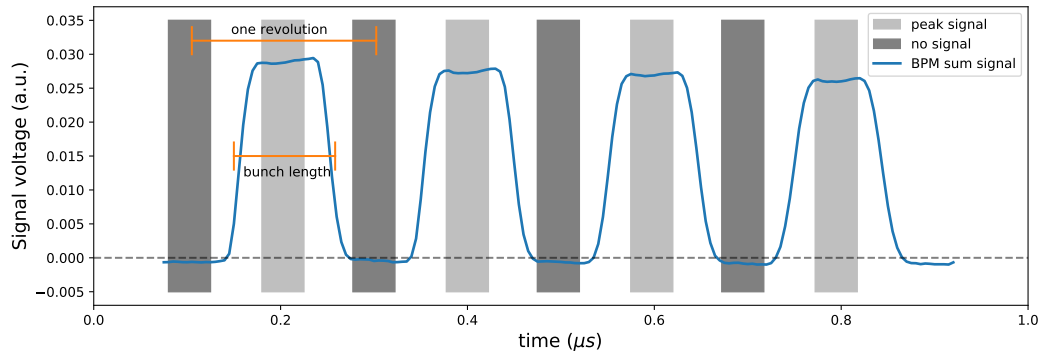

Figure 4.9: Four turns of the raw sum signal data from a single BPM is measured. The dark gray boxes represent the portion of the signal averaged for the no beam signal level. The light gray boxes represent the portion of signal averaged for the peak beam signal. The difference between these two points represents a single number measuring the BPM sum signal.

the floating signal is not constant in time, but changes from turn to turn and that this measurement must be repeated through each turn. Separately, the bunches in UMER are very long with respect to the machine circumference. The unbunched beam measures roughly 100 ns in length while the machine circumference is around 200 ns, meaning the single bunch in UMER fills half the ring. With such a long flat top beam the peak current is not a single point, but an average across the window of the beam. The flat top shape also depends on the beam current and will evolve over many revolutions of the beam within the accelerator. The light gray boxes in Figure 4.9 show the range of points used for the peak current measurement; these points are averaged to generate a single mean peak current across the bunch. A similar routine is done for the zero reference signal inbetween the peak beam currents, represented by darker gray boxes in Figure 4.9.

A question that might arise in processing BPM signal data is where longitudinally should the peak beam current be measured? Ideally measurements should be

near the center of the bunch as picking a range near the head and tail of the beam will cause noticeable differences in tune and orbit motion. For the purpose of this dissertation, the majority of BPM data is collected such that peak beam current is measured at the longitudinal center of the flat top beam distribution. Depending on the bunch length, the number of data points used to average the peak beam current is roughly 50% of the length of the longitudinal flat top portion of the bunch. For the case of bunched beams with the RF system turned on, the longitudinal distribution of the beam resembles that of a delta function. In this case the peak current is taken as the max value of the delta function; this approach is similar to how larger accelerator facilities measure signal data with their BPM systems.

4.3.2 True Current Measurements

UMER uses a single bunch coasting beam for its experiments. The beam is nominally 100 ns in length while the accelerator is 200 ns in circumference, meaning the injected single bunch fills half the ring. Without any RF system to longitudinally confine the beam, the bunch ends will expand at a rate dependent on the beam current.

Figure 4.10 shows a diagram representation of how the beam expands in time through a series of four steps 1-2-3-4. In step '2' the head and tail ends of the bunch start to expand out. At step '3' the first crossing/overlap occurs when the head and tail ends meet. Step '4' occurs several turns later when the ends of the bunch have crossed over several times and very little of the original bunch core

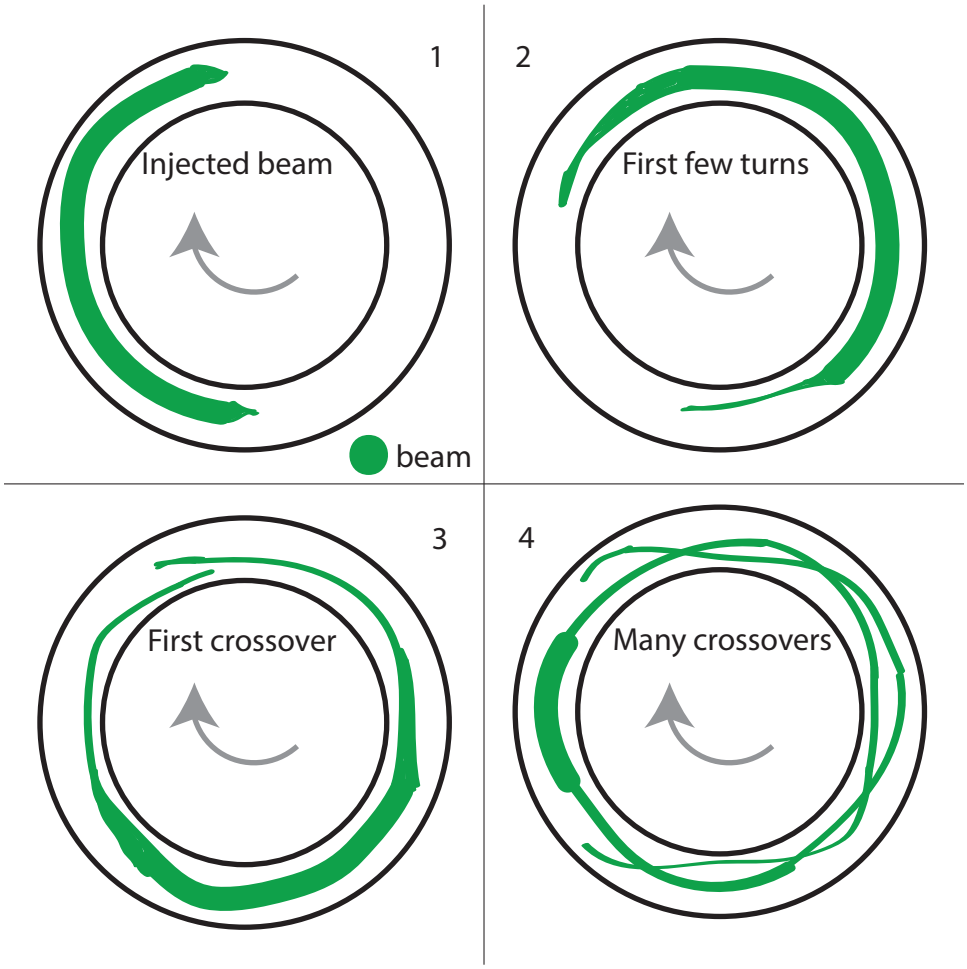

Figure 4.10: Schematic diagram showing the process of an expanding beam in UMER. The process starts from 1 - 2 - 3 - 4.

remains. Eventually the bunch expands enough to uniformally fill the entire ring, making measurements with the wall current monitor ineffective as there is no longer a reference zero current to measure from. Like the BPM signal measurements in Figure 4.8, the wall current monitor finds the beam current by measuring the voltage difference between 'beam' and 'no beam' passing through it. When the ends of the bunch overlap, there is no longer any 'no beam' reference point to use when measuring the beam current.

One way around the beam current measurement issue is to use an electrostatic

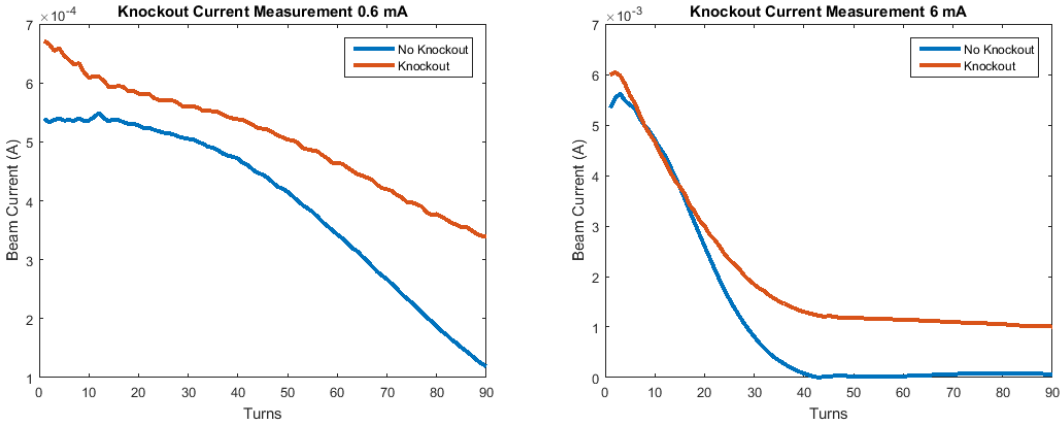

Figure 4.11: Beam current as a function of turns using the knockout measurement technique for (left) a 0.6 mA beam and (right) a 6.0 mA beam.

kicker to knock part of the beam out of the vacuum pipe. By knocking out the beam current, a zero signal reference measurement point can then be used to calculate the beam current. See this paper for more information [10]. Figure 4.11 shows a beam current measurement with and without the knockout technique being applied. For the 6 mA beam there is little difference in current over the first 20 turns. For the 0.6 mA beam there is a larger difference in beam current. All the beam current measurements in this dissertation do not use the knockout technique as it is quite tedious and difficult to setup for every experiment and measurement. Thus, the current measurements presented are not truly the real current values because the zero current reference point is not truly zero current due to this longitudinal expansion effect.

4.3.3 Image Processing

During, and after, transverse images have been taken using the cameras and phosphor screens discussed in section 3.2.3, a fair amount of image processing is

done to ouput usable measurements. Once the image processing is done, important beam characteristics such as centroid location and rms beam size can be calculated from the moments of the image. For a continuous function $f(x, y)$, the moments of order $(a + b)$ are found to be:

$$M_{ab} = \int_{-\infty}^{\infty} x^a y^b f(x, y)\, dx\, dy \tag{4.22}$$

In the case of a discrete image with pixel intensity values $I(x, y)$, the moments are:

$$M_{ij} = \sum_x \sum_y x^i y^j I(x, y) \tag{4.23}$$

Given that a beam in an image is likely not going to be centered, the central moments need to be used instead of the raw moments. The central moments are defined as:

$$u_{ij} = \sum_x \sum_y (x - \bar{x})^i (y - \bar{y})^j I(x, y) \tag{4.24}$$

where $\bar{x}, \bar{y} = M_{10}/M_{00}, M_{01}/M_{00}$ is the beam centroid location. Table 4.1 summarizes the first few central moments [11]. Using these equations, beam characteristics are extracted from the images. Note the equations are only valid for transverse beam distributions with gaussian like distributions and no transverse rotations. Unusual beam distributions arrising from intense space charge and transversely rotated beams will result in bad measurements, and as such, a different technique must be used. Figure 4.12 shows the first and second central moments calculated for a few example cases.

Moment	Equation	Meaning
u_{00}	M_{00}	total intensity
u_{10}	0	x from centroid
u_{01}	0	y from centroid
u_{11}	$M_{11} - \bar{x}M_{01}$ $M_{11} - \bar{y}M_{10}$	skew
u_{20}	$M_{20} - \bar{x}M_{10}$	x rms
u_{02}	$M_{02} - \bar{y}M_{01}$	y rms

Table 4.1: The first few central image moment equations. The moments tell us the beam centroid location and the beam rms size.

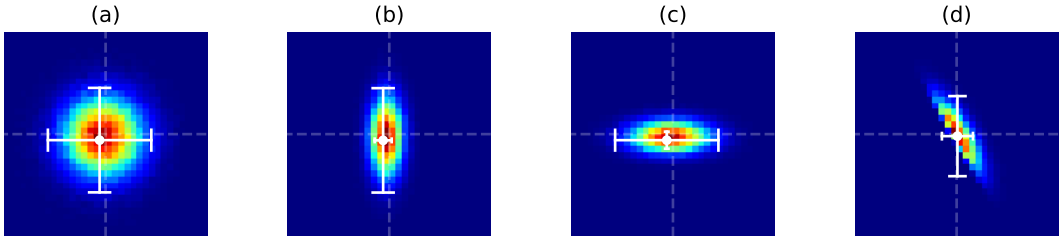

Figure 4.12: Central moments calculated for a (a) gaussian beam, (b) horizontally focused beam, (c) horizontally defocused beam, and (d) a skewed beam.

4.4 Chapter Summary

This chapter discusses the various numerical and computational algorithms and techniques employed in processing data from UMER. The different tune measurement techniques are discussed in detail with Figure 4.5 summarizing the accuracy of each method. Three different optimization algorithms are also discussed and explained in detail. These algorithms are used for beam steering, simulations, and data processing. Lastly, the different methods of data measurement techniques for BPMs, WCMs, and beam imaging is reviewed.

Chapter 4: Bibliography

[1] James W. Cooley and John W. Tukey. An Algorithm for the Machine Calculation of Complex Fourier Series. *Math. Comput.*, 19:297–301, 1965.

[2] Jacques Laskar, Claude Froeschl, and Alessandra Celletti. The measure of chaos by the numerical analysis of the fundamental frequencies. application to the standard mapping. *Physica D: Nonlinear Phenomena*, 56(2):253 – 269, 1992.

[3] Philip J. Bryant and Kjell Johnsen. *The Principles of Circular Accelerators and Storage Rings*. Cambridge University Press, 1993.

[4] David F. Sutter. Minimum data acquisition of the equilibrium orbit and tune. unpublished notes, 2017.

[5] Jonathan Barzilai and Jonathan M. Borwein. Two-Point Step Size Gradient Methods. *IMA Journal of Numerical Analysis*, 8(1):141–148, 01 1988.

[6] J. A. Nelder and R. Mead. A Simplex Method for Function Minimization. *The Computer Journal*, 7(4):308–313, 01 1965.

[7] S. Singer and J. Nelder. Nelder-Mead algorithm. *Scholarpedia*, 4(7):2928, 2009. revision #91557.

[8] Xiaobiao Huang, Jeff Corbett, James Safranek, and Juhao Wu. An algorithm for online optimization of accelerators. *Nuclear Instruments and Methods in Physics Research. Section A, Accelerators, Spectrometers, Detectors and Associated Equipment*, 726, 10 2013.

[9] M. J. D. Powell. An efficient method for finding the minimum of a function of several variables without calculating derivatives. *The Computer Journal*, 7(2):155–162, 01 1964.

[10] Timothy W. Koeth, B. Beaudoin, S. Bernal, I. Haber, R. A. Kishek, M. Reiser, P. G. OShea, Steven H. Gold, and Gregory S. Nusinovich. Measurement & simulation of interpenetration and dc accumulation of beam in the university of maryland electron ring. *AIP Conference Proceedings*, 1299(1):608–613, 2010.

[11] Ming-Kuei Hu. Visual pattern recognition by moment invariants. *IRE Trans. Information Theory*, 8:179–187, 1962.

Chapter 5: Model Building and Simulation Tools

Just as experiments are able to enlighten us with new knowledge for a given system, so can simulations and analytical models. In trying to experimentally study a particle accelerator, it is equally important to be able to build a set of simulation tools because both the experimental machine and simulation model mutually benefit each other. Experimental measurements are used to tune the simulations, and once there is agreement between the two, simulations are used to extend knowledge of the accelerator that would otherwise not be possible in the experimental machine, .e.g. details of phase space not easily measurable.

This chapter describes in detail the steps taken to build a model and simulation of UMER. Section 5.1 discusses the process of modeling magnets in UMER. In section 5.2 UMER is fully constructed in different types of simulation codes and benchmarked. Lastly, section 5.3 discusses the optimization methods and algorithms implemented to match simulations of UMER to the experimental machine. Appendix D contains more details on everything discussed in this chapter.

5.1 Magnet Modeling

Unlike traditional accelerator facilities which use iron core magnets, UMER uses PCB magnets. The details in the method used for designing these magnets can be found here [1]. Modeling such thin and short magnets is a difficult challenge due to fact that they are entirely made up of fringe fields. This section explains the techniques used in transforming the detailed fields into an equivalent hard edge model. The two models of magnets are extensively compared to minimize differences between them. This section will mostly discuss the dipole and quadrupole magnets. Other magnets on UMER, including the pulsed magnets and corrector magnets, are presented in Appendix D.

5.1.1 Gridded models

An in-house Biot-Savart solver called MAGLI is used to calculate electromagnetic fields represented on an array of grid points [2]. This results in a set of calculated gridded field data for each of UMER's PCB magnets. The solver is able to model the PCB magnets by up to 18 million conductor segments in a one-gigabyte-memory space. Starting first with the dipole magnet in UMER, transverse slices of the gridded field calculated from MAGLI are plotted in Figure 5.1. Within the region of the physical aperture, the dipole field is uniform. The corner regions with nonlinear fields are primarily at the edge of the aperture, a location that a steered beam will most likely avoid. Note at fringe field locations of $z = \pm 2.5$ cm, the fields are small in magnitude, making fringe field effects minimal in the PCB dipoles. The

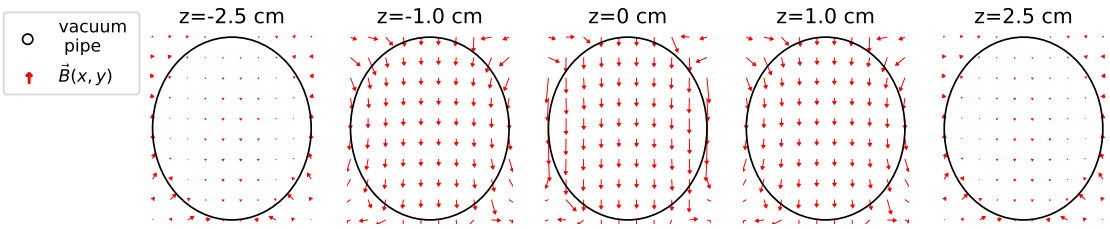

Figure 5.1: Transverse field slices plotted as a function of the longitudinal position through the dipole gridded field. Here z=0 is the longitudinal center of the magnet. The magnet is physically 4.4 cm long, roughly ±2.2 cm on each side. The black circle represents the physical aperture in UMER, about a 2.5 cm radius.

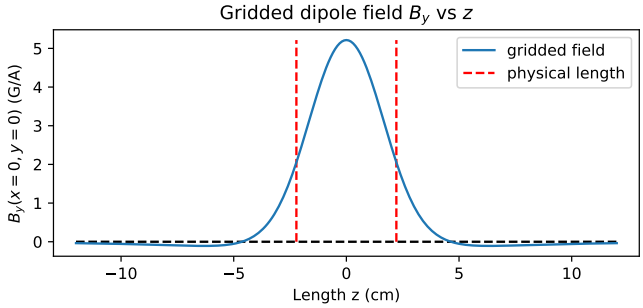

Figure 5.2: The vertical component of the magnetic field, B_y is plotted as a function of z through the magnet. The field is measured at the transverse center, $(x, y) = (0, 0)$. Physical length is plotted in red.

PCB dipole is also designed such that these fringe fields cancel each other out when integrating the field through the short magnets. The length of UMER's dipoles are about 4.4 cm based on the integrated longitudinal path through the magnet center.

A longitudinal scan can be done to measure the integrated strength of the dipole gridded field. Figure 5.2 shows a measurement of the vertical component of the magnetic field as a function of the longitudinal position through the magnet. Note the gaussian like shape as opposed to the typical flat top magnet profile. Due to how short UMER's magnets are, there is no flat top region in the field profile. The tails of the field in Figure 5.2 also has negative field components which contribute

to the overall integrated strength. The integrated strength can be calculated using:

$$\int_0^L B_y(x,y)\,dz \tag{5.1}$$

where L is the longitudinal length of the magnet including fringe fields. Similarly, the effective length of the magnet can be calculated by dividing the integrated strength with the peak field:

$$l_{\text{eff}} = \frac{1}{B_0}\int_0^L B_y(x,y)\,dz \tag{5.2}$$

For the dipole gridded field the integrated strength is chosen as 19.917 G-cm/A and the calculated effective length is 3.819 cm using a peak strength of 5.215 G/A. These values both depend on the integration limits in Eq. 5.1 and the assumption of a straight path through the magnet. In theory the integrated dipole path should be much greater than the radius of curvature, but in reality the integration limits can only extend so far before fields from upstream and downstream magnets interfere in the calculation. Thus, the values calculated here are subject to slight change based on the integration limits in the calculation. The overall difference is assumed to be minimal and neglected for simulations.

The UMER quadrupole gridded field is also analyzed in a similar way to that of the dipole field. In the case of the dipole, the vertical field was integrated through the magnet while in the quadrupole's case the gradient of the vertical component is integrated through the magnet. i.e. for a sextupole magnet, the second gradient would be integrated and so on. This is based off the multipole expansion in Eq. 2.6

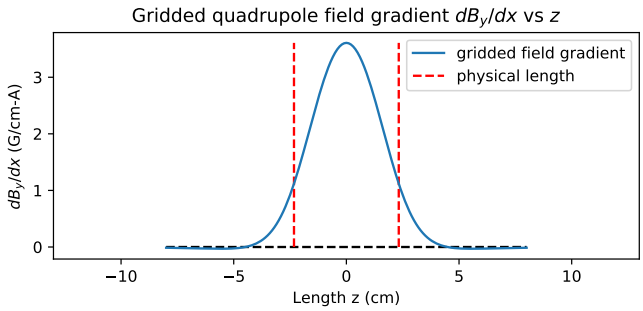

Figure 5.3: The vertical gradient component of the magnetic field, dB_y/dx is plotted as a function of z through the magnet. The field is measured at the transverse center, $(x, y) = (0, 0)$. Physical length of the magnet housing is plotted in red.

Magnet	Integrated Field	effective length	Peak field
dipole	19.917 G-cm/A	3.819 cm	5.215 G/A
quadrupole	13.501 G/A	3.742 cm	3.607 G/cm-A
YQ	5.544 G/A	5.237 cm	1.059 G/cm-A
QR1	5.457 G/A	5.262 cm	1.037 G/cm-A
PD-Rec	1.934 G-cm/A	4.903 cm	0.394 G/A

Table 5.1: integrated field, effective length, and peak field values calculated for the various types of magnets in UMER.

where the first order of each magnet is used. The quadrupole integrated strength is calculated to be 13.501 G/A with an effective length of 3.742 cm. The peak strength used is 3.607 G/cm-A. Figure 5.3 shows the integrated curve. Integration limits for the quadrupole are much shorter than the dipole case. The fringe fields extending out to negative values are not as large in the quadrupole case, requiring not as along of an integration range.

The remaining magnets are analyzed in Appendix D.1. Results are summarized in Table 5.1. The table contains information for the main dipole and quadrupole magnets in UMER as well as the three pulsed magnets in the transfer section leading into the ring.

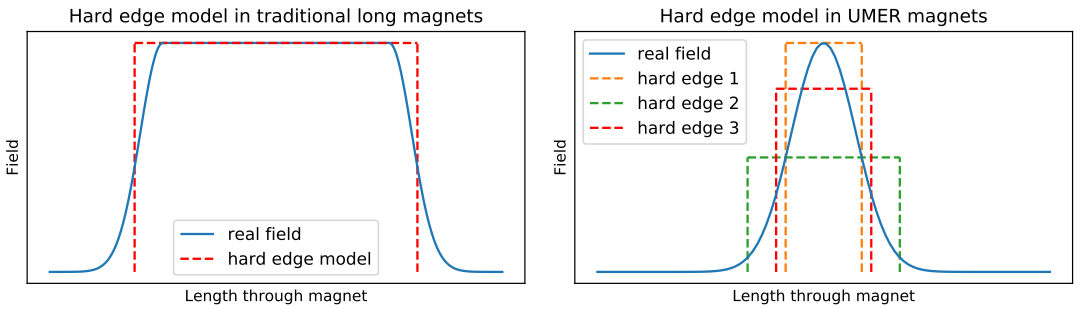

Figure 5.4: (left) Typical magnet profile in most accelerator facilities along with an equivalent hard edge model. (right) Typical profile and hard edge equivalents for UMER's magnets.

5.1.2 Hard edge models

Tracking and simulating particle beams through magnetic fields in accelerators is a computationally expensive task. Often a hard edge equivalent magnetic field profile can be used to reduce computation time while sacrificing little in accuracy. The left side of Figure 5.4 shows a typical magnet profile along with the equivalent hard edge profile. If the flat top region is much longer compared to the edge rise/fall time of the magnet, a hard edge model is a good approximation. In UMER's case the magnets are so short that the field profile looks like a gaussian. See right side of Figure 5.4. The entire magnet is composed of edges without a flat top region. This brings into question using the assumed hard edge model typical at most other accelerator facilities.

Work on creating a hard edge model for UMER's quadrupoles can be found here [3]. The approach taken in this dissertation is to start with the calculated values from Table 5.1. These values are then tuned until the simulations agree with the experimental measurements. In essence, an experiment based optimization is

being done to forcibly build a model that matches as closely as possible with the experiment. More about this is discussed in section 5.3.

5.1.3 Benchmarking gridded vs hard edge models

A simulation test is done to benchmark the performance of a hard edge magnet model over a gridded model. Both models are built in Warp, a particle in cell (PIC) code [4]. The hard edge model is built such that it matches the gridded field in strength and longitudinal length. Particles are generated with different initial conditions at the start of each magnet model and tracked through the magnet. After passing through the magnet, the particle's final conditions are recorded. In essence, a transfer map is made for each magnet model and tested with a large range of initial conditions to see if the two models agree with each other. Figure 5.5 shows the measurement done for a quadrupole magnet. Four plots are shown tracking a particle's position and angle (x, x_p) in the transverse plane through the quadrupole magnet. The left side shows the initial conditions entering the magnet and the right side shows the final conditions. Overall there is very good agreement between the gridded and hard edge models.

Figure 5.6 shows similar plots for the dipole fields. In the case of the dipole, no coordinate bend was incorporated to keep the models simple. A 'box' or 'rectangular' dipole model was used for the hard edge case. The agreement in the dipole case is also excellent, but not as great as the quadrupole case. Note what seems to be off in the dipole case is the quadrupole focusing term due to the edge effects in the

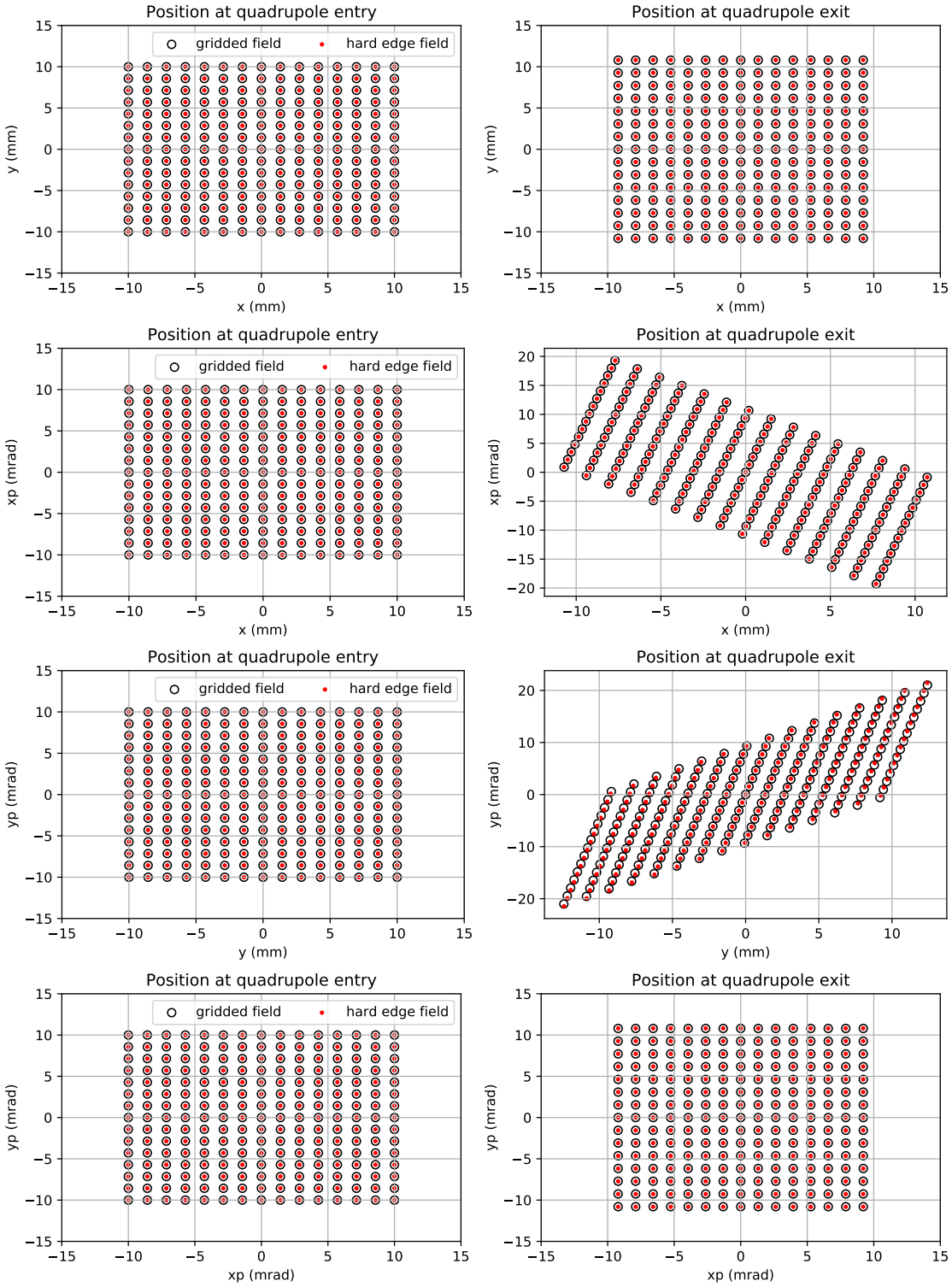

Figure 5.5: A set of initial conditions in (x, x_p, y, y_p) is tracked through a gridded and hard edge equivalent field for a quadrupole magnet.

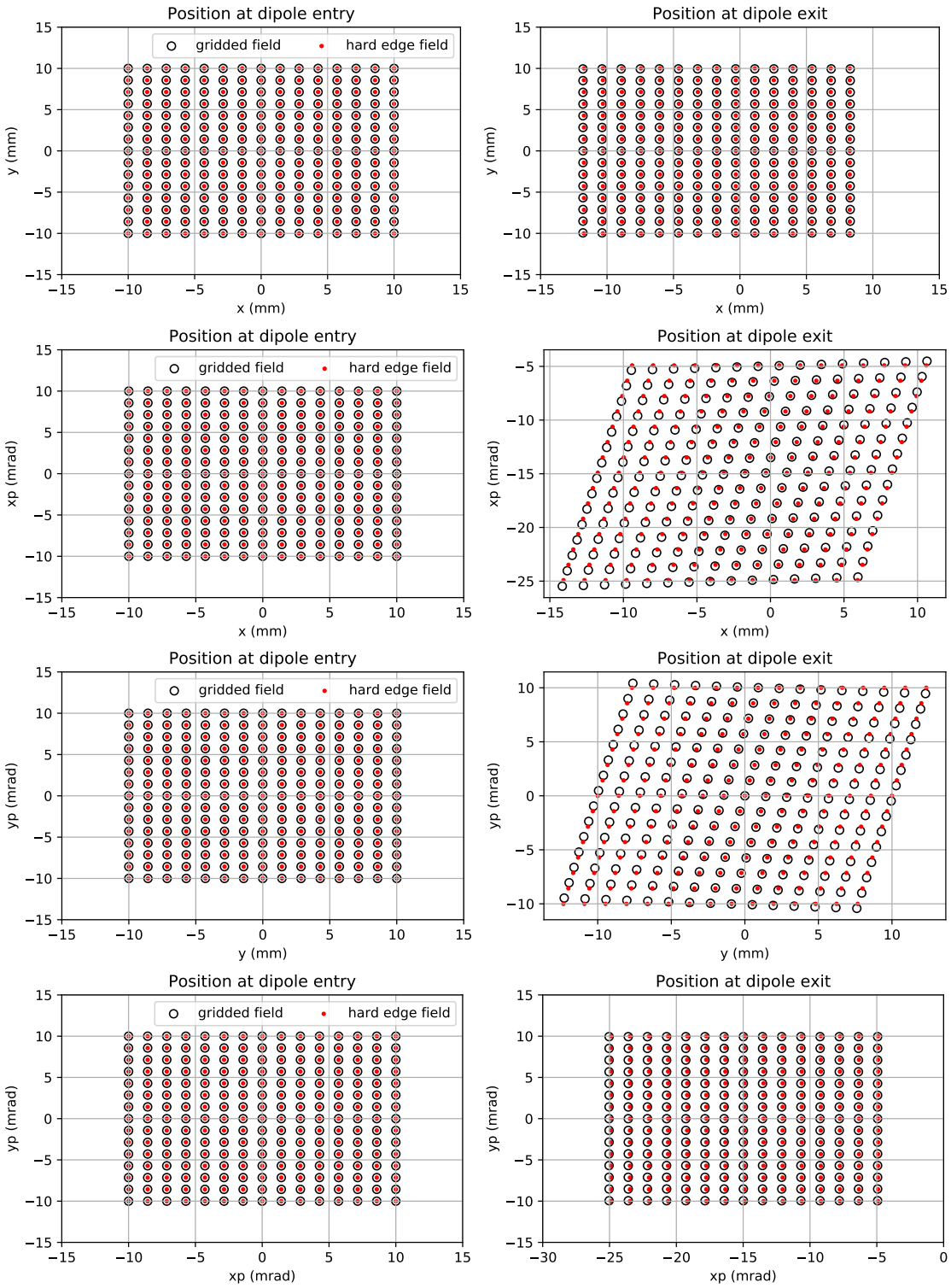

Figure 5.6: A set of initial conditions in (x, x_p, y, y_p) is tracked through a gridded and hard edge equivalent field for a dipole magnet.

magnet. Adjusting this term in the hard edge model might be able to correct for the slight differences observed in the figure. Details on the simulation setup that generated Figure 5.5 and Figure 5.6 can be found in Appendix D.2

The results show that a hard edge equivalent model can be used to replicate the behavior of UMER's complex PCB magnets. Even with the short gaussian like profiles, the hard edge model works. This is an important result as the gridded fields take signifcantly longer to generate and run in simulations. Using hard edge fields reduces the run time of the simulations. The hard edge models are also able to be easily incorporated in other simulation codes such as Elegant and Accelerator Toolbox (AT), making UMER's models not restrictive to a PIC code requirement [5, 6]. The remainder of the simulations done in this dissertation will be using hard edge models for the magnets unless stated otherwise.

5.2 Building a simulation model of UMER

There are many simulation tools used within the field of accelerator physics to track particle beam motion through a set of magnets. These codes work by integrating the particles through a set of magnetic fields defined by each individual magnet in the accelerator lattice. For circular rings the particles go around many millions of times in a matter of seconds, thus it is important that these individual magnets are setup properly in order to get accurate results. Simulation tools are also required to be symplectic, where the Hamiltonian is conserved; this dictates that energy is conserved in the system.

In the case of a single particle code, the beam is advanced through a series of transfer maps representing magnets. With a PIC code the beam is pushed in finite time steps with the electromagnetic fields calculated at each step. Understanding the physics involved in UMER requires simulating the machine in both a single particle code and a PIC code. The PIC code is able to properly model the collective space charge effects, but runs at a signficantly slower speed compared to the single particle model. Thus, the single particle code is used to do fast optimizations in order to match simulation results to the experiment. Afterwards, the optimized model is transfered to the PIC code and higher order corrections, such as space charge, are included in order to achieve a more accurate model. This section discusses the technical aspect of building UMER within both codes.

5.2.1 Single particle model

The single particle code used is called Accelerator Toolbox (AT) [6]. It is a Matlab based code with core tracking done in C. The code uses fourth order symplectic integrators to maintain a conserved Hamiltonian when tracking particles [7]. AT also has the ability to track particles via transfer matrices and can include synchrotron radiation effects.

Transfer matrices are capable of tracking particle trajectories through a series of accelerator magnets. They are useful in computing accelerator parameters and beam properties, and so a brief description is presented here. Using Eq. 2.10, a set of standard transfer matrixes can be defined for different magnets. Eq. 5.3 shows a

transfer matrix for a drift section and a horizontally focusing quadrupole:

$$M_{\text{drift}} = \begin{bmatrix} 1 & s \\ 0 & 1 \end{bmatrix} \quad M_{\text{quad·F}} = \begin{bmatrix} \cos\sqrt{K}s & \frac{1}{\sqrt{K}}\sin\sqrt{K}s \\ -\sqrt{K}\sin\sqrt{K}s & \cos\sqrt{K}s \end{bmatrix} \tag{5.3}$$

Here s is the magnet length and K is the quadrupole focusing strength, proportional to the quadrupole field gradient. Appendix D.3 lists the remaining magnet transfer maps. Tracking a particle through a FODO lattice requires multiplying the transfer maps one at a time:

$$\begin{pmatrix} x \\ x' \end{pmatrix} = M_{\text{quad·D}} M_{\text{drift}} M_{\text{quad·F}} M_{\text{drift}} \begin{pmatrix} x_0 \\ x'_0 \end{pmatrix} \tag{5.4}$$

For this dissertation a standard cell in UMER consists of two FODO cells with two dipoles, seen in Figure 5.7. With 36 bends, each one bends the beam a total of 10 degrees. The elements are all fixed at locations 8 cm apart, i.e. the distance between the center of element n and $n+1$ is 8 cm in length. An experimental measurement was done to determine the accuracy of such an assumption. The average error between element spacing was measured to be 10 microns, justifying the use of fixed element spacings in simulations. With each element at a fixed location, the element's hard edge model approximation is the parameter tuned to adjust simulations. That is the element's effective length and peak strength is varied while keeping their longitudinal spacing from each other at a fixed 8 cm.

The low energy beam in UMER results in the earth's magnetic field having

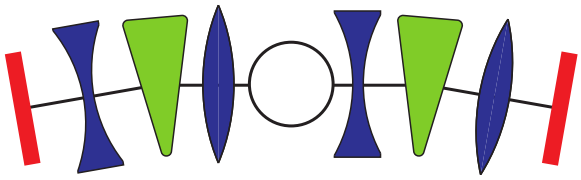

Figure 5.7: A standard UMER cell. Blue magnets are quadrupoles, green are dipoles, and red are vertical correctors. The circle represents a BPM.

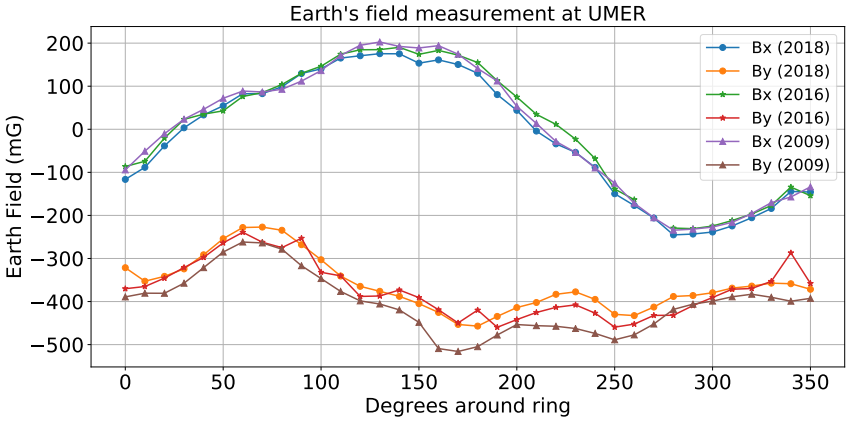

Figure 5.8: The earth's magnetic field plus the field of the IREAP building measured around the ring in UMER. Measurements are done about twice a year.

a noticeable impact on the beam trajectory. Figure 5.8 measures the earth's field around the beam trajectory in UMER for several years. The measurement of the earth's field in the lab changes year to year due to the movement of large magnetic objects around the lab, e.g. large magnetic server racks and cabinets. The non-uniform field adds significant complexity to the simulations; it can not be defined as a single transfer map element. The strength of the earth's field is sufficient enough to affect around $20-30\%$ of the bending around the ring. In a 10 degree ring bend the earth's field will bend the beam by $2-3$ degrees across an entire UMER section and so the dipole must be adjusted to bend the remaining difference such that the total bending adds up to 10 degrees. In the vertical direction the vertical corrector magnets in combination with helmholtz coils are used to counteract the horizontal

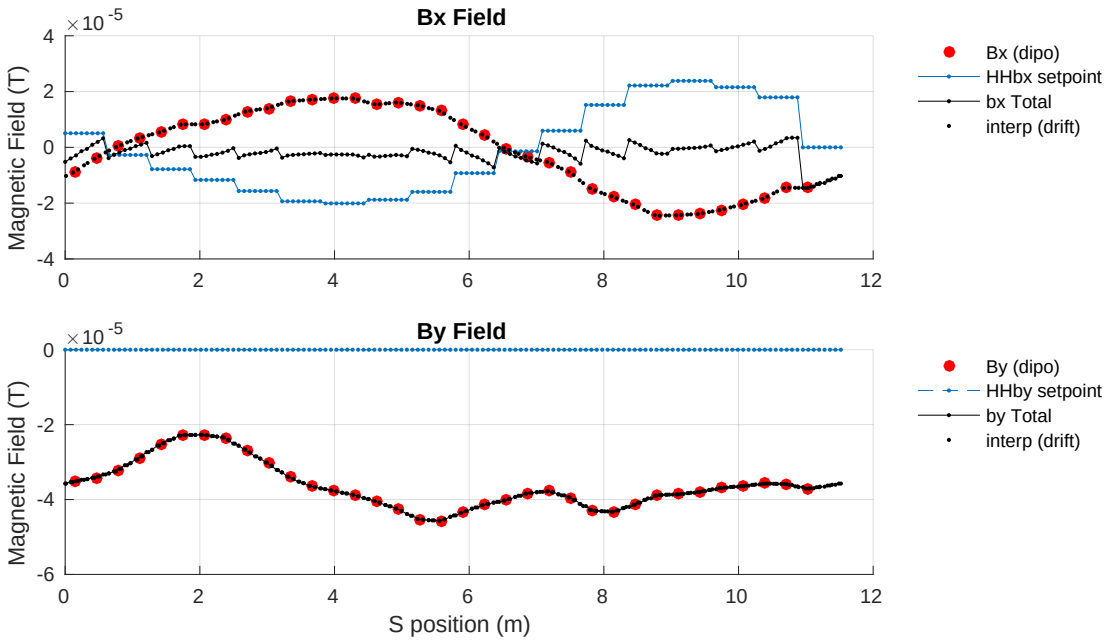

Figure 5.9: Red circles represent measurements of the earth's field at the dipole locations in UMER (Bx (dipo)). Black dashed line over the red circles shows an interpolation. Blue line represents the setpoints for the helmholtz coils that stretch across entire lattice cells in UMER (HHbx setpoint). The black line in the middle shows the sum of the total fields (bx Total). Note there are no helmholtz coils for the horizontal direction.

component of the earth's field. Figure 5.9 shows a simulation of the helmholtz coils canceling out the effect of the horizontal component of the earth's field in the vertical direction.

Representing the earth's field into a single particle code is a nontrivial problem. The field changes across the entire ring making it not immediately clear how such an effect can be included in a transfer matrix. Nonetheless, a method was thought of and implemented; it involves first calculating an interpolated earth field value across the entire lattice. A set of zero length corrector magnets are then added across drift sections throughout the lattice. Given a corrector, the interpolated field is integrated across a region $\pm\epsilon/2$ where ϵ ranges from $1-3$ cm. The kick angle through the zero length corrector is then determined by the integrated field strength

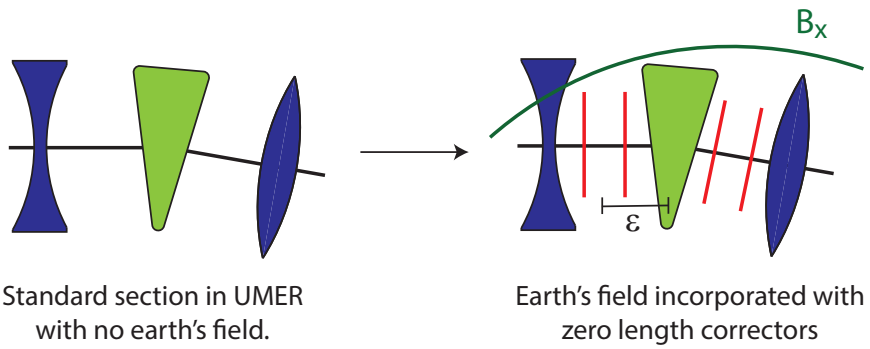

Figure 5.10: A set of zero length correctors (red) are added inbetween standard magnets to model the earth's field. Each corrector's strength is determined by the integrated strength of the earth's field between a region $\pm\epsilon/2$ around the corrector.

of the earth's field:

$$\theta_{x,y} = \frac{1}{B\rho}\int_{-\epsilon/2}^{\epsilon/2} B_{y,x}ds \tag{5.5}$$

where $B_{y,x}$ is the earth's field and $B\rho$ is the beam rigidity. Figure 5.10 shows a representation of the earth field correctors being added between a half cell in UMER. In implementing the earth's field this way, 144 zero length correctors are evenly distributed throughout the lattice and give the beam a kick proportional to the strength of the earth's field. The assumption in this technique is that the earth's field only provides a kick to the beam and that there are no focusing or higher order effects.

The earth's field makes calculating an equilibrium orbit a complex problem. An example being the implementation of dipole magnets. Global parameters such as the accelerator tune and closed orbit path are dependent on both the entrance and exit angles of a dipole as well as the strength of the dipole. Consider a single dipole in UMER, represented in Figure 5.11. In reality this dipole is powered to bend 7 degrees as the earth's field bends the remaining 3 degrees inside the 10 degree pipe

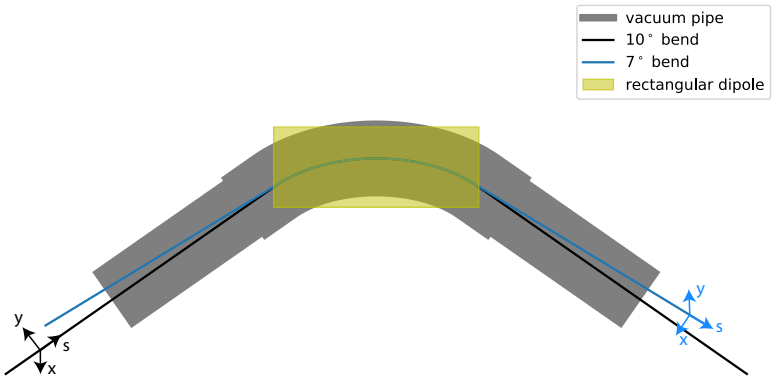

Figure 5.11: Closed orbit path through a typical dipole in UMER. The orbit for a 7 degree and 10 degree bend is plotted.

bend. If a 10 degree bending dipole is used in simulation it would have incorrect entrance and exit angles leading to inaccurate beam focusing terms and resulting in a bad model. Adding in the 3 degree bend in the earth's field will also result in 13 degrees of bending, also wrong. The alternative is to then use a 7 degree dipole bend. In this case the entrance and exit angles would be correct leading to accurate simulations of the focusing terms. The issue then becomes that the coordinate system is defined based on a 7 degree bend. Adding in the earth's field and the resulting 3 degree extra bend will cause the beam to travel off the 7 degree defined coordinate system. The simulations will show the beam several millimeters off the central 7 degree orbit, making simulation based steering result in wrong values.

In the single particle code a 7 degree dipole is implemented along with zero length correctors to represent the earth's field. Such a setup results in correct tune calculations. This is important as model to experiment based optimizations rely on tune values. No model based steering optimization is done as the 7 degree defined closed orbit will give inaccurate results in simulation. This is only a problem in the single particle code. The PIC code model of UMER has enough flexibility to

implement dipoles and the earth's field in a more realistic fashion.

5.2.2 PIC model

The particle-in-cell (PIC) code used for simulations is called Warp, a Fortran based particle and plasma accelerator code with a python front-end interface [4]. Simulations use a 2D slice model to advance particles through finite longitudinal steps. For hard edge magnets Warp uses a linear model and advances particles according to their transverse position. At each longitudinal position step Warp solves for space charge fields, and in concert, uses the magnet fields to advance particles. The space charge solver is self consistent. Warp can calculate particle phase space parameters at each infinitesimal position and accounts for the continously varying space charge forces in a self consistent manner where a single particle code would not be able to model space charge this way. In general, Warp's usefulness is its ability to properly implement higher order effects like space charge; however, it ends up being more computationally expensive.

In including the earth's field in Warp, a similar scheme of zero length corrector magnets are used. The difference being these can be placed anywhere in the lattice, including overlapping other magnets. As a result, the interpolated earth's field is placed uniformally around the entire ring. In Warp the earth's field is added at 1000 locations around the ring compared to only 144 locations in the single particle code. Similarly, the large helmholtz coils are added to the lattice as long vertical dipoles stretching across entire cells. Figure 5.12 shows a simulation of the vertical

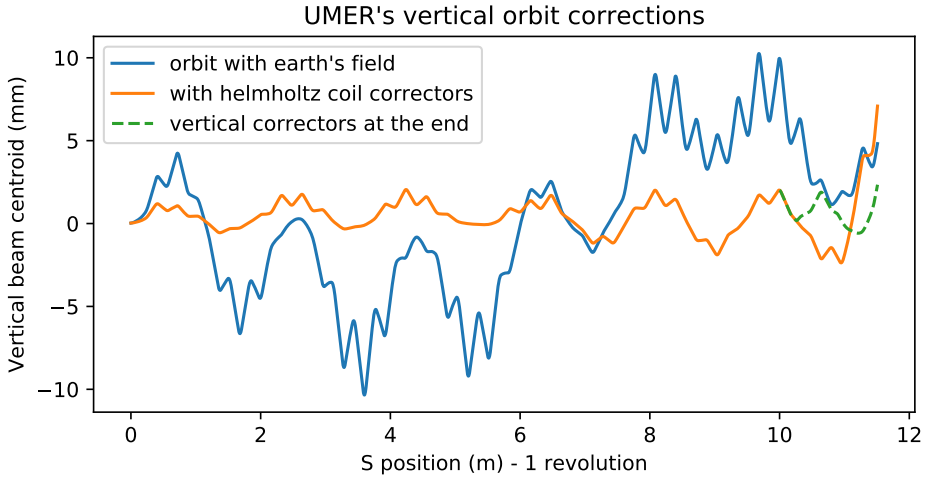

Figure 5.12: The vertical closed orbit path for UMER. The orbit is plotted with the earth's field present. Vertical helmholtz coil correctors are then turned on to correct the orbit. Two vertical corrector magnets are also used at the end of the ring to adjust for the final section in UMER which is without a helmholtz coil. Calculated using Warp.

orbit in UMER. The orbit distortion due to the earth's field is corrected with the helmholtz coils. Due to the fact that there is no helmholtz coil over the transfer section in UMER, the orbit jumps over the last section of the ring. The vertical correctors in that section are used to correct for the absense of the helmholtz coil. The simulation in Figure 5.12 is done without any space charge.

Figure 5.13 shows the horizontal orbit in UMER. There are two cases plotted based on Figure 5.11. In one case the closed orbit is defined based off the strength of the dipole magnets. Since the dipoles are powered to a lower level because of the inclusion of the earth's field, orbits are viewed as being far off the coordinate center. In the second case the coordinate system is centered around the 10 degree pipe bends. The dipoles are still powered at a lower level and the earth's field included, but orbits are now centered properly around the coordinate center. Each case is a

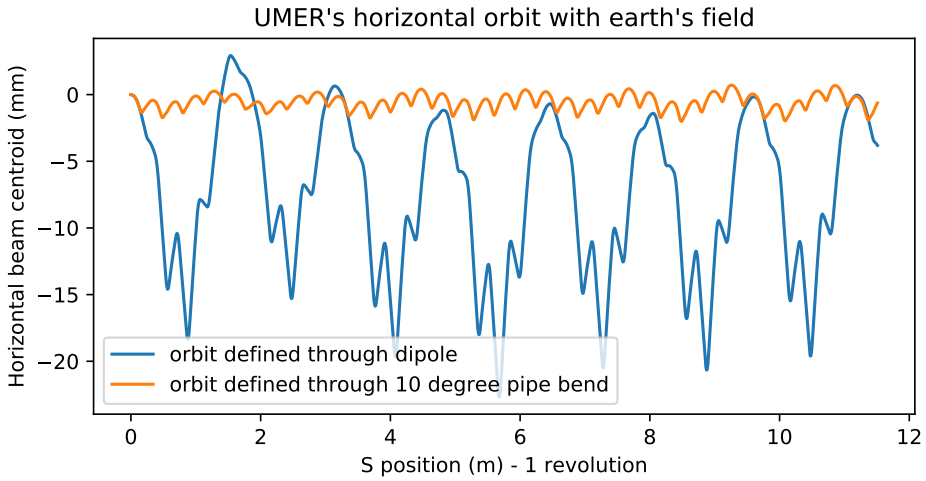

Figure 5.13: The vertical closed orbit path for UMER. The orbit is plotted with the earth's field present. Vertical helmholtz coil correctors are then turned on to correct the orbit. Two vertical corrector magnets are also used at the end of the ring to adjust for the final section in UMER which is without a helmholtz coil.

different type of model that can be used for simulations. If accurate simulations are required for orbit steering, the second case is used. For simulations based off tune measurements, beta functions, and anything not dependent on absolute tranverse positions, both model cases can be used.

5.2.3 Measurements in simulations

Accelerator parameter measurements are done in a similar way for both the single particle and PIC simulations. The technique involves using the general form of the one turn tranfer map:

$$\boldsymbol{M} = \begin{pmatrix} \cos\phi + \alpha\sin\phi & \beta\sin\phi \\ -\gamma\sin\phi & \cos\phi - \alpha\sin\phi \end{pmatrix} \tag{5.6}$$

where β is the betatron amplitude and ϕ is the betatron phase, discussed in section 2.2.2 and 2.2.3. α is relate to β as $\alpha = -\dot{\beta}/2$ and γ is related as $\gamma = (1+\alpha^2)/\beta$. α, β, and γ are referred to as the Courant-Snyder parameters (also called twiss parameters). In simulation the map $\boldsymbol{M}$ can be calculated numerically by using two test particles:

$$\begin{pmatrix} x_{0,1f} \\ x'_{0,1f} \end{pmatrix} = \begin{pmatrix} m_{11} & m_{12} \\ m_{21} & m_{22} \end{pmatrix} \begin{pmatrix} x_{0,1i} \\ x'_{0,1i} \end{pmatrix} \tag{5.7}$$

Tracking the two particles' initial and final conditions results in four equations with four unknowns. The four unknowns are each an entry in the transfer matrix $\boldsymbol{M}$. Calculated equations can be found in Eq. D.3. Note the matrix $\boldsymbol{M}$ is only valid over a periodic region, e.g. over one full turn or one periodic cell.

Given the values in the general transfer matrix $\boldsymbol{M}$, the Courant-Snyder parameters can be solved for:

$$\begin{aligned} \cos\phi = \frac{1}{2}\mathrm{Tr}(M) &= \frac{1}{2}(m_{11}+m_{22}) \\ \alpha &= \frac{1}{2\sin\phi}(m_{11}-m_{22}) \\ \beta &= \frac{m_{12}}{\sin\phi} \\ \gamma &= \frac{-m_{21}}{\sin\phi} \end{aligned} \tag{5.8}$$

These parameters can then be calculated at each element location through the use of the magnet transfer map in Eq. 5.9. Here the matrix elements $M_{11}, M_{12}, M_{21}, M_{22}$ represent standard magnet transfer maps from Eq. 5.3.

The Courant-Snyder parameters are used to build and adjust accelerator mod-

els. The goal being to match these parameters between the model and experimental machine. Important terms like the phase advance and betatron tunes can be calculated using these parameters. Note that the equations discussed in this section refer to the beam centroid where space charge effects are small.

$$\begin{pmatrix} \beta_2 \\ \alpha_2 \\ \gamma_2 \end{pmatrix} = \begin{pmatrix} M_{11}^2 & -2M_{11}M_{12} & M_{12}^2 \\ -M_{11}M_{21} & M_{11}M_{22} + M_{12}M_{21} & -M_{12}M_{22} \\ M_{21}^2 & -2M_{21}M_{22} & M_{22}^2 \end{pmatrix} \begin{pmatrix} \beta_1 \\ \alpha_1 \\ \gamma_1 \end{pmatrix} \tag{5.9}$$

5.3 Matching of Model and Experimental Results

One of the goals in accelerator physics is to have a tuned model that is able to accurately simulate the same physics going on in the accelerator. This is done by measuring a set of parameters on the machine and try to match to the same parameters in the simulation. In order to match the two sets of parameters in the simulation and experiment, a range of correction terms are created and tuned for the individual magnets in the accelerator. These correction terms could be applied to magnet strengths, magnet lengths, magnet offsets, etc.

The standard technique in model and experiment optimization is the use of the orbit response matrix, sometimes called LOCO, Linear Optics From Closed Orbits [8]. The technique is performed by perturbing each magnet in the accelerator and measuring the change in the beam's closed orbit at different BPM locations. The results are placed in a large matrix where an inverse of the matrix gives the correction

terms needed to match the simulation to the experiment. This method is difficult to do in UMER for a number of reasons. Including things like the helmholtz coils, which overlap several magnets, and the varying earth's magnetic field can cause problems within LOCO. Another issue is the fact that UMER's beams have space charge. LOCO assumes a emittance dominated, highly relativistc beam; it is not clear how the technique would work with space charge dominated beams and their nonlinear behavior.

At UMER a set of routines were developed for model and experiment matching. The main routine being the tune fitting optimization technique. This section discusses the technique and shows its effectiveness in UMER. At the end of the section final magnet fit parameters values are summarized and discussed.

5.3.1 Tune fitting

Tune fitting is similar to the orbit response matrix technique, i.e. a magnet is perturbed and a response is measured and optimized between model and experiment. The difference comes in what is measured after the perturbation. In LOCO the change in the closed orbit is measured while in UMER the change in the tune is measured. It is easier and more accurate in UMER's case to model and measure a change in tune than a change in the closed orbit. The method assumes that UMER's accelerator lattice can be modeled as a simple FODO lattice. A periodic FODO cell can be set equivalent to the generalized transfer matrix from Eq. 5.6. Using equations for the phase advance from Eq. 5.8, expressions can be derived for

the tune within a FODO cell. Appendix D.5 goes further into detail on deriving the relevant equations. More information can also be found here [9].

The tune fitting equations are approximated to:

$$Q_x = C_0 + C_x k_x - C_y k_y + k_x k_y C_{xy} = f(k_x, k_y) \tag{5.10a}$$

$$Q_y = C_0 - C_x k_x + C_y k_y + k_x k_y C_{xy} = f(k_x, k_y) \tag{5.10b}$$

where k_x, k_y are the quadrupole magnet strengths in the FODO lattice. Constants C_0, C_x, C_y are dependent on quadrupole and FODO cell lengths. The equations show an explicit relationship between the quadrupole strengths and the transverse tune in the accelerator. By varying the magnet strengths by Δk, tune space can be measured and mapped over a range of values. See equation Eq. 5.11a.

$$(Q_x)_{ij} = f(k_x + i\Delta k, k_y + j\Delta k) \tag{5.11a}$$

$$(Q_y)_{ij} = f(k_x + i\Delta k, k_y + j\Delta k) \tag{5.11b}$$

$$i, j = 1, 2, ..., M, 1, 2, ..., N$$

As a result a set of grid like scans can be done, shown in Figure 5.14. This is done experimentally and in simulation using a model of the ring. The distance between the tunes is calculated for a given value of k_x, k_y:

$$d_{ij} = \sqrt{(Q_{x,\text{exp}} - Q_{x,\text{sim}})^2 + (Q_{y,\text{exp}} - Q_{y,\text{sim}})^2} \tag{5.12}$$

The tunes are found using the same NAFF algorithm in both simulation and experiment in order to maintain consistency. Depending on which beam currents are in use, a different range of turns are used for the tune calculations. The diferent beam currents mean different amounts of space charge. More space charge in UMER's case results in faster longitudinal expansion of the beam, and without the RF system on, the beam bunch fills the ring faster such that there are less turns available. Less space charge corresponds to a longer surviving beam which allows for more data to be collected. Typically a range of 32 or 64 turns of BPM data are taken for tune measurements.

Next a Nelder-Mead optimization algorithm is used to minimize the distance between tunes for each grid point, d_{ij}, using the following objective function:

$$\text{obj} = \min: \sum_{ij} d_{ij} \tag{5.13}$$

based on fit parameters for the quadrupole strengths k_x, k_y as well as other magnets. In order to speed up the optimization, about a dozen grid points that are evenly

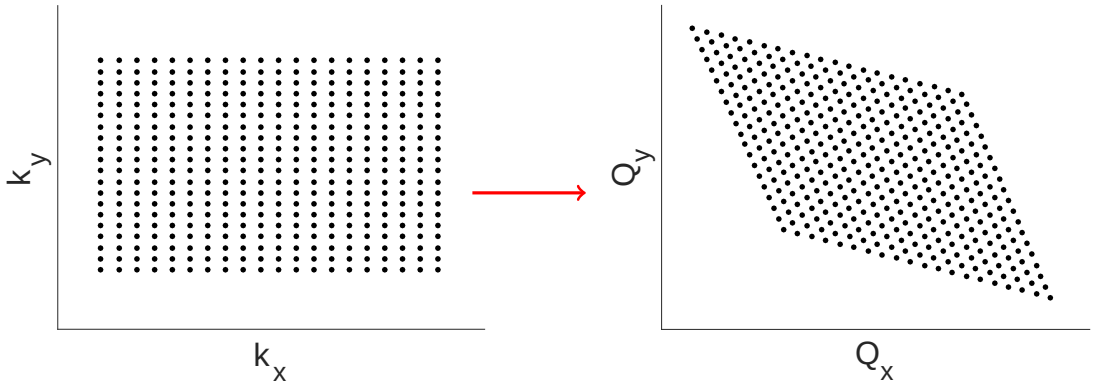

Figure 5.14: A schematic of a gridded tune scan. Focusing strengths, k_x, k_y, are varied creating a response in the beam's tune, Q_x, Q_y.

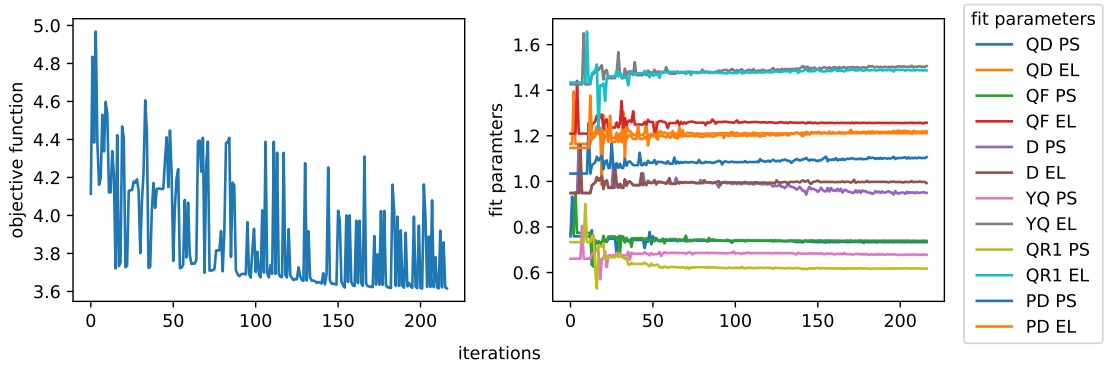

Figure 5.15: A tune fitting optimization run. (left) The objective function plotted as a function of iteration number. (right) All 12 magnet fit parameters plotted as a function of iteration number. Note 'EL' stands for effective length and 'PS' stands for peak strength.

spread out in tune space are picked to optimize on; this reduces the time it takes to run simulations for each grid point during each optimization iteration.

The fit parameters are the effective lengths and peak strengths for six families of magnets: horizontally focusing quadrupoles (QF), horizontally defocusing quadrupoles (QD), dipoles (D), injection focusing quadrupole (QR1), injection defocusing quadrupole (YQ), and injection dipole (PD). This results in 12 total fit parameters being optimized based on the objective function. Magnets like vertical correctors and helmholtz coils are not expected to impact tune measurements as there is no focusing involved so they are excluded from the fitting. Initial values are set based on the effective length analysis discussed in section 5.1.2 and realistic upper and lower bounds are set for the parameters. Separately, a constraint is placed on fit values such that the integrated strength, effective length times effective strength, is held to be constant based on gridded magnet field calculations from section 5.1.

Figure 5.15 shows an example run of the optimization. A set of initial parame-

ters are picked and simulations are done to find a set of values that match up to the experimental tune measurements. Parameter values are normalized such that the magnet physical lengths and measured peak strengths are equal to one. Note the sharp peaks in the objective function plot in Figure 5.15; these correspond to set-points where beam is lost and the objective function blows up. i.e. in a case where fit parameters lead to a lost beam the objective function sharply rises to dissuade the optimization from going further in that direction.

Note the tune fitting technique does not optimize simulation models for beam steering. The optimization has to have good betatron tune, betatron phase advance, and betatron amplitude measurements; these are needed in order to design new lattices for planned experiments. Steering the beam based off simulations requires optimization of steering magnets, helmholtz coils, and the earth's field which is a much more complicated problem to model and tune for. Steering is done online and live on the accelerator and will be discussed later in chapter 8.

5.3.2 Summary of model fit parameters

The results presented here are from running tune fitting measurements during early January 2020. This is mentioned because experimental setups can drift over time requiring retuning of parameters. A 0.6 mA beam running through the normal FODO cell lattice in UMER is used to generate numbers. Results are shown in Table 5.2. The length fit value is multiplied by the physical length value in order to calculate an effective length. A similar process is done to find the effective peak

Magnet family	length fit value	physical length (cm)	peak strength fit value	peak strength
QD	1.1625	4.65	0.7230	5.215 G/cm-A
QF	1.1568	4.65	0.7411	5.215 G/cm-A
D	0.9437	4.437	0.9132	1.059 G/A
YQ	1.4022	5.40	0.6521	1.059 G/cm-A
QR1	1.4241	5.40	0.7092	1.037 G/cm-A
PD	1.1407	4.40	0.9982	0.394 G/A

Table 5.2: Values for magnet fit parameters after running tune fitting technique.

strength. As an example, a length fit value of 1.2 means the effective length is 20% longer than the physical length for a magnet.

Different combinations of fit values were tested and simulated until finding the best results using the six families of magnets. Table 5.2 has the fit values generated. The justification here is that all regular ring quadrupoles (QF,QD) are built using the same design and should have a similar fit value. The reason for splitting the ring quadrupoles into families of focusing (QF) and defocusing (QD) is to account for space charge and other nonlinear behavior in the fitting. Similarly, all the dipoles (D) are built with an identical design and are represented by a single fit value. The transfer section magnets (YQ,QR1, and PD) are each a set of unique magnets used for injection and have their own respective fit values.

5.4 Chapter Summary

This chapter discusses in detail the effort put into designing and creating realistic simulation models for the UMER accelerator. The chapter starts by explaining

the short printed circuit magnet models used in UMER. These magnets generate unique fields that need to be benchmarked against different types of magnet models in simulations. A gridded field model is compared to a hard edge model and verified to give similar results, justifying the use of a hard edge model for simulations. Using a hard edge model, simulations are built of the UMER accelerator in a single particle tracking code and a PIC code. Lastly, these simulations are used with experimental measurements to optimize and tune the models in order to generate behavior similar to the experiment. Further details are discussed in Appendix D.

Chapter 5: Bibliography

[1] W. W. Zhang, S. Bernal, H. Li, T. Godlove, R. A. Kishek, P. G. O'Shea, M. Reiser, V. Yun, and M. Venturini. Design and field measurements of printed-circuit quadrupoles and dipoles. *Phys. Rev. ST Accel. Beams*, 3:122401, 2000.

[2] Hui Li. Magli manual for windows and linux. unpublished notes, 2012.

[3] S. Bernal. Technical note: New approach to effective length and strength of umer quadrupoles. unpublished, 2006.

[4] Alex Friedman, Ronald Cohen, D.P. Grote, Steven Lund, William Sharp, Jean-Luc Vay, I. Haber, and Rami Kishek. Computational methods in the warp code framework for kinetic simulations of particle beams and plasmas. volume 42, pages 1–1, 06 2013.

[5] M. Borland. elegant: A Flexible SDDS-Compliant Code for Accelerator Simulation. In *6th International Computational Accelerator Physics Conference (ICAP 2000) Darmstadt, Germany, September 11-14, 2000*, 2000.

[6] Andrei Terebilo. Accelerator modeling with matlab accelerator toolbox. *PACS2001. Proceedings of the 2001 Particle Accelerator Conference (Cat. No.01CH37268)*, 4:3203–3205 vol.4, 2001.

[7] Ronald D Ruth. A canonical integration technique. *IEEE Trans. Nucl. Sci.*, 30(CERN-LEP-TH-83-14):2669–2671. 3 p, Mar 1983.

[8] J. Safranek. Experimental determination of storage ring optics using orbit response measurements. *Nucl. Instrum. Meth.*, A388:27–36, 1997.

[9] Santiago Bernal. *A Practical Introduction to Beam Physics and Particle Accelerators*. Morgan & Claypool Publishers, 2018.

Chapter 6: Tunes and Resonances with Space Charge

As new accelerators aim for higher space charge intensities, the impacts of Coulomb interactions on resonance structure dynamics needs to be better understood [1]. Many researchers have created different theories and simulations of potential behavior, but not much work has been done in the way of experimental verification on an accelerator system [2, 3, 4, 5, 6]. Specifically, on the topics of structural resonance stop band shifting and suppression because of the space charge forces within the beam. Expanding the understanding of these topics will help researchers better deal with resonance-based beam loss at the space-charge dominated regime. Especially so with future accelerators whose designs are pushing the boundaries for high intensity machines.

Space charge and resonance studies at UMER has been on going since the accelerator's original inception two decades ago [7, 8]. This chapter discusses the most recent work on the topic from the last few years. Section 7.1 covers experimental measurement of transverse tunes with space charge. Techniques of measuring tune vs time are discussed. Section 7.2 examines methods of determining and measuring resonances. Lastly, section 7.3 investigates the direct effects that space charge has on the transverse resonances within UMER.

Common name	Measured current (mA)	Perveance, K_{sc}
micro beam	0.10	1.5×10^{-6}
0.6 mA beam	0.6	9.0×10^{-6}
6 mA beam	5.6	8.4×10^{-5}
12.7 mA beam	12.7	3.5×10^{-4}

Table 6.1: A list of the beam currents used in this chapter. The different beams are referred to by their common name. The measured current is the actual current of that beam measured using the WCM in UMER. The perveance is a measure of space charge mentioned in Eq. 2.45.

6.1 Experimental Tune Measurements

Section 4.1 covered the various tune measurement algorithms used within the accelerator field and compared their theoretical accuracies. In this section the discussion continues using experimental data and measurements. Tunes are measured in UMER for beams with space charge values based on 0.1, 0.6, 6, and 12.7 mA current levels. Each of these beams behave differently, and as a result, have different experimental tune measurement accuracies that will be studied. Table 6.1 summarizes the different beams. Separately, measurement techniques for looking at tune vs time are also discussed.

6.1.1 Tune Measurements with space charge

Using the 14 BPMs in UMER, transverse position data is collected for each of the four different beams mentioned in Table 6.1. The magnet settings in the ring section of the accelerator are kept the same throughout the measurements. Instead the injection into the ring is adjusted for each beam such that the beam injects off

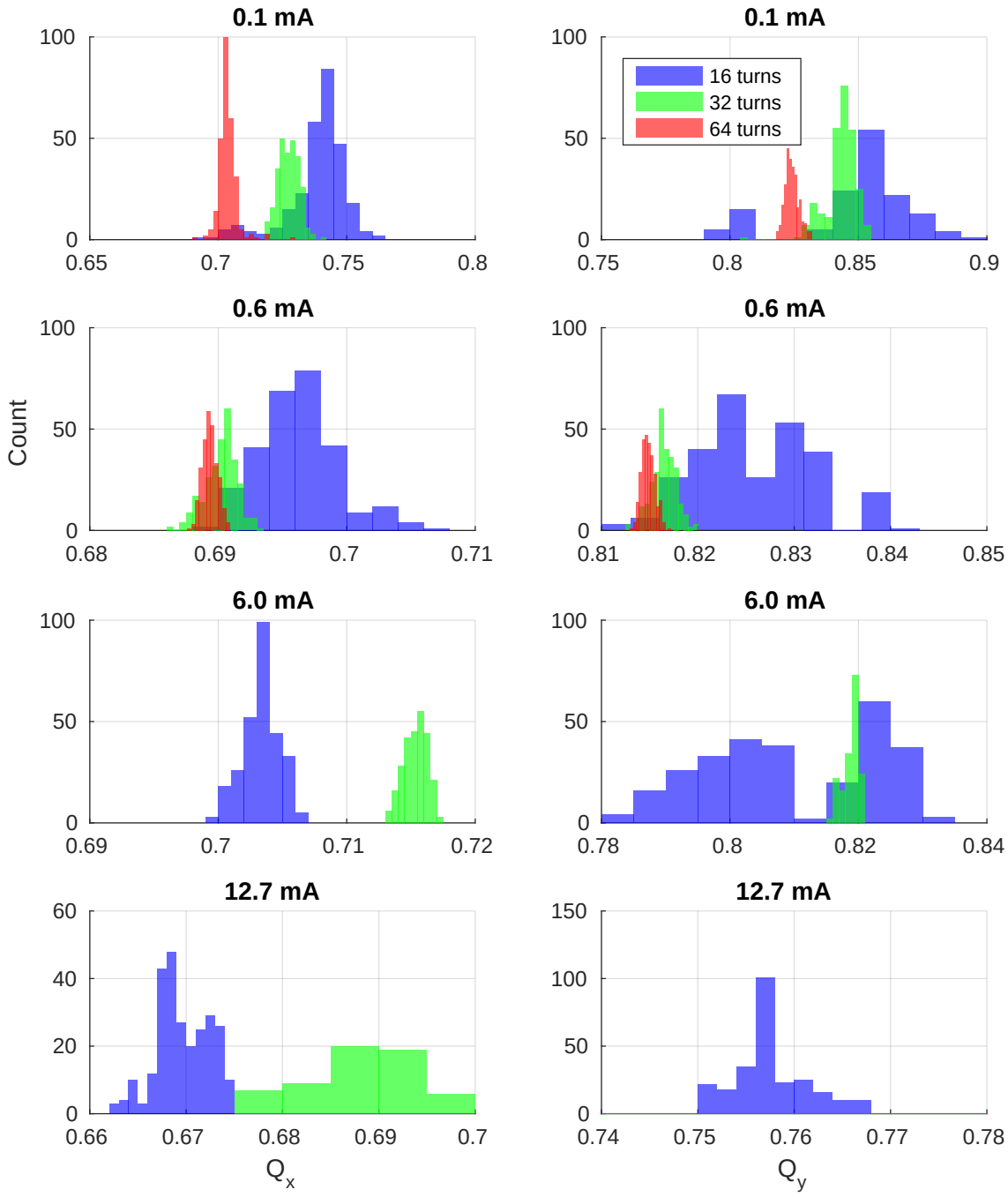

Figure 6.1: Horizontal and vertical fractional tune measurements for beams with 4 different current values. Tunes are measured using 16, 32, and 64 turns of data.

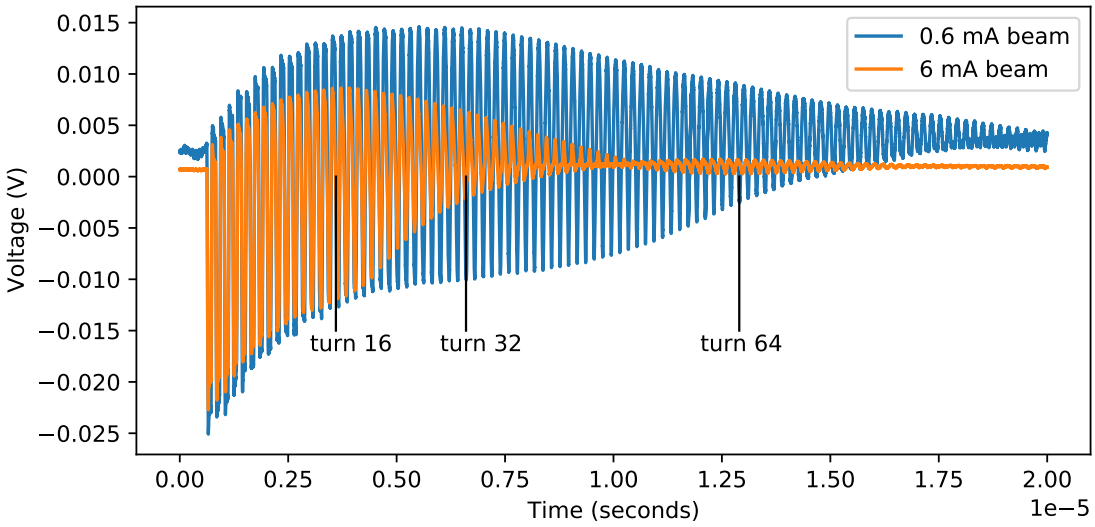

Figure 6.2: The voltage vs time for the 0.6 and 6 mA beams are plotted. The voltage values for the 6 mA beam are reduced by 10x in order to have similar scales for both curves. The locations for the 16th, 32nd, and 64th turns are marked.

the closed orbit and induces betatron oscillations that can be measured with the BPMs. 20 repeat measurements are performed using 14 BPMs totaling around 280 tune measurements. The measurements are summarized in Figure 6.1 with a set of histogram plots.

Figure 6.1 conveys a substantial amount of information that needs to be discussed. Looking at the measurements, for the 0.1 mA and 0.6 mA beams a 64 turn tune measurement is performed whereas it is not for the 6.0 and 12.7 mA beams. This is because at the higher current levels the space charge force causes the beam's longitudinal expansion to occur too fast to allow for viable data past about turn 30 for the 6 mA and turn 16 for the 12.7 mA beam. Figure 6.2 shows the beam current measurements as a function of time for the 0.6 and 6 mA beams. In the plot the beam current for the 6 mA beam rapidly starts to decrease starting around turn 20 to the point where it 'flips' polarity around turn 40. In reality, the beam, acting like

a fluid, is expanding longitudinally until it uniformly fills the ring circumference, making the current measurement from the wall current monitor diagnostic appear to be zero. The appearance of the polarity flip in current around turn 40 is the result of the beam bunch core moving to the opposite side of the ring, or 180 degrees out of phase with the wall current monitor diagnostic. More on this longitudinal space charge expansion phenominon is briefly discussed in section 4.3.2.

Besides limiting the amount of viable data for tune measurements, the longitudinal expansion of the beam presents another problem. Section 2.4.3 shows that the beam's tune is dependent on the space charge. If the beam is expanding longitudinally from the moment it is injected into the ring, it means the space charge force is also changing causing the tune value to change with it. This is evident in the data from Figure 6.1, especially for the 0.1 and 0.6 mA beams where measurements are able to be done up to 64 turns. In the histograms the tune measurements are noticably different at 16, 32, and 64 turns because the longitudinal space charge force is different. The tune difference is also not the same across different beams as the more space charge a beam bunch has, the faster it will expand. Thus, it is important to understand that the tune measurements in this case are 'average' tune measurements across a given range of turns, accepting the fact that in reality the tune is changing throughout and can not be thought of as a constant in UMER.

There is work being done to incorporate a UMER specific RF system that will allow confinement of the beams. This should solve many of the problems discussed here. See section 3.1.5 for more information on this development. For the remainder of this chapter measurements will focus around the 0.6 and 6 mA beams as these

provide the most accurate experimental measurements. The noise to signal ratio for the small 0.1 mA beam is too large to provide useful and consistant measurements. For the 12.7 mA beam, the strong space charge force causes the beam to expand too fast, not allowing enough useful data to be collected for most measurements. Wherever measurements are feasible, results will be presented for the 0.1 mA and 12.7 mA beams, otherwise the discussion is centered around the 0.6 and 6 mA beams.

6.1.2 Tune measurements in time via sliding window

The longitudinal expansion of the beam causes the space charge force to change over each revolution around the accelerator. This results in the beam's transverse tunes also changing over each revolution, making the tunes a function of time. A sliding window FFT technique is developed and used to measure the tune change in time. The technique helps quantify the tune change occuring as a function of time and space charge within UMER.

The technique starts by measuring position data over many turns using a BPM. A window size is choosen such that it ranges over a fraction of the full BPM signal. The position data over this window length is transformed via an FFT and used to measure the beam's tune. The window is then moved forward in position space to a new range of position data where another FFT is taken and the tune remeasured. The window continues to be moved across the full position data with FFT transforms taken at intermediate steps. Figure 6.3 demonstrates this technique.

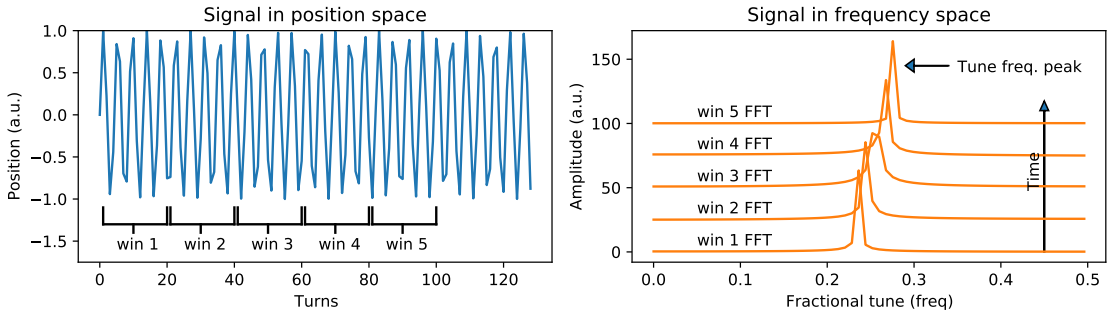

Figure 6.3: (left) A position signal is broken down to a set of different window lengths. (right) The position data across each window length is transformed via FFT and plotted in frequency space.

A BPM position data signal is plotted on the left with a few window lengths marked out. Over each window length the data is transformed via FFT and plotted on the right side in frequency space. Moving forward in position space is equivalent to moving upward in the frequency space plot.

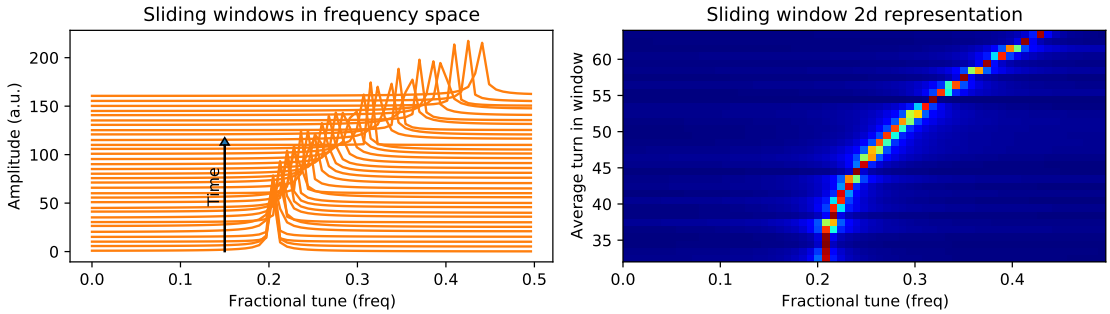

Figure 6.4: (left) The FFT transform plotted in frequency space for data in each sliding window range over many slides. (right) The same data plotted, but with color representing the amplitudes of each frequency line in the left plot. Red indicates large amplitude and blue indicates small amplitude. The vertical axis is the average turn number in the window range used to generate the data.

The problem with the graph on the right side of Figure 6.3 is that the vertical axis units do not mean anything quantitatively, all that is known by moving upward is moving forward in time. This problem is fixed by representing the data on a 2D

plot and using color to serve as the size of the frequency signal amplitudes. Figure 6.4 shows an example of this procedure. On the left side is a frequency space plot based on many sliding window steps. The right side plot takes the same data and makes a new plot with color intensity representing the size of the amplitudes in each frequency line on the left. The vertical axis represents the average position of the sliding window range used to generate that frequency data. For example, a vertical axis value of 45 turns means the window range was centered around the 45th turn of the position data when the frequency transform was done. In this way the vertical axis now is an accurate measure of 'time' with the horizontal axis representing frequency. The color represents the strength (amplitude) of different frequencies in the underlying position data signal.

The sliding window technique is used to measure the transverse fractional tunes for the 0.6 and 6 mA beams in UMER. Results are shown in Figure 6.5. For the 0.6 mA, there is no measurable shift in tune over the 32 turn time range. In the case of the 6 mA beam, there does appear to be a shift in tune, more so in the horizontal direction. The fractional horizontal tune in Figure 6.5 starts at ≈ 0.75 before shifting close to ≈ 0.8 at the end of the 20 turn time window. The vertical plane is less clear, but there is also a shift occuring.

6.1.3 Induced tune shifts using RF phase adjustments

Fast crossings of resonances is an active area of research in accelerator physics that focuses on shifting a beam's tune quickly across a resonance such that the

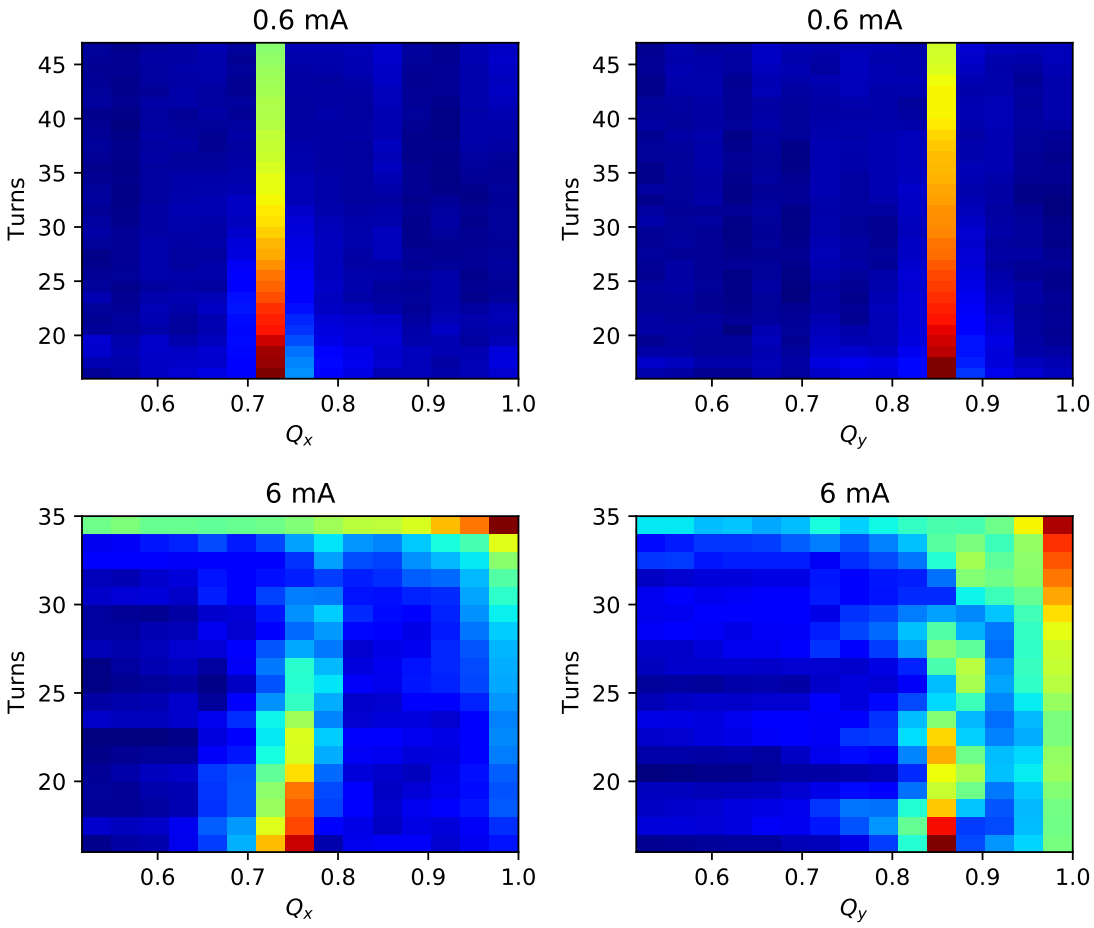

Figure 6.5: The transverse fractional tunes for the 0.6 mA and 6 mA beams are measured using the sliding window technique discussed above. The window was 32 turns wide and the step size was 1 turn. 20 steps are taken for 6.0 mA beam and 32 steps for the 0.6 mA beam.

instability from the resonance does not have enough time to grow and cause beam loss [9, 10]. An initial experiment was done to test the feasibility of such an idea in UMER using the RF system and the sliding window technique. This section discusses the experiment and results.

Using the 0.6 mA beam and the new RF system (see section 3.1.5), the beam is confined and configured to operate for roughly 1000 turns. Figure 6.6 shows BPM position data over several hundred turns with RF confinement turned on. Relying

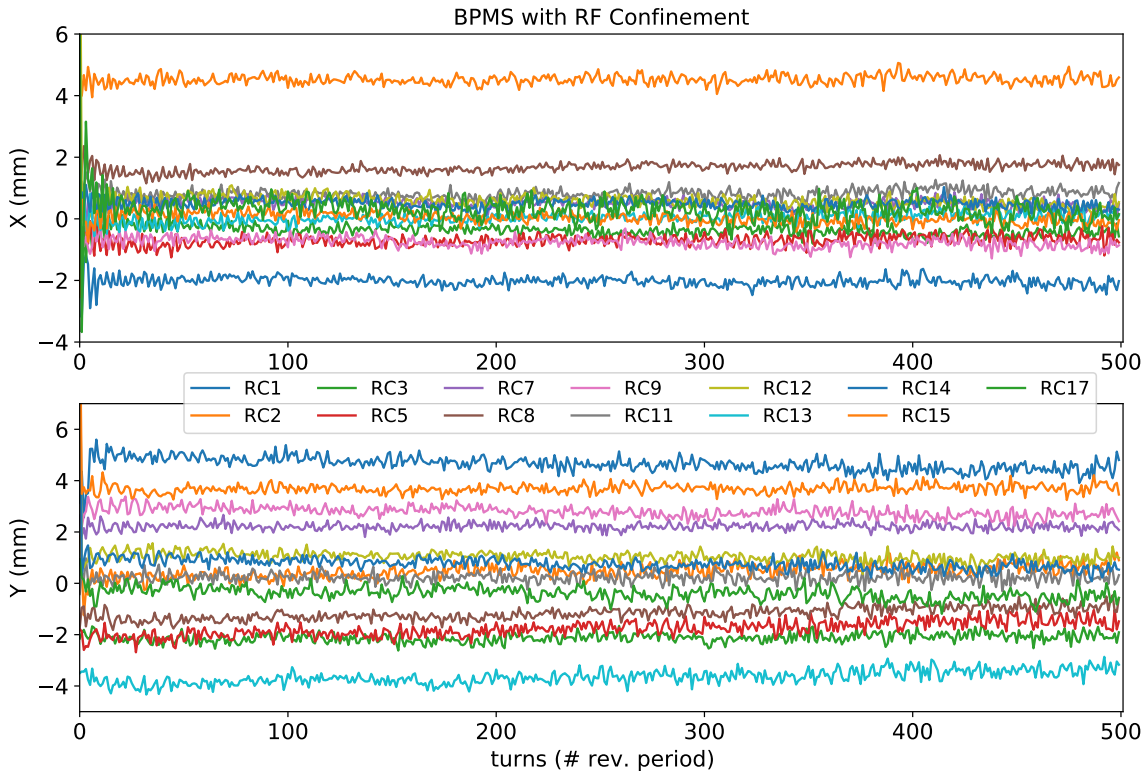

Figure 6.6: Transverse position data measurements are plotted from the BPMs over 500 revolutions for the 0.6 mA beam. Each line represents data from a different BPM.

on the first 32 turns of betatron oscillations at injection for tune measurements is no longer reasonable with an RF system that allows several hundreds of turns. The initial oscillations at injection damp down too quickly to be useful when measuring tunes with 64, 128, or higher amounts of turns. To deal with this issue an electrostatic fast kicker is used to excite periodic oscillatory motion in the beam so that the tune can be measured using many more than 32 turns, allowing for a more accurate measurement. For the electrostatic kick, a BPM is repurposed to apply a high voltage field across its four plates to 'excite' the beam. BPM data with the kick is shown in Figure 6.7. In this case the beam is rekicked every few dozen turns to re-excite betatron oscillations, otherwise the linear restoring force in the magnets

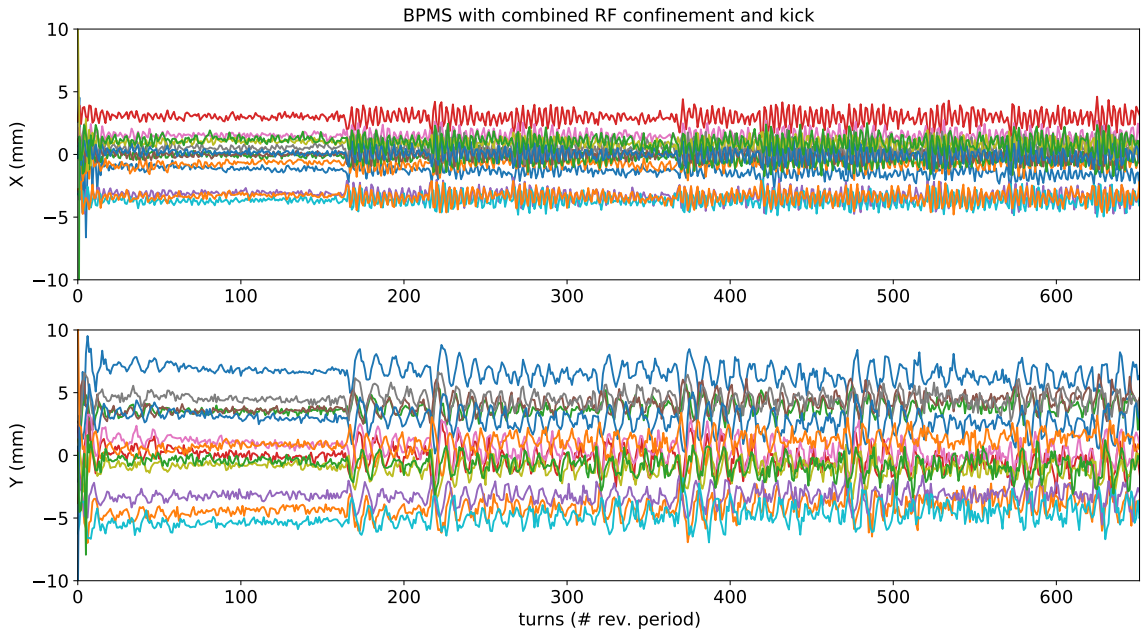

Figure 6.7: Transverse position data measurements are plotted from the BPMs over 600 revolutions for the 0.6 mA beam. Each line represents data from a different BPM. The beam is excited with an electrostatic kick at around 150 turns in and continues to be kicked roughly every 50 turns.

cause the beam to damp back down to the closed orbit.

With the RF system allowing for many more turns of data to be generated, a sliding window tune measurement is performed for the 0.6 mA beam. Results are shown in Figure 6.8. Figure 6.8 has a much higher resolution than Figure 6.5, since the RF allows for a larger window size and slide step. Next the fast tune shift is applied using the RF system. At a particular point in time the RF phase is immediately changed by a few degrees within a single revolution around the accelerator. The phase change causes the beam to either accelerate or decelerate, changing its momentum and energy. The change in momentum causes a direct change in the beam's tune; this energy dependence on tune is shown explicitly in chapter 2 (see Eq. 2.9 for example), but can also be deduced qualitatively. For

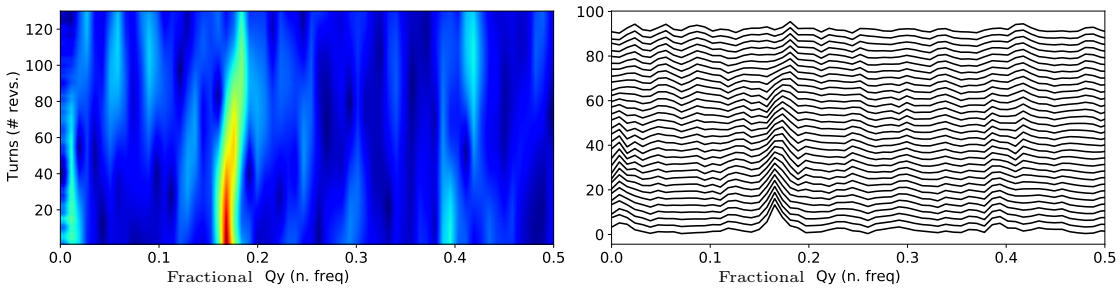

Figure 6.8: The vertical transverse tune is measured over 120 time steps using a window size of 128 turns. The frequency spectrum is shown on the right. This is a measured using a single BPM.

example, if the beam's energy increases it will be able to slightly resist the focusing being applied on it by the quadrupole magnets, this in turn results in a lower tune value. Thus, a fast (within one revolution) change in the RF phase will cause the beam's tune to also quickly change. This quick change is then measured using the sliding window technique.

Results of an RF induced fast tune shift are shown in Figure 6.9. The RF phase is adjuted forward and backward by 9 degree steps to accelerate and decelerate the beam and cause a measurable tune shift. Figure 6.9 shows measurements for the vertical tune, similar results were seen for the horizontal tune. Data is collected across the different BPMs and plotted in a time series of fractional tune vs turns for each RF phase setting. The graph is in Figure 6.10. It shows that a ± 20 degree RF phase change in UMER will shift the fractional tunes by about 0.02 in both planes.

While the setup and measurement for the experiment were successful, the conclusion is that such a technique would not be useful for fast tune change across a resonance. The small tune shifts of 0.02 generated are not large enough to make it across a resonance stopband which can at times be greater than 0.1. Another

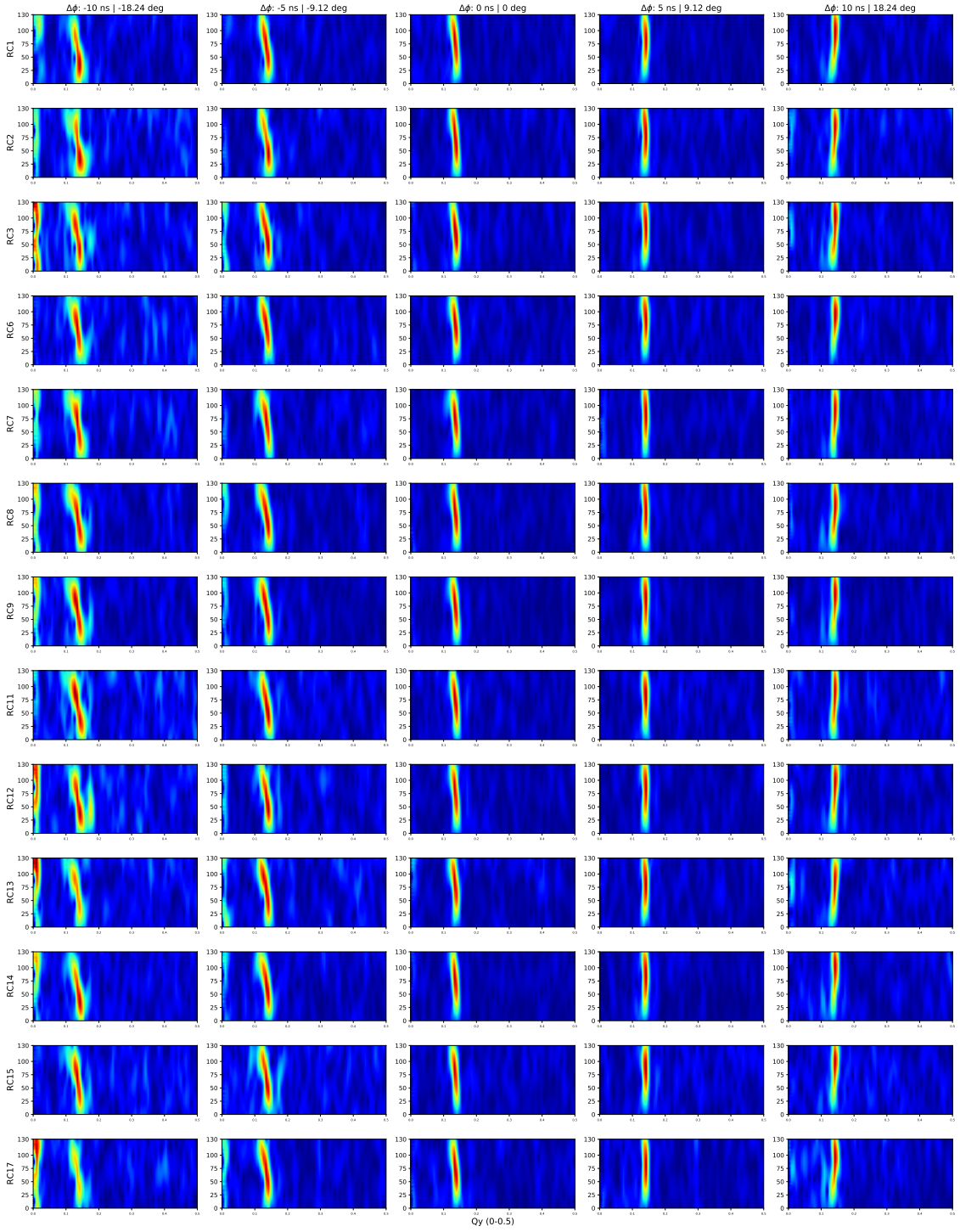

Figure 6.9: Each row represents measurements with a BPM, 14 rows means 14 BPMs were used. The middle column is a sliding window tune measurements with 0 RF phase change. Columns to the right change the RF phase by 5 and 10 ns. Columns to the left change the RF phase by -5 and -10 ns. These are results for the vertical tune, a similar graph is generated for the horizontal tune.

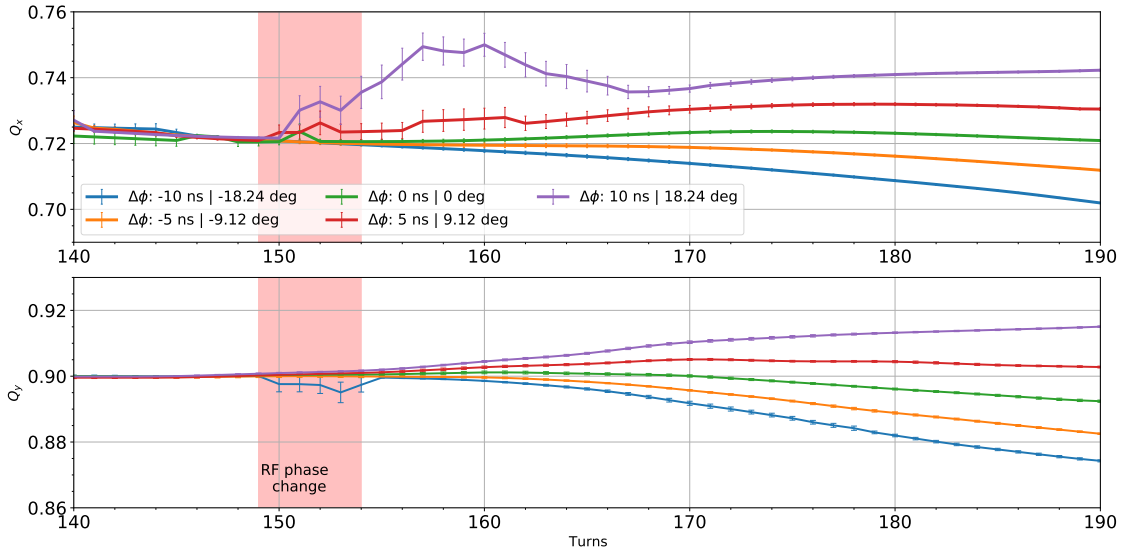

Figure 6.10: Both graphs show fractional horizontal and vertical tune measurements vs turns around the ring. At around turn 150 the RF phase is changed by increments ranging from -18.24 degrees to +18.24 degrees. At each increment the tunes are measured via sliding window technique.

possibility is using a fast pulsed quadrupole magnet to change the beam tune in a similar fashion to the RF phase change method. The fast quadrupole tune shift might allow for a big enough tune shift on the order of 0.1+. UMER has the ability to pulse a single quadrupole based on William Stem's thesis project, so the experiment is feasible [11]. It would be an interesting project for the future.

6.2 Measuring Resonances in UMER

Directly measuring the presence of transverse resonances in UMER is not easy to do experimentally. Destructive resonances are measured by looking at beam loss via the wall current monitor diagnostic, while stable resonances are detected by analyzing anomalous measurements of tune near any active stable resonance lines in tune space. This section discusses the experimental measurement techniques used

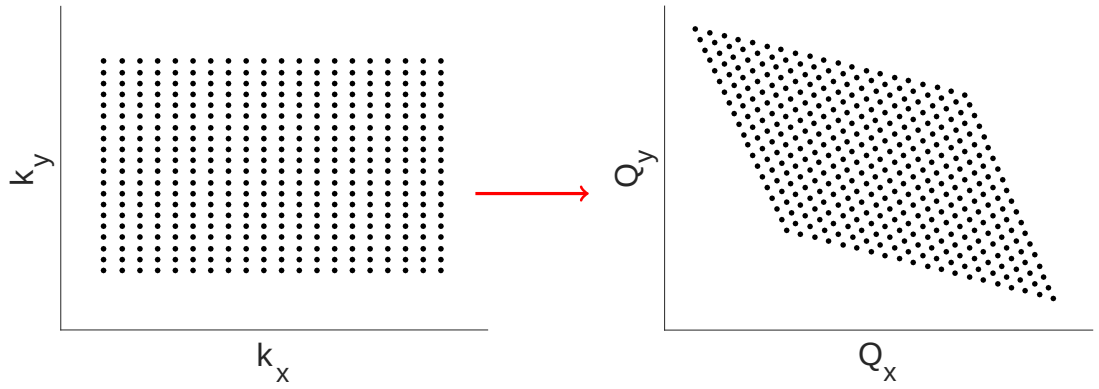

Figure 6.11: A schematic of a gridded tune scan. Focusing strengths, k_x, k_y, are varied creating a response in the beam's tune, Q_x, Q_y.

to find resonances. Techniques for both destructive and nondestructive resonances are considered.

6.2.1 NAFF based quadrupole tune scans

As discussed in section 5.3.1, assuming a simple hard edge model of a FODO lattice, a set of equations can be derived through matrix multiplication that relate the change in phase advance to the focusing and defocusing quadrupoles [6]. Eq. 6.1a, 6.1b and Figure 6.11 demonstrate the mapping:

$$(Q_x)_{ij} = f(k_x + i\Delta k, k_y + j\Delta k) \tag{6.1a}$$

$$(Q_y)_{ij} = f(k_x + i\Delta k, k_y + j\Delta k) \tag{6.1b}$$

$$i, j = 1, 2, ..., M, 1, 2, ..., N$$

where k_x, k_y are the magnet strengths of the quadrupoles, proportional to the magnet gradient. By varying the collective strengths of all the focusing and defocusing quadrupoles in UMER the tunes can be changed in a predictable way.

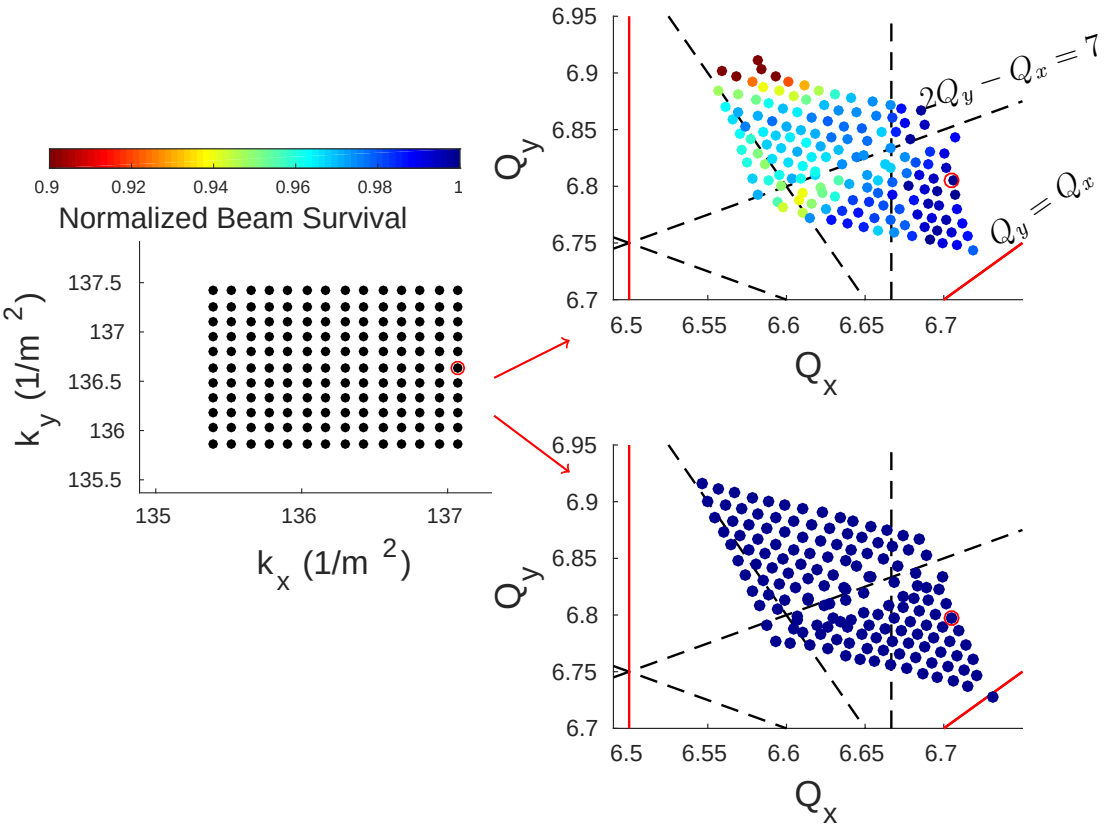

Figure 6.12: (top right) Experimental measurement. (bottom right) Simulated measurement. On the tune diagram, red lines are 2nd order and black lines are 3rd order resonances. The red circle indicates nominal operating point.

Since UMER is not exactly a FODO cell lattice, it is important to test Eq. 6.1a and 6.1b using simulations and experiments to see how well the FODO lattice assumptions hold true. The results of the test are shown in Figure 6.12. Here the focusing and defocusing quadrupole strengths are varied and the tunes are measured. This is done experimentally on the machine as well as simulated using a model of the accelerator. The bottom right plot in Figure 6.12 is the simulation measurements while the top right is the experimental measurements. Resonance lines up to second order are plotted for reference. Separately, at each point in the scan the beam loss is measured using the wall current monitor. The loss is highlighted in the

plots using color with red indicating large beam loss. Figure 6.12 shows that even though UMER is not exactly a FODO lattice, it mostly behaves like one, making the assumptions used for the equations valid in this case. One last thing to note is the mapping equations have no concept of resonances built in, they only map magnet strengths to tune values. In the actual measurements within Figure 6.12 the model equations break down near resonances as the beam motion becomes unstable and highly unpredictable.

Aside from scanning a grid of points like that in Figure 6.12, long horizontal or vertical line scans can also be performed. A line scan can provide much more detail in the measurements while taking the same amount of time to collect data. This is important because large grid scans take a significant amount of machine time to measure, 1-2 days on average. An experimental example of a line scan is shown in Figure 6.13. The discontinuities in the line indicates the presence of resonances. The color, representing beam survival, shows which of these resonances are actually destructive to the beam.

With the high accuracy tune measurements using NAFF, the quadrupole scans provide a good way to look at fine scale resolution within tune space. The increase in resolution proves especially useful in detecting resonances and measuring their positions and sizes.

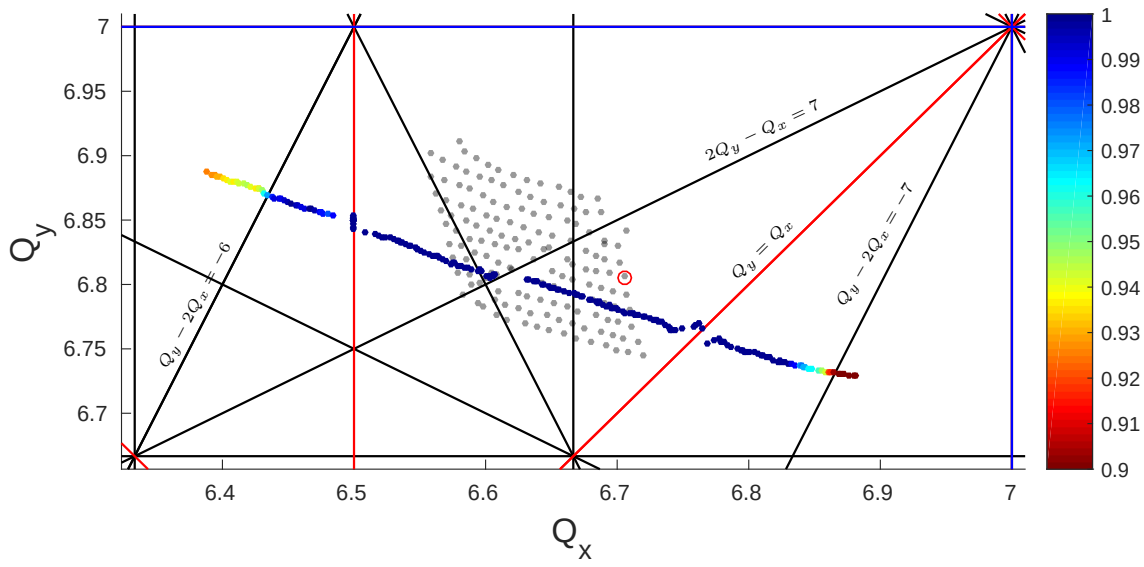

Figure 6.13: Long horizontal tune scan. Gray points are the same tune measurements from Figure 6.12. Color represents normalized beam survival.

6.2.2 Quadrupole tune scans and beam losses

While NAFF based quadrupole scans provide detail at a finer scale, beam loss based quadrupole scans help map out large sections of tune space over multiple integers. In this type of scan no tune is actually measured, instead only beam loss is measured and the tune value is estimated using equations 6.1a and 6.1b. An example plot is shown in Figure 6.14. In this scan the quadrupole currents are varied from 1.65 amps to 2.10 amps while measuring beam loss using the wall current monitor. Beam loss is measured as the normalized percent of beam that survived by the 10th turn. Color represents beam survival, red indicating large beam loss and blue indicating beam survival.

Figure 6.14 shows the stability over multiple integers in tune space. Large integer resonances are clearly defined and represent unstable operating regions. Only

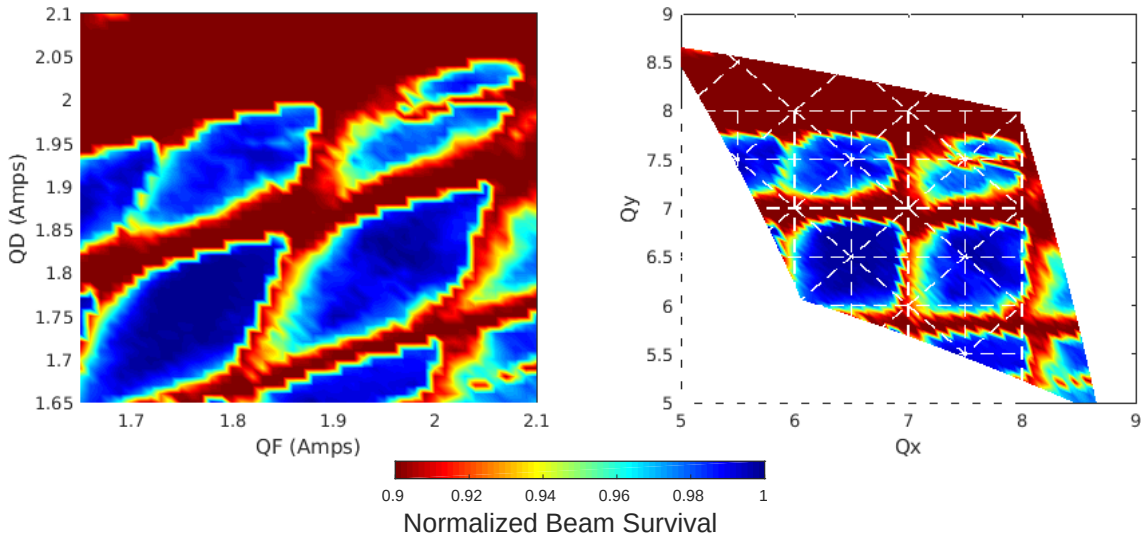

Figure 6.14: (left) Defocusing quadrupole strength vs focusing quadrupole strength with beam loss plotted as color at the 10th turn of the 6.0 mA beam. (right) Same data, but the quadrupole strengths are transformed to tune values using Eq. 6.1a and 6.1b.

resonances where beam is lost are visible, any stable resonance with no beam loss will not show up in such a scan. In UMER's case, the beam's tune during normal settings is $Q_x, Q_y = 6.70, 6.82$, between the 6.0 and 7.0 integer resonances. The scans shows that the machine could potentially operate in the 7.0 to 8.0 regions as well.

Both the beam-loss-based quadrupole scans and the high resolution NAFF scans provide the tools to look at resonances in UMER. A typical experimental procedure would have the beam-loss-based quadrupole scans map out a large region of tune space. Then a specific resonance would be further analyzed by performing a NAFF-based tune scan nearby. In this case the tools would allow for a measure of the resonance width and position, which is the focus of the next section.

6.3 Space Charge Impact on Resonances

Using the set of tools discussed above, the effect of space charge on transverse particle resonances is investigated. Experiment and simulation are used to attempt verification of theory that predicts the shifting of transverse resonances due to space charge forces. A second theory of resonance supression due to space charge forces is also tested.

6.3.1 Resonance theory with space charge

There are many theories on the topic of space charge effects on resonances with some ideas being developed as recently as 2019 [2, 3, 4, 5, 12]. In order to avoid reviewing the work of several different authors, a basic overview is given about the topic based on the work of a single author, Baartman. Baartman's theory on resonances with space charge is described in a paper from 1998; this section will briefly summarize the work from that paper [2].

Based off the Floquet transformation from section 2.2.3, the equation for a particle in a circular accelerator is written as:

$$\eta'' + Q^2\eta = 0 \tag{6.2}$$

where Q was defined as the tune and $\eta = x(s)/\beta^{1/2}$ with β being the betatron amplitude. η can be thought of as the normalized transverse position of the particle. A resonance is then just a driving term to this equation caused by some field

perturbation in the magnets:

$$\eta'' + Q^2\eta = F(\eta, \phi) \tag{6.3}$$

Assuming a linear space charge model, the space charge can be added as another force into Eq. 6.3:

$$\begin{aligned} \eta'' + Q^2\eta &= F_{sc} + F(\eta, \phi) \\ \eta'' + Q^2\eta &= \alpha(\eta - \bar{\eta}) + F(\eta, \phi) \end{aligned} \tag{6.4}$$

Note the space charge force is centered on the beam and not the reference orbit through the magnets.

For the case of an integer resonance $F(\phi)$ is independent of η. To find the behavior of the center of charge, the average of Eq. 6.4 is taken giving the result:

$$\bar{\eta}'' + Q^2\bar{\eta} = F(\phi) \tag{6.5}$$

Thus, the motion of the center of charge is unaffected by space charge forces. In this case the coherent motion of the beam will become unstable if the bare tune, Q, is equal to an integer value. Here the bare tune is ignoring the tune shift from image forces. Regardless of space charge, the integer resonance should not shift position or change in size.

The approach for the half-integer resonance case is different from the integer

resonance case. The single particle equations used previously must be tossed out in order to use a correct self-consistent approach to formulate the problem in terms of beam size. The detailed derivations are presented in Baartman's paper [2]; this section will just provide a summary of the results relevant for understanding the experimental work in the rest of the chapter [13].

Starting from the resonance equation in section 2.3.3:

$$mQ_x + nQ_y = p \tag{6.6}$$

and including space charge effects:

$$m(Q_x - \Delta Q_{xeff}) + n(Q_y - \Delta Q_{yeff}) = p \tag{6.7}$$

where ΔQ_{eff} is the expected incoherent tune shift due to space charge. Looking at the one dimensional case, the tunes are assumed to be equal in both transverse planes such that the resonance equation can be written as:

$$m(Q - \Delta Q_{eff}) = p \tag{6.8}$$

where $Q = Q_x = Q_y$. The coherent mode coefficient C is introduced next as:

$$\begin{aligned} \Delta Q_{eff} &= C\Delta Q \\ \Delta Q &= Q - Q_0 \end{aligned} \tag{6.9}$$

where ΔQ is the incoherent tune shift and Q_0 is the bare tune. C represents the envelope mode instabilities that occur at different resonances, discussed in section 2.4.2. The resonance equation is finally rewritten as:

$$m(Q - C\Delta Q) = p \tag{6.10}$$

For integer resonances $m = 1$ and $C = 0$ confirming the same conclusion reached earlier in the section, that space charge has no effect on integer resonances. For half-integer resonances $m = 2$ and $C = 1/2, 3/4$ corresponding to the symmetric and antisymmetric envelope modes discussed in section 2.4.2. The resonance equations then become:

$$Q - \frac{1}{2}\Delta Q = \frac{p}{2} \ , \ C = \frac{1}{2} \tag{6.11a}$$

$$Q - \frac{3}{4}\Delta Q = \frac{p}{2} \ , \ C = \frac{3}{4} \tag{6.11b}$$

Eq. 6.11a and 6.11b thus predict a shifting of the half integer resonances in the presence of space charge forces. In deriving these equations there is an assumption of an isotropic beam, meaning equal beam emittances, magnet focusing, and tunes. The beam is also assumed to have a K-V equivalent distribution.

To summarize, the theory predicts that in the presence of space charge the integer resonances should be uneffected. There should be no shifting of stopband growth for integer resonances. In the case of half-integer resonances, the equations predict a shifting of the resonance bands. The exact amount of shifting depends

on parameters such as the beam emittance, beam current, and beam tune value – specifically the values for p in Eq. 6.10, which represents the harmonics of the magnet errors. The next section attempts to verify this theory by experimentally measuring the positions of resonances within UMER as a function of beam current.

6.3.2 Resonance strength and shifting

Many different types of tunescan measurements and simulations are used to investigate the strength and shifting of resonance bands due to space charge forces. Initially a large range tunescan is performed for three beams with currents of, 0.6, 6, and 20 mA. The scans are shown in Figure 6.15. In this case the steering solution is kept the same for all three scans. Injection into the ring is tweaked for each beam current to account for matching into the ring. The scans show similar positions for the transverse resonances across all three beam currents regardless of space charge. The integer resonances are clearly defined due to the large beam loss that occurs, but other than the $Q_y = 7.5$ resonance, no second order resonances appear. This does not mean they are not there, but that no beam loss occurs at those resonances. As a result, no conclusion on half integer resonance shifting can be made from these scans. Previous experiments showed a potential shifting of the half integer resonance, but under different, non optimized, machine conditions [6]. The strength of the resonances appear to be the same across beam currents, indicating the resonance strength did not change with space charge. A NAFF based tunescan, where the tune is experimentally measured is used next.

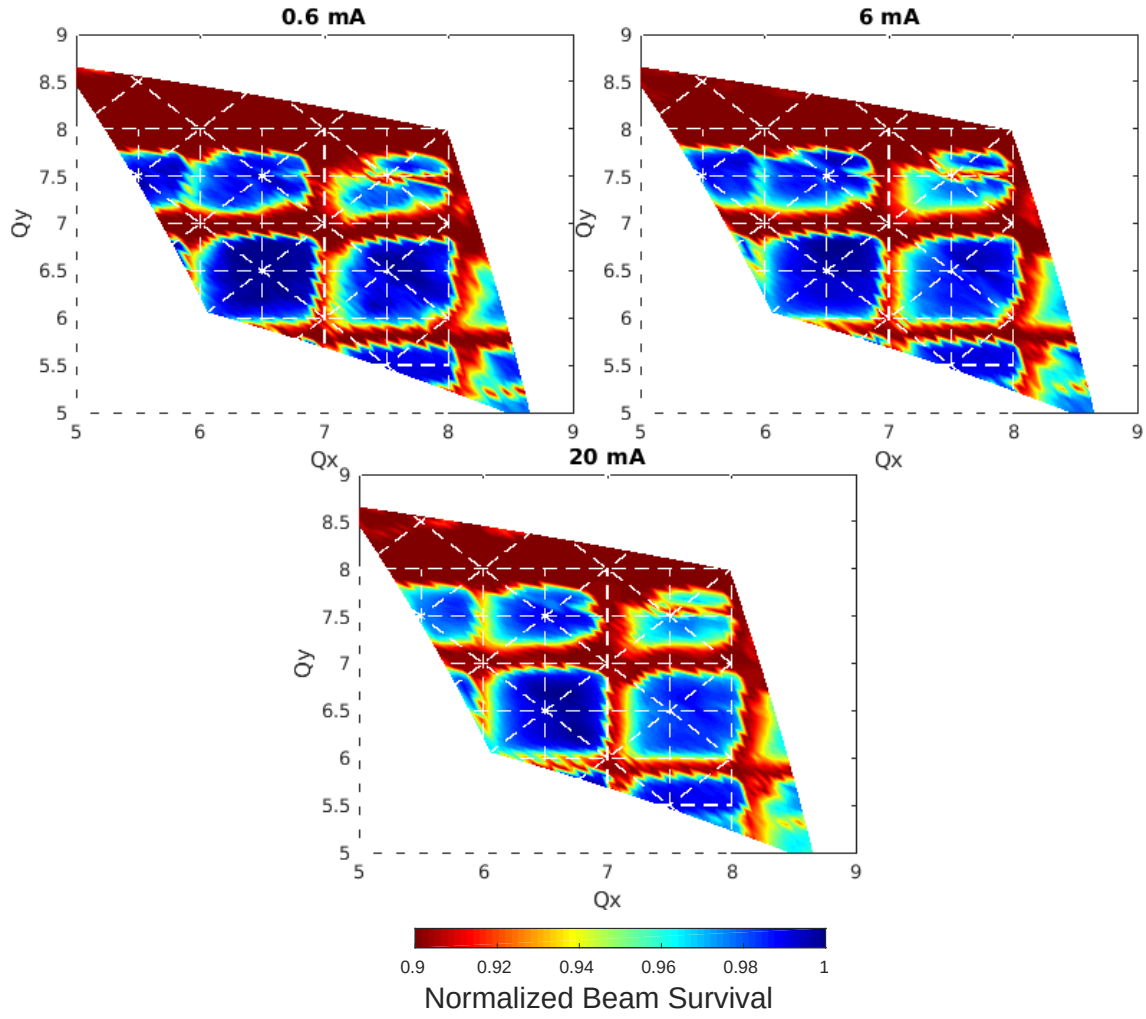

Figure 6.15: Tunescans for beams with three different beam currents. The quadrupoles were varied from 1.65 amps to 2.10 amps in steps of 0.01 amps. Injection quadrupoles QR1 and YQ were fixed.

A NAFF-based tune scan is performed by keeping the defocusing quadrupole magnets fixed and varying the focusing quadrupole magnets. This results in a linescan similar to Figure 6.13 where the tune is moved in a linear path across several resonances. In this case only the 0.6 and 6 mA beams could be used for accurate measurements. Figure 6.16 shows the measurement. On the left side the beam loss based tunescan data from Figure 6.15 is plotted in the background as a reference. On the right side is the same data plotted with only resonance lines up to third

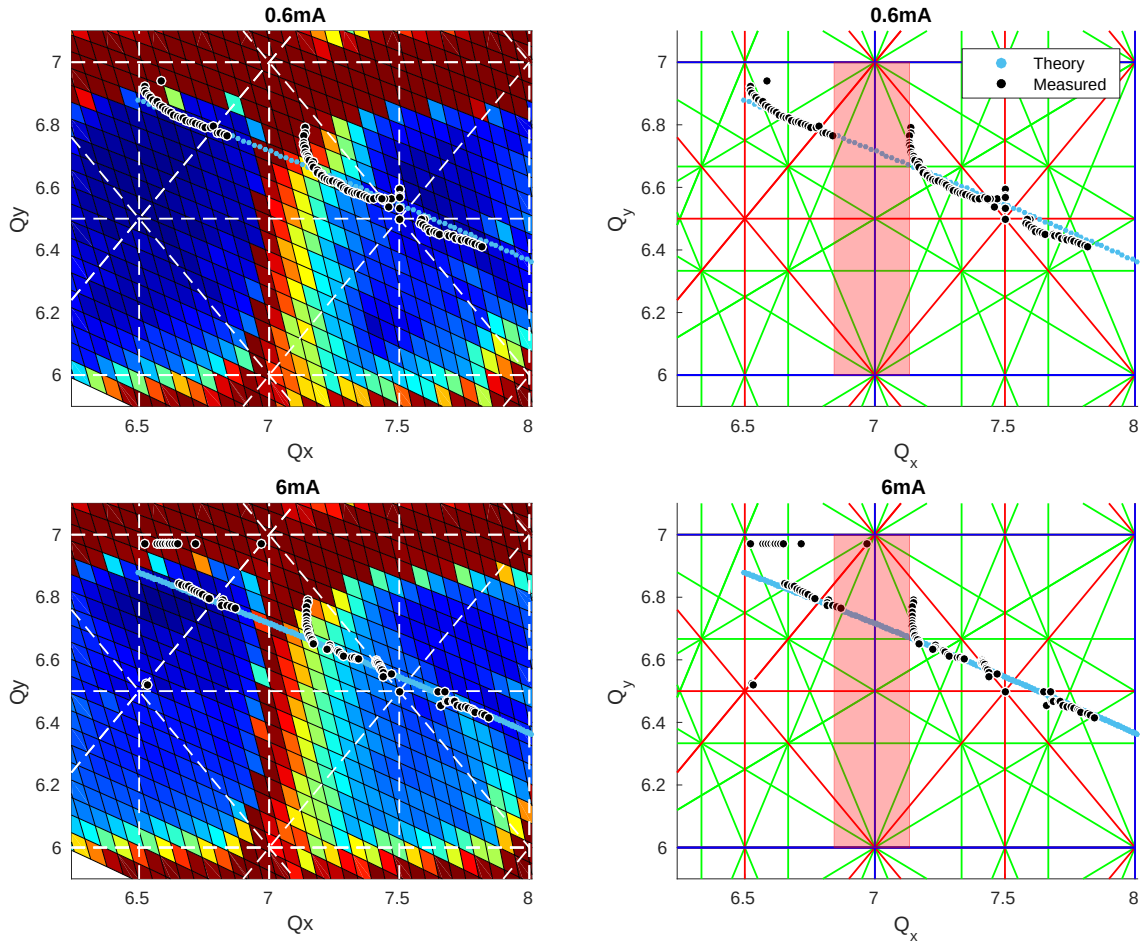

Figure 6.16: NAFF-based tunescan measurement. The tune is shifted and measured from Q_x= 6.5 to Q_x = 8.0. The left side overlays the tunescan data from Figure 6.15 while the right side shows the same data with only resonance lines up to third order in the background.

order. The blue dotted points in Figure 6.16 labeled 'Theory' represent tune values calculated using Eq. 6.1a and 6.1b. These are ideal values that assume a FODO lattice and no resonances. The black point in the same plots represent experimental measurements of the tune. The red colored rectangle is the approximate size of the integer $Q_x = 7$ resonance stopband based on the tune measurements on each side.

Some key observations can be made from Figure 6.16. The $Q_x = 7$ integer stopband does not shift or change size between the 0.6 and 6 mA beams. Space

charge does not seem to affect the integer resonance. Approaching the $Q_x = 7$ resonance from the left side is quite different than approaching from the right side. The vertical value of the tune on the right side of the integer resonance appears much higher than theory predicts. This means measuring beam loss due to resonances using the theoretical values for tune vs the experimentally measured values will result in a potentially deceiving result. The predicted starting and ending locations of resonances are going to be different from the measured ones as seen in Figure 6.16.

One set of information missing from the NAFF scans in Figure 6.16 is the measured beam loss at each tune location. This information is included and the data replotted in Figure 6.17. The measured tunes are plotted as a function of the focusing quadrupole strength, $Q_x = f(k_x, k_y)$ and $Q_y = f(k_x, k_y)$. For the line scan the defocusing quadrupole strength is fixed. Similarly, the normalized beam loss is plotted against the same function, $B = f(k_x, k_y)$ for comparison. Plotting data this way better reveals resonances that were not apparent in Figure 6.16. Slight beam loss occurs at the $Q_x = 7.5$ and $Q_y = 6.5$ resonances. The integer stopbands, especially $Q_x = 7.0$ appear much bigger. An interesting observation in Figure 6.17 is that all the resonances, integer and half-integer are not behaving in a symmetric way. The drop off in beam current when entering a resonance band from the left side is signficantly steeper than when exiting on the right side.

A set of simulations in WARP were run to compare to the experimental results in Figure 6.17. In the simulations 1000 particles were tracked across 35 turns using three beam currents: 0.6, 6.0, and 20 mA. The simulations replicate the experiment

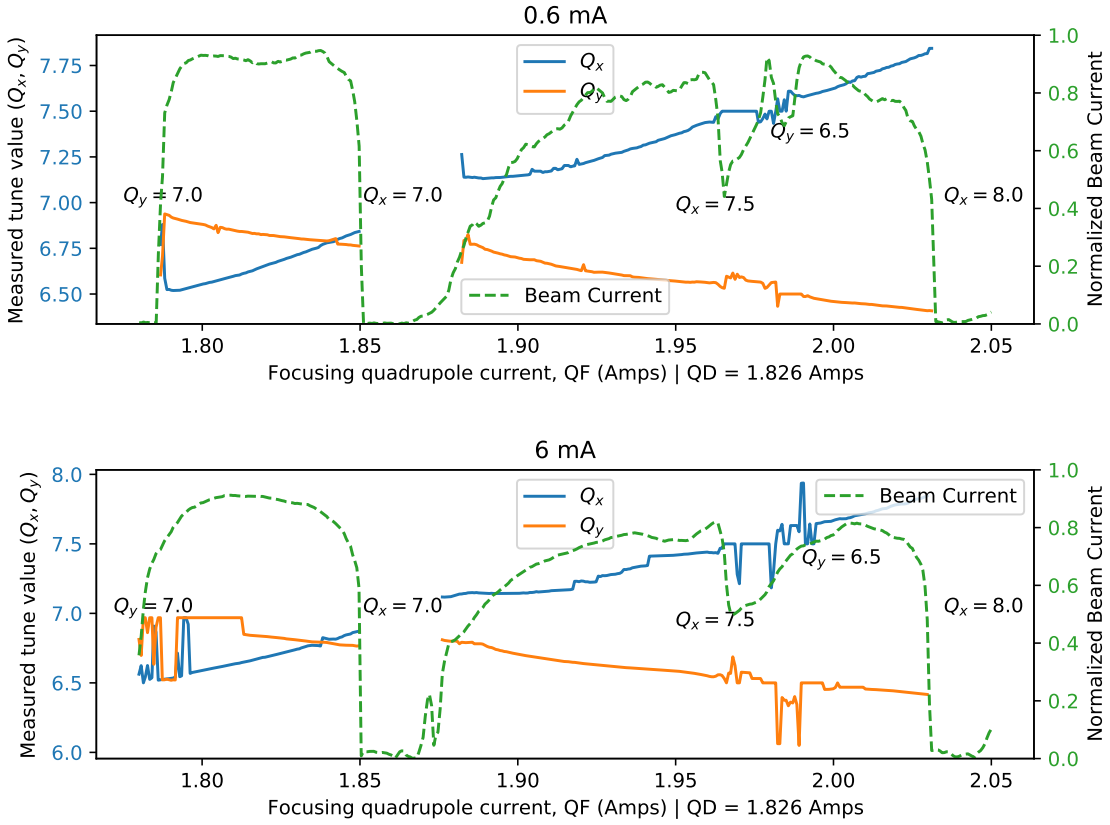

Figure 6.17: Same data from Figure 6.16. Tunes (Q_x, Q_y) are plotted as functions of the focusing quadrupole strength along with the measured beam current. The beam loss is measured on the 25th turn for the 0.6 mA beam and the 15th turn for the 6 mA beam.

by having the focusing quadrupoles varied to cause the tune to move across several resonances. Beam loss was measured as the fraction of particles that survived on the 35th turn. Tunes were measured using the NAFF algorithm with 16 to 32 turns of position data.

Looking at the simulations in Figure 6.18, the results are noticeably different from experimental measurements in Figure 6.17. The resonance band widths for the different horizontal resonances, $Q_x = 6.5, 7.0, 7.5$, are smaller. This is likely because the real machine has stronger alignment and field errors whereas the simulations

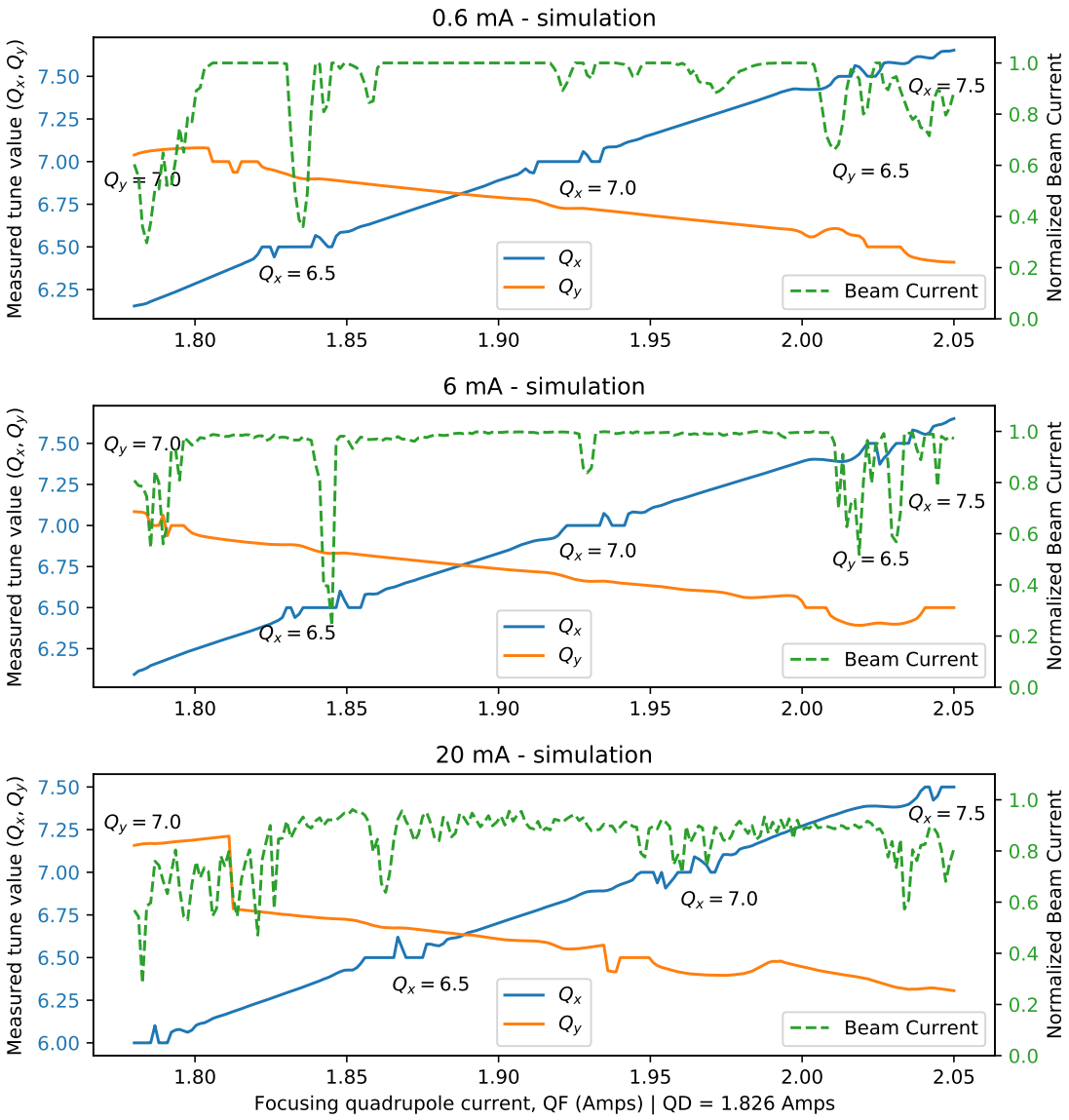

Figure 6.18: A WARP simulation of the tunescan experimental measurements from Figure 6.16.

assume no such errors. Less beam loss occurs near the integer resonances, but the same amount occurs at the half-integer resonances near $Q_x = 7.5$ and $Q_y = 6.5$. This indicates that the dipoles in UMER, which are responsible for integer resonances, have large errors in them. Previous measurements with a theodolite showed magnet misalignments in UMER on the order of 0.1 mm. The half-integer resonances are roughly the same size in simulations and experiments, showing that the quadrupole magnets on UMER have minimal field errors associated with them. In the simulations there does not seem to be any half-integer resonance band shift or strength change due to the different space charge intensities.

Lastly, a set of grid based NAFF tunescans are experimentally measured with different beam currents to observe the general tune space structure around integer and half-integer resonances. This is a measurement similar to the graphs in Figure 6.11 and 6.12, only over a larger range. Figure 6.19 shows a scan using the 0.6 mA beam and 64 turns of position data to calculate tunes. Two scans were performed with and without varying the injection quadrupole magnet named QR1. There does not seem to be any large differences in the measurements; this is important as all previous measurements in the section kept the injection quadrupole fixed. This shows that none of the previous measurements would show any signficant differences if the injection quadrupoles were not kept fixed.

The measurements in Figure 6.19 reveal a lot of detail within the tunespace structure in UMER. The horizontal integer stopband $Q_x = 7.0$ can be seen starting around $Q_x = 6.85$ as beam loss begins to occur. Similarly, the vertical integer stopband at $Q_y = 7.0$ starts around $Q_y = 6.9$. None of the third order resonances

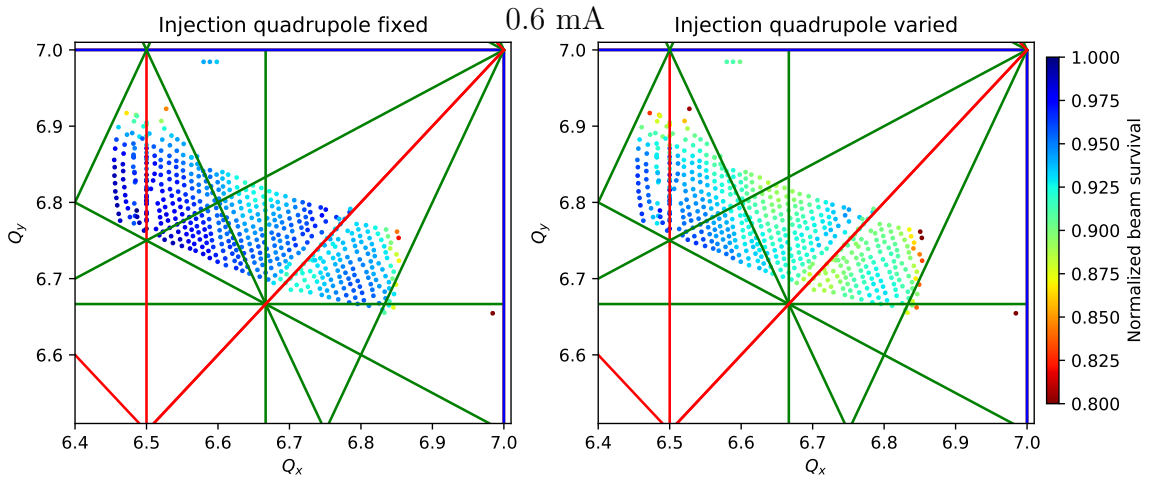

Figure 6.19: An experimental grid scan near the operating point of UMER ($Q_x, Q_y = (6.70, 6.82)$). Two measurement are done with and without varying the injection assisting quadrupole magnet QR1.

have a measurement impact on the beam. The difference resonance line, $Q_y = Q_x$ exists within the machine, but does not cause beam loss. Theory predicts that this difference resonance is supposed to be stable, which is proven by the measurement in Figure 6.19.

Next a set of NAFF based grid scans is experimentally measured for the four available beam currents: 0.1, 0.6, 6.0, and 20 mA. To keep comparisons fair, 16 turns of position data were used to calculate tunes across all four scans. Results are plotted in Figure 6.20. The beam survival was measured at the 15th, 25th, 15th, and 7th turns for the 0.1, 0.6, 6.0, and 20 mA beams respectively; this is because the space charge longitudinal expansion occurs at different rates in the different beams. In terms of where the $Q_x = 7.0$ resonance begins, it appears to be at the same location for all four scans. The $Q_x = 6.5$ resonance does not shift, but does have a different band width across the scans. The 0.1, 6, and 20 mA scans disagree with the 0.6 mA scan in terms of the size of the $Q_x = 6.5$ resonance. It is hard to say

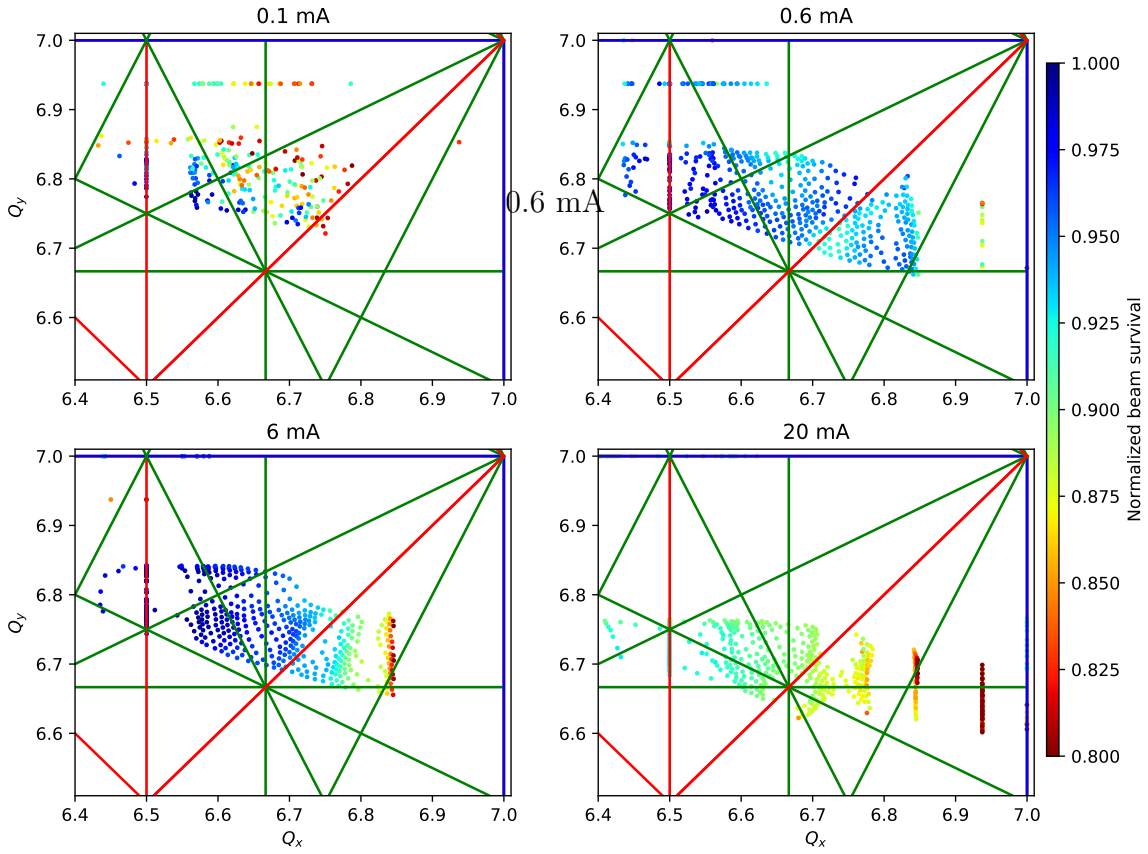

Figure 6.20: An experimental grid scan near the operating point of UMER ($Q_x, Q_y = (6.70, 6.82)$). Four measurements are done with 0.1, 0.6, 6.0, 20 mA beams. 16 turns of data were used to calculate tunes for each scan.

exactly why this is, but it might be due to the limited 16 turns of data available for tune calculations in the measurements.

6.4 Chapter Summary

This chapter discusses the experimental work in studying tunes and resonances with space charge. Experimental tune measurements are discussed in the first section. Development of advanced tune measuring techniques are described and applied to UMER. The second section demonstrates the tunescan methods of experimentally measuring the presence of resonances. Many examples are shown. The third section

applies all the techniques discussed in the previous sections to experimentally measure the effect of space charge dominated beams on transverse particle resonances within UMER. The experimental measurements agreed with theory for the case of integer resonances, but disagreed with theory for the half-integer resonances. In the integer resonance case, there was no measured shifting of the resonance band as a function of space charge; this was the predicted behavior from theory discussed in section 6.3.1. The same theory predicted a shifting of the half-integer resonance due to space charge forces. However, the experimental measurements showed no measured shift of the half-integer resonance band with space charge.

Chapter 6: Bibliography

[1] Martin Reiser. *Theory and Design of Charged Particle Beams*. John Wiley and Sons, Ltd, 2008.

[2] R. Baartman. Betatron resonances with space charge. *AIP Conf. Proc.*, 448(1):56–72, 1998.

[3] Ingo Hofmann. *Space Charge Physics for Particle Accelerators*. Springer International Publishing, 2017.

[4] Marco Venturini and Robert L. Gluckstern. Resonance analysis for a space charge dominated beam in a circular lattice. *Phys. Rev. ST Accel. Beams*, 3:034203, Mar 2000.

[5] K. Kojima, H. Okamoto, and Y. Tokashiki. Empirical condition of betatron resonances with space charge. *Phys. Rev. Accel. Beams*, 22:074201, Jul 2019.

[6] Santiago Bernal. *A Practical Introduction to Beam Physics and Particle Accelerators*. Morgan & Claypool Publishers, 2018.

[7] Chao Wu, Eyad Abed, Santiago Bernal, Brian Beaudoin, Rami Kishek, Shea, M Reiser, and D Sutter. Linear resonance analysis of beams with intense space charge in the university of maryland electron ring (umer). *HB 2008 - 42nd ICFA Advanced Beam Dynamics Workshop on High-Intensity, High-Brightness Hadron Beams*, 01 2008.

[8] S. Bernal, B. Beaudoin, I. Haber, T. Koeth, Y. Mo, E. Montgomery, K. P. Rezaei, K. Ruisard, W. Stem, D. Sutter, H. Zhang, and R. A. Kishek. Nonlinear dynamics with space-charge in a small electron recirculator. *AIP Conference Proceedings*, 1777(1):100003, 2016.

[9] K. Moriya, K. Fukushima, K. Ito, T. Okano, H. Okamoto, S. L. Sheehy, D. J. Kelliher, S. Machida, and C. R. Prior. Experimental study of integer resonance crossing in a nonscaling fixed field alternating gradient accelerator with a paul ion trap. *Phys. Rev. ST Accel. Beams*, 18:034001, Mar 2015.

[10] Zhicong Liu, Chao Li, and Qing Qin. Structure resonance crossing in space charge dominated beams. *Physics of Plasmas*, 26(5):053104, 2019.

[11] William Stem. *Novel Emittance Measurement Through Experimental Study of Envelope Mode Resonance in a High-Intensity Particle Beam*. PhD thesis, University of Maryland College Park, 2018.

[12] P J Bryant. Betatron frequency shifts due to self and image fields. 1987.

[13] Santiago Bernal. Resonances with space charge. July 2017.

Chapter 7: Nonlinear Integrable Optics

A novel approach to transverse resonance suppression in next generation high-intensity accelerators is the use of nonlinear optical elements to induce large tune spreads which result in reduced responses to resonance driving perturbations while still maintaining global longterm beam orbit stability [1]. This technique in accelerator physics is known as nonlinear integrable optics (NIO) theory. NIO aims to fundamentally change the way accelerators have been built since the 1952 groundbreaking work by Courant, Livingston, and Snyder [2].

Experimental work has been going on at UMER in order to test the feasibility of NIO theory [3, 4]. This chapter covers all recent NIO work at UMER over the last two years. Section 7.1 introduces the relevant NIO theory required to understand the experimental work in this dissertation. A linear, single-invariant, and fully-invariant set of integrable systems are discussed in detail. The simulation tests of NIO with a UMER lattice are discussed in section 7.2. Experimental work is discussed in section 7.3. Lastly, there is a discussion on the future outlook of the experiment in section 7.4.

7.1 Nonlinear Integrable Optics Theory

Accelerators today are built based off alternating-gradient focusing systems introduced in 1952 [2]. In such a system, a series of alternating field quadrupole magnets are used along side dipole magnets to create an accelerator lattice that on average keeps the beam focused and guarantees long term stability; this is often referred to as a FODO lattice, see Figure 2.2. The Hamiltonian contains two invariants of motion, often called the Courant-Snyder invariants, which guarantees the system as fully integrable. This specific case of a linear integrable system is discussed in the next section. In practice no accelerator system can be perfectly integrable due to slight errors and perturbations in the beam dynamics. However, KAM theory states that even in the case of small perturbations, invariants of the motion can continue to exist [5]. Thus, in a real accelerator, operating near integrability is enough to guarantee long term beam orbit stability.

NIO theory is better able to deal with some of the short comings of a traditional linear FODO lattice. Linear systems tend to be susceptible to resonance driving perturbations which cause beam losses. Nonlinear based focusing lattices, which cause amplitude dependent frequency shifts in the beam, can better handle these resonance driven particle losses. The increase in nonlinearities creates a spread in beam frequencies which causes a reduced response to single frequency driven resonances. The nonlinearities in the accelerator lattice are also much more inherently stable to perturbations vs a linear lattice. The challenge comes in finding a nonlinear system that contains the necessary invariants of motion to guarantee long term

beam stability. The following sections discuss the theory needed to solve this issue.

7.1.1 Hamiltonian invariants with linear optics

If a Hamiltonian system is conserved and fully integrable, then a solution can be obtained by transforming to a new set of canonical coordinates called action-angle variables (J, θ) [6]. In such a transformation all coordinates and momenta (J_i, θ_i) are constants of motion, in other terms, invariants of the motion. The special case of a FODO lattice consisting of linear magnets can be shown to be fully integrable via such a canonical transformation.

Using the second order approximation to the single particle Hamiltonian from Eq. A.22 along with the appropriate vector potential from Eq. 2.4, the Hamiltonian for a linear system can be written as:

$$H = \frac{1}{2}k(s)(x^2 - y^2) + \frac{1}{2}(p_x^2 + p_y^2) \tag{7.1}$$

Eq. 7.1 is similar to the Hamiltonian for a quadrupole shown in Eq. 2.7. In this case there is an assumption of no energy spread and no dispersion, $\delta = 0, 1/R = 0$. The term $eG(s)/P_0$ is also rewritten as simply $k(s)$, the focusing strength of a quadrupole.

The canonical transformation from phase space variables (x, p_x) to (θ_x, J_x) requires the use of the following type one generation function:

$$F_1(x, \theta_x, s) = -\frac{x^2}{2\beta_x(s)}(\tan\theta_x - \frac{\dot{\beta}_x(s)}{2}) \tag{7.2}$$

where $\beta_x(s)$ is the horizontal betatron amplitude function. Remember that $\dot{\beta} = d\beta/ds$ and $\beta' = d\beta/dt$. Note the same generating function would be used for the vertical coordinate transformation from (y, p_y) to (θ_y, J_y). In order to not repeat equations, the rest of the section only deals with the horizontal direction. By using the equations of transformation for a type one generation function:

$$J_x = -\frac{\partial F_1}{\partial \theta_x} \quad , \quad p_x = \frac{\partial F_1}{\partial x} \tag{7.3}$$

a transformed Hamiltonian can be written as:

$$\tilde{H}(\theta_x, J_x, s) = H(x, p_x, t) + \frac{\partial}{\partial s} F_1(x, \theta_x, s) \tag{7.4}$$

Eq. 7.4 is known as the Hamilton-Jacobi equation [6]. The challenging part of the derivation is accounting for the periodic focusing term, $k(s)$, in the Hamiltonian; this is substituted out through the use of the betatron amplitude function from Eq. 2.12. The full derivation of the transformed Hamiltonian is carried out in Appendix F.1. The solution is:

$$\tilde{H}_x = \frac{J_x}{\beta_x} \tag{7.5}$$

with the full 2D system written as:

$$\tilde{H} = \tilde{H}_x + \tilde{H}_y = \frac{J_x}{\beta_x} + \frac{J_y}{\beta_y} \tag{7.6}$$

The action, J, is a constant, and as such, the invariant of motion in the linear

FODO system. For a 2D system there are two invariants of motion, J_x and J_y, making the system fully integrable. The action represents the amplitudes of the particle motion and is equivalent to the single particle emittance. As a comparison to the solution of Hill's equation from Eq. 2.11, $J = \epsilon/2$. The action is a measure of the volume of phase space enclosed by the particle orbits.

7.1.2 Single invariant with nonlinear optics

To create a nonlinear integrable system, a potential is added to the Hamiltonian from Eq. 7.1. The potential $V(x, y)$ requires that $n + m > 2$ for $x^n y^m$. An assumption is made that the focusing in the transverse planes are equal, $\beta_x = \beta_y = \beta$. Equations for the horizontal plane are used for convenience. The vertical direction equations can be similarly written.

$$H = \frac{1}{2}k(s)(x^2 + y^2) + \frac{1}{2}(p_x^2 + p_y^2) + V(x, y, s) \tag{7.7}$$

The first step in the process requires a normalization of the Hamiltonian in Eq. 7.7 through a type two generating function:

$$F_2(x, p_{x,n}, s) = p_{x,n}\frac{x}{\sqrt{\beta}} + \frac{x^2\dot{\beta}}{4\beta} \tag{7.8}$$

The generating function equation is used to find a new set of canonical variables:

$$x = \sqrt{\beta}x_n \ , \ p_x = \frac{p_{x,n}}{\sqrt{\beta}} + \frac{x\dot{\beta}}{2\beta} \tag{7.9}$$

and solve the Hamilton-Jacobi equation:

$$H_n(x_n, p_{x,n}) = H(x, p_x, s) + \frac{\partial}{\partial s} F_2(x, p_{x,n}, s) \tag{7.10}$$

Using a similar process to what was done in Section 7.1.1, the resulting 2D transformed Hamiltonian becomes:

$$H_n = \frac{1}{2\beta(s)}(x_n^2 + y_n^2 + p_{x,n}^2 + p_{y,n}^2) + V(\sqrt{\beta(s)}x_n, \sqrt{\beta(s)}y_n, s) \tag{7.11}$$

A final transformation is required to remove the $\beta(s)$ dependence. The independent variable s is substituted for Ψ. Where $\partial\Psi/\partial s = 1/\beta$, similar to the Floquet transform done in Sections 2.2.2 and 2.2.3.

$$\dot{x_n} = \frac{\partial x_n}{\partial s} = \frac{\partial x_n/\partial \Psi}{\partial s/\partial \Psi} = \frac{1}{\beta}\frac{\partial x_n}{\partial \Psi} \tag{7.12}$$

The new normalized Hamiltonian becomes:

$$H_N = \frac{1}{\beta}H_n = \frac{1}{2}(x_N^2 + y_N^2 + p_{x,N}^2 + p_{y,N}^2) + \beta(s)V(\sqrt{\beta(s)}x_N, \sqrt{\beta(s)}y_N, s) \tag{7.13}$$

Eq. 7.13 represents the single particle Hamiltonian with a nonlinear potential added. The single invariant here is the Hamiltonian itself, H_N, but this is only true if the s dependence can be removed from Eq. 7.13. A potential V needs to be found such that it cancels out any dependence on $\beta(s)$ in the Hamiltonian. The potential must obey Laplace's equation and from an experimental perspective, be practical

enough to physically construct. Looking at the set of multipole potentials from Eq. 2.4, where potentials scale as x^m, y^m, it is clear that the required potential must be of the form $V \propto \beta^{-1-\frac{m}{2}}$.

Picking a pure octupole potential ($m = 4$),

$$V_{\text{octu}}(x, y, s) = O(s)(\frac{1}{4}x^2y^2 - \frac{1}{24}x^4 - \frac{1}{24}y^4) \tag{7.14}$$

results in the following potential to substitute into Eq. 7.13:

$$V = \frac{\kappa}{\beta^3(s)}(x^4 + y^4 - 6x^2y^2) = \frac{\kappa}{\beta(s)}(x_N^4 + y_N^4 - 6x_N^2y_N^2) \tag{7.15}$$

where $\kappa = -O(s)/24$ is characterized as the strength of the octupole field and is used to scale the potential. The Hamiltonian then becomes:

$$H_N = \frac{1}{2}(x_N^2 + y_N^2 + p_{x,N}^2 + p_{y,N}^2) + \kappa(x_N^4 + y_N^4 - 6x_N^2y_N^2) \tag{7.16}$$

Eq. 7.16 has a single invariant of motion which is the Hamiltonian itself. Since this is a 2D system with one invariant, it is sometimes referred to as 'quasi-integrable'. The invariant here is the orbit energy and is bounded, but chaotic. This single invariant case through the use of a octupole potential is the focus of the simulation and experimental work done in this chapter on NIO. The octupole potential was chosen over other potentials due to the ease of physically constructing such a potential for experimental work on UMER.

Several new requirements now need to be met in order to use this octupole

potential. First, the canonical transform to normalize coordinates requires the beam to be round when passing through the potential ($\beta_x = \beta_y = \beta$). Next the potential needs to scale as $1/\beta^3$ in order to cancel the s dependence in the Hamiltonian. Thirdly, there should be an $\Delta\Psi = n\pi$ phase advance between the nonlinear potentials. i.e. each time the beam leaves the nonlinear potential and arrives at the next nonlinear potential it must have advanced $n\pi$ in phase with n being an integer.

If all the requirements are met, an accelerator lattice can be built using such a nonlinear potential to deal with the short comings of a traditional linear focusing lattice. The nonlinear potential is able to cause particle detuning, i.e. spreading of particle frequencies; this results in particle beams being less susceptible to resonances. At the same time the Hamiltonian has a invariant of motion and can guarantee a stable beam orbit. The drawback is that since only a single invariant exists in the 2D system, the particle orbit will be stable, but chaotic. If a second invariant of motion can be found, then the solution will be fully integrable and no longer chaotic.

7.1.3 Full invariant with nonlinear optics

While the fully integrable solution for NIO exists, it is not the focus of this dissertation. This section briefly describes the derivation of such a system. More information can be found here [1]. The Integrable Optics Test Accelerator (IOTA) at Fermilab aims to build and test a fully integrable nonlinear accelerator [7].

As discussed in [1], a potential can be found such that the normalized Hamil-

tonian, H_N, has two invariants of motion. The second invariant has the following form:

$$I = (ay^2 + c^2)p_x^2 - 2axyp_xp_y + ax^2p_y^2 + D \tag{7.17}$$

where a, b, and D are constants. Letting $a = 1$, $c \neq 0$, and using Bertrand-Darboux PDE leads to the following equation:

$$xy(U_{xx} - U_{yy}) + (y^2 - x^2 + c^2)U_{xy} + 3yU_x - 3xU_y = 0 \tag{7.18}$$

The solution to Eq. 7.18 is:

$$U(x, y) = \frac{f(\xi) + g(\eta)}{\xi^2 - \eta^2} \tag{7.19}$$

where

$$\eta = \frac{\sqrt{(x+c)^2 + y^2} + \sqrt{(x-c)^2 + y^2}}{2c} \ , \ \xi = \frac{\sqrt{(x+c)^2 + y^2} - \sqrt{(x-c)^2 + y^2}}{2c} \tag{7.20}$$

The full second invariant has the final form:

$$I(x, y, p_x, p_y) = (xp_y - yp_x)^2 + c^2p_x^2 + 2c^2\frac{f(\xi)\eta^2 + g(\eta)\xi^2}{\xi^2 - \eta^2} \tag{7.21}$$

with the Hamiltonian becoming:

$$H_N = \frac{1}{2}(x_N^2 + y_N^2 + p_{x,N}^2 + p_{y,N}^2) + \frac{f(\xi) + g(\eta)}{\xi^2 - \eta^2} \tag{7.22}$$

The potential is still required to satisfy Laplace's equation and must be physically buildable. A set of external magnets have been built and are being used to test the fully integrable case at IOTA [8].

7.2 Simulation of Integrable Optics

A plethora of simulation work is needed before any experimental tests can be done with NIO on UMER. The octupole potential needs to be designed, simulated, and tested. Similarly the lattice used for NIO work needs to go through the same process. Optimizations need to be done in order to generate realistic enough simulations to justify experimental work. Effects such as space charge forces, dispersion, and chromaticity need to be considered as well. If the majority of the NIO theory works via realistic simulations, it is then reasonable to move onto experiment. This section describes the latest simulation work done for the NIO experiment at UMER. Information on previous simulation work can be found here [3].

7.2.1 Octupole field design

Magnets need to be designed to replicate the octupole potential needed for NIO experiments at UMER. Based on Section 7.1.2 the octupole strength for the field needs to scale as $1/\beta^3$. The octupole magnet should also be able to fit around the other existing magnets in UMER. It was decided that a set of octupole PCB magnets similar to the ones discussed in Section 5.1 would be built. A long, 32 cm sized, octupole channel would be made and placed in UMER. This channel would

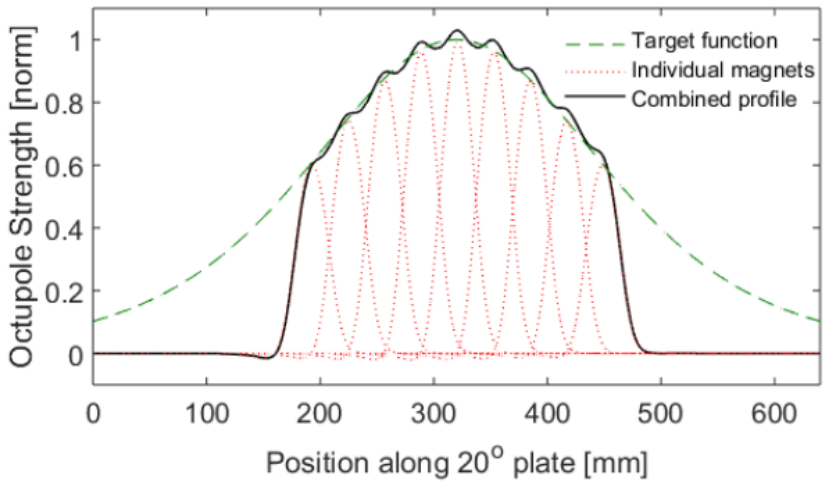

Figure 7.1: Individual octupole PCB magnet potentials plotted vs the longitudinal direction. The sum of the individual fields is added up to match the $1/\beta^3$ target function goal. Figure taken from [9].

be able to fit 7 overlapping octupole PCB magnets that would be able to generate the required octupole potential. More info about the channel design can be found here [10].

Figure 7.1 shows a visual representation of the octupole fields from the octupole channel. The target function represents the $1/\beta^3$ scaling that needs to be met. Adding up the fields for the 7 individual octupole PCB magnets allows the scaling requirement to be met to a good enough approximation. This is further discussed here [3]. For simulations, a hard edge model is assumed for the octupole magnets.

In both experiments and simulations, each of the 7 octupole magnets is powered individually. The control allows each magnet to be adjusted through optimization in order to meet the given beta function requirement. Due to imperfections in the physical construction, e.g. some field errors due to overlapping PCBs, experimental optimizations were done on a magnetic measurement stage. More info on

these optimizations can be found here [11].

The field in each of the individual octupole PCBs is determined by the peak octupole field gradient. The gradient is found from the multipole expansion in Eq. 2.6 and using the same techniques discussed in Section 5.1:

$$b_3 = \frac{1}{3!}\frac{\partial^3 B_y}{\partial x^3} = 50\,T/m^3 \text{ for 1 amp peak current} \tag{7.23}$$

For both the simulations and experiments a 50 T/m^3 gradient is assumed for all octupole PCB magnets. The nonlinear scaling potential, κ, discussed in Section 7.1 is a function of the gradient b_3 and is the free parameter used to adjust the strength of the octupoles. In this case the current applied through the PCBs is the specific parameter being adjusted. As such, the octupole magnet strengths are adjusted via current placed through the magnets.

7.2.2 Lattice design and optimization

One of the biggest challenges in the NIO experiment is designing a lattice for UMER that meets all the requirements discussed in the previous sections. An early design assumed a 3-period symmetric lattice with the nonlinear potential appearing three times in the lattice. The high tolerance steering requirements in this specific lattice made it difficult to measure accurate results with the nonlinear octupole channel. Secondly, while UMER is a FODO cell lattice, the non uniform earth's field distributed around the ring turns it into a single-period symmetric lattice; this makes it essentially impossible to design higher-period lattices without properly

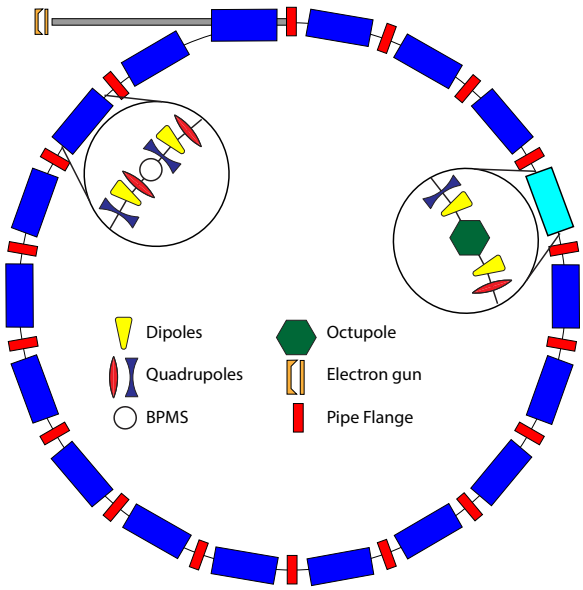

Figure 7.2: A diagram of the UMER lattice with the octupole channel incorporated.

dealing with the earth's field.

The latest lattice design, which will be the focus in this dissertation, assumes a 1-period symmetric UMER lattice. The nonlinear potential is incorporated in the lattice as a matching section. This matching section must meet all the nonlinear potential requirements within the section and must match the beam's phase space coordinates (x, x', y, y') through the section. Figure 7.2 shows a visual diagram of where the octupole channel is placed in the ring. Note the 18 main FODO sections in UMER. Without the earth's field a 3-period and 6-period symmetric lattice design could have been used.

The lattice needs to meet the following requirements:

1. The beam must be round, $\beta_x = \beta_y = \beta$, within the nonlinear potential.

2. The octupole channel potential must scale as $1/\beta^3$.

3. The phase advance between subsequent entrances into the nonlinear potential

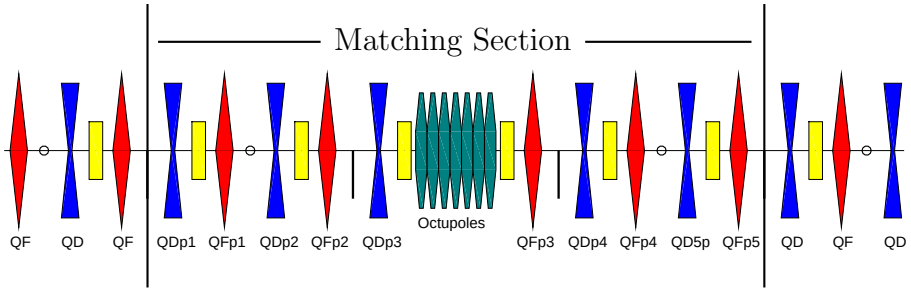

Figure 7.3: A diagram of the matching section used for the octupole channel. Magnet color scheme is the same as Figure 7.2. Quadrupoles labeled QF,QD are regular ring quadrupoles. Quadrupoles labeled $\mathrm{QFp1}-5, \mathrm{QDp1}-5$ are the set of magnets tuned to meet optimization goals.

region must be $n\pi$.

4. The beam must be matched coming into and out of the matching section, $(x_1, x_1', y_1, y_1') = (x_2, x_2', y_2, y_2')$.

On top of the requirements above, in order to realistically implement the lattice experimentally, a few more points must be considered in the design:

1. In order to fit the beam into the ring, particle motion must be as small as possible, $\min_{s\in L} \beta_x(s), \beta_y(s)$

2. The transverse tunes should be equal. The fractional tunes should be near $q_{\mathrm{frac}} \approx 0.13$ for the greatest impact.

3. Dispersion through the matching section should be zero, $h = 0$.

4. The strength of quadrupole and dipole magnets should be close to values used for normal UMER operations as it will ease the amount of work needed to configure a completely new lattice on the accelerator.

Meeting all the theoretical and experimental requirements in the lattice turns

into a large optimization problem. 14 total parameters, all quadrupoles, are tuned to meet the objective goals. Note the different families of quadrupoles shown in Figure 7.3. There are five quadrupoles before and after the octupole channel labeled $\mathrm{QFp1}-5, \mathrm{QDp1}-5$. The remaining quadrupoles in the UMER lattice are separated into two families: focusing quadrupoles, QF, and defocusing quadrupoles, QD. All magnets in a family have the same quadrupole strengths (k values). The 14 tuning parameters are the ten quadrupoles within the matching section, the QF and QD families of magnets, and the special injection quadrupoles QR1, YQ. Several different sets of tuning parameters were tested over the optimization process and the best results came from the use of these 14 parameters. Some other tuning parameters used included dipole magnets, more quadrupole magnets, and a combination of both.

All of the requirements above are summarized into a single objective function that contains 7 sub-objectives:

$$\min f = \min \sum_{i}^{7} w_i g_i \tag{7.24}$$

where w is the weight assigned to each sub-objective g:

$$g_1 = \min \beta_x(s) \text{ outside channel} \tag{7.25a}$$

$$g_2 = \min \beta_y(s) \text{ outside channel} \tag{7.25b}$$

$$g_3 = \min \beta_x(s) \text{ inside channel} \tag{7.25c}$$

$$g_4 = \min \beta_y(s) \text{ inside channel} \tag{7.25d}$$

$$g_5 = \min \left(|Q_x - Q_{x,\text{goal}}| + |Q_y - Q_{y,\text{goal}}|\right) \tag{7.25e}$$

$$g_6 = \min \left(|\Delta\Psi_x - n\pi| + |\Delta\Psi_y - n\pi|\right) \tag{7.25f}$$

$$g_7 = \min |\beta_x - \beta_y| \text{ inside channel} \tag{7.25g}$$

The first four objectives, g_{1-4}, are used to minimize the absolute amplitudes of the particle oscillations. The smaller the amplitude, the better steering and orbit control that can be achieved experimentally. Objective g_5 fits the lattice tunes to a desired value and makes sure they are equal in both transverse planes. g_6 is used to meet the $n\pi$ phase advance requirement outside the octupole channel. Phase advances outside should also be equal. Finally, g_7 is to optimize the beta functions to be equal inside the octupole channel, $\beta_x = \beta_y = \beta$. The sub-objectives were changed over time with the final set of objectives listed in the equations above.

The optimization itself uses the Nelder-Mead technique, see section 4.2.2. Weights are needed due to the large range of values for each objective. The 14 tuning parameters make the optimization a 14 dimensional problem. In this large dimensional space lots of singularities exist. For example: beam oscillations grow

and hit the pipe wall when tunes approach a destructive resonance, betatron ampltiudes become too large in specific sections, or certain large changes in $d\beta/ds$ cause beam instabilities to occur. In the case of destructive resonances, the optimization does not know that beyond such a resonance a better objective function result might exist. As a result, some manual inputs and modifications are needed to get proper convergence of the optimization.

7.2.3 Example optimization run

The general procedure of the optimization is as follows. First weights for all objectives except g_5 are set to zero. The starting values for all the quadrupoles (input parameters) are based on the default UMER lattice setting. For this example the goal for the tunes is $Q_x, Q_y \approx 7.13$. The starting strengths of the QF and QD quadrupole families are manually tweaked such that the tune is within the $7.0 - 7.5$ range so as to avoid any resonance based singularities in the optimization. 400 iterations are run. g_5 as a function of iterations is plotted in 7.4. Notice the large

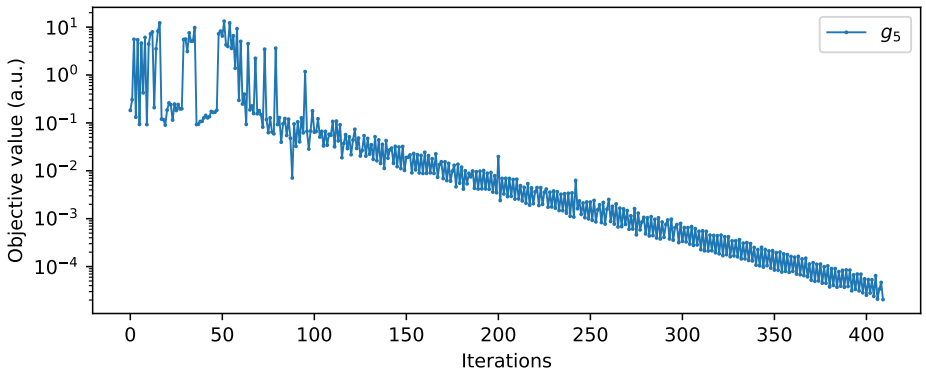

Figure 7.4: The g_5 sub-objective as a function of iterations.

spikes during the first 75 iterations.; this is the optimization hitting resonances at

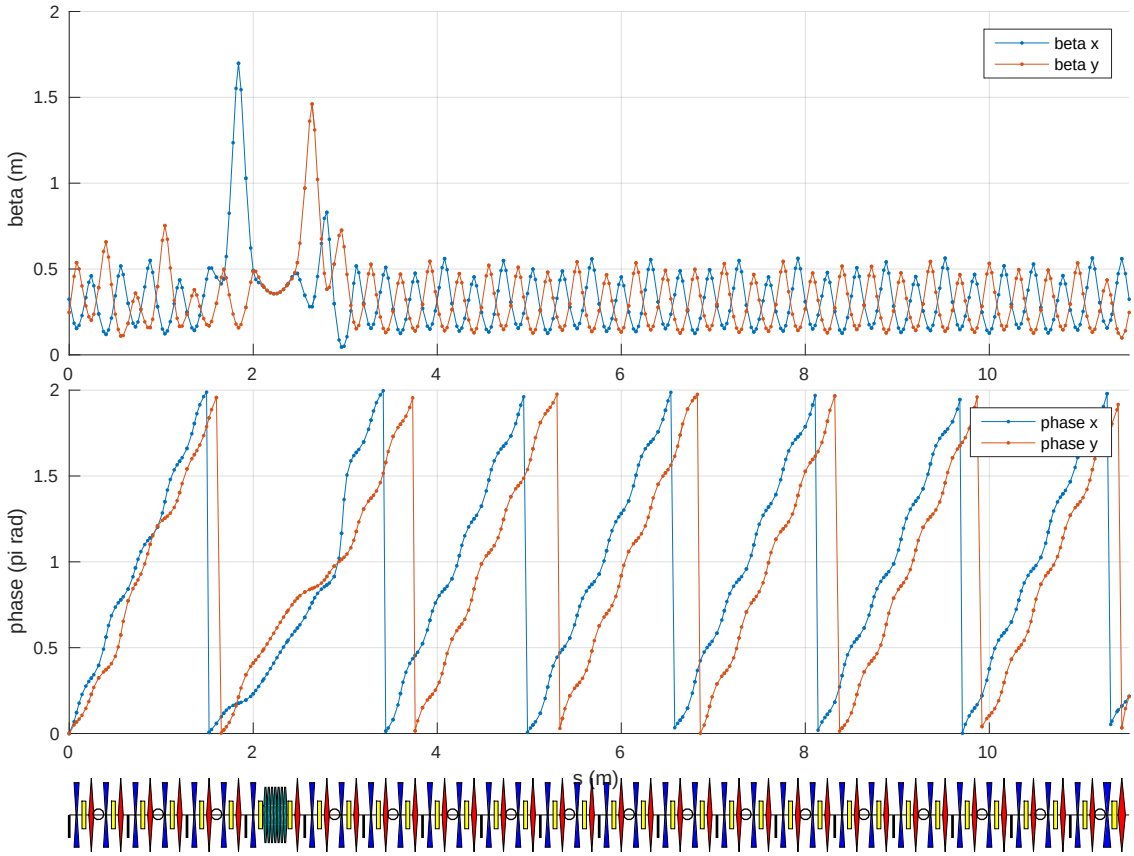

Figure 7.5: The final beta functions and phase advances are plotted after optimization. Note the phase advance is cyclic and returns from 2π back to 0.

7.0 and 7.5 causing fluctuations in the objective. Once the optimization settles near a range of acceptable input parameters, it quickly is able to find the direction toward minimization. A value of 10^{-3} is an acceptable minimum for this objective; it represents a tune accuracy of 0.001, which is below the measurement capabilities of the UMER BPMs (≈ 0.01).

Next the weights for the remaining sub-objectives are manually turned on and tweaked over many optimization runs. Depending on the number of iterations, runs can take a few seconds to several minutes. For now the weight tweaking is done manually with plans to automate the process in the future.

For this specific example the final lattice functions are plotted in Figure 7.5. The tunes end up being $Q_x, Q_y = 7.109, 7.108.$ with $n = 14.002, 14.00$ for the $n\pi$ phase advance $\Delta\Psi_x, \Delta\Psi_y$. Outside the nonlinear section the lattice is nicely matched and within the nonlinear section $\beta_x = \beta_y$. The two large beta function peaks before and after the nonlinear section are due to the fact that this was the only way the optimization could get the betas to be equal inside the nonlinear section. The smaller the betas near the center of the nonlinear section, the larger the spikes have to be entering and exiting the section. Note outside the nonlinear section the betas do not exactly match; this is because of the focusing effects in the dipoles. All dipoles are set to slightly different values to compensate for the earth's field which results in slight variations of focusing throughout the ring. Based on all the constraints in the problem, this was the optimal calculation from the optimization routine.

The quadrupole current setpoints required for this optimization are summarize in Table F.1. These set of values are also the most updated values for the NIO simulations. When starting experiments these are the initial setpoints for the magnets before starting any steering or orbit optimizations. The optimization so far have been done in a single particle code (AT) with space charge effects being ignored. Secondly, the vertical helmholtz coils are turned off along with the earth's field; this should not be a problem since the optimization is measuring properties (beta function, tune, phase advance, etc...) that are not dependent on these extra magnets and fields – that is the assumption made here. No steering or orbit control optimizations are done; this is done experimentally on the accelerator.

Parameter	Common Name	Value (amps)
QDp1	QR10	1.6736
QFp1	QR11	1.1566
QDp2	QR12	1.7884
QFp2	QR13	1.5742
QDp3	QR14	1.2138
QFp3	QR17	0.7373
QDp4	QR18	1.5599
QFp4	QR19	2.1255
QDp5	QR20	1.6194
QFp5	QR21	2.4905
QD	QR2-QR70, even	2.0232
QF	QR3-QR71, odd	1.9113
YQ	YQ	5.5380
QR1	QR1	5.0222

Table 7.1: The final setpoint currents after running the optimization routine presented above.

7.2.4 Simulation measurements

Given the optimized lattice from the previous section, a set of simulation based measurements are performed to determine the viability of the configured lattice. These initial measurements are done with a uniform nonlinear field instead of a field scaling as $1/\beta$. In looking at the simulations, there was only small difference in results from using a uniform field over a scaling field for the octupole channel section.

First a phase space measurement is done with and without the nonlinear po-

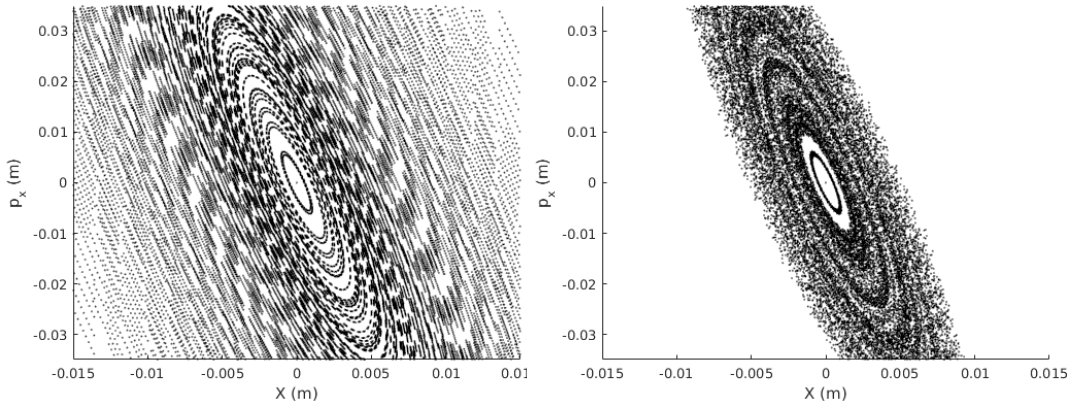

Figure 7.6: (left) Phase space with octupoles turned off. (right) Phase space with octupoles turned on to 0.2 amps. Note the difference vertical scales.

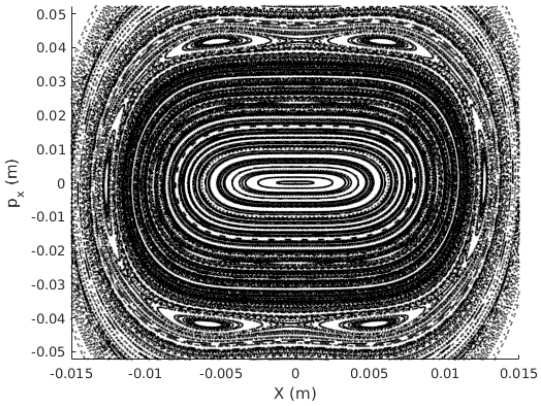

Figure 7.7: Phase space through the octupole channel only. Octupole strength set to 1 amp.

tential turned on in Figure 7.6. As expected, without the nonlinear potential the linear lattice has ellipse shaped stable orbits in phase space. The available stable orbits get signifcantly reduced when the nonlinear potential is turned on. Certain orbits also start to become chaotic. Figure 7.7 shows the phase space going through just the nonlinear octupole potential. All phase space measurements are done by tracking a set of particles with random initial conditions (x, p_x) through 512 turns in the NIO lattice.

One important property of nonlinear elements in an accelerator lattice is the amplitude dependent tune shifts that occur. Normally the tune is only a function of the focusing strength in a lattice, $\Delta Q = f(k(s))$, but with nonlinear elements the tune also becomes a function of particle amplitude. As such, a good way to measure the amount of nonlinearity present in a given lattice is to measure these tune shifts with amplitude; this technique is called a frequency map analysis (FMA) [12]. The measurement is done by kicking particles out to large amplitudes and allowing the linear restoring force to slowly damp the betatron oscillations back down onto the stable orbits. Given N turns of data, tunes are measured using the first $N/2$ as well as the second $N/2$ turns. A variable called diffusion is then calculated from the tune data:

$$D = \log |Q_{x,2} - Q_{x,1}| + |Q_{y,2} - Q_{y,1}| \tag{7.26}$$

where Q_2 and Q_1 are the tunes measured during the second half and first half of turns $(N/2)$.

Figure 7.8 shows a measurement of the FMAP for the NIO lattice. The tune shifts from the $(7.13, 7.13)$ bare tune towards the integer resonances. A tune shift on the order of $\Delta \approx 0.1$ can be expected based on this simulation. Note the asymmetric shape of the shift. In a theoretically ideal FODO lattice the tune shifts would be symmetric. UMER has each of its rectangular dipoles set to different strengths to compensate for the earth's field; this results in an asymmetric focusing effect. The left side of Figure 7.8 shows a dynamic aperture measurement (DA). In this case the particle amplitudes are plotted with color still representing Diffusion. Such a

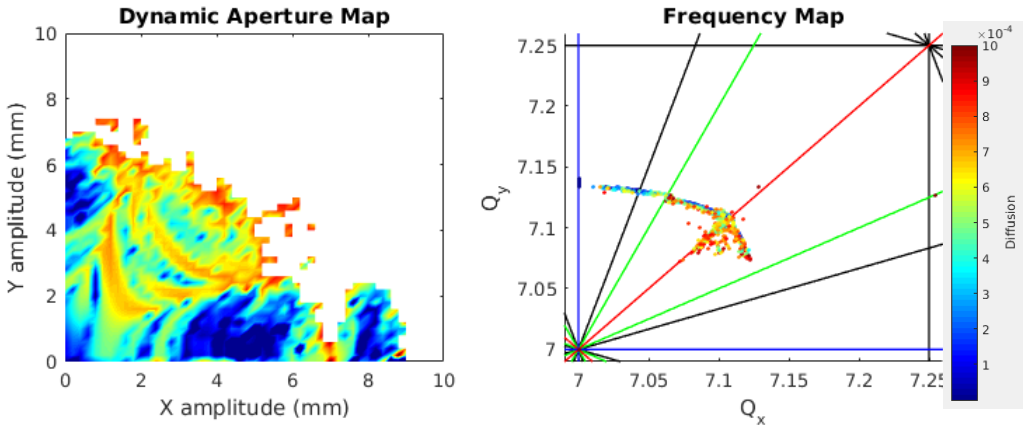

Figure 7.8: (left) Dynamic aperture measurement. (right) Frequency map measurement. Color represents diffusion D calculated using Eq. 7.26. Color can be thought of as the regularity of the orbits. Blue is very stable and red is very nonlinear.

plot is useful in identifying stable regions of the particle orbit in real space.

Figure 7.9 shows an extreme example of resonance damping with the octupole channel. In this case a particle beam is simulated and brought close enough to the $Q_x = 7.5$ half-integer resonance such that all particles are lost within the first few turns. The particle beam is made up of 500 particles with a gaussian distribution in x and y using a standard deviation of 15 mm in amplitude. The phase space distribution for both x and y is random between values of -0.01 rad to 0.01 rad. Looking at the top plot of Figure 7.9, we see that the particle survival rate increases drastically as the octupole potential is increased in strength. In this case any particle outside of 15 mm in amplitude is considered lost, a realistic approximation for UMER. After a certain octupole strength the survival rate starts to drop as the nonlinear potential becomes too start and starts knocking particles off their stable orbits. This simulation shows there exists an ideal octupole strength that will be able to damp out resonance behavior and maximize particle survival rate. The middle

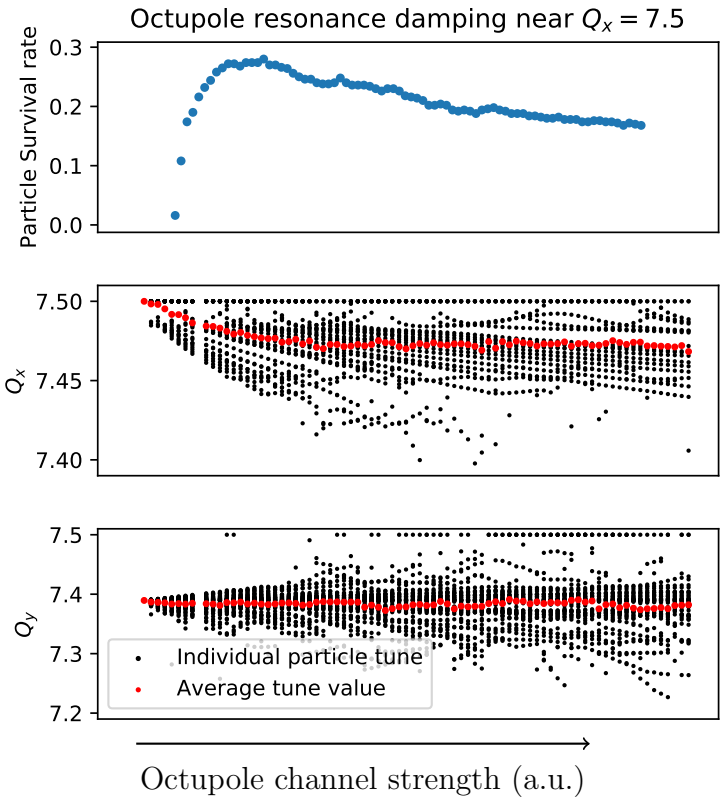

Figure 7.9: The particle beam, made up of 500 particles, is moved near the destructive $Q_x = 7.5$ half-integer resonance. (top) Particle survival rate vs strength of the octupole channel. (middle) Individual particle horiztonal tunes measured and plotted as a function of octupole strength. (bottom) Individual particle horiztonal tunes measured and plotted as a function of octupole strength.

and bottom plots in Figure 7.9 show the individual particles tunes as a function of octupole strength; these show the clear tune spreading that is occuring due to the nonlinear octupole potential.

Next the Hamiltonian from Eq. 7.16 is measured. Particles are launched at increasing amplitudes in x and y into the NIO lattice. Phase space coordinates, (x, p_x, y, p_y), are tracked across many turns. The calculated Hamiltonian is plotted in Figure 7.10 for two cases: with and without the nonlinear potential turned on. Without the nonlinearity the Hamiltonian is oscillatory with a roughly 400 turn

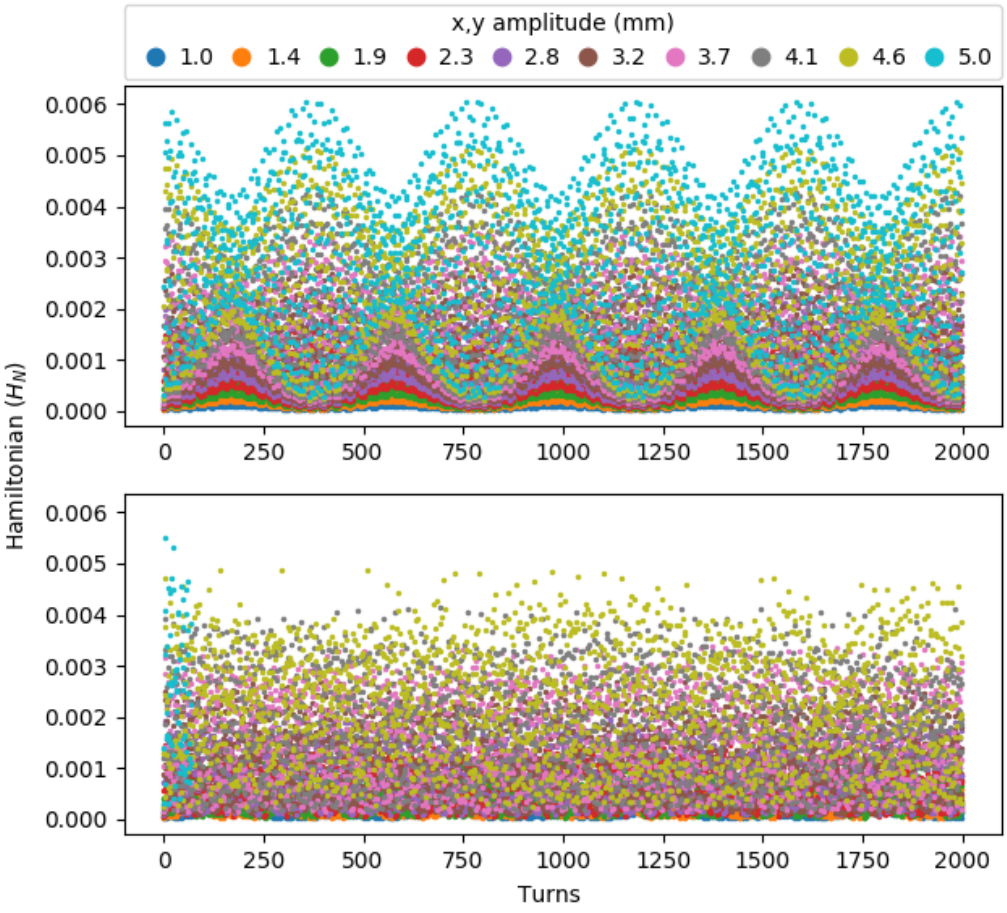

Figure 7.10: (top) Hamiltonian measured over 2000 turns for the case of no nonlinear potential. (bottom) Same measurement with the nonlinear potential turned on. Particles were launched at increasing amplitudes in x and y, marked by color in the plots.

period. With the nonlinearity the motion over many turns becomes a lot more chaotic.

The simulations discussed in this section serve as a starting point on what to expect when doing experimental measurements. While experimental phase space and Hamiltonian measurements will need to be model dependent, frequency maps are purely experimental. The simulated FMAP shows the expected level of tune shift with amplitude and octupole channel strength. If experimental results are

close to these simulations it is a good signal that the models developed here are quite accurate.

7.3 Experiments with Integrable Optics

Experimentally testing NIO theory on UMER involves significant planning and setup. The physical octupole channel needs to be constructed, tested, and installed.The special NIO lattice requires steering work and orbit optimizations. Once a closed orbit is generated the lattice parameters need to be measured and compared to the simulations. When everything related to the lattice and orbit are in an acceptable position, beam measurements with the octupole channel can start. A tune shift measurement is done to determine the level of nonlinearity generated from the channel itself.

7.3.1 Apparatus setup

The installation of the channel on UMER will be discussed in this section. Work on building and testing the octupole channel itself can be found here [10, 11]. Looking at the lattice diagrams in Figure 7.2 and 7.3, the octupole channel is placed in the fourth sector within UMER. A pair of focusing and defocusing quadrupoles are removed to make room. The channel is a tight fit with only a few millimeters of drift space on either end. Extra alluminum plates are squeezed in under the channel to keep it properly elevated and minimize long term movement drifts. A pair of levels are used to reduce any skew rotations in the channel. Heating also becomes

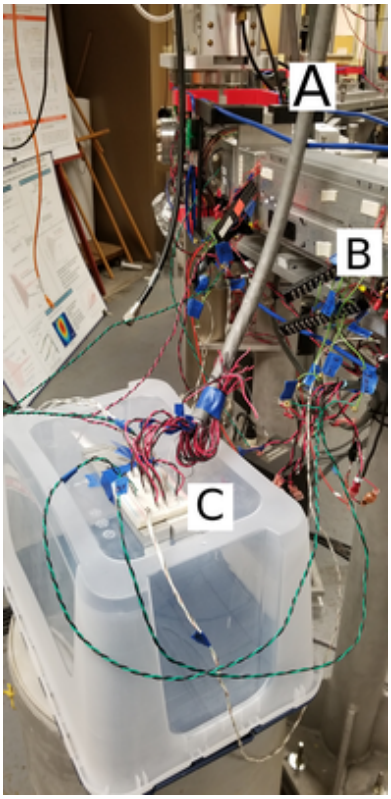

Figure 7.11: The setup of the octupole channel on UMER. (A) Power cables for a set of power supplies dedicated to powering each of the seven octupoles. (B) The octupole channel intself installed in UMER. (C) Breadboard based connection hub for all the octupole power supplies.

an issue as you have several octupole PCBs overlayed on top of each other inside the channel. The heating issue is delt with by not keeping the octupoles powered on for more than a few hours at a time.

Figure 7.11 shows a picture of the octupole channel setup. A new bundle of power supplies were installed with a redirected set of cables to power each individual octupole. A breadboard was used as a connection hub to connect each specific octupole to its dedicated power supply. More details on this connection can be found in appendix F.2. It is important to be careful here as each power supply is programmed in the controls system for a specific octupole; mixing these cables up

will cause lots of problems down the line. There is no automated polarity switch for the octupoles; it requires manually switching the connections on the breadboard. A magnetic compass is used to verify all the octupoles are operating at the same polarities.

7.3.2 Experimental based steering optimizations

Using the simulations, a collection of setpoint values are generated for all the quadrupoles in UMER. Once the quadrupoles are set to their new values steering optimizations are done to improve the orbit in the machine. The simulation generated quadrupole values from Table 7.1 are used as the starting experimental values. The 0.6 mA beam is used throughout the experimental measurements in this chapter. An initial orbit measurement in UMER is first performed. Results can be seen in Figure 7.12.

Figure 7.12 shows a standard set of experimental measurements performed when analyzing the orbit in UMER. The top plot shows a signal measurement from the WCM diagnostic (see section 5.2); this diagnostic provides a way to measure the beam current in the machine at a fast (20 Mhz) frequency. The WCM will be able to show any beam scraping and current loss happening in the ring. In this case we see a steady signal decline over many turns which tells us the beam is immediately scraping on entry into the ring and losing the majority of its current within a few turns. The middle and bottom plots show beam orbit measurements in the horizontal and vertical planes using all available BPMs (see section 5.2). In

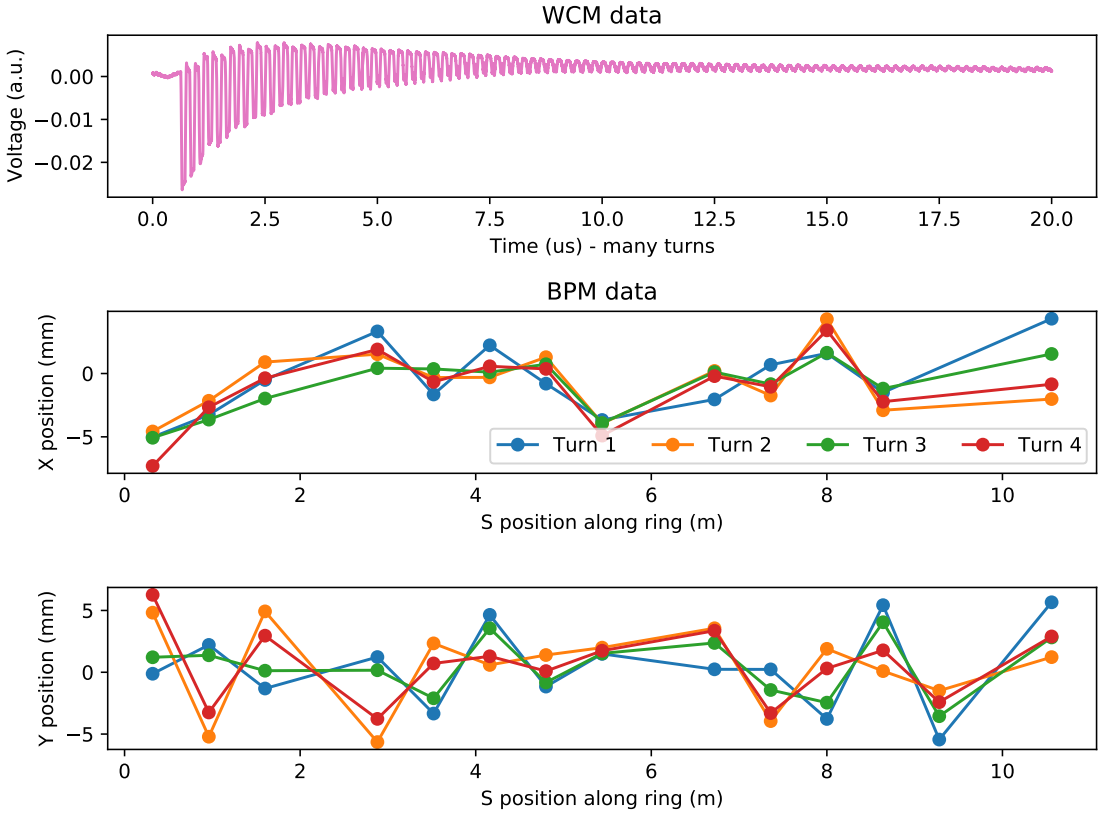

Figure 7.12: (top) A WCM trace. The voltage signal from the WCM is plotted vs time. For reference the beam does 100 revolutions in about 20 μs. (middle and bottom) The BPM signal from all 14 BPMs around UMER plotted for the first four turns. This measurement shows the closed orbit in the ring across four turns. For reference UMER's circumference is 11.52 m.

these plots each line represents one revolution around the ring with measurements taken at each individual BPM. From the four turns of measurements taken it is clear that no distinctive closed orbit is established in this case.

The initial orbit from Figure 7.12 is further improved by running an RCDS optimization routine. The RCDS algorithm from section 4.2 is used along with the objective function from Eq. 8.11 in section 8.2. To summarize, a set of corrector magnets are perturbed to minimize the beam current loss occuring in the ring. The orbit after the optimization is shown in Figure 7.13. The current signal from the

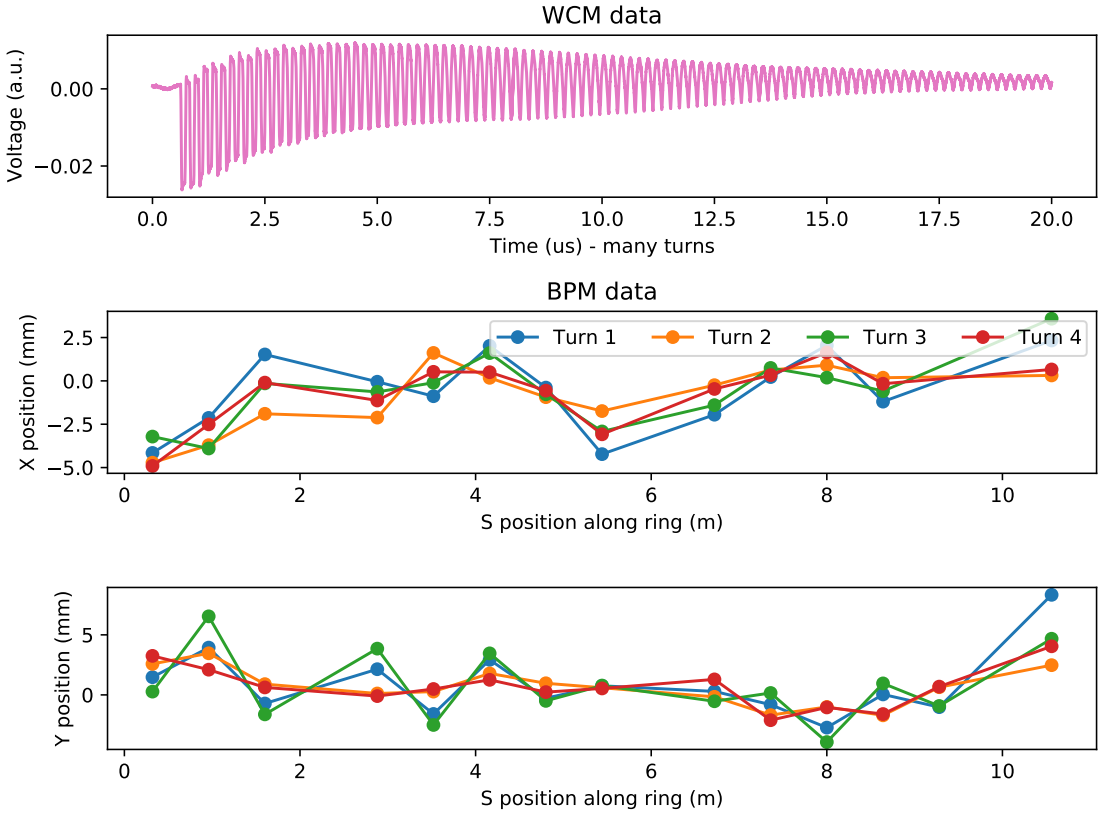

Figure 7.13: Similar plot as Figure 7.12. (top) A WCM trace. (middle and bottom) The BPM signal from all 14 BPMs around UMER plotted for the first four turns.

WCM is significantly improved to the point where there is no longer measurable beam loss occuring. The gradual decrease in current is from the longitudinal expansion of the beam, discussed in section 4.3. Since there was no orbit optimization done, the orbits from Figure 7.12 and 7.13 are only minimally changed due to new corrector magnet setpoints.

Using the newly optimized experimental lattice, a tune response measurement is done. The results of this measurement are inputted back into the simulation model of UMER. Simulation parameters are adjusted to account for the new setpoints of magnets that were tuned during the experimental optimization. The simulations

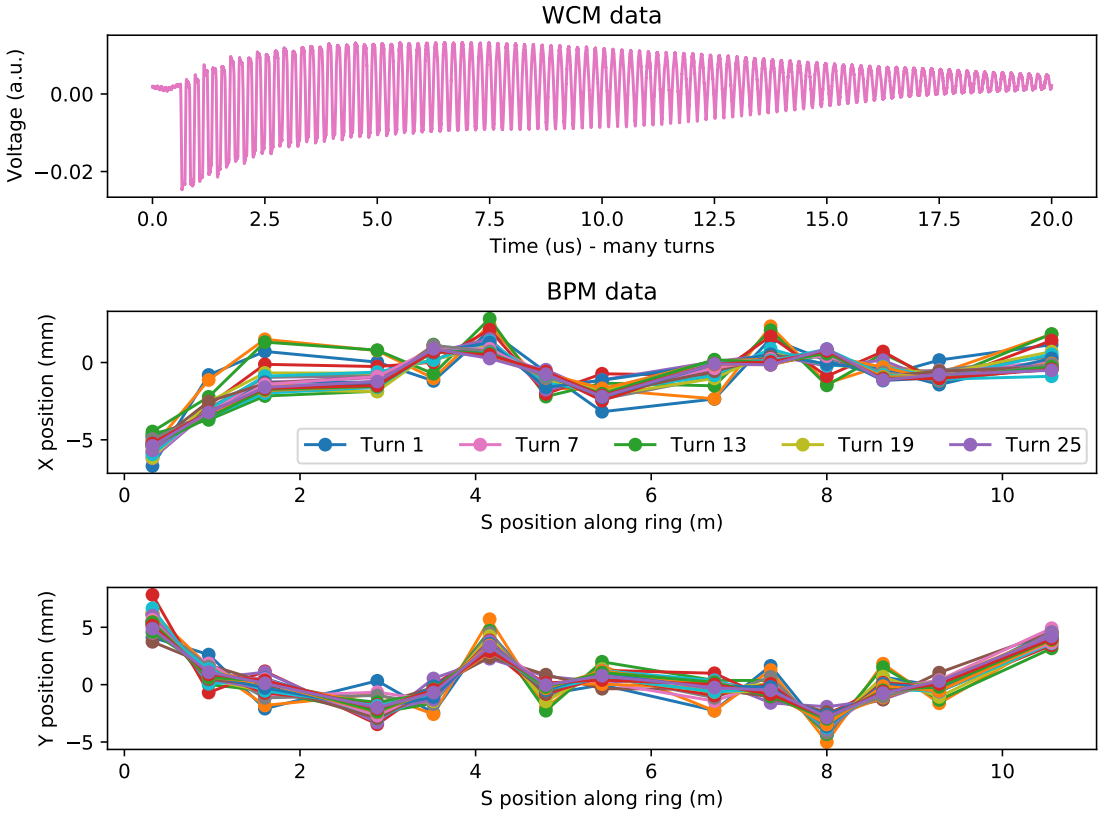

Figure 7.14: Similar plot as Figure 7.12. (top) A WCM trace. (middle and bottom) The BPM signal from all 14 BPMs around UMER plotted for the first four turns.

then output adjusted quadrupole setpoints to account for the experimental optimization of magnets. The new setpoints are setup again on UMER. A repeat of this procedure is done until the experimental beam orbit is at an acceptable position such that measurements can be done with the octupole channel for the nonlinear optics experiment.

Using a 0.6 mA beam, Figure 7.14 shows the final optimized orbit for the nonlinear integrable optics experiment. There is a clear closed orbit established and minimal beam loss. For measuring fractional tunes, injection magnets are perturbed to purposely inject the beam off the closed orbit. As a result, the injection will induce

Q_x	σ_x	Q_y	σ_y
7.155	0.004	7.178	0.005

Table 7.2: Mean and standard deviations of the tunes from an experimental measurement using 14 BPMs and 5 repeat measurements.

large betatron oscillations around the closed orbit allowing for the BPMs to sample the beam's motion. In both the horizontal and vertical directions the orbit is well bounded between ±5 mm. With a beam pipe aperture radius of about 20 mm, the small bounded orbit will allow for a large range of betatron oscillations. If the closed orbit is too large, inducing betatron oscillations would scrape the beam against the pipe walls and cause current loss to occur along with bad measurement data.

Lastly a tune measurement is done to understand where the machine is operating with respect to the nearby resonances. Using BPMs, 5 repeat position measurements were taken. 32 turns of data was used with the NAFF algorithm to calculate the fractional tunes in both the horizontal and vertical directions. The results are plotted in a tune diagram via Figure 7.15. The operating tune is very close to the stable different resonance, $Q_y = Q_x$. The experimental tunes are about $\Delta = 0.05$ off from the simulations, which in UMER's case is close agreement. The tune measurement shows the lattice is in a good location to continue with the octupole channel measurements.

7.3.3 Lattice parameter measurements

Lattice parameters such as betatron amplitudes and phase advances are measured for the NIO experiment lattice. For betatron amplitudes the technique per-

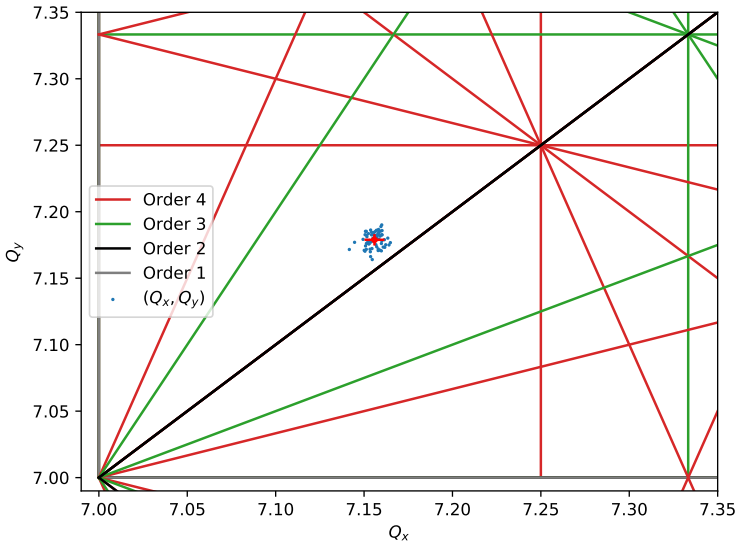

Figure 7.15: A tune diagram with resonances up to 4th order plotted. The blue dots show tune measurements using UMER's BPMs.

turbs each individual quadrupole and measures the tune response of the beam; this is used along with the effective length of the quadrupole to measure an estimate of the betatron function at the quadrupole location. The model dependence comes from the value used for the effective length of the quadrupoles, discussed in 5.1. In equation form this looks like:

$$\beta_{x,y} \approx \pm 4\pi \frac{\Delta Q_{x,y}}{\Delta k} \tag{7.27}$$

where Q is the tune and k is the quadrupole strength. The approximation assumes a small tune change on the order of $2\pi\Delta << 1$ [13].

Results of the betatron measurement is shown in Figure 7.16. The theoretical value based off the model is plotted alongside the experimental value. Note there are no quadrupoles in the octupole channel section so no measurements exist within

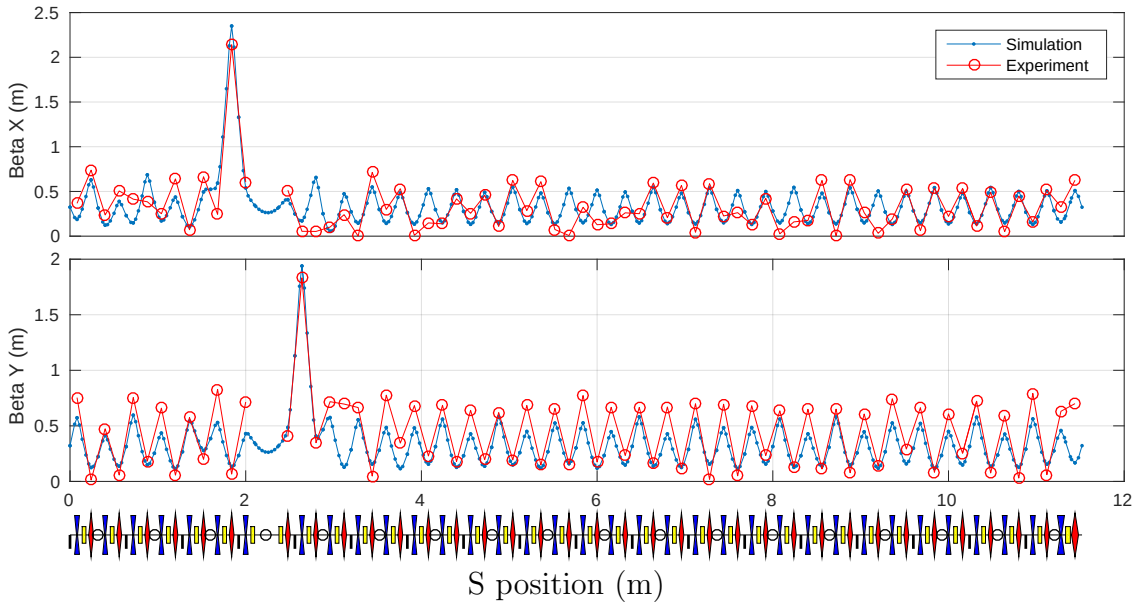

Figure 7.16: Betatron amplitude measurements for the NIO experiment lattice.

the region. The measurement depends on how accurately the tune can be measured. In UMER's case precision tune measurements are easier in the vertical direction as opposed to the horizontal. The high density of dipole magnets in the ring along with the earth's field tend to significantly suppress horizontal betatron oscillations. The large amplitude offsets needed in the horizontal direction in order to induce better betatron oscillations results in large scraping of the beam.

Figure 7.16 shows good agreement between the model and experimental measurements. Betatron function values near the octupole channel region are in close agreement with the model. Outside the octupole channel agreement is still good. In the vertical plane all the measurements are in the right direction, but shifted to a slightly higher betatron value in the experiment; this shows that a slight tweak of the vertical tune in the model should bring the experiment into closer agreement. As discussed in the previous paragraph, horizontal tune measurements are harder to

accurately measure, hense the larger disagreement between model and experimental betatron functions in the horizontal plane. In quadrupole locations where an accurate horizontal tune was able to be measured, there is good agreement between model and experiment. The small values in betatron amplitudes require being able to measure a small change in the tune, which is difficult with UMER's BPMs.

The results in Figure 7.16 show the general procedure taken in designing and simulating the NIO experimental lattice works. While there are plenty of models of UMER, they are mostly static/fixed models, i.e. simulations only agree with experiment for fixed magnet strengths. Once the magnets are perturbed, the agreement is lost. In this case the simulations agreed with experiment for a set of fixed magnet strengths; these magnets were then signficantly changed from their default positions in the simulation in order to design the NIO experiment lattice. At these new setpoints the predictions from the simulations still agreed with what occured on the accelerator. This was achieved by including almost all aspects of the experiment in the simulation, e.g. helmholtz coil fields, corrector magnets, the earth's field; these factors were all included within the simulation and did not have any 'fudge' factors added to them to give better agreement.

Figure 7.17 shows the measurement of the phase advances in the NIO experiment lattice. Phase advances are measured at BPM locations using Fourier analysis on the position signal data; it is an experimental measurement with no model dependence. The experimental data agrees well with the simulations at the BPM measurement locations. The errors ranged from $1 - 20$ degrees in difference. The data also helps confirm that the integer part of the tune in the lattice is indeed 7.0.

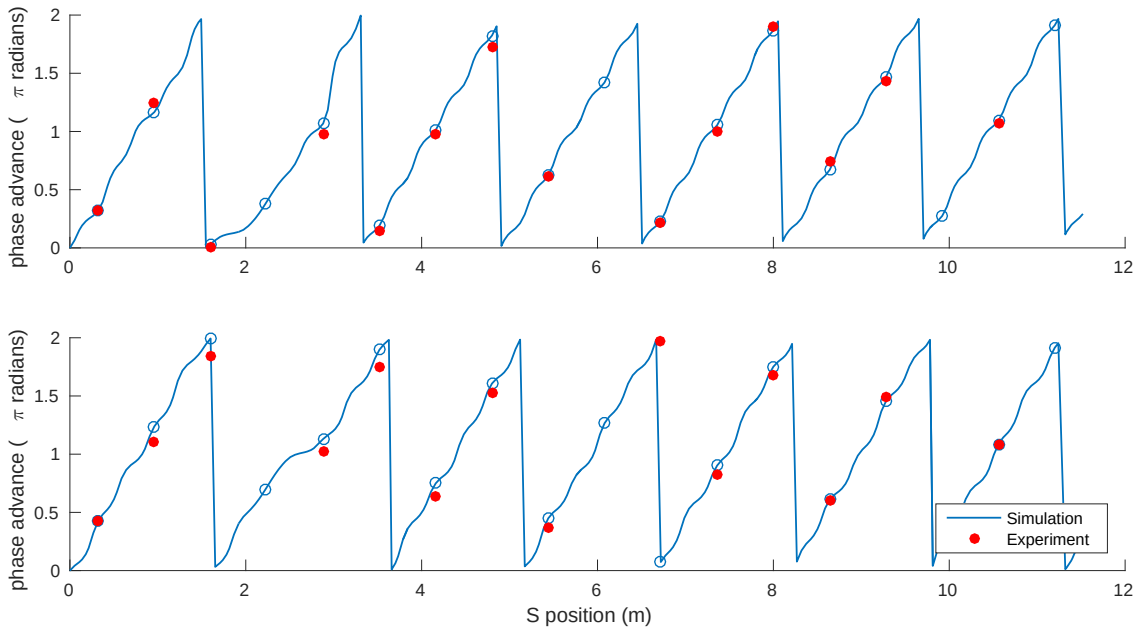

Figure 7.17: Phase advances for the NIO experiment lattice. The circles are BPM locations where measurements are taken. Red circles represent experimental measurements.

The phase advance data allows the ability to measure the $n\pi$ phase advance requirement condition for the NIO theory. The theory requires the phase advance outside the octupole section to be an integer of π, $\Delta\Psi = n\pi$. Using the measurement data along with required simulation data, an approximate value for the phase advance outside the octupole section can be calculated. Looking at Figure 7.18, $n\pi = A - B$, meaning the phase advance outside the octupole channel is equal to the phase advance across the full ring minus the phase advance through the octupole channel section. The problem is that there are no BPMs at the locations needed to perform this measurement. The distance 'D' in Figure 7.18 is the phase advance between BPMs 3 (RC3) and 5 (RC5), this is the only measurement that can be done experimentally. Thus, some simulation based phase advance values have to be used along with the experimental data to measure the $n\pi$ requirement. In this case

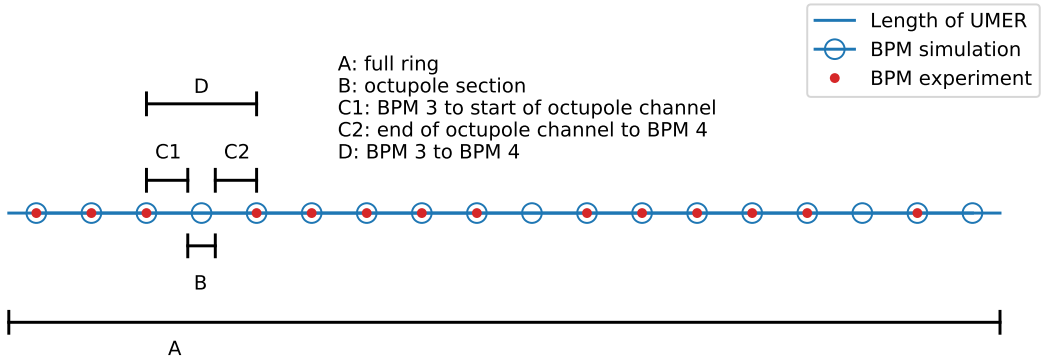

Figure 7.18: A schematic to help illustrate the calculation method used for measuring the $\Delta\Psi = n\pi$ phase advance requirement.

	Simulation (π)	Experiment (π)	Error (%)
$\Delta\Psi_x = n\pi$	$n = 14.01$	$n = 14.07$	0.4
$\Delta\Psi_y = n\pi$	$n = 14.01$	$n = 13.97$	0.3

Table 7.3: Simulation and experimental values for the $n\pi$ phase advance requirement in NIO theory.

'C1' and 'C2' are phase advances from the BPM to the octupole channel; this data is taken from the simulation. With this data the phase advance across the octupole section is $B = D - (C1 + C2)$ and the $n\pi$ phase advance is:

$$\Delta\Psi = n\pi = A - D + (C1 + C2) \tag{7.28}$$

where A, C1, and C2 are all phase advances from simulation and 'D' is the phase advance from experiment. Results are shown in Table 7.3 and show good agreement with percent error being $< 1\%$.

The measurements in this section show that the experimental lattice meets all the required conditions to properly test NIO theory. The betatron amplitudes match

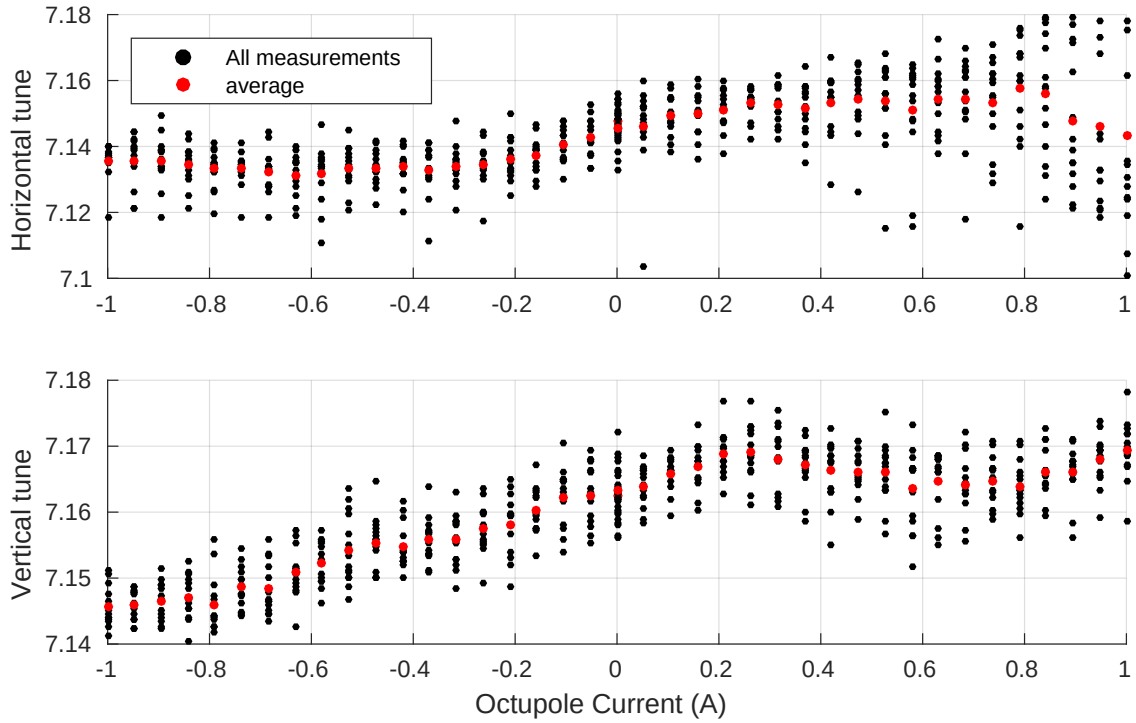

Figure 7.19: A experimental measurement of the transverse tune vs the strength in the octupole channel. The black dots represent all measurements with every BPM. The red dots are the average measurement across BPMs.

the simulations and are equal through the octupole channel section. The phase advances meet the $n\pi$ requirement to within one percent, based on a model dependent measurement. The measured tunes also match the tunes from the simulations.

7.3.4 Nonlinear tune shift measurements

A transverse tune measurement is the simplest way to quantitatively measure the amount of nonlinearity the octupole channel introduces into the accelerator system. The transverse tune in the accelerator is a function of the nonlinear octupole magnet strengths. Measuring the tunes gives a measurement of the amount of nonlinearity. These experimental measurements can then be compared to simulation.

The first measurement looks at the shift in tune as a function of octupole channel magnet strength. Figure 7.19 shows these results. The octupole strength is slowly increased from 0 to 1 amp while measuring the transverse tunes using the BPMs. 32 turns of position data along with the NAFF algorithm were used to measure the tunes. In order to get a measurement at negative octupole strengths/currents, the power cables for the octupole magnets are flipped; this is done manually, making the measurement in Figure 7.19 actually two separate measurements at positive and negative currents. The measurements show a tune shift on the order of $\Delta Q_x \approx 0.02$ and $\Delta Q_y \approx 0.03$, which is very small.

The results from Figure 7.19 are taken and plotted in tune space along with nearby resonances up to 4th order. Figure 7.20 shows the measurements. There is no clear pattern in the tune shift from Figure 7.20. The nearby difference resonance, $Q_x = Q_y$, is not a destructive resonance and does not negatively affect the beam. It is also unclear at what amplitudes in the transverse direction, x and y, the beam passes through the octupole channel. To better understand the experimental measurement in Figures 7.19 and 7.20 a simulation is done using the same conditions of the experimental measurement. Since the transverse amplitudes of the beam through the octupole channel is unknown, a range of different amplitudes is used in simulation. Results are shown in Figure 7.21. Here the beam is injected with various transverse amplitudes. The tune is then measured as a function of the octupole strength. Like the experiment, 32 turns of position data along with the NAFF algorithm is used for tune measurements.

From Figure 7.21 it is clear that the tune shift as a function of octupole

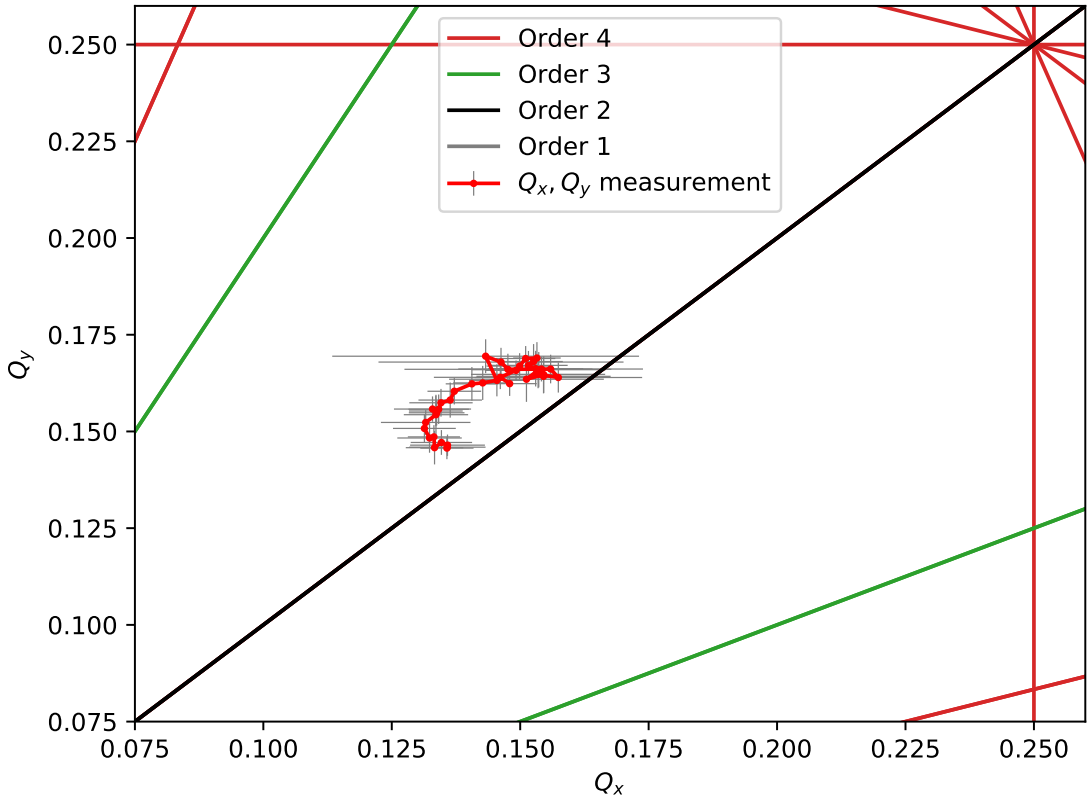

Figure 7.20: The fractional tune measurements from Figure 7.19 are replotted in tune space. The mean values are in red and the error bars represent the standard deviations of each measurement point. Note the measurement is plotting tune as a function of octupole strength in tune space.

strength is significantly different depending on the beam's transverse amplitude. The middle plot in Figure 7.21 with 2 mm transverse amplitudes is the closest to the experimental measurement in Figure 7.20. One thing the simulations also show is that replicating the frequency map level of tune shifts from Figure 7.8 is not possible by doing a tune shift vs octupole strength measurement. Thus instead of having a fixed beam oscillation amplitude and varying the octupole strength, the octupole strength must be fixed while varying the beam's oscillation amplitudes. Before attempting such a measurement experimentally, simulations are done to show the

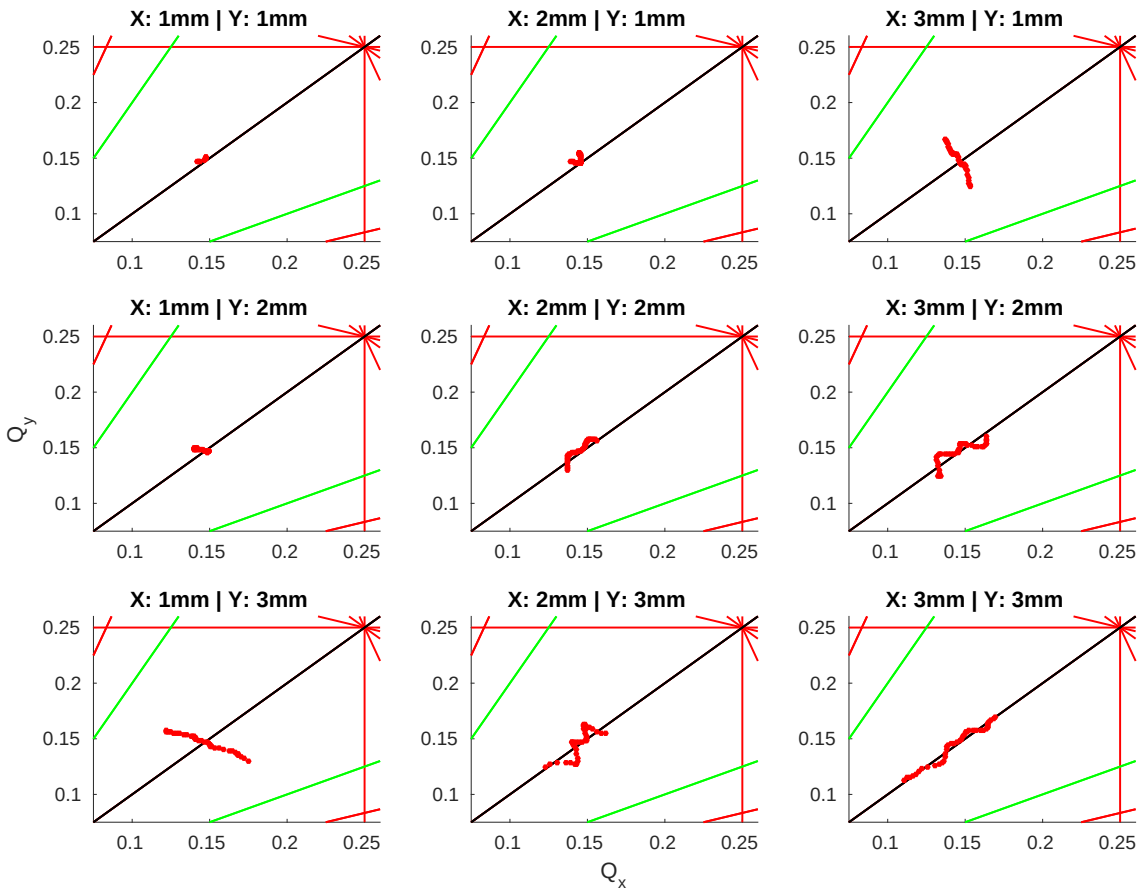

Figure 7.21: Simulation of the measurement from Figure 7.20. The beam is injected at a fixed transverse amplitude. The fractional transverse tunes are then measured as a function of the octupole strength.

expected tune shift behavior.

Figure 7.22 shows a simulation of the expected transverse tune shift as a function of varying beam oscillation amplitude. Simulations are done for various settings and cases to serve as a basis for understand the eventual experimental measurements. In this case measurements are done at three different octupole channel strengths, 0.25, 0.5, 1.0 amps, and using three different lengths of position data at 16, 32, 64 turns. The pattern in the simulations is clear: the stronger octupole strength creates a larger amplitude dependent nonlinear tune shift. The more turns available for

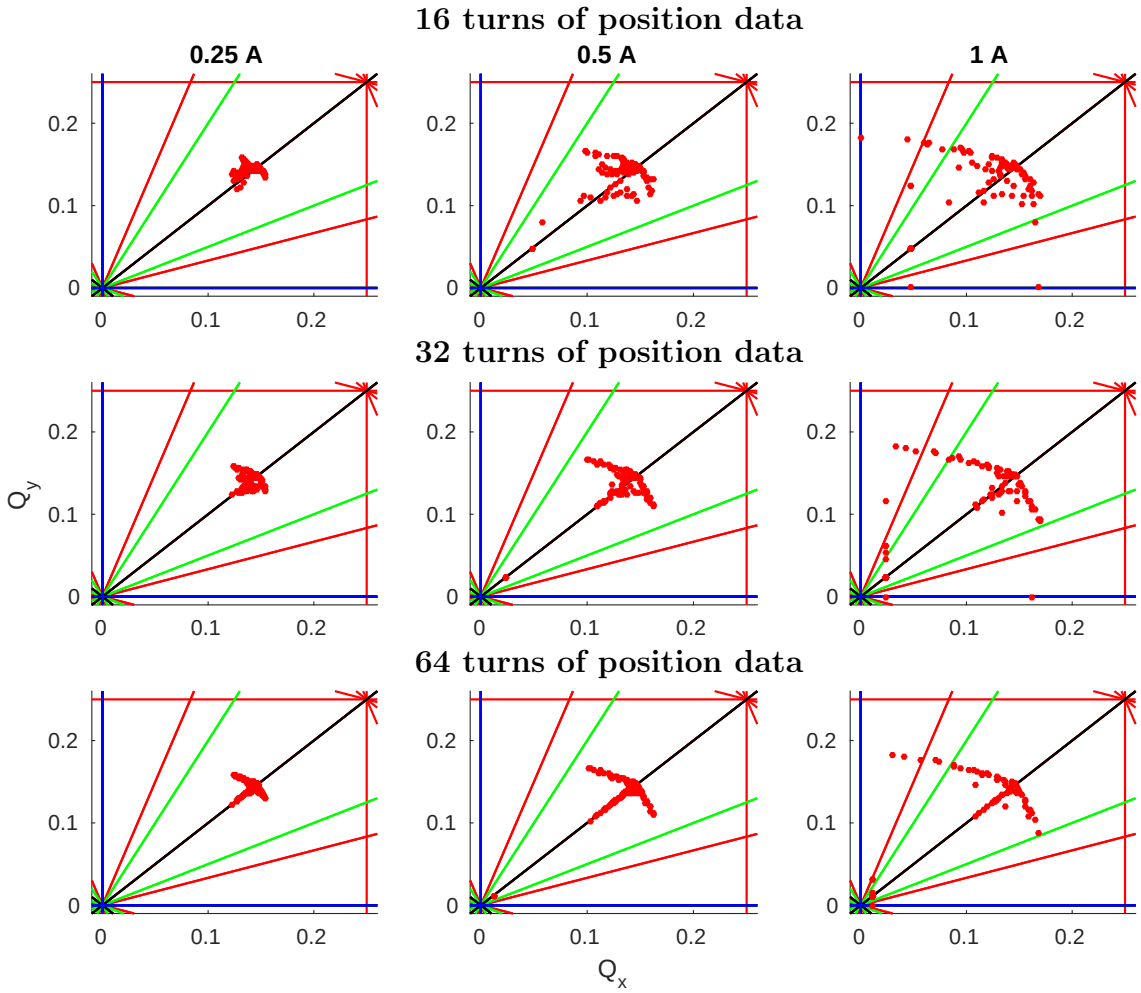

Figure 7.22: Simulation of the tune shift through the octupole channel with varying transverse beam oscillation amplitudes. Simulations are done at three different octupole strengths using 16,32, and 64 turns of position data. The beam's amplitudes are varied from 0.1 to 5 mm in both the horizontal and vertical directions.

analysis results in more accurate tune measurements, meaning the nonlinear tune shift will be much more defined in the data.

An experimental measurement is ran to compare results to the simulations from Figure 7.22. The results are in Figure 7.23. In order to create the desired transverse amplitude variations for the measurement two corrector magnets in the injection line (SD6H,SD5H) were used to inject the beam into the ring at different transverse amplitudes. For the experimental measurement only 16 and 32 turns

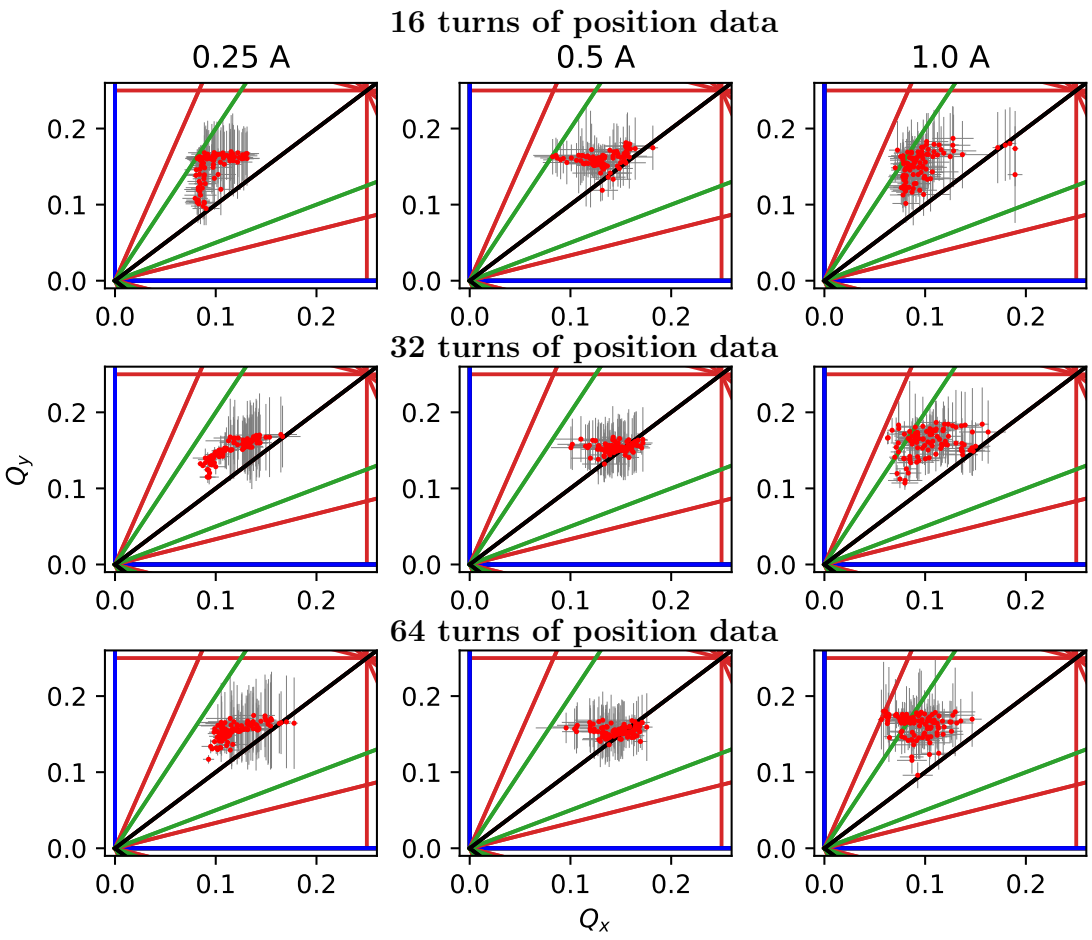

Figure 7.23: Experimental measurement of the tune shift through the octupole channel with varying transverse beam oscillation amplitudes. Measurements are done at three different octupole strengths using 16,32, and 64 turns of position data. The red dots are fractional tune measurements and the grey lines are the standard deviations of the measurement across different BPMs.

of position data is accurate enough to use for the 0.6 mA beam. The longitudinal expansion due to space charge does not allow good measurements up to 64 turns. In terms of octupole channel strength, 0.25 and 0.5 amps result in the best usable data. With 1 amp through the octupole channel it is difficult to establish a closed orbit centered enough to induce large amplitude oscillations without significant amounts of beam scraping. Any large amount of beam scraping makes it impossible to accu-

rately measure the transverse tunes.

Looking at Figure 7.23, the results at the low octupole strength of 0.25 Amps show the best results, especially for the 32 turn data. In this case the measurements have the smallest error bars and the clearest tune shifts occuring. At the same time the tune shift does not match the expected pattern from the simulation in Figure 7.22; it almost seems like the experimental measurement of tune shift is rotated compared to the simulations.

Figure 7.23 summarizes the final measurements in a single graphic. To get to that point a lot of detailed analysis was performed on the experimental data. Much of this work is left out of the chapter and discussed in the Appendix. The reader is encouraged to refer to Appendix F.3 for a more in-depth exploration of the measurement data.

7.4 Chapter Summary

This chapter discusses all the work involved with the nonlinear integrable optics experiment at UMER over the last two years. The chapter is broken down into three sections. The first section discusses the theory of nonlinear integrable optics including the case of a quasi-integrable invariant. The second section discusses the efforts taken to design and simulate the quasi-integrable optics experiment. Different lattices are setup and optimized to meet the theory requirements and practical implementation requirements in UMER. The third section discusses the experimental setup of the octupole channel and UMER lattice. Steering optimizations are

done on the implemented lattice to adjust the closed orbit. Lattice parameters are measured experimentally and compared to the simulation results to see how the two compare. Lastly nonlinear amplitude dependent tune shift measurements are taken using the octupole channel magnets. Results are compared to simulations. Appendix F further discusses the experimental measurements in detail.

Chapter 7: Bibliography

[1] V. Danilov and S. Nagaitsev. Nonlinear accelerator lattices with one and two analytic invariants. *Phys. Rev. ST Accel. Beams*, 13:084002, Aug 2010.

[2] Ernest D. Courant, M. Stanley Livingston, and Hartland S. Snyder. The strong-focusing synchroton—a new high energy accelerator. *Phys. Rev.*, 88:1190–1196, Dec 1952.

[3] K. Ruisard, H. B. Komkov, B. Beaudoin, I. Haber, D. Matthew, and T. Koeth. Single-invariant nonlinear optics for a small electron recirculator. *Phys. Rev. Accel. Beams*, 22:041601, Apr 2019.

[4] L. Dovlatyan, T.M. Antonsen, B.L. Beaudoin, I. Haber, D.B. Matthew, and K.J. Ruisard. Preliminary Lattice Studies for the Single-Invariant Optics Experiment at the University of Maryland. In *Proc. 10th International Partile Accelerator Conference (IPAC'19), Melbourne, Australia, 19-24 May 2019*, number 10 in International Partile Accelerator Conference, pages 367–370, Geneva, Switzerland, Jun. 2019. JACoW Publishing. https://doi.org/10.18429/JACoW-IPAC2019-MOPGW105.

[5] Vladimir Arnold, Valery Kozlov, and Anatoly Neishtadt. *Mathematical Aspects of Classical and Celestial Mechanics*. Springer-Verlag Berlin Heidelberg, 2006.

[6] H. Goldstein, C.P. Poole, and J.L. Safko. *Classical Mechanics*. Addison Wesley, 2002.

[7] S. Antipov, D. Broemmelsiek, D. Bruhwiler, D. Edstrom, E. Harms, V. Lebedev, J. Leibfritz, S. Nagaitsev, C.S. Park, H. Piekarz, P. Piot, E. Prebys, A. Romanov, J. Ruan, T. Sen, G. Stancari, C. Thangaraj, R. Thurman-Keup, A. Valishev, and V. Shiltsev. IOTA (integrable optics test accelerator): facility and experimental beam physics program. 12(03), mar 2017.

[8] F.H. O'Shea, R.B. Agustsson, Y.C. Chen, D.W. Martin, J.D. McNevin, and E. Spranza. Non-linear Magnetic Inserts for the Integrable Optics Test Accelerator. In *Proc. 6th International Particle Accelerator Conference (IPAC'15), Richmond, VA, USA, May 3-8, 2015*, number 6 in International Particle Accelerator Conference, Geneva, Switzerland, June 2015. JACoW.

[9] Kiersten Ruisard. *Design of a nonlinear quasi-integrable lattice for resonance suppression at the University of Maryland Electron Ring*. PhD thesis, University of Maryland College Park, 2018.

[10] H. Baumgartner et al. Quantification of Octupole Magnets at the University of Maryland Electron Ring. In *Proc. of North American Particle Accelerator Conference (NAPAC'16), Chicago, IL, USA, October 9-14, 2016*, number 3 in North American Particle Accelerator Conference, pages 503–506, Geneva, Switzerland, Jan. 2017. JACoW.

[11] D. Matthew, W. Curtiss, H. B. Komkov, and B. Beaudoin. Characterization of the nonlinear focusing magnet for quasi - integrable optics experiments at the university of maryland electron ring. In *2018 IEEE Advanced Accelerator Concepts Workshop (AAC)*, pages 1–4, 2018.

[12] J Laskar and D Robin. Application of frequency map analysis to the als.

[13] Frank Zimmermann. Measurement and correction of accelerator optics. (SLAC-PUB-7844):89 p, Jun 1998.

Chapter 8: Steering, Orbit Control, and Current Maximization

An important aspect in many experiments in UMER is precision beam control. The beam quality is generally dependent on the tuning of closed orbits, maximization of beam lifetimes, and the optimization of injection. The ideal goal in UMER, and many other accelerator systems, is to have the beam centered through the quadrupoles in the lattice; this results in an optimal closed orbit with minimal steering issues.

Orbit tuning is done using corrector magnets in the lattice: a type of horizontal/vertical dipole magnet that in the ideal case gives the beam a kick in the x' or y' directions without affecting the motion in x and y. In general it is beneficial to have a corrector magnet upstream from each quadrupole for the specific purpose of adjusting the beam orbit through the quadrupole center. In UMER, and shown in Figure 5.7, there is only one upstream vertical corrector per four quadrupoles and one upstream horizontal corrector per two quadrupoles. Table 8.1 summarizes the total number of correctors in the ring. With 72 quadrupoles, there is 36 horizontal correctors with one extra to help with injection. Note that UMER does not have traditional horizontal correctors. Instead each dipole magnet is individually powered and used as a corrector. Unlike other rings with fixed dipoles, UMER has to

Magnet	Total
Quadrupoles	72
Horz. Correctors (dipoles)	37
Vert. Correctors	31
BPMs	14

Table 8.1: UMER storage ring magnets.

adjust its dipole magnets each time the closed orbit requires retuning. In the vertical direction there are 18 correctors for 72 quadrupoles. Recently 13 more vertical correctors have been added with the goal being to increase the number of vertical correctors to 36, matching the number of horizontal correctors.

The nonuniform earth's field and the limited number of corrector magnets means there are not enough free parameters to center the beam through every quadrupole; this presents a challenge in beam steering within UMER. As a result, a set of unique techniques have been developed for steering and orbit control. This chapter discusses these techniques in detail. Section 8.1 covers first-turn steering and the establishment of a closed orbit. Section 8.2 discusses orbit control tuning and current maximization. These methods are performed as necessary in UMER for different experiments. The experimental results in have been found to depend on the relative success of the steering done beforehand. Thus it is important to discuss exactly how these methods are performed on the accelerator.

8.1 First-Turn Steering

There are many challenges that need to be overcome when commissioning UMER for a new experiment. One of these challenges is getting the particle beam through the first turn of the accelerator. Different methods have been developed within the accelerator physics community for exactly this purpose with active research ongoing with in the field [1]. UMER is a unique facility in regards to comissioning work; it is a small machine with the capability to setup different lattice configurations for different experiments in a short amount of time.

New lattices in UMER can move very quickly from the design and simulate stage to the experiment stage. As an example, a lattice design for the nonlinear integrable optics experiment can be simulated and experimentally setup in a single day. A set of computational software tools were designed to help the entire design to experiment process move quickly. This section presents on the computational techniques that go into commissioning the beam through the first turn for a given lattice.

8.1.1 Beam-based quad centering

As discussed above, steering the beam through the center of quadrupole magnets reduces the amount of changes that can occur in the closed orbit when perturbing quadrupole magnets. Centering the beam through a quadrupole magnet can be done using an upstream corrector magnet and a downstream BPM. The centering technique is as follows:

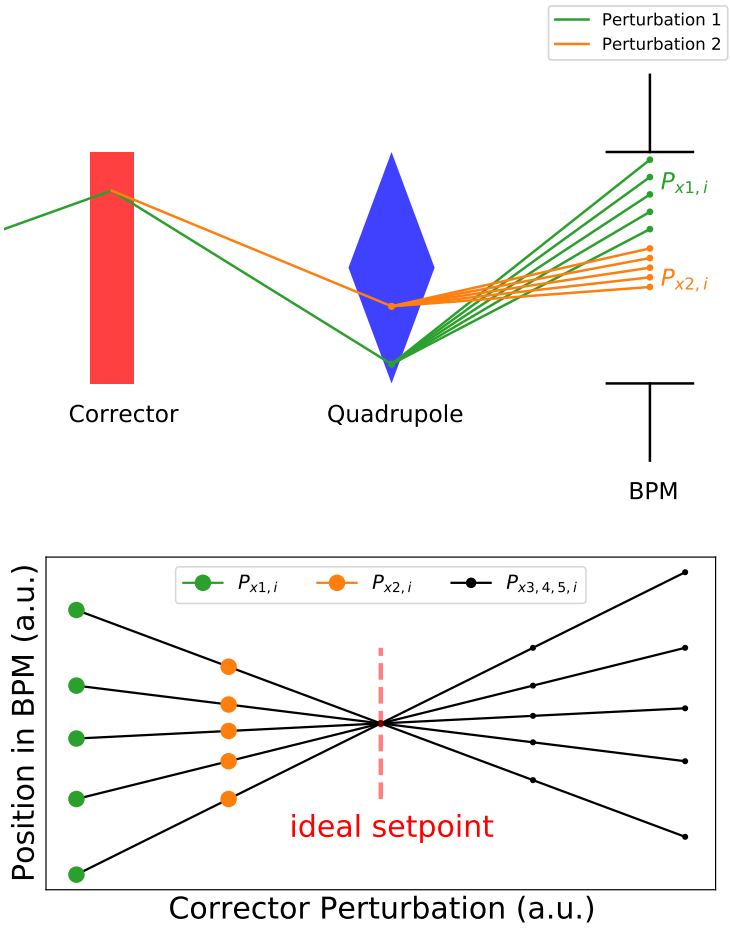

Figure 8.1: (top) A schematic showing how the beam will respond when perturbing a corrector and quadrupole. (bottom) A plot of the BPM responses from perturbing the corrector and quadrupole.

1. For a given corrector magnet operating strength, perturb the quadrupole strength and measure the beam response at the BPM location.

2. Continue perturbing the corrector magnet operating strength to new values and repeat the quadrupole perturbation and BPM response measurement at each corrector magnet operating strength.

The top of Figure 8.1 shows a schematic of the quadrupole centering technique. If the measurements are accurate, a plot similar to the bottom of Figure 8.1 is

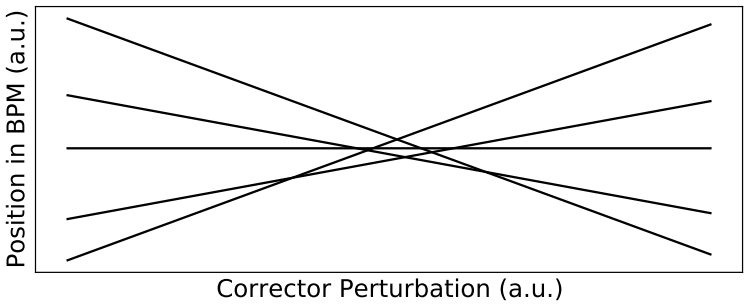

Figure 8.2: A quad centering measurement similar to Figure 8.1, but with imperfect BPM data.

generated. The lines show the BPM responses plotted vs corrector setpoint. At each corrector value the quadrupole is perturbed and BPM responses measured. Ideally if the beam is passing through the center of the quadrupole, there should be no response in the BPM when said quadrupole is perturbed. Looking at the plot in Figure 8.1, this point corresponds to the intersection of all the lines. The corrector setpoint at that location results in the beam passing through the center of the quadrupole. In an ideal perfect world only two points, and as a result, two perturbations would be needed to find an equation for the line in Figure 8.1. Experimentally, many measurements and perturbations are taken to account for noise and errors when finding an equation for the line.

Experimentally, the lines in Figure 8.1 are never going to intercept perfectly. A more realistic result is shown in Figure 8.2. Visually it is easy to see where the ideal interception point would be in Figure 8.2. The challenge comes in trying to quantitatively calculate the closest interception point. The problem is presented as trying to minimize the distance between the interception point, $P(x_0, y_0) = (x_0, y_0)$, and all the quadrupole perturbation lines, $L_i(a, b, c) = ax + by + c = 0$, where i

ranges from one to the total number of lines, N. Mathematically:

$$C = \min: \sum_{i}^{N} d_i^2 \tag{8.1}$$

where d_i is the perpendicular distance between a line and the closest interception point:

$$d(L_i(a,b,c), P(x_0,y_0)) = \frac{|ax_0 + by_0 + c|}{\sqrt{a^2+b^2}} \tag{8.2}$$

Eq. 8.1 is minimized by taking partial derivatives with respect to x_0, y_0 and solving the set of equations for the interception point, $P(x_0, y_0)$, as a function of all the perturbation lines, L_i:

$$\frac{\partial C}{\partial x_0} = 0 \ , \ \frac{\partial C}{\partial y_0} = 0 \tag{8.3}$$

The details of the calculation are nontrivial and left to Appendix G.1.

The calculation allows a quantitative measure of the setpoint required in a corrector magnet to center the beam through a specific quadrupole. The coefficients of the perturbation lines in Figure 8.2 and 8.1 are experimentally measured by doing a linear fit on the BPM data. In order to speed up the process of centering the beam through the many quadrupoles, a software controls tool was developed within Matlab, shown in Figure 8.3. The tool allows the ability to select a corrector magnet (horizontal or vertical), a quadrupole, and a BPM to apply the centering algorithm. A measurement is done by perturbing the corrector and quadrupole five times each. Results are plotted within the GUI. The calculated interception point is shown and a button allows the corrector setpoint to be changed to the newly calculated point.

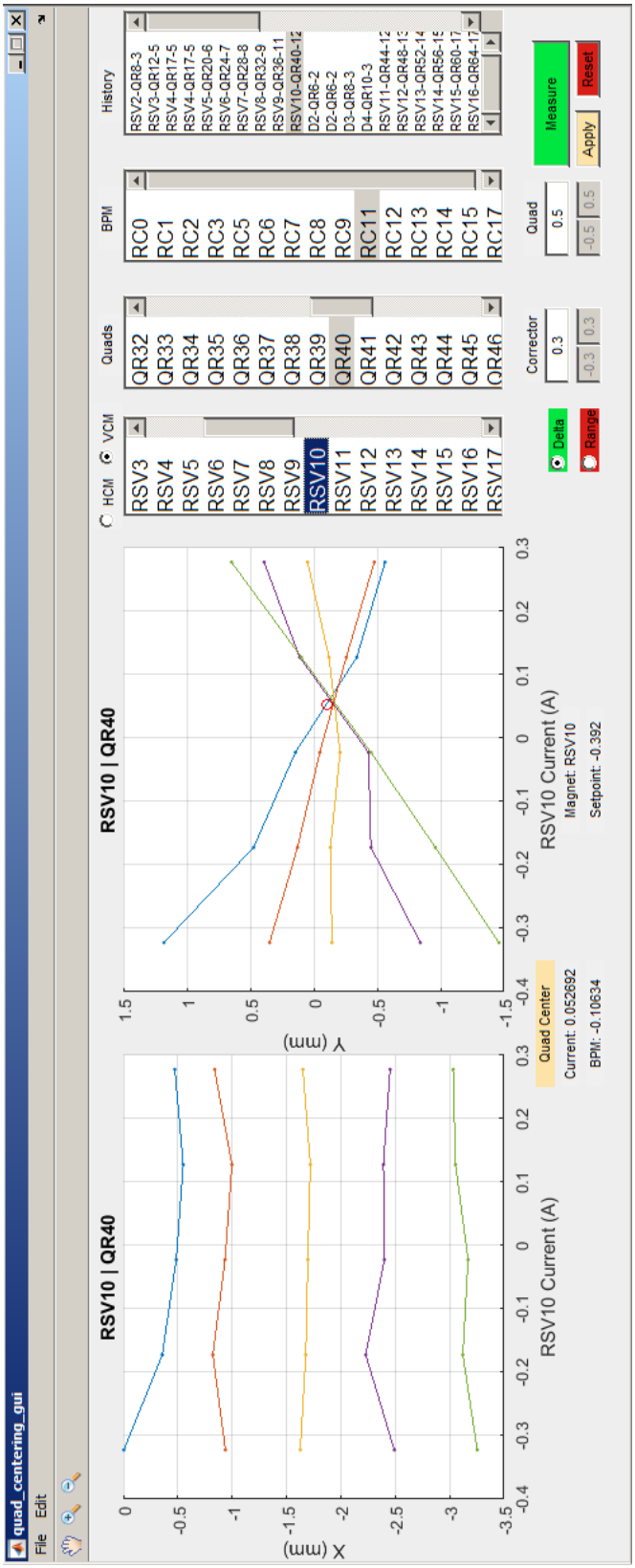

Figure 8.3: Software tools developed to quickly run quadrupole centering algorithms on UMER.

A history is kept of every measurement and automatically saved. Old measurements can be reloaded up to look at plots and old setpoints.

Looking at Table 8.1, there are not enough correctors for centering through every quadrupole. Each section in UMER has 1 vertical corrector, 2 horizontal correctors, and 4 quadrupoles. As a result, the beam can be centered through one quadrupole vertically and two quadrupoles horizontally per a section in UMER (UMER has 18 sections). The question then becomes which of the four quadrupoles should the beam be centered through? For the vertical corrector it is the third quadrupole and for the horizontal correctors it is quadrupoles two and four. Simulation was done to show that centering through these quadrupoles best minimizes deviations of the orbit from the magnet center [2].

8.1.2 Quadrupoles as virtual BPMs

The high density of magnets and other equipment on particle accelerators limits the room for diagnostics equipment; this has lead to the skillful development of beam-based virtual diagnostics. In this case it is the use of a quadrupole magnet as a BPM. This technique only works on the first revolution around an accelerator as it assumes the beam's initial conditions into the quadrupole do not change when said quadrupole is perturbed; this condition is only true on the first pass through the magnet. Extensive work has been done on this topic at UMER, see for example [2, 3]. This section provides a brief overview of the technique with experimental examples. For more information the reader is encouraged to refer to the references.

When a beam passes through a quadrupole magnet at a position x_Q, the position at a downstream BPM can be calculated as:

$$\begin{pmatrix} x_{bpm} \\ x'_{bpm} \end{pmatrix} = M_{Q\to BPM} \begin{pmatrix} x_Q \\ x'_Q \end{pmatrix} \tag{8.4}$$

where $M_{Q\to BPM}$ is the transfer map between the quadrupole and BPM. If the quadrupole is perturbed a response will occur at the BPM location. Perturbing the quadrupole will change x'_Q, but not x_Q, i.e. $\Delta x_Q = 0$. The peturbed equation can then be written as:

$$\Delta x_{bpm} = M_{12} \Delta x'_Q \tag{8.5}$$

with M_{12} being the matrix element in $M_{Q\to BPM}$. Through some algebra it can be shown that the change in angle through the quadrupole is related to the perturbation of the quadrupole strength:

$$\Delta x'_Q = \frac{l_{eff} B}{B\rho} \frac{\Delta I}{I} = \frac{l_{eff}\, x_Q\, g_{eff}}{B\rho} \frac{\Delta I}{I} \tag{8.6}$$

where l_{eff} is the effective length of the quadrupole, B is equal to the quadrupole gradient at the location x_Q in the quadrupole, $B\rho$ is the beam rigidity, and I is the quadrupole strength in units of amps. Combining Eq. 8.5 and 8.6 leads to:

$$x_Q = \frac{\Delta x_{bpm}}{\Delta I} \frac{B\rho\, I}{l_{eff}\, g_{eff}} \frac{1}{M_{12}} \tag{8.7}$$

Eq. 8.7 shows that the position of the beam inside a quadrupole, x_Q, can be

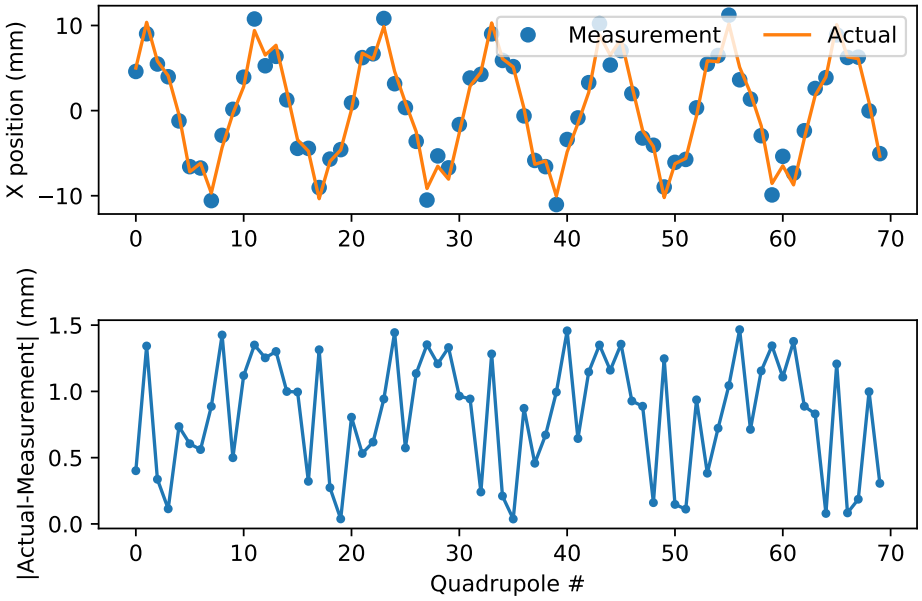

Figure 8.4: (top) A simluation that uses Eq. 8.7 to measure the position in a quadrupole and compare it to the true position. (bottom) The difference from the measurement and actual value.

indirectly found by perturbing said quadrupole and measuring the response at a downstream BPM. The effective length and strength, l_{eff}, g_{eff}, of the quadrupole needs to be known. The values come from Table 5.1 or 5.2. The matrix element, M_{12}, between the quadrupole and BPM is calculated via simulation. A betatron phase advance of 90 degrees between the chosen quadrupole and BPM will result in the largest value for M_{12} giving the smallest sensitivity error.

Figure 8.4 shows a simulation measurement using Eq. 8.7. The position in each quadrupole is measured and compared to the true positions. No random noise error was added to the simulation. The bottom of Figure 8.4 shows the relative difference between the simulated measurement and the actual position values to be on the order of 1 mm. For comparison, the uncertainty in experimental BPM measurements is on the order of 0.1 mm (see Figure 3.15).

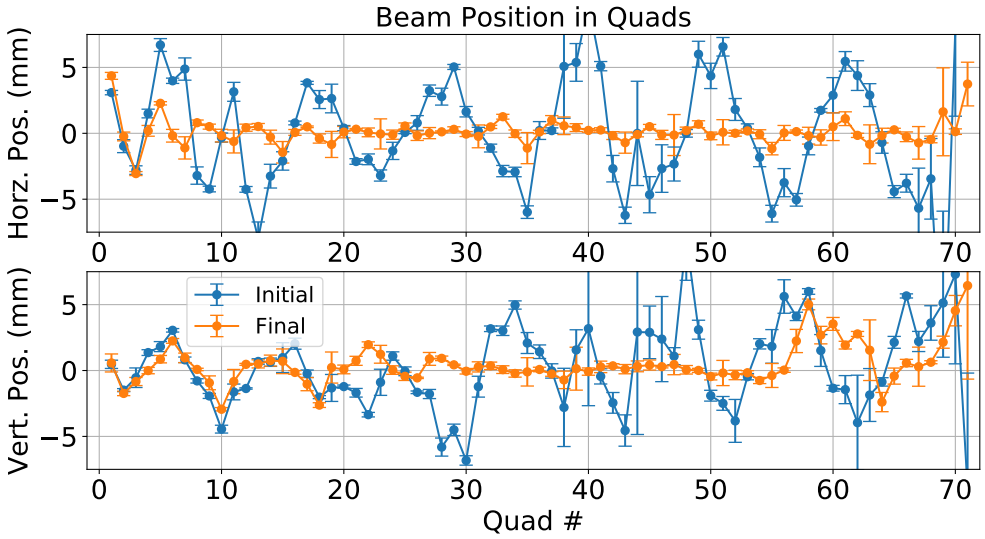

Figure 8.5: Experimental measurement where the beam is centered through the quadrupoles on the first pass through UMER. The quadrupoles as virtual BPMs technique is used to experimentally measure the beam's location at the quadrupoles.

Combining the quadrupole centering technique and the virtual BPMs allows for centering the orbit through the quadrupoles and then measuring the positions within the quadrupoles to verify accuracy and errors in centering of the orbit. This is demonstrated in Figure 8.5. The initial orbit is measured via virtual BPM technique. The beam is then centered through a set of quadrupole magnets. After centering, the positions in the quadrupoles are re-measured. The result of the quadrupole centering is a smaller orbit closer to the magnet centers. Note that the vertical orbit near quadrupoles 65-70 is large because of a missing helmholtz coil at the time. The larger orbits near the injection point, near quadrupoles 1-5 and 65-70, is a result of the fast pulsed magnets and the nonlinear fields they generate in the region. A set of corrector magnets near injection are also used to match and close the orbit from turn one to turn two. This is done by using an experimental optimization

technique, usually RCDS (this is discussed in the next section). The error bars in Figure 8.5 correspond to the errors in the linear fits done to calculate the $\Delta x_{bpm}/\Delta I$ term from Eq. 8.7.

8.2 Orbit Tuning and Beam Loss Minimization

After guiding the beam through the first turn of an accelerator and establishing a closed orbit, a new set of tools are used to tune and optimize said closed orbit. Using model based tools such as LOCO – briefly discussed at the beginning of section 5.3 – is a common approach to orbit tuning. If the model of the accelerator system is accurate enough it can be used to predict the magnet adjustments needed to tune the experimental accelerator. There are however situations where model based tuning is not possible. Difficult to model sections of an accelerator such as transfer/injection sections require more direct experiment based tuning. Often times an experienced operator will manually tune magnets around injection to maximize the amount of beam current that makes it into the accelerator. If such tasks can manually be done by a human operator, then a set of algorithms should be able to be developed to perform the same tasks.

In recent years machine learning has made its way into the accelerator physics field. The algorithms have been applied to many problems within the community [4]. One set of problems being accelerator controls. Machine learning techniques are helpful in optimizing orbits and maximizing beam currents in nonlinear lattices. This section discusses the uses of the RCDS algorithm (discussed in section 4.2) to

perform orbit tuning and beam current maximization techniques within UMER.

8.2.1 Tuning orbits with optimization algorithms

Once a closed orbit has been achieved via first-turn steering techniques, the orbit needs to be tuned to meet the required operating conditions as the first-turn achieved orbit is not good enough for multi-turn operations. At UMER the orbit tuning is ran live on the accelerator using the RCDS algorithm. This is done by having the RCDS optimizer incorporated into the UMER controls system. This allows for the optimizer to be utilized for many different tasks other than orbit tuning.

RCDS requires a set of input parameters to tune and an objective function to minimize. In this case the input parameters, or 'actuators', are the UMER corrector magnet setpoints. The setpoints are normalized taking into account each magnet's maximum setpoint value such that the inputs into RCDS all range from 0 to 1. The objective functions for RCDS commonly consist of BPM measurements. The BPMs are able to quantify the requirements needed for the orbit tuning. Data is collected from each of the BPMs and reduced to a BPM matrix:

$$B = \begin{bmatrix} BPM_{11} & ... & BPM_{1,N} \\ ... & BPM_{i,j} & ... \\ BPM_{M,1} & ... & BPM_{M,N} \end{bmatrix} \tag{8.8}$$

where each entry in the matrix contains position data for a specific BPM at a specific

turn. For example a horizontal BPM matrix of size 10x100 would have turn-by-turn transverse horizontal position data measured at 10 BPMs over 100 turns.

The first type of objective function used is the minimization of the rms of matrix B_{ij}:

$$\text{obj} = \text{min: } \sqrt{\sum_i \left(\sqrt{\sum_j (B_{ij})^2} \right)^2} \tag{8.9}$$

In essence Eq. 8.9 is trying to reduce the closed orbit at the BPM locations to zero. While UMER's ideal orbit does not necessarily go through the zero point at the BPMs, the objective is useful in trying to reduce the amplitudes of the overall closed orbit in order to minimize possible beam scraping. Figure 8.6 shows an example run using the objective from Eq. 8.9. Here 14 BPMs are used over 4 turns in the transverse horizontal plane. The original horizontal orbit size was in the range of ± 5 mm and the minimization was able to reduce the orbit to within ± 1 mm. In terms of the specific objective function from Eq. 8.9, it was reduced from 3.1 ± 0.3 to 0.4 ± 0.1 mm.

Minimization runs like that from Figure 8.6 are helpful because they work and run fast on the live accelerator. Depending on the number of iterations, such a run can take only a few minutes. Even for long term experiments where the lattice is fixed for several weeks at a time orbit drifts can still occur. Movement of large magnetic materials in the lab and power supply drifts can cause orbit shifts that occur on the time frame of weeks. The RCDS minimizer is used to correct these types of orbit shifts.

Another type of objective function is one where the orbit in the BPMs is

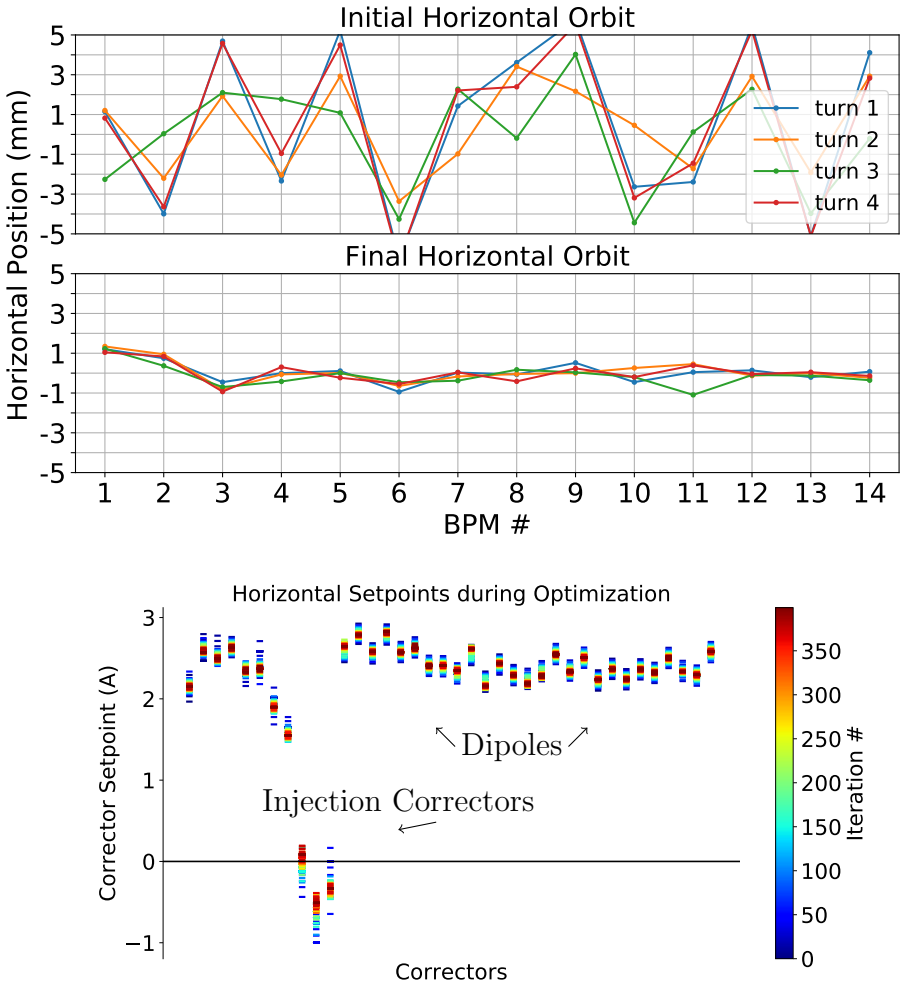

Figure 8.6: (top) Horizontal position data plotted over four turns using BPMs. The orbit is plotted before and after the minimization. (bottom) Every input magnet used for the minimization is plotted. The color represents the change in magnet setpoints through the iterations of the run.

minimized to a specific 'golden' orbit:

$$\text{obj} = \min: \sum_i \left(\sqrt{\sum_j (G_i - B_{ij})^2} \right) \tag{8.10}$$

where G_i is the 'golden' closed orbit trying to be minimized to. G_i is usually derived analytically or from a simulation model. Figure 8.7 shows an example run using the objective from Eq. 8.10. In this case the vertical orbit is tuned using the vertical correctors to match an ideal orbit. The objective function is reduced from 3.9 ± 0.4 to 1.2 ± 0.2 mm. The plots in Figure 8.7 are similar to those of Figure 8.6.

A few important things to note about RCDS and the live orbit tuning. As discussed in section 4.2, RCDS is able to account for noise in its minimizations. In order to accurately do this, the input signal noise level must be known. This means the noise level of BPMs needs to be quantized and fed into RCDS. BPM noise levels are discussed in section 3.2 and summarized in Figure 3.14 and 3.15. Noise levels change based on the beam current. For different current beams the noise levels are different and must be accounted for in RCDS.

The number of input knobs/corrector magnets used by RCDS is limited. Based on experimental measurements within UMER it is best to use around 10 input knobs for each minimization run. Using more than 10 tends to slow down the optimization to the point where other methods perform better. In UMER's case there is a total of 61 correctors (see Table 8.1) which means not all the correctors can be fed into RCDS at once. Instead the method used is to move around the ring and input a group of 10 correctors at a time into an RCDS run. Over a set of 6-7 runs all

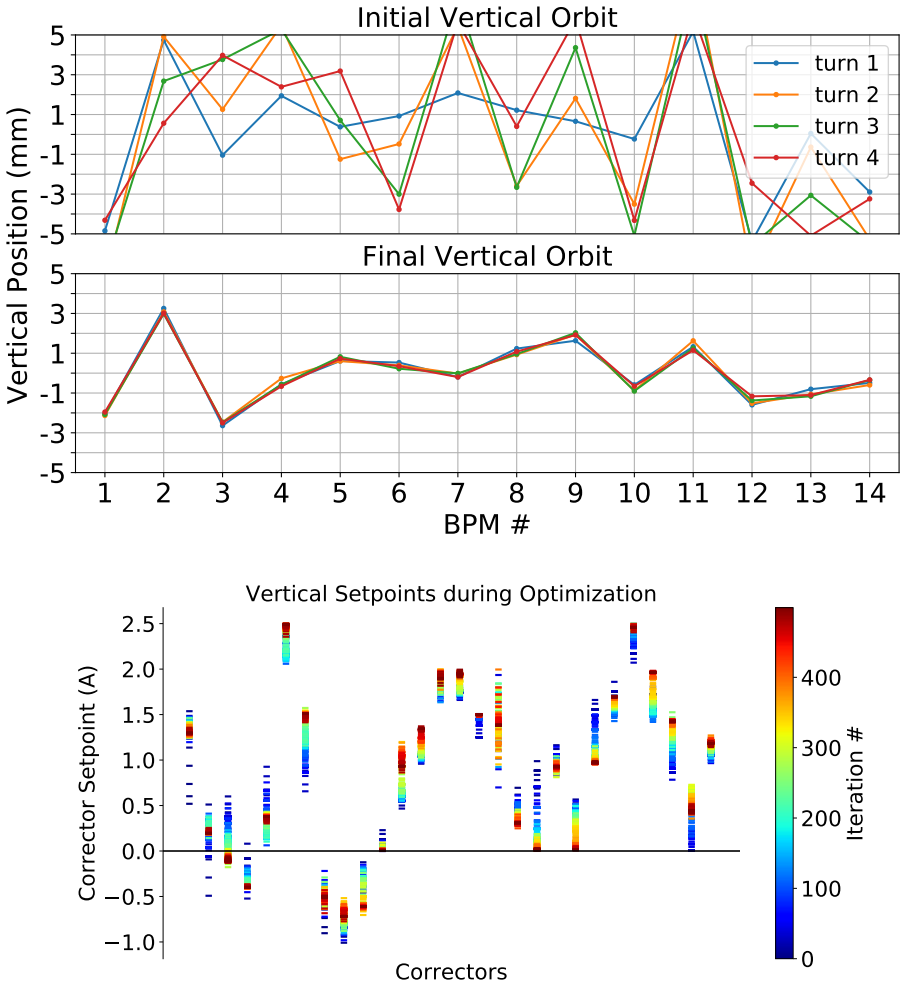

Figure 8.7: (top) Vertical position data plotted over four turns using BPMs. The orbit is plotted before and after the minimization. (bottom) Every input magnet used for the minimization is plotted. The color represents the change in magnet setpoints through the iterations of the run.

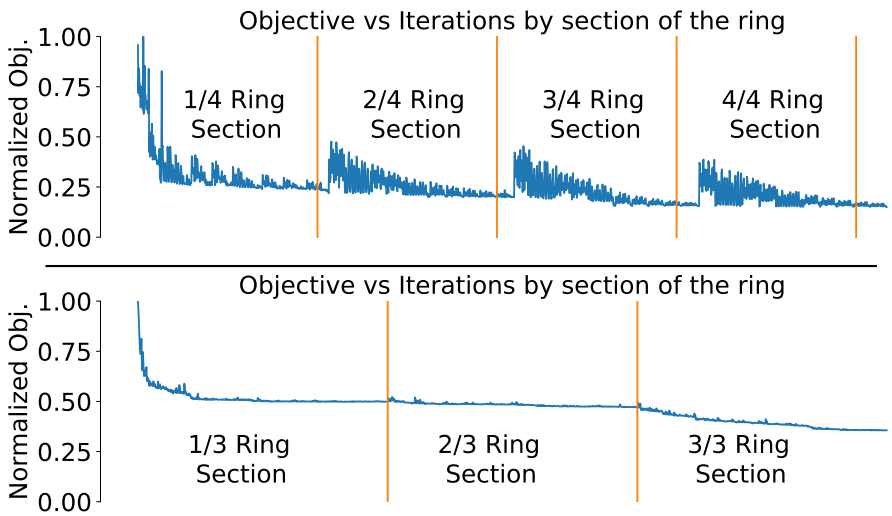

Figure 8.8: (top) Objective function for Eq. 8.9 and Figure 8.6. (bottom) Objective function for Eq. 8.10 and Figure 8.7.

the correctors feed through as input parameters in the RCDS minimization. This is repeated 2-3 times so that each corrector runs through RCDS more than once. Figure 8.8 shows an example of this. The figure tracks the objective function as the corrector inputs are serially used in the minimizer. Most of the minimization happens when using the corrector magnets near the beginning of the ring, where injection occurs. This is encouraging as it has been observed experimentally that adjusting injection can fix a lot of the orbit tuning problems that occur at UMER.

Lastly it is important to keep in mind that the RCDS minimizer, and any other optimization routine, is going to perform whatever is necessary in order to reduce the objective function. This can result in undesired effects on one's accelerator. An example in UMER's case was the RCDS algorithm purposely guiding the beam into a wall as it saw that as the best way to minimize the objective function from Eq. 8.9. As a result all cases must be thoroughly vetted when testing an objective

function. To deal with this specific problem in UMER a new objective function was introduced that would maximize the beam current in the accelerator; this is discussed in the next section. The current maximization objective was added as a weight to the objectives from Eq. 8.9 and 8.10 which then prevented the algorithm from guiding the beam into the wall to achieve the best results.

8.2.2 Current maximization with RCDS

The most commonly used RCDS objective function in UMER is the beam current maximizer. The maximizer uses a set of corrector magnets as inputs into the algorithm. There are two types of objective functions used. One is the BPM matrix B_{ij} from Eq. 8.8 where each value represents the sum signal from the BPM; this is a measure of the beam current. The objective in that case is to minimize $1/B_{ij}$ so that B_{ij} is maximized. The second, and more frequently used, objective function uses data only from a single wall current monitor in the ring. This is the focus of the section. A discussion on UMER's wall current monitor can be found in section 3.2.

The wall current monitor measures turn-by-turn beam current data in UMER. The objective function in this case would be:

$$\text{obj} = \text{min: } \frac{1}{\sum_j I_j} \tag{8.11}$$

where I_j is the beam current measured each turn around the ring. The number of turns of data used is different for each of UMER's beam currents. Lower current

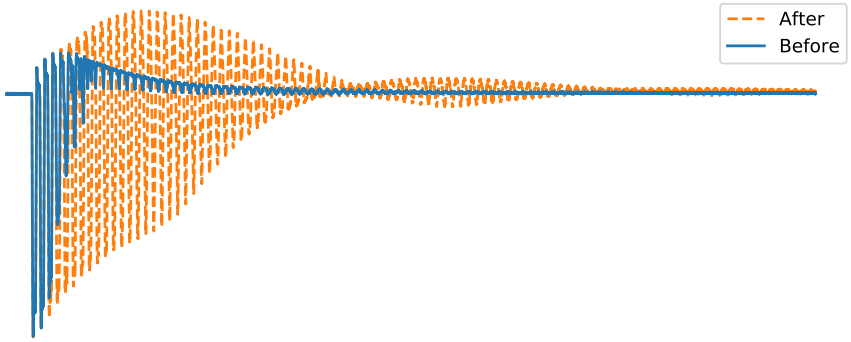

Figure 8.9: Wall current monitor signal measured before and after running the objective function from Eq. 8.11. The 6 mA beam was used.

beams survive longer in the ring and more turns can be used. Higher current beams last for much shorter periods so fewer viable turns are available for use. As an example, the 0.6mA beam uses 50 turns for the objective while the 6mA beam only uses 20 turns of data.

Figure 8.9 shows the results of the objective from Eq. 8.11. In this example a dozen vertical corrector magnets are randomly set to bad values to mimic a bad steering solution. Using beam current data from the single wall current monitor, and not using any BPM data, the RCDS minimizer is able to establish a much better orbit and reduce beam scraping by finding better values for the dozen 'bad' correctors. Since data was only being collected from a single wall current monitor diagnostics, as opposed to 10+ BPMs, the minimization was able to run faster than the BPM based methods discussed in the previous section. Measuring a set of BPM data takes about 30 seconds while measuring data from a single wall current monitor takes 1-2 seconds.

It is encouraging how well the current based objective function works. The

minimizer knows nothing about the system other than a measure of the beam current across a few revolutions. With only this information it is able to adjust dozens of corrector magnets such that it establishes a working closed orbit system.

One final technique is the use of several different objective functions in a weighted fashion:

$$\text{obj} = \sum_i w_i \, \text{obj}_i \tag{8.12}$$

where multiple objectives are used at once by adding weights to each one. Objectives can serve multiple purposes, say maximizing beam current while trying to minimize the size of a closed orbit. Such techniques have had mixed results as they depend highly on what the weights are for each objective. It is a technique that has good potential to work well in UMER, but requires more time to properly develop.

8.3 Chapter Summary

This chapter discusses the steering techniques developed and used on UMER for the various experiments presented in this dissertation. The first half discusses the methods employed for first turn steering; this includes quadrupole centering and quadrupole as BPM measurements. The second half discusses the use and development of the live RCDS minimizer at UMER. The minimizer uses a model-independent approach to experimentally tune the closed orbits and maximize the circulating beam current. A set of objective functions for the minimizer are introduced and discussed.

Chapter 8: Bibliography

[1] Thorsten Hellert, Philipp Amstutz, Christoph Steier, and Marco Venturini. Toolkit for simulated commissioning of storage-ring light sources and application to the advanced light source upgrade accumulator. *Phys. Rev. Accel. Beams*, 22:100702, Oct 2019.

[2] Kiersten Ruisard. *Design of a nonlinear quasi-integrable lattice for resonance suppression at the University of Maryland Electron Ring*. PhD thesis, University of Maryland College Park, 2018.

[3] Kamal PoorRezaei. Measuring beam position centroid in quadrupoles. unpublished, 2012.

[4] Auralee Edelen, Christopher Mayes, Daniel Bowring, Daniel Ratner, Andreas Adelmann, Rasmus Ischebeck, Jochem Snuverink, Ilya Agapov, Raimund Kammering, Jonathan Edelen, Ivan Bazarov, Gianluca Valentino, and Jorg Wenninger. Opportunities in machine learning for particle accelerators, 2018.

Chapter 9: Conclusion & Future Work

9.1 Summary of Dissertation

This dissertation describes the experimental work in studying and mitigating destructive resonances using space charge dominated beams. Tune and resonance measurements were conducted using beams with different space charge levels. No resonance shifting of the integer or half-integer resonances ($Q_x = 7.0, Q_x = 6.5, Q_x = 7.5, Q_y = 6.5$) were detected using any of the beams. On a separate project, new work was done on the nonlinear integrable optics experiment at UMER. A quasi-integrable lattice was designed, simulated, and experimentally tuned for measurements. Nonlinear amplitude dependent tuneshifts due to the octupole channel magnet were measured. Various numerical techniques and tools were developed for the design, simulation, and experimental work presented in this dissertation.

9.1.1 Resonance studies

Experimental tune measurements are done using the NAFF algorithm and four different UMER beams. The measurements show a coherent tune shift due to space charge. A novel sliding window tune measuring technique is also discussed

as a way to experimentally measure tunes as a function of the beam circulating around the accelerator. Techniques for detecting and measuring resonances are discussed. Along with the more traditional beam loss based tune scans, a new NAFF based tune scan measurement technique is developed. This new technique is used to measure the presence of destructive and non-destructive resonances within UMER. The impact of the resonance on the particle beams along with any potential resonance shifting because of space charge is experimentally tested. The measured results show no shifiting of integer or half-integer resonances. Theory predicts a shift of the half-integer resonance and no shift of the integer resonance.

9.1.2 Nonlinear integrable optics

A new acclerator lattice is designed to test quasi-integrability within UMER. The lattice is different from previous designs in that it is no longer a symmetric design. Instead the insert is built as a matched section in the lattice making the accelerator have a 1-turn symmetry – no repeat magnet configuration occurs within that one turn. The lattice parameters are designed such that the integrability requirements are able to be met while near UMER's default accelerator operating range (tunes near $Q_x, Q_y = 6.70, 6.82$). This is done to allow better experimental steering and tuning of the new lattice as knowledge of how the accelerator works at UMER's default operating range is very well known.

A model-experiment based optimization routine is employed to tune the simulations and experiments until all integrability requirements are met within UMER.

This includes phase advance, betatron function, and betatron tune requirements. Detailed experimental tune measurements are conducted with the nonlinear octupole channel insert. Clear nonlinear tune shifts are measured using the manget. Amplitude dependent tune shifts are measured. The results are not as clear as the simulations predict. Improving the steering tolerances on UMER should improve future measurements for the experiment.

9.2 Future Work

The space charge resonance studies look very promising. While lots of theory and simulation has been done on this topic, very little experimental verification exists. With a large range of space charge dominated beams, UMER is a good facility to conduct these experiments. Better containment of the larger current beams would be a starting point for this work. Being able to generate more turns of data for the 6 mA and 23 mA beams would allow for much more accurate tune measurements. The tune measurements would provide more resolution in measuring resonances. Right now the 6 mA beam tune measurements only work with 32 and 16 turns. The 23 mA beam works with only 16 turns. Having an RF system that is able to confine large beams with more space charge would open the possibility for new detailed measurements.

For the quasi-integrabililty experiments, the conclusion is that UMER can not meet the strict steering and tolerance requirements in order to get an accurate amplitude dependent tune measurement. The improvements needed to fix this issue

seem to large at the moment. A set of horizontal helmholtz coils are needed to create a constant magnet field in the vertical direction. The octupole channel needs to be properly re-measured and potentially re-built. Better confinement and steering is needed within the UMER beams. In order to use a very low current, low space charge beam, an upgrade of the BPM amplifiers is needed as the signal is currently too small to generate accurate enough measurements within the diagnostics.

Overall the focus on these two experiments should be shifted towards the space charge resonance studies. This project can continue with all the existing hardware within UMER. Only minor improvements in steering and RF upgrades would be needed to get better experimental results. The work done on model development in this dissertation can also be used for simulations studies on the topic as well.

9.2.1 Ideas for resonance studies

While this dissertation only had time to investigate resonance impacts due to coherent tune shifts, lots of potential experiments can still be done. One interesting test would be to setup the knockout apparatus from Figure 3.18 to measure the envelope instabilities that develope near half-integer resonances. The quadrupole magnets would be adjusted to bring the bare tune near the $Q_x = 6.5$ or $Q_y = 6.5$ resonances. The knockout apparatus would then be used to image the beam and see if the parallel and antiparallel instabilities can be observed.

Very little experimental work has been done on the observance of nonlinear resonances in the presence of space charge. As seen in Figure 6.13, third order

nonlinear resonances existing within UMER. Further detailed measurements of the behavior of these resonances as a function of space charge would be interesting to study. A potential sextupole magnet can be designed, built, and installed on UMER to amplify the nonlinear resonances. Such measurements would bring new insight on the topic of space charge and nonlinear resonances.

Appendix A: Additional notes on single particle equations

A.1 Derivation of single particle Hamiltonian

The complete hamiltonian for a single particle in an accelerator can be derived through a set of canonical transformations and approximations presented below. A thorough derivation can be found in standard accelerator physics textbooks [1].

We start with the relativistic Hamiltonian from Eq. 2.1:

$$H = q\phi + c\sqrt{m^2c^2 + (\vec{P} - q\vec{A})^2} \tag{A.1}$$

Where the ϕ is the electostatic potential and $\vec{A}$ is the magnetic vector potential. The conjugate momentum, $\vec{P}$, is defined as the sum of the mechanical and field momenta, $\vec{P} = \vec{p} + q\vec{A}$. The first step requires a canonical transformation to the Frenet-Serret coordinate system, summarized by the equations from Eq. 2.2:

$$\hat{s} = \frac{d\vec{r_0}}{ds}, \qquad \hat{x} = -R\frac{d\hat{s}}{ds}, \qquad \hat{y} = \hat{x} \times \hat{s}, \tag{A.2}$$

A generating function of the third kind will be used for the canonical trans-

formation:

$$F_3(\vec{P}; x, y, s) = -\vec{P} \cdot (\vec{r_0}(s) + x\hat{x} + y\hat{y}) \tag{A.3}$$

where $\vec{P}$ is the conjugate momentum in the old cartesian coordinates and (x, y, s) are the new transformed coordinates in the Frenet-Serret system. The new field momentum vector can be calculated as:

$$p_x = -\frac{\partial F_3}{\partial x} = \vec{P} \cdot \hat{x}\,, \quad p_y = -\frac{\partial F_3}{\partial y} = \vec{P} \cdot \hat{z}\,, \quad p_s = -\frac{\partial F_3}{\partial s} = (1 + \frac{x}{R})\,\vec{P} \cdot \hat{s} \tag{A.4}$$

with the vector potential $\vec{A}$ being represented as:

$$A_x = \vec{A} \cdot \hat{x}\,, \quad A_y = \vec{A} \cdot \hat{y}\,, \quad A_s = \vec{A} \cdot \hat{s} \tag{A.5}$$

These set of transformations now allow the Hamiltonian to be written in the Frenet-Serret coordinate system as a function of coordinates (x, y, s) and conjugate momenta (p_x, p_y, p_s):

$$H = q\phi + c\sqrt{m^2c^2 + (p_x - qA_x)^2 + (p_y - qA_y)^2 + (\frac{p_s}{1 + \frac{x}{R}} - qA_s)^2} \tag{A.6}$$

Diagnostics, magnets, and other instrumentation in particle accelerators are often referred to by their s location along the ring. As such, it is more natural to work with a set of equations where the independent variable is s and not t; this gives the ability to work with coordinates as $x(s)\,, y(s)$ and not $x(t)\,, y(t)$. This is done by finding the inverse function $t(s)$ from $s(t)$ which allows $x(t)$ to be written

as $x(t(s))$.

Using the following relations, expressions can be derived for a new set of Hamilton's equations:

$$x' = \frac{dx}{ds} = \frac{dx/dt}{ds/dt} = \frac{\partial H}{\partial p_x}\left(\frac{\partial H}{\partial p_s}\right)^{-1} = \frac{\partial(-p_s)}{\partial p_x}$$
$$p'_x = \frac{dp_x}{ds} = \frac{dp_x/dt}{ds/dt} = \frac{-\partial H}{\partial x}\left(\frac{\partial H}{\partial p_s}\right)^{-1} = \frac{\partial(p_s)}{\partial x} \tag{A.7}$$

Note that $-p_s$ represents a new Hamiltonian i.e.

$$\dot{q} = \frac{\partial H}{\partial p}\,,\ \dot{p} = -\frac{\partial H}{\partial q} \qquad \rightarrow \qquad x' = \frac{\partial(-p_s)}{\partial p_x}\,,\ p'_x = -\frac{\partial(-p_s)}{\partial x} \tag{A.8}$$

A similar set of equations can be written for (y, p_y) coordinates. For the coordinates (s, p_s) an inverse of the following equations is taken:

$$\left(\frac{ds}{dt}\right)^{-1} = \left(\frac{\partial H}{\partial p_s}\right)^{-1} \quad \rightarrow \quad t' = \frac{dt}{ds} = \frac{\partial p_s}{\partial H} = \frac{\partial(-p_s)}{\partial(-H)} \tag{A.9}$$

The new Hamiltonian represented by $-p_s$ is referred to as K. K is derived by solving Eq. A.6 for $-p_s$. This new Hamiltonian, K, now has an independent variable s instead of t. The phase space coordinates of K are given as $(x, p_x, y, p_y, t, -H)$.

$$K = -(1 + \frac{x}{R})qA_s - (1 + \frac{x}{R})\sqrt{\frac{(H - q\phi)^2}{c^2} - (p_x - qA_x)^2 - (p_y - qA_y)^2 - m^2c^2} \tag{A.10}$$

Most accelerators are built with only transverse static magnetic fields. This

gives the freedom to choose a a set of scalar and vector gauges such that we eliminate the scalar potential and reduce the vector potential to one dimension:

$$\phi = 0 \quad A_x = 0 \quad A_y = 0 \tag{A.11}$$

The Hamiltonian is then simplified to:

$$K = -(1 + \frac{x}{R})qA_s - (1 + \frac{x}{R})\sqrt{\frac{H^2}{c^2} - (p_x)^2 - (p_y)^2 - m^2c^2} \tag{A.12}$$

The transverse momenta, (p_x, p_y), are considered small quantities compared to the total momentum because particles tend to move longitudinally on a closed orbit and only move at very small angles off this orbit. These small momenta allows the use of approximations to further simplify the Hamiltonian. The first approximation introduces the reference momentum P_0. P_0 is usually defined as the nominal momentum of an accelerator, the design energy of a machine; it is the energy a particle needs to travel on a closed orbit. Normalizing the momenta by the reference momentum keeps Hamilton's equations unchanged:

$$p_{x,y} \;\rightarrow\; \tilde{p}_{x,y} = \frac{p_{x,y}}{P_0} \tag{A.13}$$

The substitution in Eq. A.13 only works if the Hamiltonian is also scaled,

$$K \;\rightarrow\; \tilde{K} = \frac{K}{P_0} \tag{A.14}$$

The new phase space coordinates are $(x, \tilde{p}_x, y, \tilde{p}_y, t, \tilde{p}_t = -\frac{H}{P_0})$ and the Hamiltonian becomes:

$$\tilde{K} = -(1 + \frac{x}{R})a_s - (1 + \frac{x}{R})\sqrt{\left(\frac{\tilde{p}_t}{c}\right)^2 - (\tilde{p}_x)^2 - (\tilde{p}_y)^2 - \frac{m^2c^2}{P_0^2}} \tag{A.15}$$

Note the vector potential is also scaled by the nominal momentum $a_s = q\frac{A_s}{P_0}$.

One last canonical transformation is needed. A type two generating function will be used to transform variables from $(t, \tilde{p}_t)$ to $(\Delta z = (s - v_0 t), \delta = \frac{\Delta P}{P_0})$. Where v_0 is the nominal beam velocity and ΔP is the change in total momentum from the nominal, $P - P_0$.

$$F_2(t, \delta, s) = \frac{c}{\beta_0}(1 + \beta_0^2\delta)(\frac{s}{\beta_0 c} - t) \tag{A.16}$$

The new variables are found by solving the generating function equations. An assumption is made that $\beta_0 \approx 1$ since beams are highly relativistic and close to the speed of c.

$$p = \frac{\partial F_2}{\partial q} \;\rightarrow\; -\frac{E}{P_0} = -\frac{c}{\beta_0}(1 + \beta_0^2\delta) \;\rightarrow\; -\frac{E}{P_0 c} = 1 + \delta$$

$$Q = \frac{\partial F_2}{\partial P} \;\rightarrow\; \Delta z = c\beta_0(\frac{s}{\beta_0 c} - t) \;\rightarrow\; \Delta z = s - v_0 t$$

$$\frac{\partial F_2}{\partial s} = \frac{1}{\beta_0^2}(1 + \beta_0^2\delta) = 1 + \delta \tag{A.17}$$

E here is the Hamiltonian H in Eq. A.12. The final Hamiltonian then becomes:

$$H = -(1 + \frac{x}{R})a_s - (1 + \frac{x}{R})\sqrt{(1 + \delta)^2 - (p_x)^2 - (p_y)^2} + (1 + \delta) \tag{A.18}$$

with phase space variables $(x, p_x, y, p_y, \Delta z, \delta)$. The tilde over p_x, p_y have been dropped to simplify notation as well as $\tilde{K}$ being replace by H.

A.2 Hamiltonian approximation

An approximation of the full Hamiltonian from Eq. A.18 is often used to provide a set of simpler equations to work with. In practice simulation codes will expand terms out to third order or above in order to guarantee a symplectic Hamiltonian.

As a demonstration of the approximation up to second order, we start by pulling $(1+\delta)^2$ from under the square root:

$$H = -(1+xh)a_s - (1+xh)(1+\delta)\sqrt{1 - \left[\frac{(p_x)^2 + (p_y)^2}{(1+\delta)^2}\right]} + (1+\delta) \tag{A.19}$$

Here we have rewritten $1/R$ as h to simplify the visual clutter of the equation. Next a binomial expansion of the form:

$$\sqrt{1+x} \approx 1 + \frac{1}{2}x - \frac{1}{8}x^2 + ... \tag{A.20}$$

is applied and any terms above second order are excluded:

$$H = -(1+xh)a_s - (1+xh)(1+\delta)(1 - \frac{1}{2}\Big(\frac{(p_x)^2 + (p_y)^2}{(1+\delta)^2}\Big)) + (1+\delta) \tag{A.21}$$

Multiplying out Eq. A.21 and excluding third order terms $(p_x^2\delta, p_x^3, p_x p_y^2$, etc...), a final form of the second order approximated Hamiltonian is achieved:

$$H = \frac{p_x^2 + p_y^2}{2(1+\delta)} - hx - hx\delta - (1+xh)a_s \tag{A.22}$$

A.3 Solution of Hill's Equation

Starting with Hill's equation:

$$\ddot{x} + k(s)x = 0 \tag{A.23}$$

a solution can be written in the form of:

$$x(s) = \epsilon\sqrt{\beta}e^{i\Psi(s)} \tag{A.24}$$

Taking two derivatives of the solution gives:

$$\begin{aligned} \dot{x} &= \epsilon(\frac{1}{2}\frac{\dot{\beta}}{\beta^{1/2}} + i\beta^{1/2}\dot{\Psi})e^{i\Psi} \\ \ddot{x} &= \epsilon(\frac{1}{2}\frac{\ddot{\beta}}{\beta^{1/2}} + \frac{1}{2}\frac{i\dot{\beta}\dot{\Psi}}{\beta^{1/2}} - \frac{1}{4}\frac{\dot{\beta}^2}{\beta^{3/2}} + \frac{1}{2}\frac{i\dot{\beta}\dot{\Psi}}{\beta^{1/2}} + i\beta^{1/2}\ddot{\Psi} - \beta^{1/2}\dot{\Psi}^2)e^{i\Psi} \end{aligned} \tag{A.25}$$

Plugging the results back into Eq. A.23 leads to two equations for the real and imaginary parts:

$$\left[\frac{1}{2}\ddot{\beta}\beta - \frac{1}{4}\dot{\beta}^2 - \beta^2\dot{\Psi}^2 + k(s)\beta^2\right] + i\left[\dot{\beta}\dot{\Psi} + \beta\ddot{\Psi}\right] = 0 \tag{A.26}$$

Looking at the imaginary part first:

$$\dot{\beta}\dot{\Psi} + \beta\ddot{\Psi} = 0 \;\rightarrow\; -\frac{\dot{\beta}}{\beta} = \frac{\ddot{\Psi}}{\dot{\Psi}} \;\rightarrow\; -\int \frac{d\beta}{\beta} = \int \frac{d\dot{\Psi}}{\dot{\Psi}} \;\rightarrow\; \ln\frac{1}{\beta} + C = \ln\dot{\Psi} \quad \text{(A.27)}$$

Setting the integration constant $C = 0$ gives the relation:

$$\dot{\Psi} = \frac{1}{\beta} \quad \text{(A.28)}$$

Plugging this result back into the real part of Eq. A.26 gives the second equation as:

$$\frac{1}{2}\beta\ddot{\beta} - \frac{1}{4}\dot{\beta}^2 + k(s)\beta^2 = 1 \quad \text{(A.29)}$$

A.4 Transformation of Hill's equation

Using the following tansformations:

$$\eta \equiv \frac{x(s)}{\beta^{1/2}}\,, \quad \phi \equiv \frac{\Psi(s)}{Q}\,, \quad \dot{\phi} \equiv \frac{\dot{\Psi}(s)}{Q} \equiv \frac{1}{Q\beta(s)} \quad \text{(A.30)}$$

Hill's equation, Eq. A.23, can be transformed into a simple harmonic oscillator equation. First take two derivatives with respect to s:

$$\dot{x} = \frac{1}{2}\frac{\eta\dot{\beta}}{\beta^{1/2}} + \frac{\eta'}{Q\beta^{1/2}}$$

$$\ddot{x} = \frac{1}{2}\frac{\ddot{\beta}\eta}{\beta^{1/2}} - \frac{1}{4}\frac{\dot{\beta}^2\eta}{\beta^{3/2}} + \frac{\eta''}{\beta^{3/2}Q^2} \tag{A.31}$$

Note a dot above a variable means derivative with respect to s while a prime denotes a derivative with respect to ϕ, e.g. $\dot{x} = \frac{\partial x}{\partial s}$, $\eta' = \frac{\partial \eta}{\partial \phi}$ The following property was also used:

$$\dot{\eta} = \frac{\partial \eta}{\partial s} = \frac{\partial \phi}{\partial \phi}\frac{\partial \eta}{\partial s} = \frac{\partial \eta}{\partial s} = \frac{\partial \phi}{\partial s}\frac{\partial \eta}{\partial \phi} = \dot{\phi}\eta' = \frac{1}{Q\beta}\eta' \tag{A.32}$$

Next plug in Eq. A.31 into Eq. A.23 and simplify:

$$\eta'' + Q^2\eta(\frac{1}{2}\ddot{\beta}\beta - \frac{1}{4}\dot{\beta}^2) + k(s)\beta^2Q^2\eta = 0 \tag{A.33}$$

Using the amplitude equation in Eq. A.29 to substitute out the second term:

$$\eta'' + Q^2\eta(1 - k(s)\beta^2) + k(s)\beta^2Q^2\eta = 0 \tag{A.34}$$

Hill's equation reduces to:

$$\eta'' + Q^2\eta = 0 \tag{A.35}$$

Eq. A.35 is a harmonic oscillation equation. The oscillation frequency is defined by the tune, Q. This form of Hill's equation is simpler and more intuitive to work with.

The piecewise dependence is buried within the tune and independent variables.

A.5 Calculating space charge electromagnetic fields

Maxwell's equations are used to calculate the electric and magnetic fields for a round cross section of the beam with uniform charged density ρ. The equations in differential form are written as:

$$\vec{\nabla} \cdot \vec{E} = \frac{\rho}{\epsilon_0} \ , \ \frac{1}{\mu_0} \nabla \times \vec{B} = \vec{\nu} \rho \tag{A.36}$$

Integrating both sides gives:

$$\int \vec{\nabla} \cdot \vec{E} \, dV = \int \frac{\rho}{\epsilon_0} \, dV \ , \ \frac{1}{\mu_0} \int \nabla \times \vec{B} \, dS = \int \vec{\nu} \rho \, dS \tag{A.37}$$

Using Stokes' and Green's theorem transforms the integrals to:

$$\oint \vec{E} \cdot d\vec{A} = \int \frac{\rho}{\epsilon_0} \, dV \ , \ \frac{1}{\mu_0} \oint \vec{B} \cdot dl = \int \vec{\nu} \rho \, dS \tag{A.38}$$

Assuming the beam is a slice in a cylinder with length h, the integrals are calculated as:

$$2\pi r dh E = \frac{\rho}{\epsilon_0} \pi r^2 dh \ , \ 2\pi r B = \pi r^2 \mu_0 \nu \rho \tag{A.39}$$

Finally yielding the fields:

$$E_r = \frac{\rho}{2\epsilon_0} r \ , \ B_\phi = \frac{\rho \nu}{2\epsilon_0 c^2} r \tag{A.40}$$

where the common identity was used:

$$\frac{1}{c^2} = \mu_0 \epsilon_0 \tag{A.41}$$

Appendix A: Bibliography

[1] S. Y. Lee. *Accelerator Physics*. World Scientific, 2012.

Appendix B: UMER Control System

The UMER control system development was a multi-year effort in rewriting and overhauling the accelerator control software. The goal was to provide a simpler and more streamlined set of software tools similar to what one might expect at larger accelerator facilities. This appendix chapter provides a quick start guide to get up and running with the UMER controls code for experiments.

The control system encompasses hundreds of scripts that can't possible be reviewed in this section. Almost every script has detailed comments and examples written at the top of the file. Users are encouraged to open the files directly for more information on what each script does as not everything will be mentioned in this chapter. If questions still remain, the users can contact the author of this thesis for more information and any assistance that might be needed. Parts of this appendix chapter are based on an earlier UMER controls guide written by Levon Dovlatyan and Kiersten Ruisard [1]. The UMER control code was built using influences from the Accelerator Toolbox tracking code and the Matlab-Middle Layer codes [2, 3].

B.1 Quick Start Guide

B.1.1 Startup

The controls GUI should automatically initialize when Matlab is launched from the desktop icon. Upon initial launch, Matlab navigates to the current controls directory and executes the setpath.m script. A window will appear prompting the user to select a magnet configuration file, pictured on the left in Figure B.1. Selecting a file at this stage does not set any power supplies. Rather, the configuration file is read and data loaded into Matlab's memory. After a magnet configuration is chosen, a second menu appears, see right side of Figure B.1, prompting the user to specify an operational mode. The operational modes specify details on BPM and WCM scope settings, initialization of certain specialized magnets (Octupoles), and other many more experiment specific configurations [1].

Once an operational mode is selected, the controls code will run through a set of initializations and configurations, printing out diagnostics information in the Matlab command window. Some examples of the initializations include establishing a connection to the back-end server, configurating all data collection scopes, setting up power supplies settings, etc. Afterwards the main UMER control GUI will appear on the screen, seen in Figure B.2. If this window is ever closed it can be relaunched with the 'umer˙control' command.

[1] Operational modes can be added or changed in the setoperationmode.m file

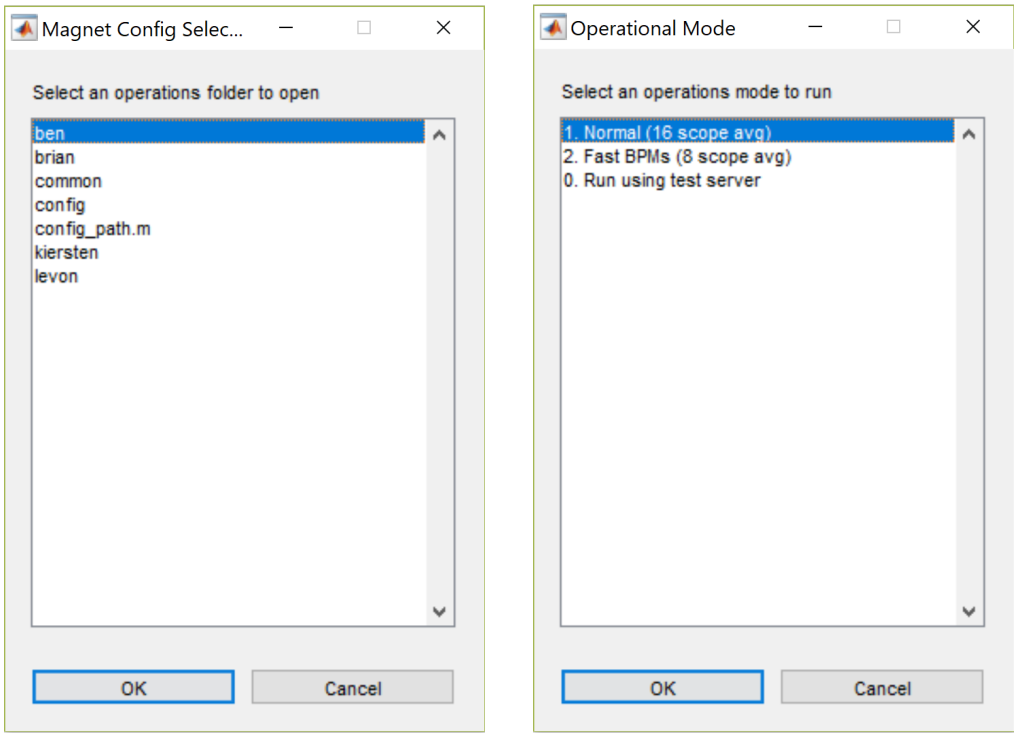

Figure B.1: Initial selection menus displayed when Matlab is launched. (left) Magnet configuration file selection. (right) Operation mode selection.

B.1.2 Cathode heating

Clicking on the 'Heater Control' button in the UMER main control GUI will launch another GUI to control the UMER gun, seen in Figure B.3. To begin ramping up the heater for the electron gun press the 'Ramp up Heater' button within in the GUI. Similarly, the 'Ramp Down Heater' will ramp down the heating on the electron gun. Pressing the large green 'Voltage' button will give a current reading of the heater power supply voltage.

The equivalent Matlab functions to run for the 'Ramp Up Heater' and 'Ramp Down Heater' buttons in the GUI are:

- setscheduleheater_rampup

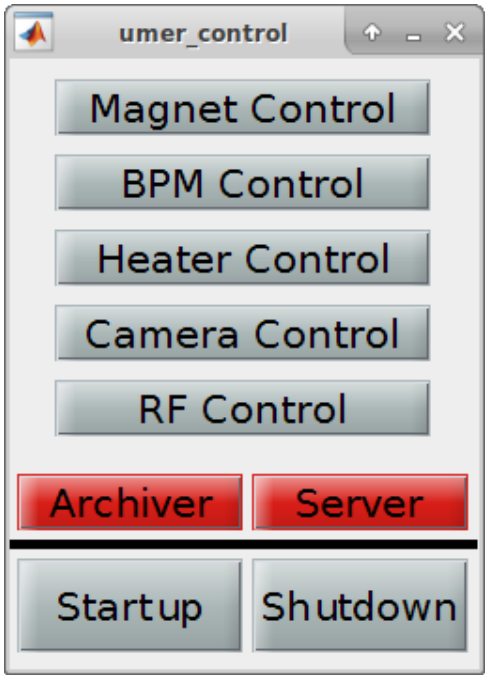

Figure B.2: The main UMER control GUI.

- setscheduleheater_rampdown

These commands are what is called when the GUI buttons are pressed. If a '0' argument is given to the functions, ex: setscheduleheater_rampup(0), it will launch a small calendar that allows the ramping up or down of the heater to be executed at a specific time in the future. Such a feature is useful if one wants to setup the UMER gun to power on or off the next day for an experiment. As discussed in section 3.1.1, the UMER gun takes several hours to warm up and reach equilibrium. A common experimental approach in the lab is to pre-program the electron gun to power on early in the morning, say 6 am, such that it is ready to go later in the day for an experiment.

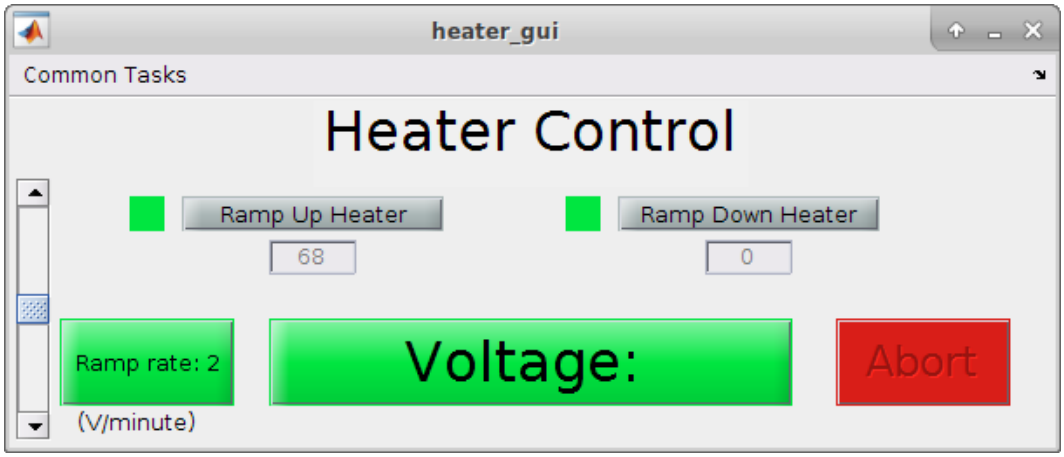

Figure B.3: Main magnet control GUI for UMER.

B.1.3 Magnet control

Pressing the 'Magnet Control' button in the UMER control GUI will launch the UMER magnet control GUI, displayed in Figure B.4. This is the largest, most sophisticated, and most used GUI interface in the controls system. The magnet control GUI is used to interact, set, and read back values from all the magnets in UMER. Families of magnets are broken down into different sections within the GUI to keep things organized. Each section of the GUI is made up of three main columns: the magnet display name, the magnet set value, and the magnet read back value. There are four buttons at the top of each section: 'Set', 'Get', 'Reset', 'Off'. The 'Set' can be used to set the value of every magnet in the section to a specific value by entering that value in the box next to the 'Set' button and then pressing 'Set'. The 'Get' button will perform a read back on every magnet in the section. The 'Reset' button resets the set values for all the magnets in the section to the default value. The default values being based off the magnet configuration file selected on

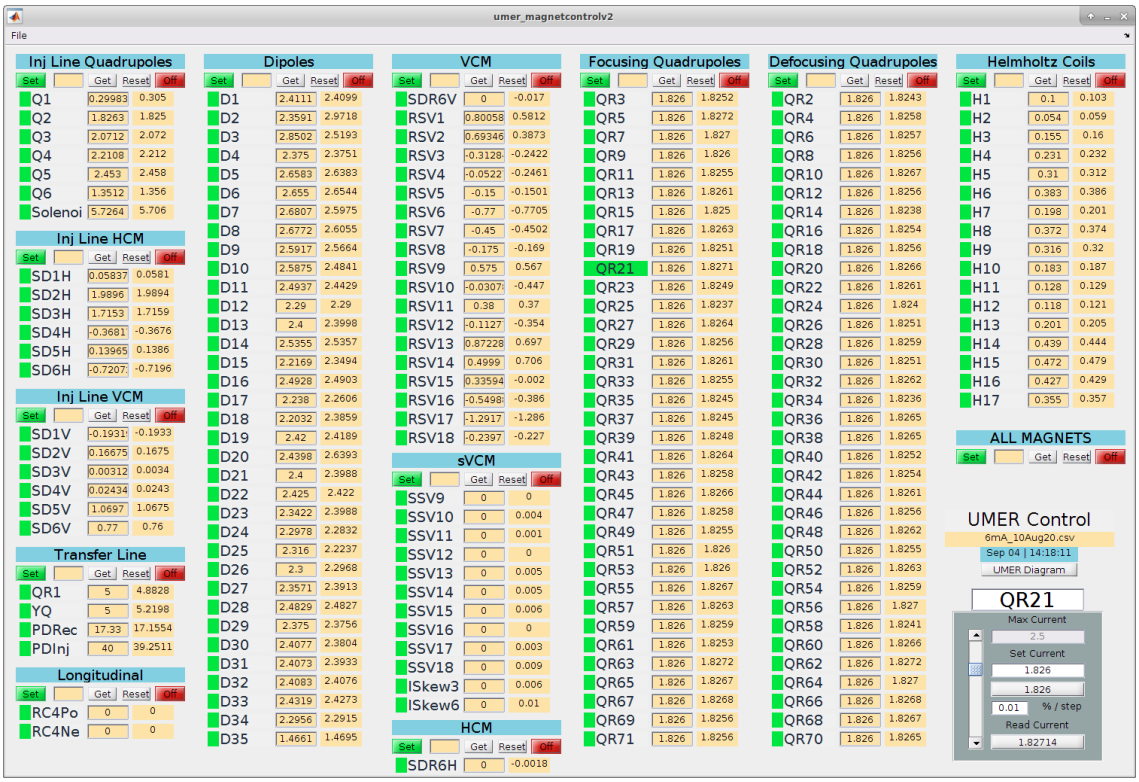

Figure B.4: Main magnet control GUI for UMER.

startup. Lastly, the 'Off' button will set the value to zero for all the magnets in a section. At the far right end of the GUI is a section labeled 'ALL MAGNETS'. The buttons in this section will apply their effects to every magnet in UMER.

For individual magnet control, the user simply clicks on a magnet name to have advanced controls appear. In Figure B.4 the manget 'QR21' is selected. Once the magnet is selected the advanced controls at the bottom right of the GUI can be used to adjust the individual magnet. Right clicking on the magnet name will also reveal advanced features. Using the 'File' menu at the top left of the GUI will allow the user to save and load different magnet configuration files.

The underlying commands/functions for magnet control are the following:

- setc - sets a magnet current

- getc - gets (read backs) a magnet current
- setp - sets a magnet current to the default
- getp - gets (read backs) a default magnet current
- setring - sets the current for families of magnets
- savering - saves the current magnet settings
- loadmagnetsettings - opens a GUI to load in a different magnet settings file.

Each of the functions have detailed comments with examples within the scripts themselves.

B.1.4 Reading BPM and WCM data

Pressing the 'BPM Control' button on the UMER control GUI will launch the GUI seen in Figure B.5. This interface is used to grab BPM measurements, plot the results, and save the data. The 'Get BPMs' button will trigger a measurement with all the available BPMs and plot the results within the GUI. The list of options at the bottom right of the screen gives the user a way to plot different parts of the BPM measurements. History of each measurement taken is displayed in the listbox on the right side. The user is able to click on and reload older measurements. The save buttons at the bottom allow the abililty to save a single BPM measurement or all the BPM measurements taken within the GUI. The saved data can be found under /Data/bpmData/.

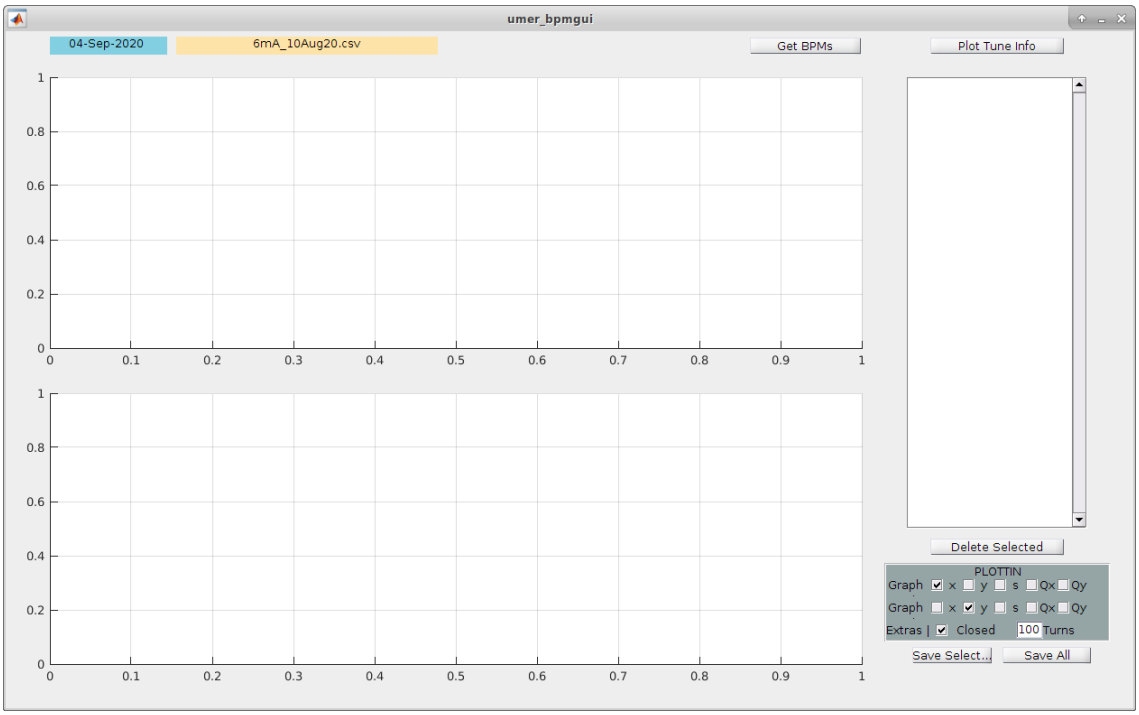

Figure B.5: BPM measurements GUI for UMER.

The main functions/commands for BPM and WCM measurements are listed below:

- get_bpm - returns bpm data for a specific bpm
- get_bpms - returns bpm data for all bpms
- get_wcm - returns data from the wall current monitor
- old_dcct - returns the measured beam current based off the wall current monitor data
- gen_bpm˙noise - generates a new set of background noise bpm data
- gen_wcm˙noise - generates a new set of background wcm noise data
- plot_bpms - plotting function for bpm data

- plot_wcm - plotting function for wcm data
- load_bpms - loads a set of saved bpm data
- save_bpms - saves a set of bpm data
- switch2bpm - switches the multiplexor to a specified BPM.

Detailed explanations of each function is presented within the scripts themselves as comments. As an example of grabbing data with the bpm functions, the following is code to measure 1 turn of BPM data from BPM 0 (IC2):

```
>> bpm = get_bpm(0,1)

bpm =

        name: 'IC2'
           X:  6.8882
           Y:  2.0231
          Xe: 1.1035
          Ye: 1.1747
         top: 0.3638
      bottom: 0.4993
        left: 0.8135
       right: 0.2348
         sum: 0.0223
```

```
        scope_data: [1000x6 double]
  scope_data_noise: [1000x6 double]
```

And an example of grabbing 4 turns of data from BPM 2 (RC2):

```
>> bpm = get_bpm(2,4)

bpm =

        name: 'RC2'
           X: [4x1 double]
           Y: [4x1 double]
          Xe: [4x1 double]
          Ye: [4x1 double]
         top: [4x1 double]
      bottom: [4x1 double]
        left: [4x1 double]
       right: [4x1 double]
         sum: [4x1 double]
  scope_data: [1000x6 double]
scope_data_noise: [1000x6 double]
```

Lastly, grabbing 4 turns of data using all the BPMs:

```
>> bpms = get_bpms(4)
```

```
bpms =

    [1x1 struct]

    [1x1 struct]

    [1x1 struct]

    [1x1 struct]

    [1x1 struct]

    [1x1 struct]

    [1x1 struct]

    [1x1 struct]

    [1x1 struct]

    [1x1 struct]

    [1x1 struct]

    [1x1 struct]

    [1x1 struct]

    [1x1 struct]

>> bpms{1}

ans =

                name: 'RC1'
```

```
                X: [4x1 double]
                Y: [4x1 double]
               Xe: [4x1 double]
               Ye: [4x1 double]
              top: [4x1 double]
           bottom: [4x1 double]
             left: [4x1 double]
            right: [4x1 double]
              sum: [4x1 double]
      scope_data: [1000x6 double]
scope_data_noise: [1000x6 double]
```

The data from the bpm measurement can then be plotted using the plot_bpms function:

```
>> plot_bpms(bpms,'x','y')
```

Generating the plot in Figure B.6

Note the BPM struct objects returned by get_bpm and get_bpms. All BPM data is contained within this object and many functions, such as plot_bpms, that interact with bpm data take this object as input. The get_wcm function returns a similar object for WCM data. More information about the BPM object data structure can be found in the comments within the get˙bpm.m script file.

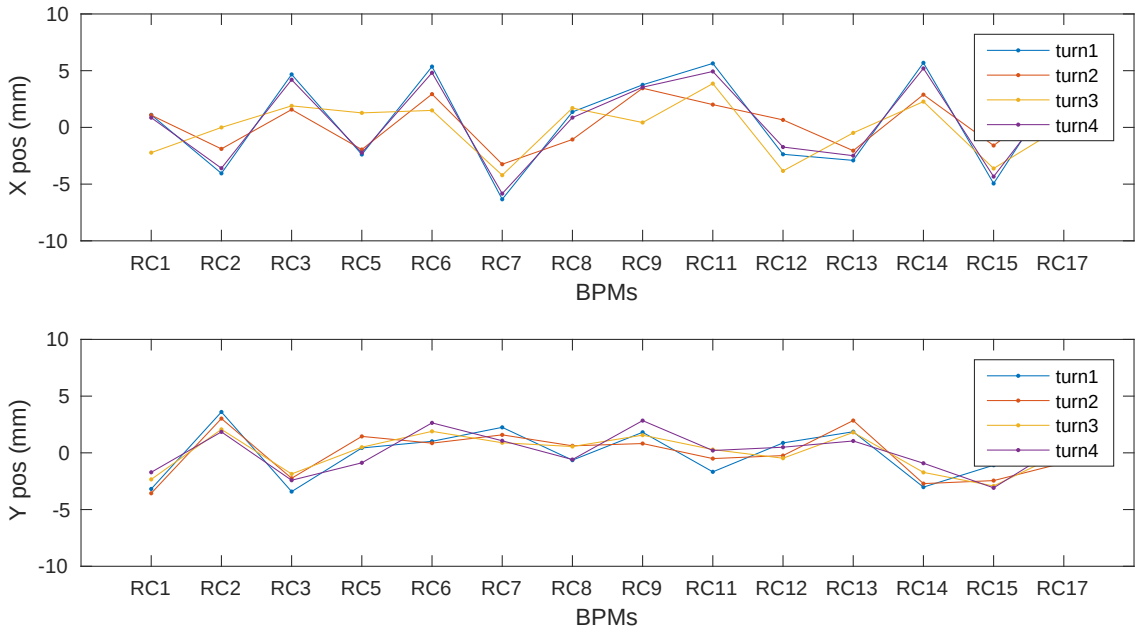

Figure B.6: Result of calling the plot_bpms function with a set of BPM data.

B.1.5 FLEA3 camera control

The 'Camera Control' button in the UMER control GUI will launch the FLEA3 camera interface, seen in Figure B.7. This GUI is used for matching the beam and imaging beam profiles on the first turn in both the ring and injection lin. The GUI has several buttons that all perform complex calculations. Detailed on what every button does in the GUI can be found here [1]. The following are the main functions used by the GUI:

- discover_cameras - return objects for all currently online FLEA3 cameras
- set_camera - choose active camera
- get_pic_info - takes a picture and returns image data along with related camera information

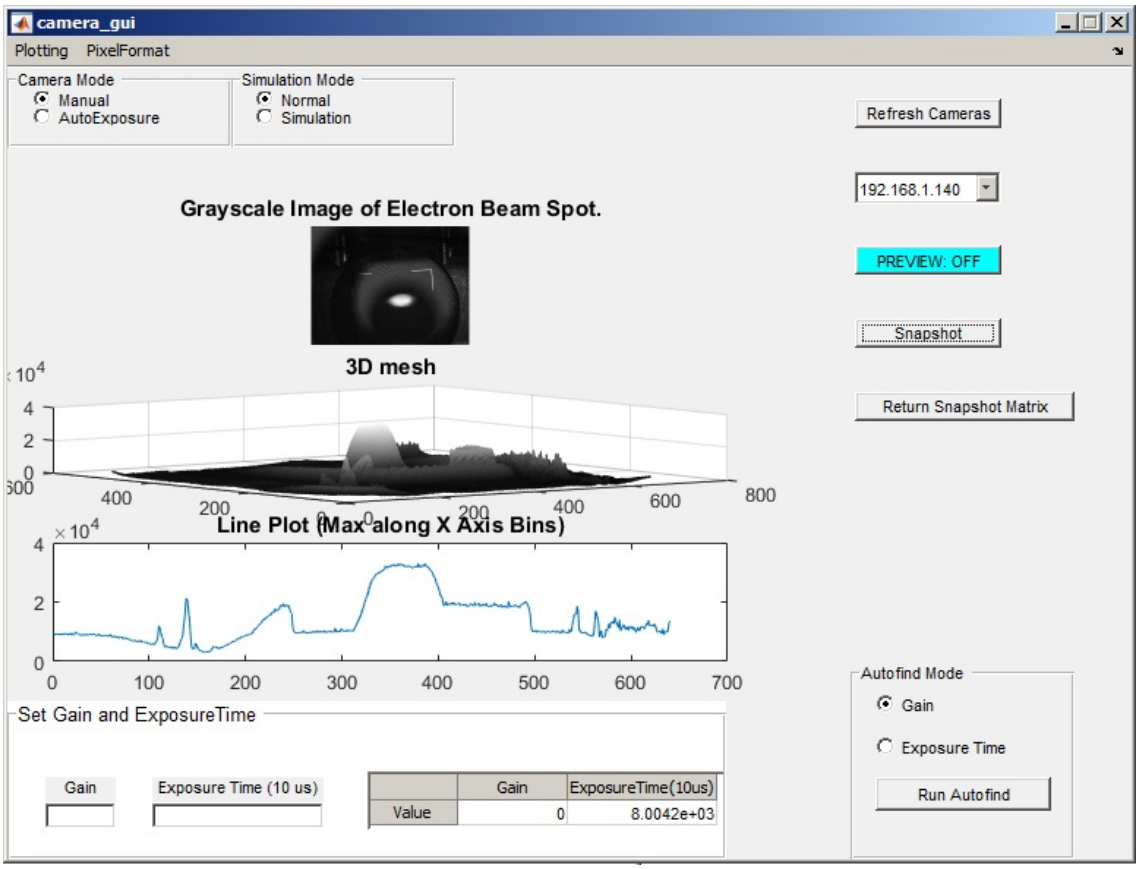

Figure B.7: Camera control GUI within UMER

- save_snap_data - saves image data to a file
- autofind - automatically set exposure/gain to avoid saturation

B.1.6 Cheat sheet functions

The following is a cheatsheat list of useful functions when working with the UMER controls software. These are all Matlab functions and have detailed comments within them explaining how they function.

- Magnet Control
  - set_current – sets a magnet current

  - get_current – gets a magnet current
  - set_voltage – sets a magnet voltage
  - get_voltage – gets a magnet voltage
  - set_setpoint – sets the default magnet current
  - get_setpoint – gets the default magnet current
  - set_PD – sets PD-Rec and PD-Inj together
  - setring – sets families of magnets
  - setc – shortcut function for set_current
  - getc – shortcut function for get_current
  - setp – shortcut function for set_setpoint
  - getp – shortcut function for get_setpoint
- BPM and WCM
  - get_bpm – returns bpm data for a specific bpm
  - get_bpms – returns bpm data for all bpms
  - get_wcm – returns the current monitor trace
  - dcct – returns the beam current measured at the wall current monitor
  - gen_bpm_noise – generates a set of bpm noise data to use in processing
  - get_bpmcalibration – returns bpm slope conversion factor
  - get_scope – return scope data for the bpm
  - get_scope_ext – checks to see if bpm scope is in extended mode
  - set_scope_bandwidth – sets the bpm scope bandwidth remotely
  - set_scope_ext – extends the bpm scope for measuring more turns
  - initialize_scope – initializes bpm scope
  - initialize_wcm – initializes wcm scope
  - list_BPMs – lists which bpms are currently working
  - load_bpm_noise – loads a set of measured bpm noise data
  - load_bpms – loads a set of saved bpm data
  - plot_bpms – plotting function to plot bpm data objects
  - save_bpms – saves a set of bpm object data
  - save_bpms_extra – saves more info than save_bpms
  - switch2bpm – switches the multiplexor to a BPM
- Heater Control
  - setscheduleheater_rampup – set a time and date to rampup the heater

  - setscheduleheater_rampdown – set a time and date to rampdown heater
  - set_heater – set the heater voltage

- thering object
  - addmagnet – add a new magnet to thering
  - buildring – build thering object from a magnet settings file
  - savering – save a magnet settings file
  - listnames – list all magnet names in thering
  - listfamily – list all families in thering
  - display_magnet – prints out info about a magnet
  - display_magnet_family – prints out magnets in a specific family
  - getfamily – returns magnet index locations in a given family
  - getname – returns magnet info and index for a given magnet names
  - getidx – returns a magnet name given the index location in thering
  - getlocation – returns magnet index locations in a specific location

- General
  - createdirectorypath - creates a list of directories in accelerator device object
  - get4closedorbit – returns closed orbit data given a set of bpm objects
  - getdatalist – returns a list of files in a specific directory
  - loadmagnetsettings – load a new set of magnet settings
  - umersendmail – send an automated email
  - calctune – calculate tune using an FFT
  - get4tune – calculate tune using four turn formula
  - naff – calculate tune using NAFF algorithm

- Orbit Response Matrix
  - findrespm_umer – measures online orbit response matrix
  - respm_solution – SVD analysis of an orbit response matrix

- RCDS
  - run_RCDS – main function that starts an rcds run
  - save_RCDS – saves the results of an rcds run
  - func_obj_current – function objective to maximize current

- Quad Steering and Measurement

  - quad_as_BPM2 – Measure the beam position at the center of the quads

- FLEA3 Camera Control
  - discover_cameras – return objects for all currently online FLEA3 cameras
  - set_camera – choose active camera
  - get_pic_info– take a picture, returns image data and related camera info
  - save_snap_data – save image data to file
  - autofind – automatically set exposure/gain to avoid saturation
  - convert_from_pixel_to_mm – look-up conversion factor by RC number.

Appendix B: Bibliography

[1] Levon Dovlatyan and Kiersten Ruisard. Umer controls guide. unpublished, 2017.

[2] G. Portmann, J. Corbett, and A. Terebilo. An Accelerator control middle layer using Matlab. *Conf. Proc. C*, 0505161:4009, 2005.

[3] Andrei Terebilo. Accelerator modeling with matlab accelerator toolbox. *PACS2001. Proceedings of the 2001 Particle Accelerator Conference (Cat. No.01CH37268)*, 4:3203–3205 vol.4, 2001.

Appendix C: Additional notes on numerical algorithms

C.1 Fourier transform tune measurement uncertainty

Starting from the discrete fourier function for betatron motion:

$$\hat{x}(Q) = \sum_{n=1}^{N} x(n)\, e^{-2\pi i Q n/N} \tag{C.1}$$

the tune is rewritten as $Q = q_{int} + q_{frac}$. The exponential term now becomes:

$$\left[e^{-2\pi i (q_{int}+q_{frac})n} \right]^{(1/N)} \tag{C.2}$$

noting that q_{int}, n, N are all integers. Using Euler's formula, the exponential term with q_{int} can be rewritten as:

$$e^{-2\pi i q_{int} n} = \cos(2\pi q_{int} n) - i \sin(2\pi q_{int} n) = 1 \tag{C.3}$$

The $q_{int}n$ term will always be an integer making the cosine term 1 and the sine term 0. This means the Fourier transform can not determine the integer part of the tune and can only measure the fractional part. As a result, the actual discrete function

transformed will be:

$$\hat{x}(Q) = \sum_{n=1}^{N} x(n)\, e^{-2\pi i q_{frac} n/N} \tag{C.4}$$

Due to the nature of trigonometric functions, there is a similar problem in determining the difference between q_{frac} and $1 - q_{frac}$. Writing out Euler's formula for $(1 - q_{frac})$ gives:

$$e^{-2\pi i(1-q_{frac})n} = \cos\left(2\pi(1 - q_{frac})n\right) - i \sin\left(2\pi(1 - q_{frac})n\right) \tag{C.5}$$

With trigonometric sum and difference identities each term can be expanded out to:

$$\begin{aligned} \cos\left(2\pi n - 2\pi q_{frac} n\right) = &\quad \cos\left(2\pi n\right)\cos\left(2\pi q_{frac} n\right) - \sin\left(2\pi n\right)\sin\left(2\pi q_{frac} n\right) && \text{(C.6a)} \\ = &\quad \cos\left(2\pi q_{frac} n\right) \end{aligned}$$

$$\begin{aligned} \sin\left(2\pi n - 2\pi q_{frac} n\right) = &\quad \sin\left(2\pi n\right)\cos\left(2\pi q_{frac} n\right) + \sin\left(2\pi q_{frac} n\right)\cos\left(2\pi n\right) && \text{(C.6b)} \\ = &\quad \sin\left(2\pi q_{frac} n\right) \end{aligned}$$

Giving the result that:

$$e^{-2\pi i(1-q_{frac})n} = e^{-2\pi i(q_{frac})n} \tag{C.7}$$

Thus, the Fourier transform can not tell the different between the fractional tunes that are above or below an integer number.

C.2 Rectangular function discrete Fourier transform

Starting from Eq. 4.9, the DFT of the rectangular function is written as:

$$\hat{w}_R(Q_j) = \frac{1}{M} \sum_{n=-\frac{M-1}{2}}^{\frac{M-1}{2}} e^{-2\pi i Q_j n} \tag{C.8}$$

Using the equation for a bounded geometric series:

$$\sum_{n=N_1}^{N_2} r^n = \frac{r^{N_1} - r^{N_2+1}}{1-r} \tag{C.9}$$

Eq C.8 can be reduced to:

$$\sum_{n=-\frac{M-1}{2}}^{\frac{M-1}{2}} e^{-2\pi Q_j n} = \frac{e^{-2\pi i Q_j(-(M-1)/2)} - e^{-2\pi i Q_j((M+1)/2)}}{1 - e^{-2\pi i Q_j}} \tag{C.10}$$

Simplifying out the linear phase terms leads to a sinc function:

$$\frac{e^{-2\pi i Q_j(-(M-1)/2)} - e^{-2\pi i Q_j((M+1)/2)}}{1 - e^{-2\pi i Q_j}} = \frac{e^{-\pi i Q_j}\left(e^{\pi i Q_j M} - e^{-\pi i Q_j M}\right)}{e^{-\pi i Q_j}\left(e^{\pi i Q_j} - e^{-\pi i Q_j}\right)} = \frac{\sin \pi M Q_j}{\sin \pi Q_j} \tag{C.11}$$

The final transformed rectangular function can then be written as:

$$\hat{w}_R(n) = \frac{\sin \pi M Q_j}{M \sin \pi Q_j} \tag{C.12}$$

Appendix D: Additional notes on simulation

D.1 Magnet integrated strengths

The integrated fields for the transfer section quadrupole magnets are plotted below in Figure D.1.

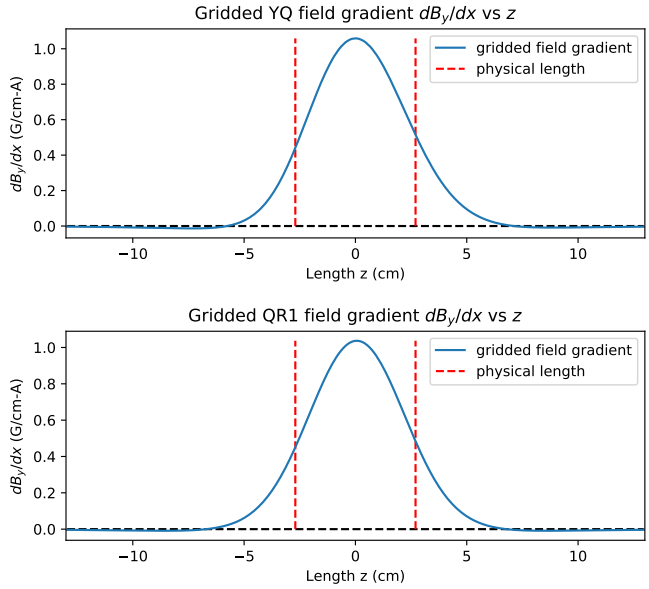

Figure D.1: The vertical gradient component of the magnetic field, dB_y/dx is plotted as a function of z through the magnet. The field is measured at the transverse center, $(x, y) = (0, 0)$. Physical length is plotted in red.

The pulsed dipole field is plotted in Figure D.2. Note the significantly weaker fields compared to that of the regular UMER dipoles. The calculated values for the pulsed magnets can be found in Table 5.1. There are no equivalent spiral PCB

gridded models for the short steerers and corrector magnets.

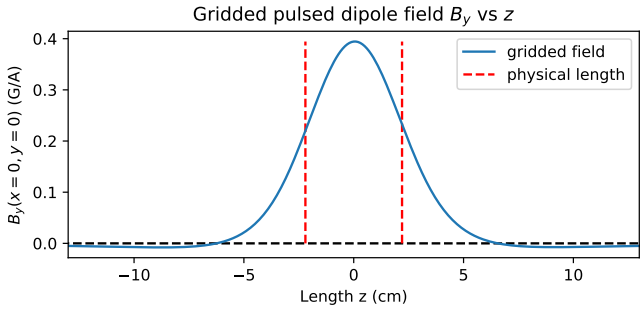

Figure D.2: The vertical gradient component of the magnetic field, dB_y/dx is plotted as a function of z through the magnet. The field is measured at the transverse center, $(x, y) = (0, 0)$. Physical length is plotted in red.

D.2 Details on gridded vs hard edge fields

A Warp simulation was setup to generate Figures 5.5 and 5.6. The simulations used a 1 mm step size with no space charge force and only a single particle. The particle energy was set to 10 keV. For each magnet a gridded field was created with the function *addnewbgrd* and a hard edge field with *addnewquad,addnewdipo*. For both the quadrupole and dipole a current of 2.5 amps was used. In the case of the dipole, a rectangular (box) dipole was incorporated.

D.3 Magnet Transfer Maps

A list of the standard 1D transfer maps are listed below:

$$M_{\text{drift}} = \begin{bmatrix} 1 & s \\ 0 & 1 \end{bmatrix} \tag{D.1a}$$

$$M_{\text{quad·F}} = \begin{bmatrix} \cos\sqrt{K}s & \frac{1}{\sqrt{K}}\sin\sqrt{K}s \\ -\sqrt{K}\sin\sqrt{K}s & \cos\sqrt{K}s \end{bmatrix} \tag{D.1b}$$

$$M_{\text{quad·D}} = \begin{bmatrix} \cosh\sqrt{K}s & \frac{1}{\sqrt{K}}\sinh\sqrt{K}s \\ \sqrt{K}\sinh\sqrt{K}s & \cosh\sqrt{K}s \end{bmatrix} \tag{D.1c}$$

$$M_{\text{dipo}} = \begin{bmatrix} \cos s/R & R\sin s/R \\ -\frac{1}{R}\sin s/R & \cos s/R \end{bmatrix} \tag{D.1d}$$

$$M_{\text{edge}} = \begin{bmatrix} 1 & 0 \\ \frac{1}{R}\tan\Psi & 1 \end{bmatrix} \tag{D.1e}$$

The maps are listed for the horizontal $+x$ direction. The vertical $+y$ is similar. R is the radius of curvature, K is the focusing strength, and Ψ is the perpendicular entrance and exit angle into the dipole.

D.4 General Transfer Map Equations

Given a set of two particles to track through a periodic cell, the general transfer map in Eq. 5.6 and 5.7 can be solved:

$$\begin{pmatrix} x_{0,1f} \\ x'_{0,1f} \end{pmatrix} = \begin{pmatrix} m_{11} & m_{12} \\ m_{21} & m_{22} \end{pmatrix} \begin{pmatrix} x_{0,1i} \\ x'_{0,1i} \end{pmatrix} \tag{D.2}$$

Multiplying out the matrix and solving for each element results in the following equations:

$$\begin{aligned} m_{11} &= \frac{x'_{0i}x_{1f} - x_{0f}x'_{1i}}{x'_{0i}x_{1i} - x_{0i}x'_{1i}} \\ m_{12} &= \frac{x_{0i}x_{1f} - x_{0f}x_{1i}}{x_{0i}x'_{1i} - x'_{0i}x_{1i}} \\ m_{21} &= \frac{x'_{0i}x'_{1f} - x'_{0f}x'_{1i}}{x'_{0i}x_{1i} - x_{0i}x'_{1i}} \\ m_{22} &= \frac{x_{0i}x'_{1f} - x'_{0f}x_{1i}}{x_{0i}x'_{1i} - x'_{0i}x_{1i}} \end{aligned} \tag{D.3}$$

These equations can then be used to calculate each matrix element.

D.5 Tune in a FODO lattice

Assuming an ideal FODO cell lattice, which UMER can be approximated to quite well, a set of equations can be derived to measure the transverse tunes as a

function of quadrupole magnet strengths. Using the transfer matrix for a focusing and defocusing quadrupole, and a drift section from Eq. D.1a, D.1b,D.1c, the FODO cell transfer matrix can be calculated:

$$M_{\text{FODO}} = M_{\text{drift}} M_{\text{quad'D}} M_{\text{drift}} M_{\text{quad'F}} = \begin{bmatrix} A & B \\ C & D \end{bmatrix} \tag{D.4}$$

Since the FODO cell matrix is periodic, it is equivalent to the general periodic transfer matrix from Eq. 5.6. An expression for the phase advance, and correspondingly the tune, can be written out for both the transverse planes:

$$\cos\phi_x = \cosh\theta_2(\cos\theta_1 - \frac{1}{\eta}\theta_1\sin\theta_1) + \sinh\theta_2\sin\theta_1(\frac{1}{2}(\frac{\theta_2}{\theta_1} - \frac{\theta_1}{\theta_2}) - \frac{1}{2\eta^2}\theta_1\theta_2 + \frac{1}{\eta}\theta_2\cot\theta_1) \tag{D.5}$$

$$\cos\phi_y = \cos\theta_2(\cosh\theta_1 - \frac{1}{\eta}\theta_1\sinh\theta_1) + \sin\theta_2\sinh\theta_1(\frac{1}{2}(\frac{\theta_2}{\theta_1} - \frac{\theta_1}{\theta_2}) - \frac{1}{2\eta^2}\theta_1\theta_2 + \frac{1}{\eta}\theta_2\coth\theta_1) \tag{D.6}$$

where $\theta_1 = \sqrt{k_x}l_{qx}$ and $\theta_2 = \sqrt{k_y}l_{qy}$. Here k_x, k_y are the quadrupole focusing strengths, l_q is the length of the quadrupoles, and η is called the fill factor and is a function of l_q and the FODO cell spacing.

Eq. D.5 and D.6 can be simplified by taylor expanding the trigonometric functions up to second order:

$$Q_x = C_0 + C_x k_x - C_y k_y + k_x k_y C_{xy} \tag{D.7a}$$

$$Q_y = C_0 - C_x k_x + C_y k_y + k_x k_y C_{xy} \tag{D.7b}$$

where C_0, C_x, C_y are constants dependent on quadrupole lengths, l_{qx}, l_{qy}, and FODO cell lengths.

Appendix F: Additional notes on integrable optics

F.1 Canonical transformation of the Hamiltonian

Considering only the horizontal direction and starting with the following type one generating function:

$$F_1(x, \theta_x, s) = -\frac{x^2}{2\beta_x(s)}(\tan\theta_x - \frac{\dot{\beta}_x(s)}{2}) \tag{F.1}$$

a canonical transformation to action-angle variables is carried out. The transformation equations need to be solved:

$$J_x = -\frac{\partial}{\partial\theta_x}F_1 = \frac{x^2}{2\beta_x}(\sec^2\theta_x) \tag{F.2a}$$

$$p_x = \frac{\partial}{\partial x}F_1 = -\frac{x}{\beta_x}(\tan\theta_x - \frac{\dot{\beta}_x}{2}) \tag{F.2b}$$

along with the following equation:

$$\frac{\partial}{\partial s}F_1 = \frac{x^2\tan\theta_x\dot{\beta}_x}{2\beta_x^2} + \frac{x^2\ddot{\beta}_x}{4\beta_x} - \frac{x^2\dot{\beta}_x^2}{4\beta_x^2} \tag{F.3}$$

Eq. F.2a, F.2b, and F.3 are then used to solve the Hamilton-Jacobi equation:

$$\tilde{H}_x(\theta_x, J_x, s) = H_x(x, p_x, s) + \frac{\partial}{\partial s} F_1(x, \theta_x, s) \tag{F.4}$$

where:

$$H_x(x, p_x, s) = \frac{1}{2} k(s) x^2 + p_x^2 \tag{F.5}$$

Note that in order to substitute out $k(s)$ the amplitude function from Eq. 2.12 is used:

$$\frac{1}{2}\beta\ddot{\beta} - \frac{1}{4}\dot{\beta}^2 + k(s)\beta^2 = 1 \tag{F.6}$$

The final resulting Hamiltonian ends up being:

$$\tilde{H}_x = \frac{J_x}{\beta_x} \tag{F.7}$$

F.2 Octupole channel connections

The setup of the octupole channel is quite complex and requires some explanation for anyone continuing the experiment in the future. The channel itself has seven octupole PCBs placed inside and overlapping each other. The locations of the PCBs are marked by 'inch' markings on the magnet. These 'inch' markings serve as the labels on wires connected to the magnets. The common names for the octupoles, used in the controls code, are OC1 to OC7. As a result, the wires coming from the power supplies used for each octupole are labeled as OC1 to OC7. The two connections, from the power supply and from the magnet, meet at a breadboard.

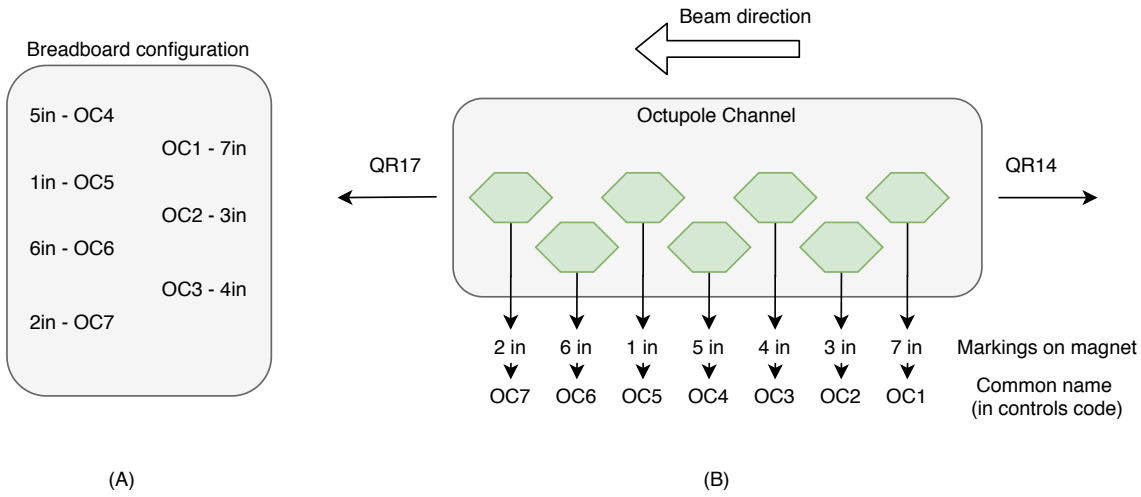

Figure F.1: (A) wire connections on the breadboard. (B) Labels on the octupole channel corresponding to each octupole common name.

Common Name	Connection 1	Connection 2
OC1	red-black	black-red
OC2	green-red	black-black
OC3	green-red	black-black
OC4	red-red	black-black
OC5	red-black	black-red
OC6	red-black	black-red
OC7	red-green	black-black

Table F.1: List of polarity connections for each octupole magnet in the octupole channel.

The breadboard, shown in Figure F.1, is the connection point for two differently labeled wires.

There is also a need to make sure all the octupoles have the same polarity set. Unlike other magnets on UMER, the octupole do not have direct polarity switches. The wire connections are flipped to change polarity. Table F.1 shows the wire connections for the default polarity setting. E.g. for OC4 the red wire from the

power supply is connected to the red wire coming from the octople and the black wires coming from each end is also connected. These connections guarantee that all the octupoles will have the same polarity.

F.3 Further analysis on tune shifts

The experimental tune shift measurements took a few weeks to properly setup and eventually collect data. An orbit was needed that would minimize beam scraping when the octupole channels were turned on. Separately this orbit needed to be as centered as possible so that large amplitude oscillations can fit within the beam pipe. The amplitude oscillations were done using a horizontal and vertical corrector magnet in the injection line to inject the beam off the closed orbit. To get a sense of how large the generated oscillations are, position data in the BPM before the octupole channel (RC3) is analyzed. Figure F.2 shows the results. Here we plot the beam's position vs turns for different injection kicks. For example, looking at the bottom left plot in Figure F.2, the vertical position of the beam is plotted for 10 different vertical injection kicks; this is done for the case where there was no horizontal kick included. From this plot we see the oscillations damp down by the 32nd turn and that the maximum vertical kick displaces the beam by about ± 4 mm, quite large in UMER's case. Another point is also the fact that the horizontal oscillations are small and damp out much quicker than the vertical oscillations; this has always been an issue in UMER due to the large density of dipoles and the uncompensated earth's field. While a good tune measurement can be made

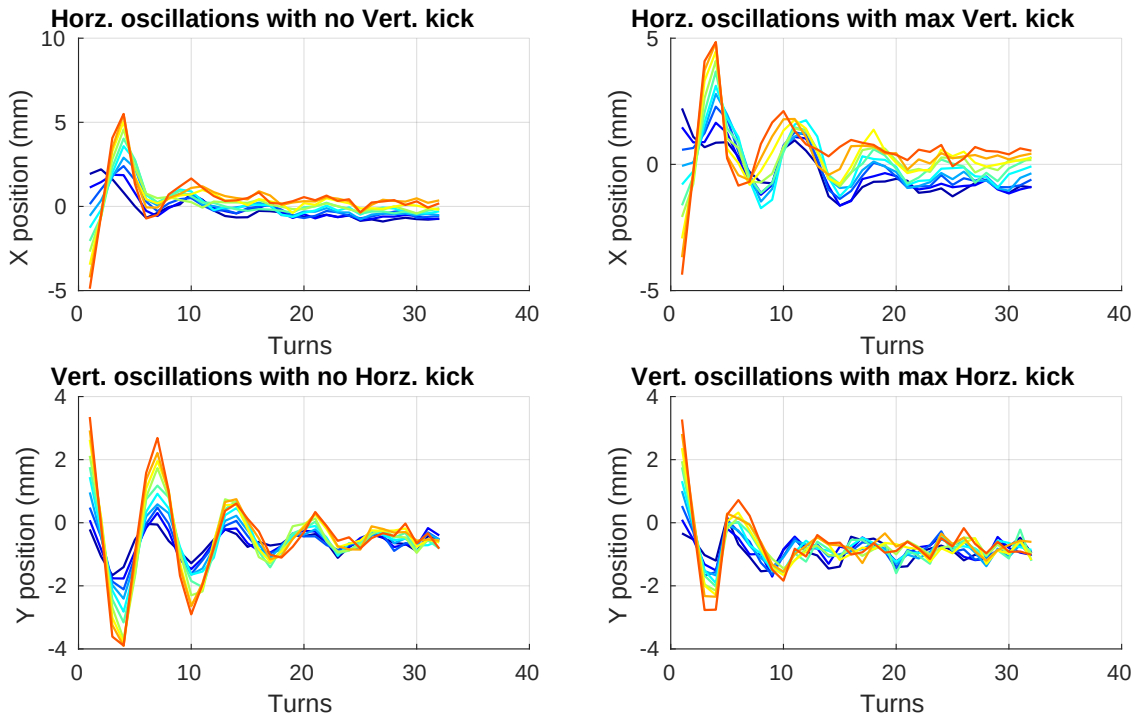

Figure F.2: Position data up to 32 turns is plotted from a single BPM (RC3). (top) Horizontal positions are plotted at different horizontal injection kicks. (bottom) Vertical positions are plotted at different vertical injection kicks. This is for the case where the octupole channel was set to 0.5 amps.

using 32 turns of vertical position data, it is much more difficult with the horizontal position data as the oscillations appear to fade after a few turns. Another point is the appearance of coupling. Looking at the horizontal oscillations with a maximum vertical kick (top right plot in Figure F.2), there is clear coupling going on. This is a known problem as some of the corrector magnets at the injection line have obvious rotation errors in them.

Next oscillations are analyzed as a function of octupole strength. The data from the bottom left plot of Figure F.2 is used as it has the clearest measurements. This data is plotted for three different octupole strengths and shown in Figure F.3. Visually one can see the octupole magnets damping the oscillations faster as their

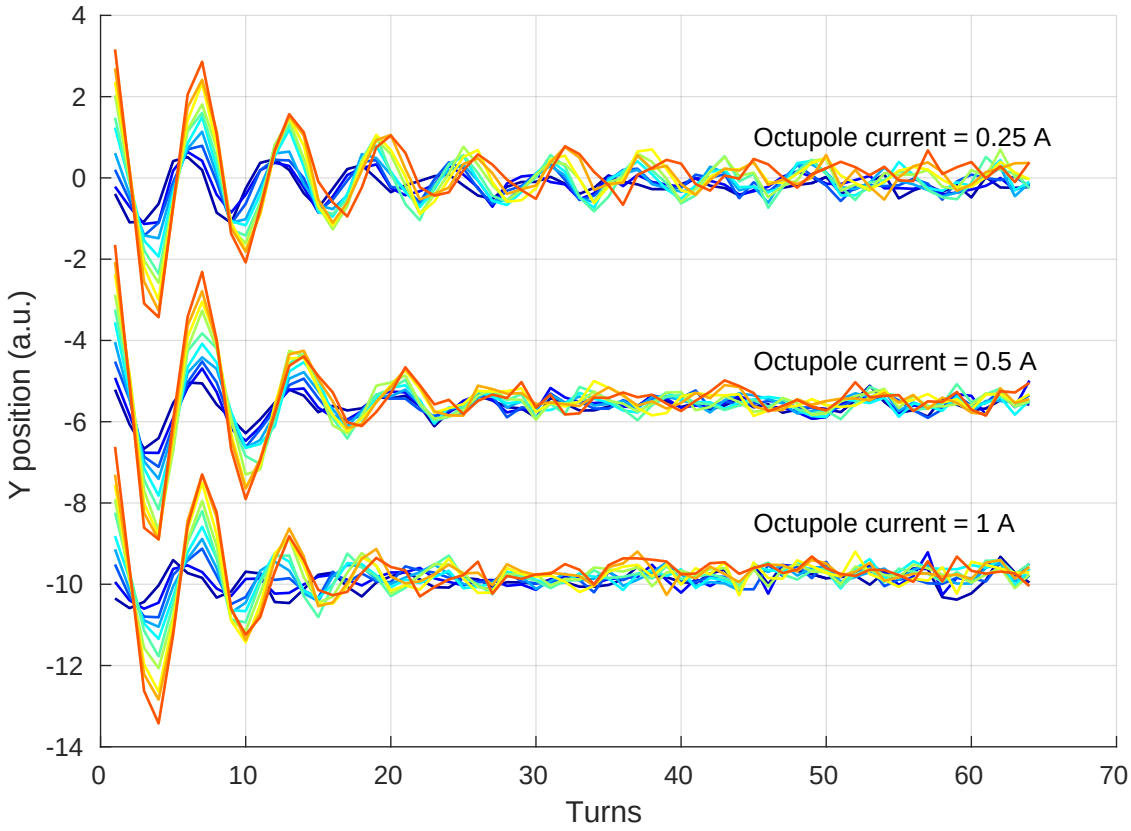

Figure F.3: Vertical oscillations with different injection kicks are plotted for 3 values of octupole strength. The data is from the BPM (RC3) before the octupole channel. The positions are plotted above each other to demonstrate the different damping times, thus the vertical axis units do not represent the actual postiions of the beam.

strength is increased. At a current setpoint of 0.25 amps, the vertical oscillations damp out around turn 40, at 0.5 amps this happens around turn 25, and at 1 amp it happens around turn 15. Such damping results in a catch-22 situation. A strong enough octupole strength is needed to be able to induce a large tune shift to measure, but such a large octupole strength results in damping of the oscillations making it difficult to get an accurate measurement of the transverse tunes.

The fourier transform signals from the position data is analyzed in Figures F.4 and F.5. In these plots the fourier transforms are plotted for three octupole strength values and three position data length values. In each plot the fourier

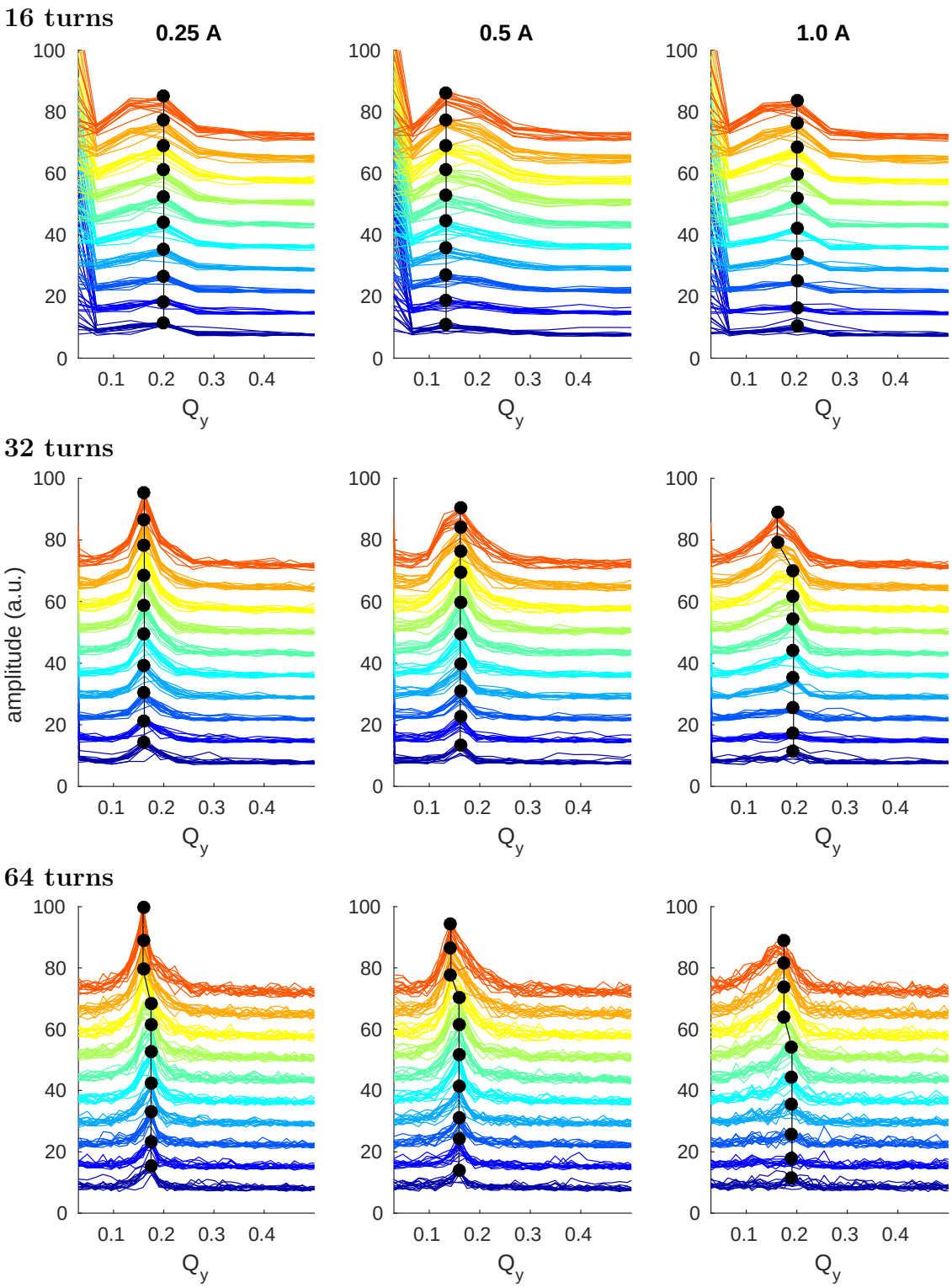

Figure F.4: FFT signals are plotted for different octupole strengths (0.25, 0.50, 1.0 A) and different number of turns used (16, 32, 64 turns). In each plot the FFT signals from 14 BPMs is plotted for different vertical amplitude oscillations. Blue color is the smallest amplitude oscillations and red is the largest.

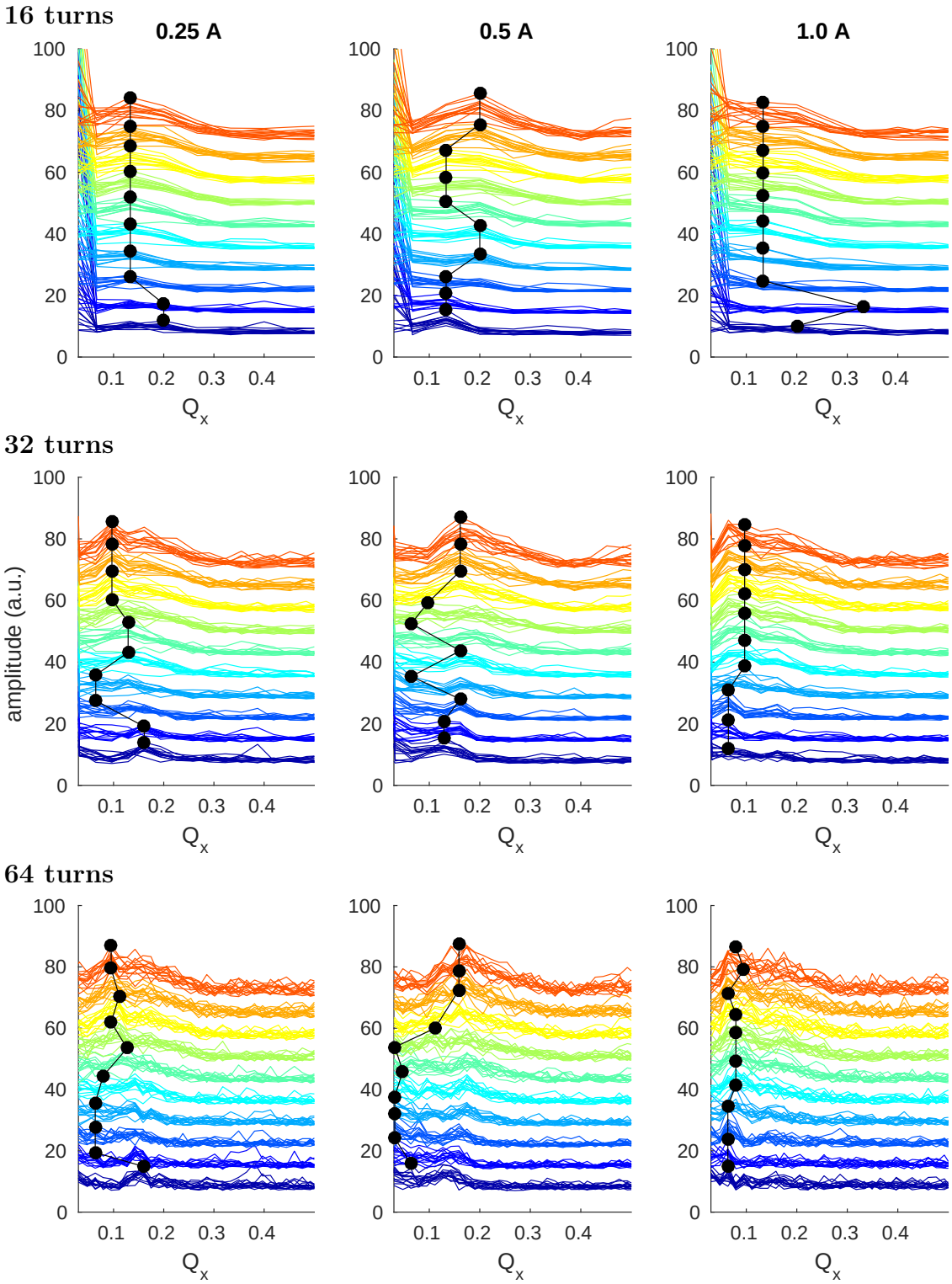

Figure F.5: FFT signals are plotted for different octupole strengths (0.25, 0.50, 1.0 A) and different number of turns used (16, 32, 64 turns). In each plot the FFT signals from 14 BPMs is plotted for different horizontal amplitude oscillations. Blue color is the smallest amplitude oscillations and red is the largest.

transform is plotted using the 14 available BPMs. The beam oscillation amplitudes are slowly increased starting with a small amplitude, blue color in the plots, to a large amplitude, red color in plots. Figure F.4 shows data for the vertical direction and Figure F.5 shows the horizontal. Looking at these plots, a lot of information about the data becomes clear. The 64 turn signals are much noisier than the 16 and 32 turn signals; this is again because the oscillations damp out by about 30 turns in, making the remaining signal essentially just noise. The vertical signal fourier transforms are much clearer than the horizontal. The horizontal data is simply too noisy and does not have enough clear oscillations in the signal to have an accurate enough fourier transform. From the data it is also clear that the resolution for the 16 and 32 turn data is not high enough to accurately detect and measure the expected levels of tune shift occuring from the nonlinear octupole channel. In Figure F.4 we can start to see a shift in the tune for the case of 64 turns of data and at the largest amplitudes (orange to red color in the plot). It is hard to say at these large amplitudes if the tune shift is truely due to the nonlinear magnets or if the scraping of the beam, and thus the change in space charge force, is the cause of the tune shift.

One last diagnostic to look at is the amount of beam loss/scraping occuring during the measurements. For every tune measurement a current measurement was also taken with the wall current monitor. The results are plotted in Figure F.6. Looking at a single subplot of Figure F.6, the color represents the normalized amount of beam loss occuring. The x axis represents increasing horizontal amplitudes and the y axis represents increasing vertical amplitudes. The plot visual shows how much

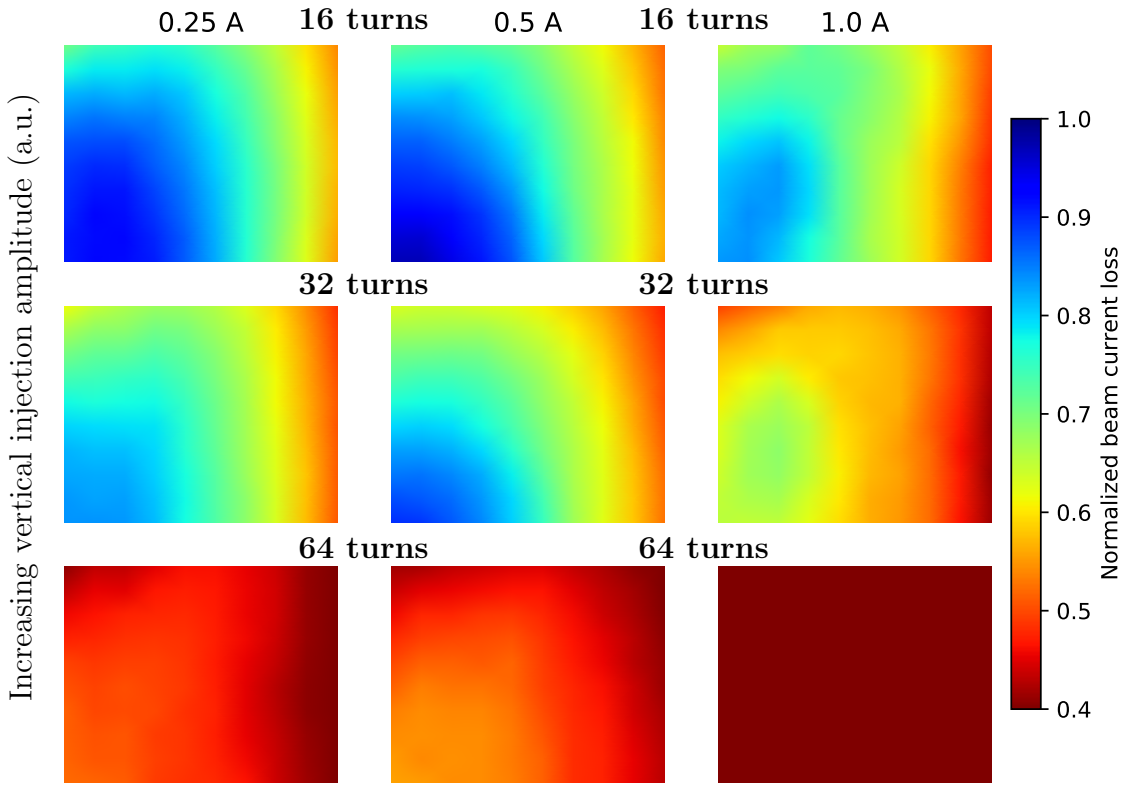

Figure F.6: Each plot shows the beam current loss as a function of increasing horizontal and vertical injection amplitudes. Blue color represents little to no beam loss and red indicates large amounts of beam loss. The nine plots are for three octupole strengths, (0.25, 0.5, 1.0 A), and three different data lengths, (16, 32, 64 turns). The current loss is measured at the 16th, 32nd, and 64th turns.

beam is being loss as the amplitudes are increased to measure transverse tune shifts. There are a total of nine plots made for different octupole strengths and different turns. The beam loss is measured at the 16th, 32nd, and 64th turn. From the figure we can tell more beam loss occurs at larger horizontal amplitudes as opposed to vertical amplitudes. Secondly, by the time the beam reaches the 64th turn more than 50% of the beam current has been lost, making the data not usable.

Appendix G: Additional notes on steering

G.1 Quadrupole centering interception point minimization

The goal is to find an interception point, (x_0, y_0), that minimizes the distance between a set of N lines:

$$C = \min: \sum_i^N \frac{|a_i x_0 + b_i y_0 + c_i|^2}{a_i^2 + b_i^2} \tag{G.1}$$

To minimize the function we take a set of partial derivatives with respect to the interception point and set the equations equal to zero:

$$\frac{\partial C}{\partial x_0} = 2 \sum_i^N \frac{(a_i x_0 + b_i y_0 + c_i)}{a_i^2 + b_i^2} a_i = 0 \tag{G.2a}$$

$$\frac{\partial C}{\partial y_0} = 2 \sum_i^N \frac{(a_i x_0 + b_i y_0 + c_i)}{a_i^2 + b_i^2} b_i = 0 \tag{G.2b}$$

Expanding out these equations leads to:

$$x_0 \sum_i^N \frac{a_i^2}{a_i^2 + b_i^2} + y_0 \sum_i^N \frac{b_i a_i}{a_i^2 + b_i^2} + \sum_i^N \frac{c_i a_i}{a_i^2 + b_i^2} = 0 \tag{G.3a}$$

$$x_0 \sum_i^N \frac{a_i b_i}{a_i^2 + b_i^2} + y_0 \sum_i^N \frac{b_i^2}{a_i^2 + b_i^2} + \sum_i^N \frac{c_i b_i}{a_i^2 + b_i^2} = 0 \tag{G.3b}$$

where each summation term is a constant calculated from the equations of each line. Variable substitutions are used for the summations to simplify the equations to:

$$Ax_0 + By_0 + C = 0 \tag{G.4a}$$

$$Dx_0 + Ey_0 + F = 0 \tag{G.4b}$$

Eq. G.4a and G.4b are then solved for the interception point:

$$P(x_0, y_0) = (x_0, y_0) = (\frac{EC - BF}{BD - EA}, \frac{AF - CD}{BD - EA}) \tag{G.5}$$

with the following variable substitutions:

$$A = \sum_i^N \frac{a_i^2}{a_i^2 + b_i^2} \tag{G.6a}$$

$$B = \sum_i^N \frac{b_i a_i}{a_i^2 + b_i^2} \tag{G.6b}$$

$$C = \sum_i^N \frac{c_i a_i}{a_i^2 + b_i^2} \tag{G.6c}$$

$$D = \sum_i^N \frac{a_i b_i}{a_i^2 + b_i^2} \tag{G.6d}$$

$$E = \sum_i^N \frac{b_i^2}{a_i^2 + b_i^2} \tag{G.6e}$$

$$F = \sum_i^N \frac{c_i b_i}{a_i^2 + b_i^2} \tag{G.6f}$$

Cumulative Bibliography

[1] C. Joshi and Thomas C. Katsouleas. Plasma accelerators at the energy frontier and on tabletops. *Phys. Today*, 56N6:47–53, 2003.

[2] A. Abada et al. FCC Physics Opportunities: Future Circular Collider Conceptual Design Report Volume 1. *Eur. Phys. J. C*, 79(6):474, 2019.

[3] Barney L. Doyle, Floyd Del McDaniel, and Robert W. Hamm. The future of industrial accelerators and applications. *Reviews of Accelerator Science and Technology*, 10(01):93–116, 2019.

[4] F.J. Sacherer. Rms envelope equations with space charge. *IEEE Trans. Nucl. Sci.*, 18:1105–1107, 1971.

[5] R.L. Gluckstern. Oscillation Modes in Two Dimensional Beams. pages H–5, 1971.

[6] I. Hofmann, L.J. Laslett, L. Smith, and I. Haber. Stability of the Kapchinskij-Vladimirskij (K-V) distribution in long periodic transport systems. *Part. Accel.*, 13:145–178, 1983.

[7] R. Baartman. Betatron resonances with space charge. *AIP Conf. Proc.*, 448(1):56–72, 1998.

[8] K. Kojima, H. Okamoto, and Y. Tokashiki. Empirical condition of betatron resonances with space charge. *Phys. Rev. Accel. Beams*, 22:074201, Jul 2019.

[9] Chao Li and R. A. Jameson. Structure resonances due to space charge in periodic focusing channels. *Phys. Rev. Accel. Beams*, 21:024204, Feb 2018.

[10] Ingo Hofmann and Oliver Boine-Frankenheim. Space-charge structural instabilities and resonances in high-intensity beams. *Phys. Rev. Lett.*, 115:204802, Nov 2015.

[11] G. Franchetti, O. Chorniy, I. Hofmann, W. Bayer, F. Becker, P. Forck, T. Giacomini, M. Kirk, T. Mohite, C. Omet, A. Parfenova, and P. Schütt. Experiment on space charge driven nonlinear resonance crossing in an ion synchrotron. *Phys. Rev. ST Accel. Beams*, 13:114203, Nov 2010.

[12] Giuliano Franchetti, Simone Gilardoni, Alexander Huschauer, Frank Schmidt, and Raymond Wasef. Space charge effects on the third order coupled resonance. *Phys. Rev. Accel. Beams*, 20:081006, Aug 2017.

[13] Ingo Hofmann. *Space Charge Physics for Particle Accelerators*. Springer International Publishing, 2017.

[14] Ernest D. Courant, M. Stanley Livingston, and Hartland S. Snyder. The strong-focusing synchroton—a new high energy accelerator. *Phys. Rev.*, 88:1190–1196, Dec 1952.

[15] Thorsten Hellert, Philipp Amstutz, Christoph Steier, and Marco Venturini. Toolkit for simulated commissioning of storage-ring light sources and application to the advanced light source upgrade accumulator. *Phys. Rev. Accel. Beams*, 22:100702, Oct 2019.

[16] V. Danilov and S. Nagaitsev. Nonlinear accelerator lattices with one and two analytic invariants. *Phys. Rev. ST Accel. Beams*, 13:084002, Aug 2010.

[17] S. Antipov, D. Broemmelsiek, D. Bruhwiler, D. Edstrom, E. Harms, V. Lebedev, J. Leibfritz, S. Nagaitsev, C.S. Park, H. Piekarz, P. Piot, E. Prebys, A. Romanov, J. Ruan, T. Sen, G. Stancari, C. Thangaraj, R. Thurman-Keup, A. Valishev, and V. Shiltsev. IOTA (integrable optics test accelerator): facility and experimental beam physics program. 12(03), mar 2017.

[18] Ben Freemire and Jeffrey Eldred. The integrable optics test accelerator, 2019.

[19] Alexander Valishev. Research at fast/iota: Strategy and priorities.

[20] Philip J. Bryant and Kjell Johnsen. *The Principles of Circular Accelerators and Storage Rings*. Cambridge University Press, 1993.

[21] S. Y. Lee. *Accelerator Physics*. World Scientific, 2012.

[22] I.M. Kapchinskij and V.V. Vladimirskij. Limitations of proton beam current in a strong focusing linear accelerator associated with the beam space charge. In *Proc. of the International Conference on High Energy Accelerators*, page 274, CERN, Geneva, 1959.

[23] Steven M. Lund and Boris Bukh. Stability properties of the transverse envelope equations describing intense ion beam transport. *Phys. Rev. ST Accel. Beams*, 7:024801, Feb 2004.

[24] W. T. Weng. Space charge effectstune shifts and resonances. *AIP Conference Proceedings*, 153(1):348–389, 1987.

[25] Helmut Wiedemann. *Particle accelerator physics; 4rd ed.* Springer, 2015.

[26] L. J. Laslett. On Intensity Limitations Imposed by Transverse Space-Charge Effects in Circular Particle Accelerators. *eConf*, C630610:324, 1963.

[27] J. R. Harris and P. G. O'Shea. Gridded electron guns and modulation of intense beams. *IEEE Transactions on Electron Devices*, 53(11):2824–2829, Nov 2006.

[28] T. Godlove M. Virgo Hui Li S. Bernal, D. Kehne. Technical note: Electron gun tests. unpublished, 2000.

[29] Kiersten Ruisard. *Design of a nonlinear quasi-integrable lattice for resonance suppression at the University of Maryland Electron Ring.* PhD thesis, University of Maryland College Park, 2018.

[30] W. W. Zhang, S. Bernal, H. Li, T. Godlove, R. A. Kishek, P. G. O'Shea, M. Reiser, V. Yun, and M. Venturini. Design and field measurements of printed-circuit quadrupoles and dipoles. *Phys. Rev. ST Accel. Beams*, 3:122401, 2000.

[31] K. Hamilton, L. Dovlatvan, D. Matthew, D. Sutter, S. Bernal, T. Antonsen, and B. Beaudoin. Implementing traditional longitudinal beam focusing in umer. In *2018 IEEE Advanced Accelerator Concepts Workshop (AAC)*, pages 1–4, 2018.

[32] Kieran Evans. The epics process variable gateway – version 2. In *10th ICALEPCS Int. Conf. on Accelerator & Large Expt. Physics Control Systems.*, CERN, Geneva, 2005.

[33] Armin Ronacher. Flask, 2019.

[34] Peter Forck, P. Kowina, and Dmitry Liakin. Beam position monitors. *CAS - CERN Accelerator School: Course on Beam Diagnostics, Dourdan, France*, 06 2008.

[35] Bryan et al. Quinn. Design and testing of a fast beam position monitor. volume 4, pages 2571 – 2573 vol.4, 06 2003.

[36] James W. Cooley and John W. Tukey. An Algorithm for the Machine Calculation of Complex Fourier Series. *Math. Comput.*, 19:297–301, 1965.

[37] Jacques Laskar, Claude Froeschl, and Alessandra Celletti. The measure of chaos by the numerical analysis of the fundamental frequencies. application to the standard mapping. *Physica D: Nonlinear Phenomena*, 56(2):253 – 269, 1992.

[38] David F. Sutter. Minimum data acquisition of the equilibrium orbit and tune. unpublished notes, 2017.

[39] Jonathan Barzilai and Jonathan M. Borwein. Two-Point Step Size Gradient Methods. *IMA Journal of Numerical Analysis*, 8(1):141–148, 01 1988.

[40] J. A. Nelder and R. Mead. A Simplex Method for Function Minimization. *The Computer Journal*, 7(4):308–313, 01 1965.

[41] S. Singer and J. Nelder. Nelder-Mead algorithm. *Scholarpedia*, 4(7):2928, 2009. revision #91557.

[42] Xiaobiao Huang, Jeff Corbett, James Safranek, and Juhao Wu. An algorithm for online optimization of accelerators. *Nuclear Instruments and Methods in Physics Research. Section A, Accelerators, Spectrometers, Detectors and Associated Equipment*, 726, 10 2013.

[43] M. J. D. Powell. An efficient method for finding the minimum of a function of several variables without calculating derivatives. *The Computer Journal*, 7(2):155–162, 01 1964.

[44] Timothy W. Koeth, B. Beaudoin, S. Bernal, I. Haber, R. A. Kishek, M. Reiser, P. G. OShea, Steven H. Gold, and Gregory S. Nusinovich. Measurement & simulation of interpenetration and dc accumulation of beam in the university of maryland electron ring. *AIP Conference Proceedings*, 1299(1):608–613, 2010.

[45] Ming-Kuei Hu. Visual pattern recognition by moment invariants. *IRE Trans. Information Theory*, 8:179–187, 1962.

[46] Hui Li. Magli manual for windows and linux. unpublished notes, 2012.

[47] S. Bernal. Technical note: New approach to effective length and strength of umer quadrupoles. unpublished, 2006.

[48] Alex Friedman, Ronald Cohen, D.P. Grote, Steven Lund, William Sharp, Jean-Luc Vay, I. Haber, and Rami Kishek. Computational methods in the warp code framework for kinetic simulations of particle beams and plasmas. volume 42, pages 1–1, 06 2013.

[49] M. Borland. elegant: A Flexible SDDS-Compliant Code for Accelerator Simulation. In *6th International Computational Accelerator Physics Conference (ICAP 2000) Darmstadt, Germany, September 11-14, 2000*, 2000.

[50] Andrei Terebilo. Accelerator modeling with matlab accelerator toolbox. *PACS2001. Proceedings of the 2001 Particle Accelerator Conference (Cat. No.01CH37268)*, 4:3203–3205 vol.4, 2001.

[51] Ronald D Ruth. A canonical integration technique. *IEEE Trans. Nucl. Sci.*, 30(CERN-LEP-TH-83-14):2669–2671. 3 p, Mar 1983.

[52] J. Safranek. Experimental determination of storage ring optics using orbit response measurements. *Nucl. Instrum. Meth.*, A388:27–36, 1997.

[53] Santiago Bernal. *A Practical Introduction to Beam Physics and Particle Accelerators*. Morgan & Claypool Publishers, 2018.

[54] Martin Reiser. *Theory and Design of Charged Particle Beams*. John Wiley and Sons, Ltd, 2008.

[55] Chao Wu, Eyad Abed, Santiago Bernal, Brian Beaudoin, Rami Kishek, Shea, M Reiser, and D Sutter. Linear resonance analysis of beams with intense space charge in the university of maryland electron ring (umer). *HB 2008 - 42nd ICFA Advanced Beam Dynamics Workshop on High-Intensity, High-Brightness Hadron Beams*, 01 2008.

[56] S. Bernal, B. Beaudoin, I. Haber, T. Koeth, Y. Mo, E. Montgomery, K. P. Rezaei, K. Ruisard, W. Stem, D. Sutter, H. Zhang, and R. A. Kishek. Nonlinear dynamics with space-charge in a small electron recirculator. *AIP Conference Proceedings*, 1777(1):100003, 2016.

[57] K. Moriya, K. Fukushima, K. Ito, T. Okano, H. Okamoto, S. L. Sheehy, D. J. Kelliher, S. Machida, and C. R. Prior. Experimental study of integer resonance crossing in a nonscaling fixed field alternating gradient accelerator with a paul ion trap. *Phys. Rev. ST Accel. Beams*, 18:034001, Mar 2015.

[58] Zhicong Liu, Chao Li, and Qing Qin. Structure resonance crossing in space charge dominated beams. *Physics of Plasmas*, 26(5):053104, 2019.

[59] William Stem. *Novel Emittance Measurement Through Experimental Study of Envelope Mode Resonance in a High-Intensity Particle Beam.* PhD thesis, University of Maryland College Park, 2018.

[60] Santiago Bernal. Resonances with space charge. July 2017.

[61] K. Ruisard, H. B. Komkov, B. Beaudoin, I. Haber, D. Matthew, and T. Koeth. Single-invariant nonlinear optics for a small electron recirculator. *Phys. Rev. Accel. Beams*, 22:041601, Apr 2019.

[62] L. Dovlatyan, T.M. Antonsen, B.L. Beaudoin, I. Haber, D.B. Matthew, and K.J. Ruisard. Preliminary Lattice Studies for the Single-Invariant Optics Experiment at the University of Maryland. In *Proc. 10th International Partile Accelerator Conference (IPAC'19), Melbourne, Australia, 19-24 May 2019*, number 10 in International Partile Accelerator Conference, pages 367–370, Geneva, Switzerland, Jun. 2019. JACoW Publishing. https://doi.org/10.18429/JACoW-IPAC2019-MOPGW105.

[63] Vladimir Arnold, Valery Kozlov, and Anatoly Neishtadt. *Mathematical Aspects of Classical and Celestial Mechanics.* Springer-Verlag Berlin Heidelberg, 2006.

[64] H. Goldstein, C.P. Poole, and J.L. Safko. *Classical Mechanics.* Addison Wesley, 2002.

[65] F.H. O'Shea, R.B. Agustsson, Y.C. Chen, D.W. Martin, J.D. McNevin, and E. Spranza. Non-linear Magnetic Inserts for the Integrable Optics Test Accelerator. In *Proc. 6th International Particle Accelerator Conference (IPAC'15), Richmond, VA, USA, May 3-8, 2015*, number 6 in International Particle Accelerator Conference, Geneva, Switzerland, June 2015. JACoW.

[66] H. Baumgartner et al. Quantification of Octupole Magnets at the University of Maryland Electron Ring. In *Proc. of North American Particle Accelerator Conference (NAPAC'16), Chicago, IL, USA, October 9-14, 2016*, number 3 in North American Particle Accelerator Conference, pages 503–506, Geneva, Switzerland, Jan. 2017. JACoW.

[67] D. Matthew, W. Curtiss, H. B. Komkov, and B. Beaudoin. Characterization of the nonlinear focusing magnet for quasi - integrable optics experiments at the university of maryland electron ring. In *2018 IEEE Advanced Accelerator Concepts Workshop (AAC)*, pages 1–4, 2018.

[68] J Laskar and D Robin. Application of frequency map analysis to the als.

[69] Frank Zimmermann. Measurement and correction of accelerator optics. (SLAC-PUB-7844):89 p, Jun 1998.

[70] Kamal PoorRezaei. Measuring beam position centroid in quadrupoles. unpublished, 2012.

[71] Auralee Edelen, Christopher Mayes, Daniel Bowring, Daniel Ratner, Andreas Adelmann, Rasmus Ischebeck, Jochem Snuverink, Ilya Agapov, Raimund Kammering, Jonathan Edelen, Ivan Bazarov, Gianluca Valentino, and Jorg Wenninger. Opportunities in machine learning for particle accelerators, 2018.

[72] Levon Dovlatyan and Kiersten Ruisard. Umer controls guide. unpublished, 2017.

[73] G. Portmann, J. Corbett, and A. Terebilo. An Accelerator control middle layer using Matlab. *Conf. Proc. C*, 0505161:4009, 2005.